



HAL
open science

A seismological study of Lucky Strike volcano and hydrothermal field, Mid-Atlantic Ridge

Soumya Bohidar

► **To cite this version:**

Soumya Bohidar. A seismological study of Lucky Strike volcano and hydrothermal field, Mid-Atlantic Ridge. Geophysics [physics.geo-ph]. Université Paris Cité, 2023. English. NNT : 2023UNIP7093 . tel-04551826

HAL Id: tel-04551826

<https://theses.hal.science/tel-04551826>

Submitted on 18 Apr 2024

HAL is a multi-disciplinary open access archive for the deposit and dissemination of scientific research documents, whether they are published or not. The documents may come from teaching and research institutions in France or abroad, or from public or private research centers.

L'archive ouverte pluridisciplinaire **HAL**, est destinée au dépôt et à la diffusion de documents scientifiques de niveau recherche, publiés ou non, émanant des établissements d'enseignement et de recherche français ou étrangers, des laboratoires publics ou privés.



Thèse préparée à l'Institut de Physique du Globe de Paris
Université Paris Cité

École doctorale Sciences de la Terre et de l'environnement
et physique de l'Univers STEP'UP n°560

IPGP - Équipe de Géosciences marines

A seismological study of Lucky Strike volcano and hydrothermal field, Mid-Atlantic Ridge

Par **Soumya BOHIDAR**

Thèse de doctorat de Sciences de la Terre et de l'environnement

Dirigée par **Wayne CRAWFORD**
Co-encadrée par **Mathilde CANNAT**

présenté et défendu publiquement le **17 mars 2023**

Devant jury composé de:

Robert SOHN Senior Scientist, WHOI, USA	Rapporteur
Ingo GREVEMEYER CR-CNRS (GEOMAR, Germany)	Rapporteur
Jean BATTAGLIA CR-CNRS (Université Clermont-Auvergne, France)	Examineur
Karin SIGLOCH DR-CNRS (GEOAZUR, France)	Examinatrice
Wayne CRAWFORD DR-CNRS (IPGP, France)	Directeur de thèse
Mathilde CANNAT DR-CNRS (IPGP, France)	Codirectrice de thèse



Thesis prepared at the Institut de Physique du Globe de Paris
Université Paris Cité

École doctorale Sciences de la Terre et de l'environnement
et physique de l'Univers STEP'UP n°560

IPGP – Marine Geosciences

A seismological study of Lucky Strike volcano and hydrothermal field, Mid-Atlantic Ridge

by **Soumya BOHIDAR**

PhD thesis in Earth and Environment Sciences

Supervised by **Wayne CRAWFORD**

Co-supervised by **Mathilde CANNAT**

presented and publicly defended on **17 March 2023**

In front of a jury composed of:

Robert SOHN Senior Scientist, WHOI, USA	Reporter
Ingo GREVEMEYER CR-CNRS (GEOMAR, Germany)	Reporter
Jean BATTAGLIA CR-CNRS (Universite Clermont-Auvergne, France)	Examiner
Karin SIGLOCH DR-CNRS (GEOAZUR, France)	Examiner
Wayne CRAWFORD DR-CNRS (IPGP, France)	PhD supervisor
Mathilde CANNAT DR-CNRS (IPGP, France)	PhD co-supervisor

“The questions are always more important than the answers.”

- Randy Pausch, *The Last Lecture*

To my parents

Résumé

Les circulations hydrothermales au niveau des dorsales médio-océaniques sont responsables des échanges thermiques et chimiques entre la terre solide et l'océan. Sur les segments de dorsales à propagation lente, on suppose que les circulations hydrothermales sont principalement contrôlées par la tectonique et entraînées par la mise en place épisodique de magma. L'étude de la circulation hydrothermale sur les dorsales lentes est particulièrement difficile car l'emplacement et la taille de la source de chaleur magmatique et la géométrie des voies de circulation des fluides hydrothermaux sont dans la plupart des cas mal définis. Dans cette thèse, j'étudie les caractéristiques spatio-temporelles de la microsismicité sous le volcan Lucky Strike et le champ hydrothermal, Mid-Atlantic Ridge pour comprendre les circulations hydrothermales et les interactions magmato-tectoniques dans un center de dorsale lente magmatiquement riche.

Dans la première partie, j'ai analysé 12 années (non continues) de données de sismomètres fond de mer (OBS) à courte période enregistrées entre 2007 et 2019. Cette étude révèle une sismicité régulière et continue de faible magnitude ($M_L \sim -1$ à 0) juste au nord du champ hydrothermal et $\sim 0.5-2$ km au-dessus du réflecteur axial de la chambre magmatique (AMC). Cette sismicité indique que les processus se produisant à la base de la circulation hydrothermale, tels que la contraction thermique des roches par un refroidissement rapide, éventuellement combinée à une expansion volumique due à la formation de minéraux hydratés et à une fissuration d'extension liée à l'écartement des plaques, sont les principales sources de sismicité dans cette région. Ces processus ne s'excluent pas mutuellement, et nous proposons donc que les changements spatiaux documentés des groupes de sismicité suivent la progression des zones d'extraction de plus forte chaleur dans la partie inférieure de la zone d'écoulement descendant hydrothermique. Le principal changement s'est malheureusement produit pendant un intervalle de données entre juin 2013 et avril 2015 : le principal groupe de sismicité s'est déplacé de ~ 800 m vers l'est et la distribution de la sismicité est passée d'un patch proche de l'AMC à un modèle vertical en forme de tuyau. Nous proposons que ce changement soit dû à des injections magmatiques récentes au-dessus de l'AMC, permettant un refroidissement plus efficace au-dessus de la région moins profonde du toit de l'AMC. Nous observons également trois périodes de

sismicité plus élevée : Avril-Juin 2009, Août-Septembre 2015, et Avril-Mai 2016. La période avril-juin 2009 a été la plus intense, commençant par un événement de magnitude relativement élevée ($M_L = 1.7$), et culminant en juin après un autre événement de plus forte magnitude ($M_L = 1.8$). Nous interprétons cette période de sismicité plus élevée comme résultant d'événements tectoniques ouvrant des canaux locaux de plus grande perméabilité pour les fluides hydrothermaux descendants. Les périodes de sismicité plus élevée de 2015 et 2016 étaient moins prononcées, mais probablement aussi dues à des événements de fissuration améliorant la perméabilité locale.

Dans la partie 2, je me concentre sur la détection de la microsismicité proche du plancher océanique près d'un site hydrothermal (Tour Eiffel; TE) en utilisant environ un an de données d'hydrophones enregistrées entre septembre 2016 et septembre 2017 à partir d'un petit réseau d'ouverture ~ 150 m. Nous détectons 740 événements peu profonds dans la gamme de magnitude locale -4 à $-0,5$. La plupart de ces événements sont dispersés sans aucun regroupement spécifique et ont une limite de profondeur de $\sim 150-250$ m sous le fond marin, parmi lesquels seulement $\sim 10\%$ des événements sont situés à l'intérieur du réseau. En guise d'interprétation préliminaire, nous considérons que ces événements ont pris naissance à la suite d'une fissuration en réponse à la précipitation d'anhydrite. Une interprétation similaire a été proposée pour la microsismicité peu profonde enregistrée sur le site hydrothermal TAG (Trans-Atlantic Geotraverse) (Pontbriand & Sohn, 2014). Les taux de sismicité à Tour Eiffel sont ~ 80 fois moins élevés qu'à TAG, ce qui serait cohérent avec les evidences chimiques d'une précipitation d'anhydrite limitée, voire absente, enregistrée dans les fluides hydrothermaux diffus de TE (Wheeler et al., soumis).

Dans la troisième partie, je présente et évalue l'utilisation de la polarisation des ondes P des événements locaux pour orienter les composantes horizontales des OBS de courte période. Cette technique est couramment utilisée pour les sites à large bande utilisant des événements téléseismiques, mais les sismomètres à courte période ne peuvent utiliser que des événements locaux. Nous montrons que la technique peut fournir des orientations fiables dans certains cas, mais ne sont pas fiables dans de nombreux cas, probablement liées à la structure locale sous la station. Nous proposons une méthode pour déterminer si les orientations locales basées sur la P-pol sont fiables.

Keywords: Microséismicité, circulation hydrothermale, interaction magmato-tectonique, Mid-Atlantic Ridge, dorsales lentes

Abstract

Hydrothermal circulations at Mid-Ocean Ridges are responsible for thermal and chemical exchange between the solid earth and the ocean. At slow spreading ridge segments, hydrothermal circulations are speculated to be predominantly tectonically controlled and driven by episodic magma emplacement. Studying hydrothermal circulation at slow spreading ridges is particularly challenging because the location and size of the magmatic heat source and the geometry of hydrothermal fluid pathways are in most cases poorly constrained. In this thesis, I study the spatiotemporal characteristics of microseismicity beneath Lucky Strike volcano and hydrothermal field, Mid-Atlantic Ridge to understand the hydrothermal circulations and magmato-tectonic interactions in a magmatically robust slow spreading segment center.

In part-1, I analyzed 12 years (non-continuous) of short period ocean bottom seismometer (OBS) data recorded between 2007 and 2019. This study reveals steady and continuous low magnitude seismicity ($M_L \sim -1$ to 0) just north of the hydrothermal field and ~ 0.5 -2 km above the axial magma chamber (AMC) reflector, indicating that processes occurring at the base of hydrothermal circulation, such as thermal contraction of rocks by rapid cooling, possibly combined with volumetric expansion due to the formation of hydrous minerals and extensional cracking related to plate spreading, are the major sources of seismicity in this region. These processes are not mutually exclusive, and we thus propose that the documented spatial shifts of the seismicity clusters track the progression of enhanced heat extraction zones in the lower part of hydrothermal downflow zone. The main shift unfortunately occurred during a data gap between June 2013 and April 2015: the main seismicity cluster moved ~ 800 m eastward and the seismicity distribution changed from a patch close to the AMC to a vertical pipe-like pattern. We propose that this shift was driven by recent magmatic injections above the AMC, allowing for more efficient cooling of hot rocks. We also observe three higher seismicity periods: April-June 2009, August-September 2015, and April-May 2016. The April-June 2009 period was the most intense, starting with a relatively high magnitude event ($M_L = 1.7$), and culminating in June after another higher

magnitude ($M_L = 1.8$) event. We interpret this higher seismicity period to have resulted from tectonic events opening enhanced local permeability channels for downgoing hydrothermal fluids. The 2015 and 2016 higher seismicity periods were less pronounced, yet also probably due to cracking events enhancing the local permeability.

In part-2, I focus on detection of near seafloor microseismicity near one hydrothermal vent site (Tour Eiffel; TE) using ~ 1 year of hydrophone data recorded between September 2016 and September 2017 from a small ~ 150 m aperture network. We detect 740 shallow events in local magnitude range -4 to -0.5 . Most of these events are scattered without any specific clustering and have a depth limit of ~ 150 - 250 m beneath the sea floor, out of which only $\sim 10\%$ of the events are located inside the network. As a preliminary interpretation, we consider these events to have originated as a result of reaction driven cracking in response to anhydrite precipitation. A similar interpretation was proposed for shallow microseismicity recorded at the TAG (Trans-Atlantic Geotraverse) vent site (Pontbriand & Sohn, 2014). Seismicity rates at Tour Eiffel are ~ 80 times less than at TAG, which would be consistent with the chemical evidence for limited to absent anhydrite precipitation recorded in the TE diffuse vent fluids (Wheeler et al., submitted).

In part-3, I present and evaluate using P-wave polarization of local events to orient the horizontal components of short period OBSs. The technique is commonly used for broadband sites using teleseismic events, but short-period seismometers can only use local events. We show that the technique can provide reliable orientations in some cases, but in many cases the orientations are not reliable, probably related to local structure beneath the station. We propose how to determine if local P-pol based orientations are reliable.

Keywords: Microseismicity, hydrothermal circulation, magmato-tectonic interaction, Mid-Atlantic Ridge, Slow spreading ridge

Résumé Substantiel

Près de 70 % de la surface de la Terre est recouverte d'océans, dont la plupart sont encore inexplorés. Le système des dorsales médio-océaniques (MOR), un ensemble continu de chaînes volcaniques sous-marines s'étendant jusqu'à 65 000 km, est l'une des principales caractéristiques du relief des fonds marins. Les dorsales médio-océaniques se trouvent le long des frontières de plaques tectoniques divergentes, où une nouvelle croûte océanique est formée par la remontée de magma lors de la fonte du manteau lorsque les plaques tectoniques s'écartent les unes des autres. Les structures tectoniques et les corps magmatiques associés à l'accrétion des plaques tectoniques forment la base de la circulation hydrothermale dans les MOR. Ce phénomène important est responsable d'échanges thermiques et chimiques importants entre la terre solide et les océans (Elderfield & Schultz, 1996; Lister, 1972; Lowell, 1995).

La morphologie des MOR, l'activité volcanique, la tectonique associées et les circulations hydrothermales sont principalement contrôlées par la vitesse d'expansion du plancher océanique. Dans les segments de MOR avec une expansion rapide/intermédiaire, l'approvisionnement en magma est élevé et il est considéré que des corps magmatiques stables entretiennent les circulations hydrothermales. En revanche, sur les segments de MOR avec une expansion lente/ultralente, on suppose que la circulation hydrothermale est principalement contrôlée par la tectonique et la mise en place épisodique de magma dans la lithosphère peu profonde située à l'axe de la dorsale (Humphris & Cann, 2000; Wilcock & Delaney, 1996). Au niveau des segments de MOR à extension lente, la mise en place et la taille de la source de chaleur magmatique, ainsi que la géométrie des voies de circulation des fluides hydrothermaux sont, dans la plupart des cas, mal connus.

On suppose que l'activité sismique qui se produit au niveau des dorsales est associée à une combinaison de processus volcaniques, tectoniques et hydrothermaux. La signature sismologique spatio-temporelle d'un segment de dorsale peut être utilisée pour comprendre et suivre divers processus dont les failles tectoniques (e.g., deMartin et al., 2007; Parnell-Turner et al., 2017, 2020),

les éruptions volcaniques (e.g., Dziak et al, 2012; Sigmundsson et al., 2015; Wilcock et al., 2016), l'inflation ou la déflation de chambres magmatiques (e.g., Wilcock et al., 2009), et la fracturation et l'altération hydrothermales (e.g., Crawford et al., 2013; Sohn et al., 1999, 2004; Tolstoy et al., 2008). La surveillance à long terme de la sismicité est donc particulièrement importante pour comprendre la structure et la dynamique de l'extension crustale et des processus volcaniques, tectoniques et hydrothermaux associés.

Le volcan Lucky Strike, situé au centre du segment Lucky Strike de la dorsale lente médio-atlantique (MAR), abrite l'un des plus grands champs hydrothermaux profonds connus (Barreyre et al., 2012; Escartin et al., 2015; Fouquet et al., 1995; Humphris et al., 2002; Langmuir et al., 1997; Ondréas et al., 2009). La circulation hydrothermale a pour source de chaleur une chambre magmatique axiale (AMC) présente à ~3.0-3.8 km sous le plancher océanique (Combiere et al., 2015; Singh et al., 2006). Les régions du volcan et du champ hydrothermal sont surveillées en permanence depuis 2007 par une branche de l'Observatoire européen multidisciplinaire des fonds marins et de la colonne d'eau (EMSO-Açores). La surveillance géophysique de l'observatoire comprend un réseau de sismomètres de fond océanique (OBS) redéployés chaque année avec une ouverture de réseau de ~6 km. Ce réseau est conçu pour étudier le système hydrothermal à l'échelle du volcan. L'observatoire comprend également, depuis 2016, un petit réseau d'hydrophones (ouverture ~150 m) près de l'un des principaux sites hydrothermaux où se trouvent des sorties de fluide, ceci afin d'étudier la circulation hydrothermale secondaire et les zones d'écoulement ascendantes peu profondes à l'échelle d'un site hydrothermaux. Dans cette thèse, j'ai étudié les caractéristiques spatio-temporelles de la microsismicité sous le volcan Lucky Strike et son champ hydrothermal au niveau de la MAR, pour comprendre la circulation hydrothermale et les interactions magmato-tectoniques dans un centre au niveau d'un segment de dorsale lente magmatiquement riche.

A l'aide de notre enregistrement de la sismicité par le réseau OBS sur une période de 12 ans de 2007 à 2019, nous avons pu observer une microsismicité persistante située dans un couloir étroit situé le long de l'axe de la MOR du nord au nord-ouest du champ hydrothermal et principalement à 0-2 km au-dessus du réflecteur de l'AMC, pour des magnitudes locales (M_L) entre -1 et 0. Les événements présentent des mécanismes au foyer mixtes entre failles normales,

inverses et décrochantes. Au cours des 12 années de notre expérience, il y a eu au moins deux migrations du principal groupe de sismicité. La première (survenue en juillet 2011) était de ~600 m, et la distribution verticale de la sismicité est restée la même pendant et après cet événement. Cette migration pourrait être un artefact, obtenu par une combinaison fortuite de biais liés au réseau, d'erreurs de sélection et/ou d'un changement de la structure de vitesse de la croûte océanique à faible profondeur. Si elle est réelle, cette migration pourrait avoir été causée par de petits événements tectoniques créant des passages locaux perméables pour la circulation hydrothermale. La deuxième migration de ~800 m vers l'est, vers le bord est du réflecteur de l'AMC, s'est produite entre juin 2013 et avril 2015. Ce déplacement est trop important pour être expliqué par une quelconque combinaison des biais mentionnés précédemment. En outre, la distribution verticale de la sismicité a changé, passant d'un patch relativement plat au-dessus de l'AMC à un motif vertical en forme de tuyau. Ce changement est très probablement dû à de récentes injections de magma dans le bord oriental de l'AMC.

Nous avons observé une période sismique plus intense et plus longue en avril-juin 2009. La période avril-juin 2009 a duré environ 13 semaines (avec un taux de sismicité > 50 événements/semaine pendant la période de plus forte activité) et a commencé par un événement de magnitude plus élevée ($M_L = 1.7$) et a culminé en juin après un autre événement de magnitude élevée ($M_L = 1.8$). Nous proposons que les deux événements de magnitude plus élevée étaient d'origine tectonique et ont conduit à l'ouverture locale de canaux perméables pour les fluides hydrothermaux descendants, ce qui a entraîné une extraction vigoureuse de chaleur via l'hydrothermalisme plus important et une sismicité plus élevée. Nous avons également observé 5 périodes plus courtes de sismicité plus élevée (~7-10 jours chacune, taux de sismicité de 20-30 événements/semaine) survenues en août-septembre 2015, et avril-mai 2016. Les événements de ces périodes ont formé un motif en forme de tuyau entre 1 km sous le réflecteur AMC et près du plancher océanique, tout comme les événements de l'ensemble de la période 2015-2019. En août-septembre 2015, nous avons également observé deux groupes de séquences de migration ascendante, mais l'intensité et l'ampleur de ces événements étaient bien plus faibles que tous les autres phénomènes d'injection de dikes documentés dans d'autres contextes de MOR. Il n'y a pas de preuve concluante qu'un événement significatif d'injection de dike s'est produit pendant la période d'absence de données sismologiques de juin 2013 et d'avril 2015, mais le changement dans

la distribution de la sismicité, la migration vers l'est, les séquences de propagation vers le haut en août et septembre 2015 et un événement d'inflation du plancher océanique fin septembre 2015 suggéré par les mesures géodésiques suggèrent un changement dans l'activité tectono-magmatique du volcan. Ce changement peut avoir impliqué de petites injections de dykes en profondeur à côté du bord oriental de l'AMC ou des événements tectoniques d'extension locaux créant de nouvelles voies pour les fluides hydrothermaux descendants dans la région orientale de l'AMC.

Nous proposons que les processus se produisant à la base de la cellule hydrothermale constituent la principale source de sismicité sous la région du volcan Lucky Strike et que le domaine de circulation hydrothermale est une interface dynamique, contrôlée par des changements spatiaux et temporels de la perméabilité et par de probables injections épisodiques de magma. Les événements sismologiques peuvent être causés par la contraction thermique des roches lors d'un refroidissement rapide et d'une altération hydrothermale, éventuellement combinée à des événements tectoniques liés à l'écartement des plaques et à des injections épisodiques de magma. Ces processus ne s'excluent pas mutuellement : la contraction thermique conduisant à un ensemble initial de fissures pourrait faciliter la circulation locale des fluides et donc l'altération hydrothermale, conduisant à une progression de la contraction thermique et de l'altération dans les roches environnantes. Ainsi, les migrations des clusters de sismicité suivent la progression des zones d'extraction de chaleur favorisée dans la partie inférieure de la zone d'écoulement hydrothermal descendant. Le taux de sismicité (~8 événements/semaine en moyenne) est inférieur à celui observé pour les systèmes hydrothermaux de la dorsale Est-Pacifique et du volcan sous-marin Axial Seamount sur la dorsale Juan de Fuca, ce qui peut s'expliquer par le taux d'extension plus faible du segment Lucky Strike et par un afflux de magma probablement plus faible.

En passant à l'échelle d'un site hydrothermal individuel, je me suis concentré sur la détection de la microsismicité proche du planche océanique près du site hydrothermal Tour Eiffel, en utilisant ~1 an de données enregistrées par un petit réseau d'hydrophones (appelé 'HydrOctopus'). Une sélection des événements proches du fond marin en fonction de la durée des formes d'onde, du nombre de phases et des spectres de fréquence a été réalisé au cours de cette thèse. Les événements sismiques près du plancher océanique sont très courts (< 1 s) avec seulement une phase P directe. L'absence d'une phase PwP visible dans les événements peu profonds est

probablement due à leur très faible libération d'énergie/faible profondeur. Nous avons détecté 740 événements peu profonds (taux de sismicité de ~ 3 événements/jour) avec des magnitudes locales entre -4 et -0,5 entre septembre 2016 et septembre 2017. Les emplacements des événements ne sont pas bien contraints en raison du nombre limité de stations/phases et de notre besoin d'utiliser un modèle simple de vitesse de la croûte supérieure à faible profondeur. Les événements sont principalement dispersés sur la zone de mesure et seulement $\sim 10\%$ d'entre eux sont situés à l'intérieur du réseau. Ils sont situés à une profondeur de $\sim 150-250$ m sous le plancher océanique et nous les interprétons comme étant dus à la fissuration par réaction liée à la précipitation d'anhydrite dans la circulation hydrothermale secondaire. Le taux de sismicité est ~ 80 fois inférieur à celui observé pour la sismicité proche du plancher océanique au niveau du monticule hydrothermal TAG (Pontbriand & Sohn, 2014), ce qui est cohérent avec les preuves chimiques d'une précipitation d'anhydrite limitée à absente enregistrée dans les champs d'événements diffus de Tour Eiffel (Wheeler et al., soumis).

Dans la troisième partie de ma thèse, j'ai présenté et évalué la méthode de polarisation des ondes P (P-Pol) pour orienter les composantes horizontales des sismomètres de fond océanique à courte période (SPOBS) en utilisant la sismicité locale. Dans la plupart des cas, les arrivées d'ondes P sur les SPOBS donnent un contre-azimut constant quelle que soit la direction réelle des événements. Ce phénomène existe sur 4 différents types de SPOBS que nous avons étudiés en utilisant des données provenant de différents environnements marins ainsi que certaines stations d'un réseau de géophones terrestres que nous avons étudiées. Nous émettons l'hypothèse que ce phénomène de contre-azimut constant est un effet des structures locales de subsurface. En raison de ce problème, les orientations P-Pol utilisant des séismes locaux ne devraient être validées que si les événements sources ont une large gamme de contre-azimuts et que l'orientation apparente est cohérente sur ces contre-azimuts. De plus, une station présentant un contre-azimut apparemment constant peut être inutilisable pour l'analyse du champ d'ondes 3D mais pourrait fournir des informations importantes sur les structures locales de subsurface.

Acknowledgements

Pursuing a PhD during the pandemic would not have been possible without the help and support of my supervisors, colleagues, my wonderful friends, and family. Doing this PhD was never about getting a degree, I just hope this experience has made me into a better person.

First, I would like to thank my supervisor, Wayne Crawford, for his constant advice, help and encouragement throughout the past 3 years. I have enjoyed all the meetings with him and appreciate his patience in looking into my rather disorganized codes and helping me with even silly coding mistakes and questions. I appreciate him for calling me every single day during the first lockdown which really inspired me to keep on working in a gloomy period. I would also like to extend my thanks to my co-supervisor, Mathilde Cannat, who has been so patient with me and has helped me understand the geological sense of the subject. Thanks for her critical suggestions and comments which have been really valuable in broadening my knowledge and understanding on the subject. I thank both Mathilde & Wayne for giving me an opportunity to be a part of the Momarsat 2020 cruise which has indeed been one the best experiences of my life. I also thank both for their thorough reviews and corrections on numerous drafts of this thesis which helped me improve my writing and graphical skills.

I thank my thesis committee members Claudio Satriano and Marcia Maia for their constructive remarks during the annual thesis committee meetings. Thanks to Claudio for helping me with NLLoc and other technical data processing errors.

I thank the IPGP OBS team: Daniel Romuald, Simon Besancon and Tom Dumouch for maintaining and helping with yearly OBS deployments. Thanks for answering my numerous questions about the instruments. Thanks to Tom who has been a good friend to me over the past 3 years and has taught me about the OBS deployment and recovery during the Momarsat 2020 cruise. I also thank Onil Goubier who has done the initial data processing on the OBS data. I would also like to thank the entire EMSO-Azores team for maintaining the observatory, and all the cruise members of all Momarsat cruises for helping with the OBS deployments.

Special thanks to other members of the Cannat family: Manon Bickert, Benjmain Wheeler, Jie Chen, Souradeep Mahato, and the newest member Antoine Demont, who have been with me in each step of this PhD. I must say Benjamin has helped me a great deal: understanding Lucky Strike geology, planning for my first cruise, or simply being my permanent French translator.

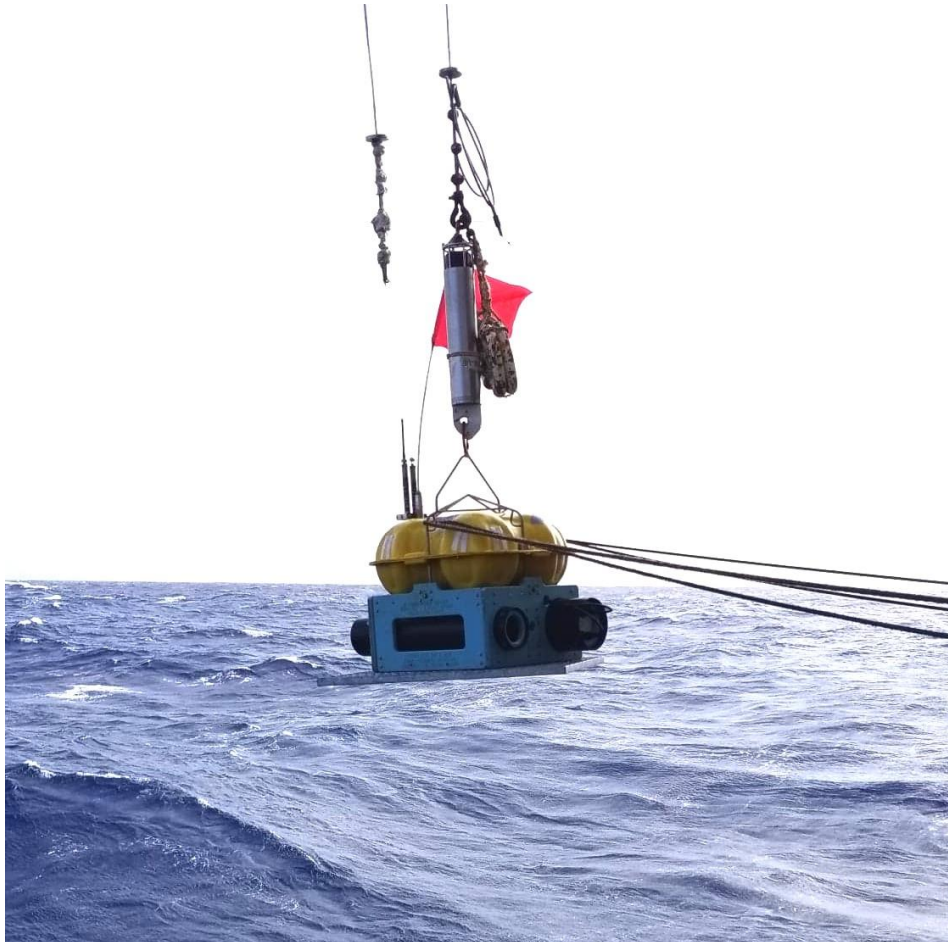
Thanks to Manon who has been so kind and helpful all these years. I thank Jie for being my permanent go to person with all GMT related problems. Many thanks to Souradeep and Nirmal Dhabaria for being wonderful colleagues, friends and flatmates. From finding an apartment in Paris to dealing with French administrations for visa applications and university registrations: all would have been a lot more frustrating without you both.

Thanks to all my officemates: Angele Laurent, Mathurin Wamba & Gaelle Benatre, who have tolerated me with my many zoom meetings, and always inspired me to a great deal. I thank Gaelle, Benjamin, Clement de Sagazan, & Valentine Puzenat for helping me translate the French abstract. I would like to thank Oceane Foix, Aude Lavayssiere and Zhiteng Yu who have helped me in the initial phase of data processing. Thanks to Vaibhav Ingle for helping me with hydrophone analysis. Many thanks to other colleagues from the Marine geoscience team: Pierre Boymond, Zhikai Wang, Venkata Vaddineni, Richard Dreo, & Fei Zhou.

I am grateful to have a wonderful group of friends even if none of them were physically present in Paris. A very special thanks to Ipsika Mohanty, who has been practically the ‘live journal’ of my life. Thanks for listening to all the real and mostly imaginary problems of my life and simply being with me at every step. Thanks to Adyasha Khuntia for those unreturned favors, cooking tips and life hacks for living in Europe. Even if Covid (and partially me!) has ruined all our Europe trip plans, knowing that both live only a few hours from Paris have always been a great solace. Thanks to Aaditya Panigrahi, for all those weekend calls and especially for visiting me and making my rather dull life in Paris a bit happening. I also thank Suman Panda, Srashti Goyal, & Maheshwori Salam for all those cheerful talks. With a special note, I thank Abhilash Borah for being my ‘muse’ all these years.

I am also thankful to all my friends from Maison de L’Inde for making my life in Paris enjoyable. Thanks to all the people of Annex second floor: specially Jahnavi, Akanksha, Youvika & Nathan for all those delicious Indian meals and cheerful parties. I also thank Debasrita Sarkar for being a wonderful partner in exploring Paris and all possible restaurants.

I would like to express my gratitude to my family who have been my safety net all my life. Thanks to my Parents, my brother Shashwat, and everyone else (it’s a long list!) who have supported and encouraged me in pursuing all my dreams. Finally, I am forever grateful to my two little chipmunks, my nieces Alice and Paakhi who have always been my happy place and the honest reason behind my smile.



OBS deployment during Momarsat 2020 cruise. © Soumya Bohidar

CONTENTS

Résumé.....	I
Abstract.....	III
Résumé Substantiel.....	V
Introduction.....	1
Chapter 1 State of the art	5
1.1 Mid-Ocean Ridge system	7
1.1.1 Axial morphology	8
1.1.2 Structure and composition of oceanic lithosphere	10
1.2 Hydrothermal circulation at Mid-Ocean Ridges	11
1.2.1 Zones of hydrothermal circulation.....	13
1.2.2 Effective crustal permeability	14
1.2.3 Heat source: Magma chambers beneath MORs.....	16
1.2.4 Hydrothermal circulation models	20
1.3 Microseismic studies at Mid-Ocean Ridges.....	21
1.3.1 Seismicity due to thermal contraction in the hydrothermal downflow zone	24
1.3.2 Seismicity related to magmatic processes.....	29
1.3.3 Seismicity related to tectonic processes.....	34
1.3.4 Near seafloor hydrothermal circulations and related microseismicity	35
1.4 A magmatically robust slow spreading segment center: The Lucky Strike volcano and hydrothermal vent field, MAR.....	40
Chapter 2 Seismic constraints on hydrothermal circulation and magmato-tectonic interactions beneath Lucky Strike volcano, Mid-Atlantic Ridge	45
2.1 Introduction	47
2.2 Geological context.....	49
2.3 Method	51
2.3.1 Data acquisition and processing.....	51

2.3.2	Earthquake Locations.....	52
2.3.3	Magnitude of completeness and b-value estimation.....	53
2.3.4	Focal Mechanisms	54
2.4	Results	55
2.4.1	Earthquake magnitude distribution.....	57
2.4.2	Temporal variation in seismicity rate, magnitude and depth.....	58
2.4.3	Spatial variation in seismicity.....	62
2.4.4	Focal mechanisms.....	65
2.5	Discussion	67
2.5.1	Sources of seismicity	67
2.5.2	Shifts of the seismicity clusters with time and HSA periods.....	71
2.6	Conclusions	74
	Supplementary materials.....	74
	Supplementary text S2.1 Earthquake relocation in HypoDD.....	76
	Supplementary text S2.2 Tests on event locations.....	76
	Supplementary figures	80
Chapter 3 Detection of near-seafloor microseismicity beneath Lucky Strike vent field, Mid-Atlantic Ridge using a hydrophone array		91
3.1	Introduction	93
3.2	Method	95
3.2.1	Experimental setup.....	95
3.2.2	Events detection and classification.....	97
3.2.3	Magnitude calculation.....	98
3.2.4	Shallow earthquake locations	99
3.3	Results & Discussion	100
3.3.1	Events classification.....	100
3.3.2	Shallow event characteristics.....	103
3.3.3	Event Locations	104
3.3.4	Potential source mechanisms	106
3.4	Summary	108
	Supplementary materials.....	109
	Supplementary text S3.1	109

Supplementary figures	111
Chapter 4 Orientation of horizontal components of short period OBSs using P wave polarization 115	
4.1 Introduction	117
4.2 Dataset	118
4.3 Methodology	121
4.4 Results	123
4.4.1 Lucky strike volcano	124
4.4.2 Offshore Mayotte	124
4.4.3 TAG hydrothermal field	125
4.4.4 Rainbow hydrothermal field	127
4.4.5 Axial Seamount	127
4.4.6 Geysers land network	131
4.5 Discussion	132
4.5.1 Effect of surface structures	132
4.6 Conclusion	133
Data acknowledgement	133
Supplementary Figures	134
Chapter 5 General conclusions and future perspectives	141
5.1 Conclusions	143
5.2 Future perspectives	146
Appendix A Data processing	147
A.1 FIR correction	149
A.2 Data Quality	149
A.3 Time drift correction	151
A.4 Magnitude of completeness (MC) and b-value estimation	154
A.5 Estimation of Vp/Vs (segment scale)	155
A.5 Earthquake locations in NLLoc	156
A5.1 NLLoc programs and control file	157
A5.2 Location using 1D velocity model	158
A5.3 Location using 3D velocity model	160
A.6 Earthquake relocation in HypoDD	162

Appendix B Tests on geophone orientation	163
B.1 Introduction	165
B.2 Instruments and Geometry	165
B.3 Data collection.....	167
B.3.1 Tests on open geophone	167
B.3.2 Tests on a closed geophone in the SPOBS frame	168
B.3.3 Second set of tests on a closed geophone in the SPOBS frame (3rd part).....	169
B.4 Results	170
B.4.1 Open geophone.....	170
B.4.2 Closed geophone	174
B.4.3 Closed geophone (second set of tests).....	176
B.5 Recommendation.....	178
B.5.1 Naming the channels	178
B.5.2 Orientation of sensor in a closed OBS	179
B.5.3 Results of tests on a closed geophone	179
B.5.4 Recommended tests to perform on an SPOBS	180
B.5.5 Orientation in an open geophone case.....	180
References	181

List of Figures

Figure 1.1. Global distribution of submarine hydrothermal fields from InterRidge Vents Database (Beaulieu & Szafranski, 2020).....	8
Figure 1.2. Axial morphologies at (a) fast, (b) intermediate, and (c) slow spreading ridges (after Buck et al., (2005)). V.E.: Vertical Exaggeration.....	9
Figure 1.3. (a) Conceptual sketches of layered and heterogeneous crusts, and corresponding seismic velocity models at fast and slow spreading ridges respectively. (b) Schematic diagram of two magmatic segments along a slow-spreading ridge (Cannat et al., 1995).....	11
Figure 1.4. Heat flow as a function of age of the ocean floor for compiled heat flow data (grey dots) and for LUCKYFLUX data from the Lucky Strike segment, MAR (red dots).....	12
Figure 1.5. Schematic representation of hydrothermal circulation at mid-oceanic ridges.	13
Figure 1.6. (a) Black smoker chimneys (focused vent) at Tour Eiffel vent site and (b) diffuse venting area highlighted by white bacterial mat and mineral deposits in cracks at Y3 vent site in Lucky Strike hydrothermal field, MAR.....	14
Figure 1.7. Global Permeability data set a function of depth from packer and single-hole flow experiments by thermal logs Fisher et al., (2008).....	15
Figure 1.8. A conceptual model for changes in permeability layering in basalt-hosted hydrothermal systems in different spreading rate environments.....	16
Figure 1.9. (a) Depth of the Axial melt lens (AML) identified below seafloor from seismic data at EPR between ~80 N to 100 N, variations coincide with fine-scale tectonic segmentation at the seafloor (Carbotte et al., 2013).	18
Figure 1.10. (a) Axial magma chamber (AMC) imaged by seismic reflections at the slow spreading MAR segment beneath Lucky Strike volcano (Singh et al., 2006). (b) Schematic 3D representation of the AMC and the crustal structure beneath the volcano based on seismic observations. EBF: Eastern Bounding Fault; WBF: Western Bounding Fault (Combier et al., 2015).....	19
Figure 1.11. Hydrothermal heat extraction from the AMC.	20
Figure 1.12. Hydrothermal fluid-flow structure after a simulation time of 100 years considering nonlinear temperature and pressure dependence of fluid's properties.....	21
Figure 1.13. Bathymetric maps from (a) 9050'N EPR, (b) Axial Seamount, JdFR, (c) Endeavour segment, JdFR, (d) TAG, MAR (e) Rainbow massif, MAR showing the key features and hydrothermal fields. Figures taken from Tolstoy et al., (2008); Kelley et al., (2014); Humphris et al., (2015); Horning et al., (2018).	24

Figure 1.14. (A) Body force representation for a thermal cracking event. Contraction is uniform in all directions, but gives rise to (B) cylindrical source volume with horizontal strain due to overburden. Figures taken from Sohn et al., (2004).	25
Figure 1.15. Schematic diagram of an along-axis hydrothermal circulation model beneath 9050'N EPR hydrothermal field based on microseismicity studies.....	27
Figure 1.16. (a) Composite focal mechanism solutions and seismicity patterns (a-1) before, (a-2) during, and (a-2) after 2015 Axial Seamount eruption, (b) Cross-section of focal mechanisms and stress perturbations from injection of magma into a sill between main Endeavour and High Rise hydrothermal fields, Endeavour segment, JdFR; adapted from Wilcock et al., (2009).	28
Figure 1.17. (a) Schematic model of crustal accretion, deformation and hydrothermal circulation at TAG, MAR showing earthquake locations, seismic velocity anomalies; adapted from deMartin et al., (2007). (b) Microearthquake density plot along with multichannel seismic reflectors at Rainbow massif, MAR; adapted from Horning et al., (2018).	29
Figure 1.18. Seismicity cycles at (a) 9 ⁰ 50'N EPR, (b) Axial Seamount, JdFR, (c) Endeavour segment, JdFR based on compilation of different seismic studies.	30
Figure 1.19. Chronology of different eruption events.	32
Figure 1.20. Cross-section of the TAG hydrothermal mound showing (a) dynamics of shallow secondary fluid circulation along with associated mineral precipitation, and (b) subsurface stratigraphy from drill holes of the ODP LEG 158; adapted from Humphris & Tivey, (2000); Tivey, (2007).....	36
Figure 1.21. Shallow seismogenic zone beneath TAG active hydrothermal mound; adapted from Pontbriand & Sohn, (2014).	37
Figure 1.22. (a) Body force representation of mode I cracking and a horizontal penny-shaped opening in the vertical direction in response to anhydrite precipitation in shallow subsurface. (b) Relationship between stress drop, source volume and earthquake size in reaction-driven cracking model. Figures taken from Pontbriand & Sohn, (2014).	38
Figure 1.23. Two-loop models for seafloor hydrothermal circulation, adapted from Lowell et al., (2003).	39
Figure 1.24. Overview maps of Lucky Strike volcano.	41
Figure 1.25. (a) Upper crustal velocity structure and (b) corresponding velocity gradient from Full waveform inversion model; adapted from Arnulf et al., (2014a).	42
Figure 1.26. Hypocenters relocations from the year 2008-2009 beneath Lucky Strike volcano region; adapted from Crawford et al., (2013).	43
Figure 1.27. Conceptual model for hydrothermal convection beneath the Lucky Strike hydrothermal field; adapted from Fontaine et al., (2014).	44

Figure 2.1. Overview of Lucky Strike Volcano, Mid-Atlantic Ridge.....	50
Figure 2.2. 3D seismic P-wave composite ('AA_TS') velocity model used for earthquake locations.....	54
Figure 2.3. Temporal distribution of seismicity beneath Lucky Strike volcano, 2007-2019.	56
Figure 2.4. Magnitude of completeness (M_c) and b-value estimation for seismicity recorded beneath the Lucky Strike volcano, 2007-2019.	57
Figure 2.5. Spatial distribution of seismicity recorded beneath the Lucky Strike volcano, plotted for each successful deployment year (i.e., 4 or more recording OBSs).....	61
Figure 2.6. Spatial shifts in the Lucky Strike volcano seismicity with time	64
Figure 2.7. Upward migration events observed on 27/08/2015 and 10/09/2015. Events are scaled according to magnitudes and color coded according to time.....	65
Figure 2.8. Focal mechanism solutions for 18 events (red dots in Figure 2.3, 2.5) from the 2010-2011 record.. ..	66
Figure 2.9. Modes of hydrothermal circulations focused only to downflow zones.....	70
Figure S2.1. Estimation of V_p/V_s . (a) V_p/V_s calculation using a modified Wadati diagram (Chatelain, 1978). (b) V_p/V_s value vs. average RMS residual of all events.....	80
Figure S2.2. Comparison of locations obtained using composite (AA_TS) model (Green circles) and TS model (Red circles) in NLLoc. Scale and symbols same as Figure 2.5.	81
Figure S2.3. Comparison of locations obtained using NLLoc (Green circles) and HypoDD LS method (Grey circles) using composite (AA_TS) model. Scale and symbols same as Figure 2.5.	82
Figure S2.4. Comparison of locations obtained using NLLoc, HypoDD LS and HypoDD SVD method for the deployment year 2015-2016.....	83
Figure S2.5. Effect of station delays/network-based biases on event locations.	84
Figure S2.6. Derived bootstrap inversion result for an event from each seismicity cluster in 2008-2009 (red), 2011-2013 (green) and 2015-2016 (blue).	84
Figure S2.7. Test on event locations with change in velocity structure.	85
Figure S2.8. (a) Histograms of local magnitudes for 2008-2009 catalog (left Y axis). Cumulative number of earthquakes (black circles, right Y axis) as a function of local magnitude.....	86

Figure S2.9. Event density maps for 3 time periods: (a) 2008-2009, (b) 2011-2013 & (c) 2015-2016.....	86
Figure S2.10. 2008-2009 seismicity locations plotted separately for background events (those outside HSA period) and April-June 2009 HSA period..	87
Figure S2.11. 2015-2016 seismicity locations plotted separately for background events (events outside HSA periods), 2015 and 2016 HSA periods.	88
Figure S2.12. Spatial locations of events which are located below the AMC reflector depth in the deployment years 2008-2009, 2015-2016 and 2018-2019.	89
Figure S2.13. Depth distribution of NLLoc event locations (all events) for the year (a) 2008-2009, (b) 2015-2016 and (c) 2018-2019.	89
Figure S2.14. Number of triggers detected by 3 OBSs (east, south and west OBSs) from July 2012 – May 2016 covering 3 deployments (2012-2013, 2014-2015 & 2015-2016).	90
Figure S2.15. Seismicity detected near the Lucky Strike segment from July 2012 – July 2014 as part of the hydroacousting monitoring of Northern Mid-Atlantic ridge (Perrot, 2012).	90
Figure 3.1. Overview map of the HydrOctopus array.....	96
Figure 3.2. Schematic representation of steps adapted to detect shallow events.....	98
Figure 3.3. Example of a shallow (type-1) event waveform on (a) HydrOctopus hydrophone and (b) N-OBS hydrophone. (c) Frequency spectrum of HydrOctopus hydrophone waveform.....	100
Figure 3.4. Example of an on-volcano deep (type-2) event waveform on (a) HydrOctopus hydrophone, (b) N-OBS hydrophone and (c) N-OBS vertical channel. (d) Frequency spectrum of HydrOctopus hydrophone waveform.....	101
Figure 3.5. Example of a segment end/off-volcano deep (type-3) event waveform on (a) HydrOctopus hydrophone, (b) N-OBS hydrophone and (c) N-OBS vertical channel. (d) Frequency spectrum of HydrOctopus hydrophone waveform.....	101
Figure 3.6. Temporal distribution of (a) shallow events (type-1), (b) on-volcano deep events (type-2), (c) segment end deep events (type-3), and (d) whale songs.....	103
Figure 3.7. Temporal distribution of shallow seismicity located in the vicinity of Tour Eiffel hydrothermal vent site, Lucky Strike hydrothermal field.....	104
Figure 3.8. Spatial distribution of shallow seismicity in the vicinity of Tour Eiffel hydrothermal vent site, Lucky Strike hydrothermal field..	105
Figure 3.9. Spatial distribution of shallow seismicity located inside the HydrOctopus network.....	106

Figure S3.1. Probabilistic Power Spectral Density (PPSD) analysis for all HydrOctopus hydrophones and existing OBS hydrophone channel.	111
Figure S3.2. Example of whale songs. (a) Waveforms on one of the HydrOctopus hydrophone, and (b) corresponding frequency spectrum.....	111
Figure S3.3. Relationship established between hydrophone channel amplitude (pressure) and OBS vertical channel amplitude (displacement) using deeper on-volcano events catalog.	112
Figure S3.4. Horizontal and vertical standard deviation, and Mean RMS values for all shallow upper crustal velocity models with seafloor starting velocity ranging from 1.5 km/s to 3.2 km/s and velocity gradient ranging from 0 to 3.6 (km/s)/km.	112
Figure S3.5. Mean RMS values for all possible HydrOctopus model configurations.....	113
Figure S3.6. Example of a shallow event waveform on (a1-a4) all HydrOctopus hydrophones, and on (b1-b4) all N-OBS channels.....	113
Figure S3.7. P travel time difference between the HydrOctopus hydrophone and N-OBS hydrophone as a function of depth (0-1000 m) of the events.	114
Figure 4.1. Overview map of the dataset and their instrument specification used in this study....	119
Figure 4.2. Principle of P-Pol method.	123
Figure 4.3. Categories of results obtained from local P-Pol measurement.....	124
Figure 4.4. P-Pol result for Mayotte stations.....	126
Figure 4.5. P-Pol result for Rainbow hydrothermal field.	127
Figure 4.6. P-Pol result for Axial Seamount. (a) Event station map. Blue outlined triangles: BBOBSs, Yellow outlined triangles: SPOBSs.	129
Figure 4.7. P-Pol result for Axial Seamount SPOBSs. (a-1 to a-4) Individual P-Pol result using local events. (b-1 to b-4) Individual P-Pol result using teleseismic events.	130
Figure 4.8. P-Pol result from Geysers network.....	131
Figure S4.1. Examples of BAZ uncertainty calculations based on location uncertainty ellipses for 2 Mayotte SPOBSs.	134
Figure S4.2. (a-1 to a-8) Individual P-Pol result from RHUM-RUM experiment using teleseisms.	135
Figure S4.3. P-Pol result from Lucky Strike volcano.....	136

Figure S4.4. (a-1 to a-9) Individual P-Pol result from Mayotte stations (Red triangles in Figure 4a) showing linearly increasing behavior.	137
Figure S4.5. P-Pol result from TAG.	138
Figure S4.6. (a-1 to a-9) Individual P-Pol result from Rainbow hydrothermal field (Red triangles in Figure 5a) showing linearly increasing behavior.....	139
Figure S4.7. Polarity of first P wave arrival of a teleseismic event in SPOBSs and BBOBSs (OO network) in teleseismic P-Pol frequency range (0.07 – 0.1 Hz).	140
Figure S4.8. (a-1 to a-2) Individual P-Pol result from Geysers (Red triangles in Figure 8a) showing linearly increasing behavior.....	140
Figure A1. Example of a FIR corrected waveform.	149
Figure A2. 50th percentile of Probabilistic Power Spectral Density (PPSD) analysis of all OBS channels.....	150
Figure A3. Time drift estimations for the deployments for which no corrections were required.	151
Figure A4. Time drift estimations for the deployments for which corrections were made for one or more OBSs. Offset values are mentioned in the text above.	153
Figure A5. Calculation of magnitude of completeness and b-value for each deployment.	154
Figure A6. V_p/V_s calculation for the entire segment using Wadati diagram	155
Figure A7. Earthquake locations using 1D velocity model, 2D travel time grid for two deployments (2008-2009 & 2015-2016).	159
Figure A8. Earthquake locations using 1D velocity model, 3D travel time grid for two deployments (2008-2009 & 2015-2016).	159
Figure A9. Original (a) TS model and (b) AA model.....	160
Figure A10. Comparison between -19^0 (Left) and $+19^0$ (Right) rotation of the grid (view from the top). Blue lines are Geographic North and East, Pink and Green arrow represents +Y and +X axis of the rotated grid respectively; white circles represent stations.	162
Figure B1. Configuration and wirings of (a) an open geophone and (b) a closed geophone with the sensors' reference directions.	166
Figure B2. Signals of (a1-a3) DAS pin up to down and, (b1-b3) pin down to up for Z^* , S^* and W^* sensors, respectively.	171

Figure B3. Signals of tapping with a cardboard on the (a) top (Z^*), (b) S^* and (c) W^* of an open geophone. 171

Figure B4. Signals of tapping with a rubber hammer on the (a) top(Z^*), (b) S^* , (c) W^* , (d) N^* , and (e) E^* of an open geophone. 172

Figure B5. Signals of jumping at 1 m distance from S^* end in (a-1) Z^* , (a-2) S^* , and (3) W^* sensors. (a-4) & (a-5) are the horizontal and vertical particle motions, respectively. (b1-b5) Same as (a1-a5), but the jumping was performed at 1 m distance from W^* end. 173

Figure B6. Signals of hitting hammer at a distance from S^* end in (a-1) Z^* , (a-2) S^* , and (3) W^* sensors. (a-4) & (a-5) are the horizontal and vertical particle motions, respectively. (b1-b5) Same as (a1-a5), but at a distance from W^* end. 173

Figure B7. Signals of lifting (a-1) Southern (S^*), (a-2) Western (W^*), (b-1) Northern (N^*), and (b-2) Eastern (E^*) end of a closed geophone from a static position. 174

Figure B8. Signals of tapping with a cardboard on the (a) top(Z^*), (b) W^* and (c) S^* of a closed geophone. 175

Figure B9. Signals of jumping at 1 m distance from S^* end in (a-1) Z^* , (a-2) S^* , and (3) W^* sensors. (a-4) & (a-5) are the horizontal and vertical particle motions respectively. (b1-b5) Same as (a1-a5), but the jumping was performed at 1 m distance from W^* end. 175

Figure B10. Signals of hitting hammer at a distance from S^* end in (a-1) Z^* , (a-2) S^* , and (3) W^* sensors. (a-4) & (a-5) are the horizontal and vertical particle motions, respectively. (b1-b5) Same as (a1-a5), but at a distance from W^* end. 176

Figure B11. Signals of lifting (a) Southern (S^*) and (b) Western (W) end of a closed geophone while the opposite end lifted. 177

Figure B12. Signals of (a) slow, and (b) fast lifting the closed geophone entirely. 177

Figure B13. Signals of rotating (a) W^* , and (b) E^* side of the closed geophone to vertical position. 178

Figure B14. Signals of squeezing the hydrophone. 178

Figure B15. Recommended sensor orientations in (a) an open geophone and (b) a closed geophone. 179

List of Tables

Table S2.1. Overview of the OBS data.....	78
Table S2.2. Focal Mechanism solutions	79
Table 4.1. Instrument specifications for dataset used in P-Pol study.....	120
Table 4.2. Orientation results for Mayotte OBSs	125
Table 4.3. Orientation results for Axial seamount OBSs.....	128
Table B1. Configuration and wirings of the geophones.....	166

List of Abbreviations

AMC	·	Axial Magma Chamber
AML	·	Axial Melt Lens
AST	·	Axial Summit Trough
bsf	·	below seafloor
bsfr	·	below seafloor reference
bsl	·	below sea level
EBF	·	Eastern Boundary Fault
EMSO	·	European Multidisciplinary Seafloor and Water column observatory
FIR	·	Finite Impulse Response
FWI	·	Full Waveform Inversion
HSA	·	Higher Seismic Activity
JdFR	·	Juan de Fuca Ridge
LVA	·	Low Velocity Anomaly
MAR	·	Mid-Atlantic Ridge
MOR	·	Mid-Ocean Ridge
MLE	·	Maximum Likelihood Estimation
NTD	·	Non-Transform Discontinuity
OBS	·	Ocean Bottom Seismometer
PDF	·	Probability Density Function
PPSD	·	Probabilistic Power Spectral Density
SWIR	·	Southwest Indian Ridge
TAG	·	Trans-Atlantic Geotraverse
TBL	·	Thermal Boundary Layer
TE	·	Tour Eiffel
WBF	·	Western Boundary Fault

Introduction

Nearly 70% of the Earth's surface is covered by oceans, with most parts still unexplored. The Mid-Ocean Ridge (MOR) system, a continuous range of underwater volcanic chains extending up to 65,000 km, is one of the central features of the seafloor terrain. MORs are divergent plate boundaries, where new crust is formed by upwelling melt from the mantle as tectonic plates spread apart.

Seafloor spreading at MORs typically involves a combination of volcanic and tectonic processes. The newly formed lithosphere is highly faulted and fissured, providing pathways for seawater to penetrate the crust. As the seawater moves deep into the crust, it can be heated by magma bodies, producing hot and chemically active fluid through mineral exchange with the surrounding rocks. When the fluids are sufficiently buoyant due to heating, they can rise back to the seafloor. The entire process creates the context of 'hydrothermal convection' at MORs, which is an important phenomenon responsible for thermal and chemical exchange between the solid earth and the ocean (Elderfield & Schultz, 1996; Lister, 1972; Lowell, 1995).

MOR morphologies, associated volcanic, tectonic activity and hydrothermal circulations are predominantly controlled by seafloor spreading rate. At fast/intermediate-spreading ridge segments, the magma supply is high and steady state magma bodies are believed to sustain the hydrothermal circulations. At slow/ultraslow-spreading ridge segments, on the other hand, hydrothermal circulation is speculated to be predominantly controlled by tectonism and episodic magma emplacement in the shallow axial lithosphere (Humphris & Cann, 2000; Wilcock & Delaney, 1996). At slow-spreading ridge segments, the location and size of the magmatic heat source, and the geometry of hydrothermal fluid pathways in most cases are poorly constrained.

Seismicity occurring at MORs is inferred to be associated with a combination of volcanic, tectonic, and hydrothermal processes. The spatiotemporal seismological signature of a MOR

INTRODUCTION

segment can be used to understand and track various processes, including tectonic faulting (e.g., deMartin et al., 2007; Parnell-Turner et al., 2017, 2020), volcanic eruptions (e.g., Dziak et al., 2012; Sigmundsson et al., 2015; Wilcock et al., 2016), inflation or deflation of magma chambers (e.g., Wilcock et al., 2009), and hydrothermal cracking and alteration (e.g., Crawford et al., 2013; Sohn et al., 1999, 2004; Tolstoy et al., 2008). Long-term monitoring of seismicity is particularly important in understanding the structure and dynamics of crustal extension and related volcanic, tectonic, and hydrothermal processes.

Lucky Strike volcano, located at the center of the Lucky Strike segment of the slow-spreading Mid-Atlantic Ridge (MAR), hosts one of largest known deep sea hydrothermal fields (Barreyre et al., 2012; Escartin et al., 2015; Fouquet et al., 1995; Susan E. Humphris et al., 2002; Langmuir et al., 1997; Ondréas et al., 2009). The hydrothermal circulation acquires heat from an axial magma chamber (AMC) present ~3.0-3.8 km beneath the seafloor (Combiér et al., 2015; Singh et al., 2006). The volcano region and hydrothermal field has been constantly monitored since 2007 by a node of the European Multidisciplinary Seafloor and water-column Observatory (EMSO-Azores). The geophysical monitoring of the observatory includes an array of yearly redeployed ocean bottom seismometers (OBSs) with a network aperture of ~6 km, which is designed to survey the volcano-scale hydrothermal system. The observatory also includes, since 2016, a small hydrophone network (aperture ~150 m) near one of the main hydrothermal vent sites, to investigate secondary hydrothermal circulation and shallow upflow zones at the scale of individual vent sites.

In this thesis, I study the spatiotemporal characteristics of seismicity beneath Lucky Strike volcano and its hydrothermal field, to understand the hydrothermal processes and magmato-tectonic interactions within a magmatically robust slow spreading segment center.

I study the overall hydrothermal circulation geometry and its evolution over time and evaluate the respective roles of magmatic and tectonic processes in controlling circulation patterns, by constraining the spatial distribution, time-variability of microseismic activity and its source mechanisms from the analysis of OBS network data recorded between 2007 and 2019. I then focus on detection of near seafloor microseismicity, to constrain near-seafloor hydrothermal circulation

INTRODUCTION

at the scale of an individual hydrothermal vent site. by analyzing ~1 year of hydrophone network data (September 2016 – September 2017, covering two consecutive deployments).

Thesis organization

This thesis comprises five main chapters and two appendices.

In chapter 1, I introduce the state-of-the-art understanding of the Mid-Ocean Ridge system, focusing on hydrothermal convection at mid-oceanic ridges, its controlling factors and circulation models. I provide a detailed summary of seismological studies carried out in different mid-ocean ridge settings and how they are used to understand the underlying processes. In the third part of this chapter, I summarize the geological context of Lucky Strike volcano and our current understanding of its hydrothermal field and circulation. This chapter establishes the bases for the work in chapters 2-4.

Chapter 2, a manuscript to be submitted to *Journal of Geophysical Research: Solid Earth*, focuses on the long-term microseismicity recorded by the volcano scale OBS network and addresses questions regarding the sources of seismicity beneath the volcano region, the geometry of hydrothermal circulation and its evolution over time.

Chapter 3 focuses on the detection of near seafloor microseismicity near one of the hydrothermal vent sites (Tour Eiffel) using a small hydrophone network. I provide a first order picture of shallow microearthquake locations in the vicinity of the Tour Eiffel vent site and discuss their possible source mechanisms.

Chapter 4 presents and evaluates a technique to orient the horizontal components of short period OBSs, based on P wave polarization using local seismicity. This work was initially started to better constrain the focal mechanisms of the earthquakes detected by the Lucky Strike OBS network but was later expanded to study other short period OBSs deployed in several other marine environments, as well as one land geophone network.

INTRODUCTION

Chapter 5 summarizes the general conclusions of my thesis and presents perspectives for future work.

Appendix-A contains detailed data processing steps carried out for the OBS data analysis. Appendix-B summarizes results from the tests conducted on the INSU-IPGP short-period OBS both directly on the geophones and on a closed short-period OBS and gives a 'standard' geophone orientation and a series of recommended tests that can be performed to test the orientation of the geophones before deployment.

Chapter 1
State of the art

1.1 Mid-Ocean Ridge system

The Mid-Ocean Ridge (MOR) system forms and evolves because of spreading of Earth's lithosphere at the divergent plate boundaries. The theory of seafloor spreading was first proposed by Hess, (1962). Mantle convection and upwelling beneath the MORs is driven by the heat from radioactive decay of mantle and other thermal processes, and magmas generated from the decompression melting of the upwelling mantle along the MORs are then intruded into the crust and erupted at the surface, forming the new oceanic crust. The global MOR has a total length of about 65,000 km with a zone of active accretion ~5-50 km wide (Figure 1.1).

The MOR system exhibits significant volcanic and tectonic activity. Tectonic fractures and magma bodies associated with volcanic activity form the basis of hydrothermal circulation at the MORs (Figure 1.1). Hydrothermal convection is an important phenomenon responsible for thermal and chemical exchange between the solid earth and the ocean. Seismicity is one of the common proxies to understand the magmatic, tectonic processes and the hydrothermal convection at MORs. Seismicity at MORs is associated with all these processes, can have different spatial-temporal characteristics based on the dominant controlling factor and can therefore provide vital information about these processes and the MOR system.

Volcanic, tectonic, and hydrothermal processes differ at various parts of MORs, and the local spreading rate is a primary factor of control. Based on the spreading rate, MORs are subdivided into superfast (> 120 mm/year, e.g., Southern East Pacific Rise), fast (> 80 mm/year, e.g., Northern East Pacific Rise), intermediate (< 80 to > 40 mm/year, e.g., Juan de Fuca Ridge), slow (< 40 to > 20 mm/year, e.g., Mid-Atlantic Ridge), and ultraslow (< 20 mm/year, e.g., Southwest Indian Ridge) spreading ridges (Figure 1.1). These differences in spreading rate give rise to distinct mid-ocean morphologies with different volcanic and tectonic features.

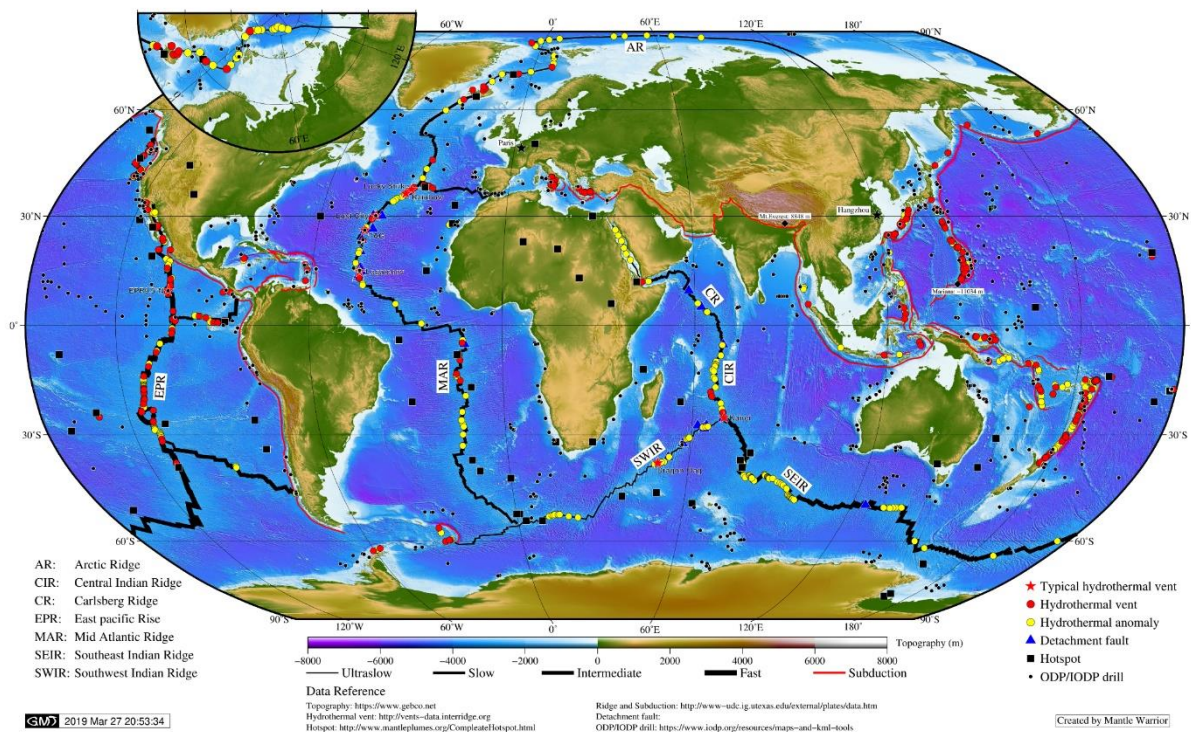


Figure 1.1. Global distribution of submarine hydrothermal fields from InterRidge Vents Database (Beaulieu & Szafranski, 2020). Black line: Mid-ocean ridges, Red line: Subduction zones. Red circles: Active hydrothermal fields, Red stars: most studied, and Yellow circles: unconfirmed hydrothermal activity. Map Courtesy: Jie Chen, IPGP. Bathymetry map of global Mid-Ocean Ridge, hydrothermal vent fields, and detachment faults. doi: 10.6084/m9.figshare.14680419.v1. <https://ndownloader.figshare.com/files/28754505>.

1.1.1 Axial morphology

At fast-spreading ridges, a continuous axial high is present, 2-10 km wide and a few hundred meters higher than the surrounding seafloor (Figure 1.2; Carbotte & Macdonald, 1992; Macdonald et al., 1984; Macdonald et al., 1991). The axial high is probably an isostatic response to the presence of melt in the shallow crust and asthenospheric mantle below the ridge (Madsen et al., 1984; Wang & Cochran, 1993). Axial high crests typically have axial summit troughs (ASTs), which are less than ~500 m wide and ~50 m deep (Figure 1.2a; Fornari et al., 1998; Soule et al., 2009). Overall, the axial high is relatively smooth, indicating robust and relatively uniform melt supply along the whole segment (e.g., Macdonald, 2001; Small, 1998).

CHAPTER 1. STATE OF THE ART

Slow and ultra-slow spreading ridges are characterized by 1-3 km deep rift valleys which are several tens of kilometers in width (Figure 1.2c). The rift valley is usually bounded by two well developed, conjugate normal faults dipping towards the spreading center on both sides and the rift valley walls rise in a series of terraces bounded by steep fault scarps. Melt supply is predominantly focused beneath the segment centers, and segment ends receive less melt with a thinner magmatic layer (Figure 1.3b; Cannat, 1993; Lin et al., 1990; Tolstoy et al., 1993). As a result, a significant part of the plate divergence at the slow-spreading ridge segment is accommodated by large offset normal faults or detachment faults (Cannat, 1993; Escartín et al., 2017; Escartín & Canales, 2011). Volcanic activity mainly takes place within the axial valley to form an axial volcanic ridge (e.g., Mendel et al., 2003; Parson et al., 1993; Searle et al., 2010) or a dome shaped volcano (e.g., Escartín et al., 2014).

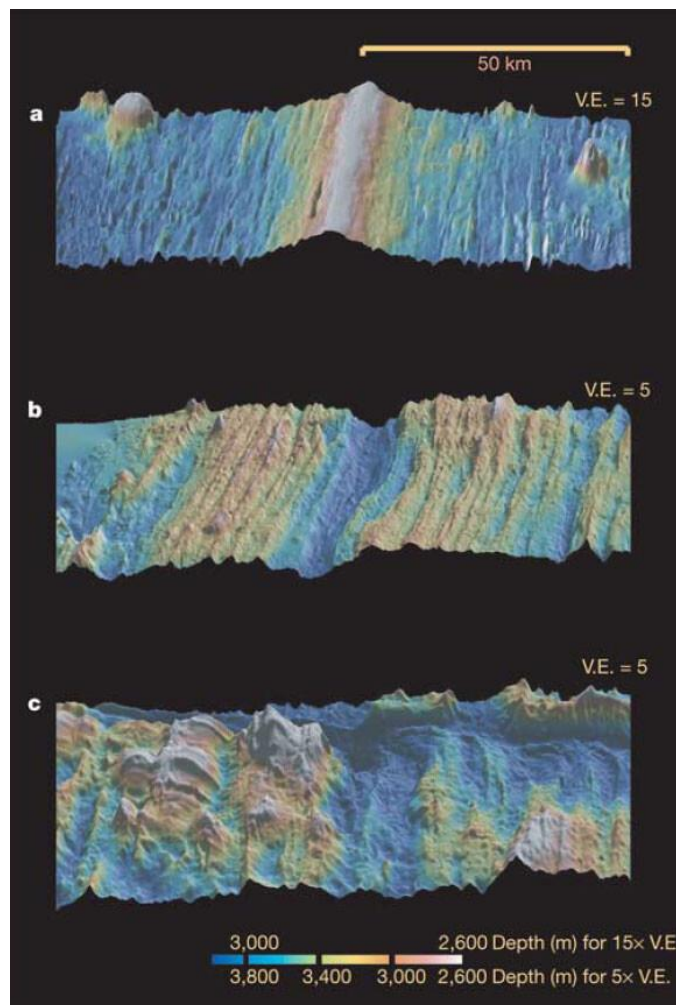


Figure 1.2. Axial morphologies at (a) fast, (b) intermediate, and (c) slow spreading ridges (after Buck et al., (2005)). V.E.: Vertical Exaggeration.

1.1.2 Structure and composition of oceanic lithosphere

The oceanic lithosphere is composed of crust and underlying upper mantle. Based on petrological and seismic studies at fast-spreading ridges (Raitt, 1963; Spudich & Orcutt, 1980), the crustal part of the lithosphere can be divided into three layers (Figure 1.3a), proposed at a Penrose conference (Penrose, 1972).

In the Penrose model, crustal layer 1 is composed of accumulated sediments with low seismic P-wave velocities ($V_p < 2.5$ km/s). This layer is generally absent near the ridge axis and gradually thickens as the crust ages (Searle, 2013). Crustal layer 2 is characterized by a sharp velocity gradient ($\sim 1-2$ s⁻¹) and can be further subdivided into layers 2A and 2B. Layer 2A has seismic P-wave velocities < 4.5 km/s (Carlson, 1998; Christeson et al., 1994) and is made up of extrusive basaltic lavas; while layer 2B has V_p in the range of 5-6.5 km/s, corresponding to the deeper basalts and sheeted dikes. A strong gradient zone between layers 2A and 2B, characterized by triplications on seismic sections, has been interpreted as corresponding to the transition from intrusive (dikes) to extrusive (lava) rocks (Christeson et al., 1992; Harding et al., 1993). However, it is also argued that the layer 2A/2B boundary does not always correlate to the structural boundary between lava and dikes but represents an alternation boundary related to hydrothermal alteration and sealing (Christeson et al., 2007). Below crustal layer 2, layer 3 is composed of crystallized gabbros and has a thickness of ~ 4.5 km (Christeson et al., 2019). Layer 3 is seismically characterized by a V_p of approximately 7.6-7.8 km/s and a low velocity gradient (White et al., 1992). Below crustal layer 3 is the upper mantle composed of peridotite. The boundary between the crust and upper mantle is termed as the Moho interface, where V_p increases rapidly to > 7.9 km/s.

At slow and ultraslow spreading ridges, the crustal composition estimated from seismic data is more heterogeneous (Figure 1.3). At the segment centers, the crustal structure is layered and similar to that found at fast and intermediate spreading ridges. But at some segment ends, the crustal structure is not layered, rather the velocity increases linearly with depth. Here, the oceanic crust contains a mixture of lava, gabbros and serpentinized mantle rocks that have been exhumed along detachment faults (Cann et al., 1997; Cannat, 1993; Escartín et al., 2017; Sauter et al., 2013; Tucholke et al., 2008).

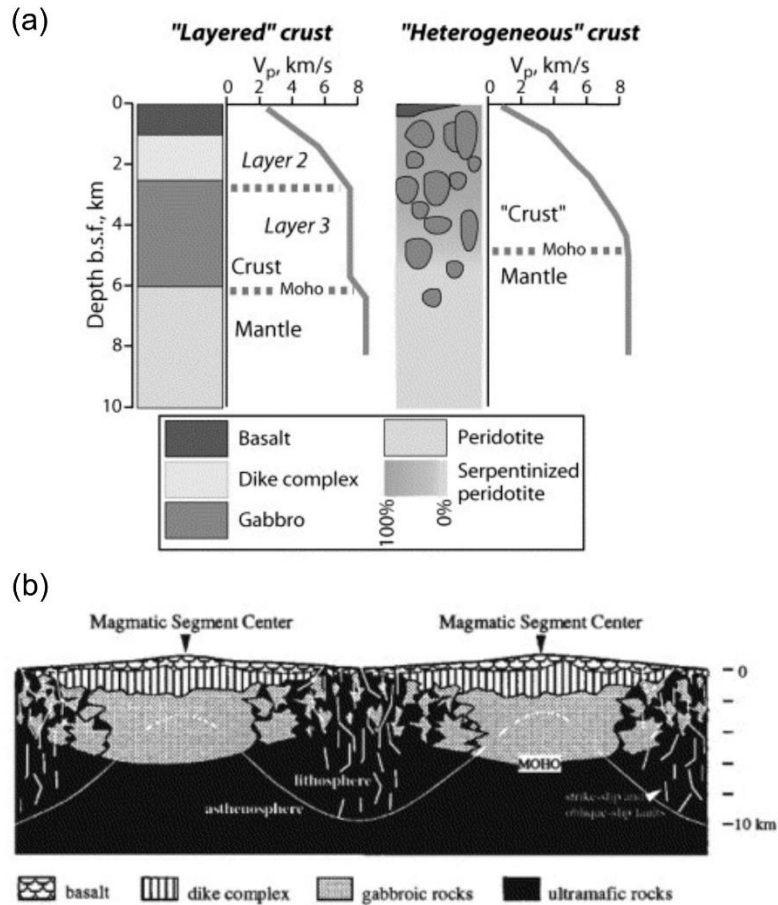


Figure 1.3. (a) Conceptual sketches of layered and heterogeneous crusts, and corresponding seismic velocity models at fast and slow spreading ridges respectively, based on lithological interpretation and seismic velocity profiles (Mével, 2003). (b) Schematic diagram of two magmatic segments along a slow-spreading ridge (Cannat et al., 1995). The lithosphere progressively thickens from segment centers to segment ends.

1.2 Hydrothermal circulation at Mid-Ocean Ridges

Hydrothermal vents at MORs were first directly observed in 1977 at the Galapagos spreading center, where a low temperature hydrothermal circulation system and a unique chemo-synthetic ecosystems thriving on the fluid and heat coming from the interior of the Earth were discovered (Corliss et al., 1979; Edmond, Measures, Mangum, et al., 1979; Edmond, Measures, McDuff, et al., 1979; Lonsdale, 1977). In 1979, the first high temperature hydrothermal vents (black smokers) were reported at the East Pacific Rise (EPR) and massive seafloor sulfides deposits were first explored (Spiess et al., 1980). Even before the direct observation of hydrothermal vents, multiple lines of arguments supported the existence of sub-seafloor hydrothermal circulation, including the discovery of red brine in the red sea and the discovery of metal rich deposits in boreholes and

ophiolites. The most striking clue was the discrepancy between the numerous heat flow measurements close to the MORs conducted during the exploration of the new theory of plate tectonics and the heat flow predicted by the conductive cooling model (Figure 1.4).

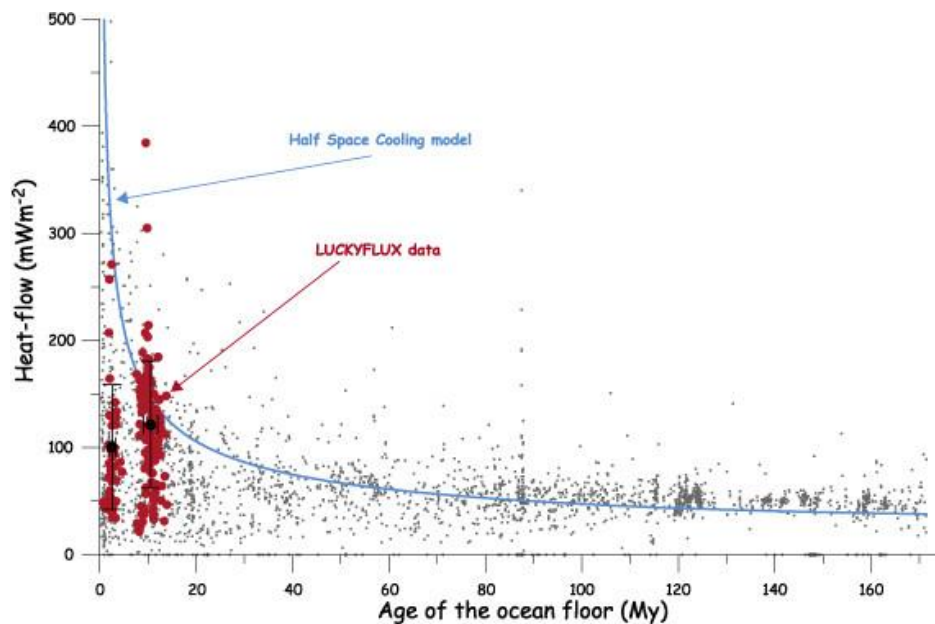


Figure 1.4. Heat flow as a function of age of the ocean floor for compiled heat flow data (grey dots) and for LUCKYFLUX data from the Lucky Strike segment, MAR (red dots). The blue line is the half space cooling model predictions for the heat flow as a function of the age of the oceanic crust. Figure taken from Lucazeau et al., (2006).

Today, more than 700 hydrothermal fields have been identified at all types of spreading ridge segments of the MORs (Figure 1.1). These discoveries provide evidence for hydrothermal circulation transporting heat and chemicals from the interior of the Earth to the seafloor (Lowell, 1995). Hydrothermal circulation accounts for approximately $1/3^{\text{rd}}$ of the global oceanic heat flux, and $\sim 30\%$ of this hydrothermal heat flux occurs at axial crust younger than 1 Ma (Lucazeau, 2019; Stein & Stein, 1994).

1.2.1 Zones of hydrothermal circulation

Hydrothermal circulation at MORs can be divided into three regions: recharge, reaction, and discharge zones (Figure 1.5a, e.g., Humphris & McCollom, 1998). Near-freezing seawater penetrates to volcanic layers in the ‘recharge zone’ (also called the ‘downflow zone’), driven by high porosity and permeability of near-surface volcanic rocks. The seawater cools the rocks and low-temperature reactions occur between the seawater and the rocks. As the fluids flow downward, permeability decreases and the temperature of the surrounding rock increases. The temperature of the rocks is maximum just above the heat source (typically a magma chamber at several km depth) in the ‘reaction zone’ (also called the ‘thermal/conductive boundary layer’), where high temperature reactions lead to the exchange of heat and chemicals between the hydrothermal fluid and the surrounding rocks (Figure 1.5b). As the fluids are heated, buoyancy drives them upwards into the ‘discharge zone’ (also called the ‘upflow zone’), where the hydrothermal fluids come out to the surface and mineral precipitation occurs.

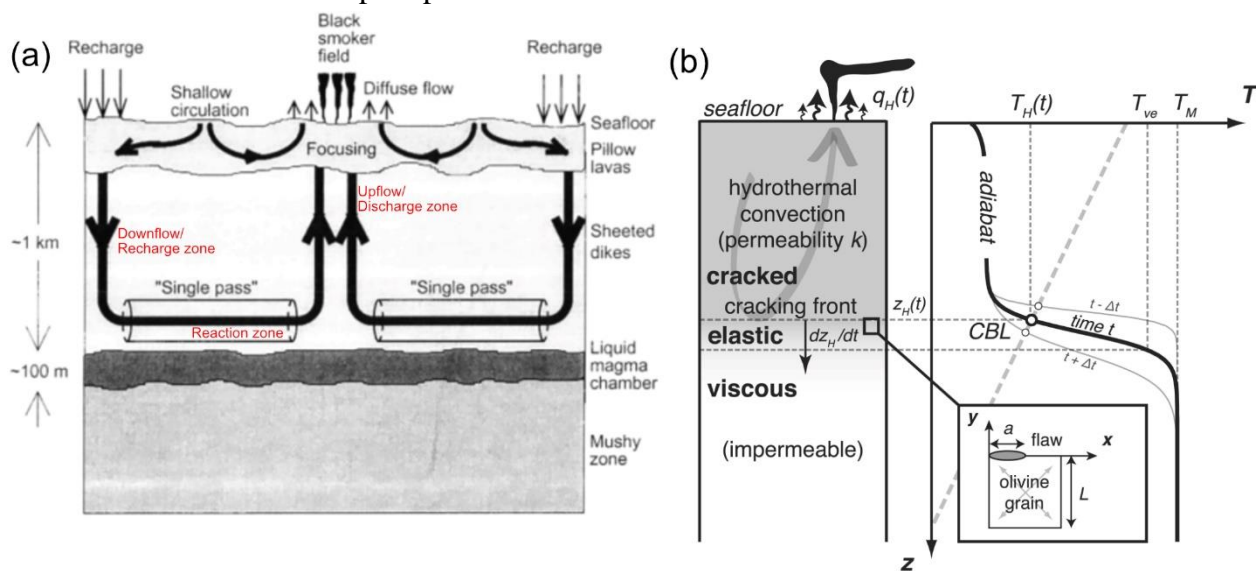


Figure 1.5. Schematic representation of hydrothermal circulation at mid-oceanic ridges. (a) One hydrothermal circulation cell can be divided into three zones: Recharge, reaction, and discharge zone; modified after Lowell & Germanovich, (1997). (b) Heat transfer from deep viscous hot rocks to the ocean. Heat is first conducted upward through a conductive boundary layer (CBL), and then taken by the hydrothermal convection system; adapted from Olive & Crone, (2018).

Sub-seafloor permeabilities affect the type of hydrothermal fluids discharged at the seafloor. If the hydrothermal fluids are focused along a high permeability pathway, high temperature and metal-rich focused hydrothermal venting occurs through black smokers (Figure

1.6a). High-temperature venting indicates that hot hydrothermal fluid did not cool much in the upflow zone, and its chemical signature is largely preserved due to limited interactions with the surrounding rocks (Edmond, Measures, Mangum, et al., 1979). Alternatively, when the hydrothermal fluids mix with the cold seawater and mineral precipitation occurs below the surface, mineral-poor fluids are released in white smoker vents or as diffuse flow (Figure 1.6b).

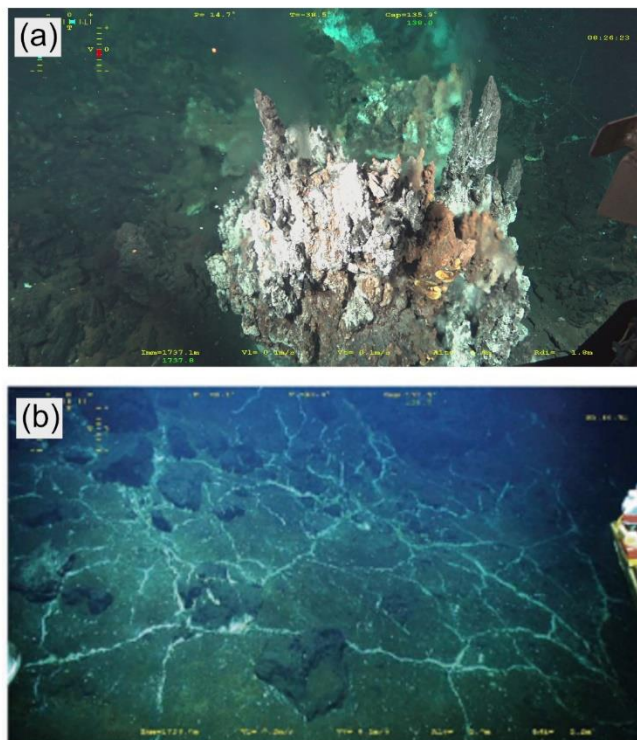


Figure 1.6. (a) Black smoker chimneys (focused vent) at Tour Eiffel vent site and (b) diffuse venting area highlighted by white bacterial mat and mineral deposits in cracks at Y3 vent site in Lucky Strike hydrothermal field, MAR.

1.2.2 Effective crustal permeability

Permeability steers the fluid circulation in the seafloor: both sea water infiltration and upflowing hydrothermal fluids (Lowell & Burnell, 1991). Permeability is highly heterogeneous in space and time; and can be quantified differently depending on the site and scale of measurement. While laboratory rock samples give estimates of permeability in small scale systems; direct in situ measurements such as drill string packers and cross-holes quantify bulk permeability at the scale of a few hundred meters (Figure 1.7; Fisher et al., 2008). There are also indirect geophysical measurements from seismic data using porosity-permeability relationship (Carlson, 2014; Evans,

CHAPTER 1. STATE OF THE ART

1994; Marjanović et al., 2019), and poroelastic response of the hydrothermal systems to tidal loading (Barreyre, et al., 2014a, b; Barreyre et al., 2018; Barreyre & Sohn, 2016), which are used to infer crustal permeabilities on the ridge axis where direct measurements are not possible. These indirect methods give the effective crustal permeability (representing the permeability of a single layer stretching between the magma chamber and the seafloor directly below venting sites) of the hydrothermal system. Based on the phase lag estimates between the observed exit-fluid temperature at the hydrothermal vents and the tide-related pressure head in the surrounding water column, the effective permeability of layer 2A in the upflow zone of black smoker fields ranges between 10^{-13} and 10^{-10} m², and for layer 2B it ranges between 10^{-17} to 10^{-12} m² (Barreyre et al., 2018).

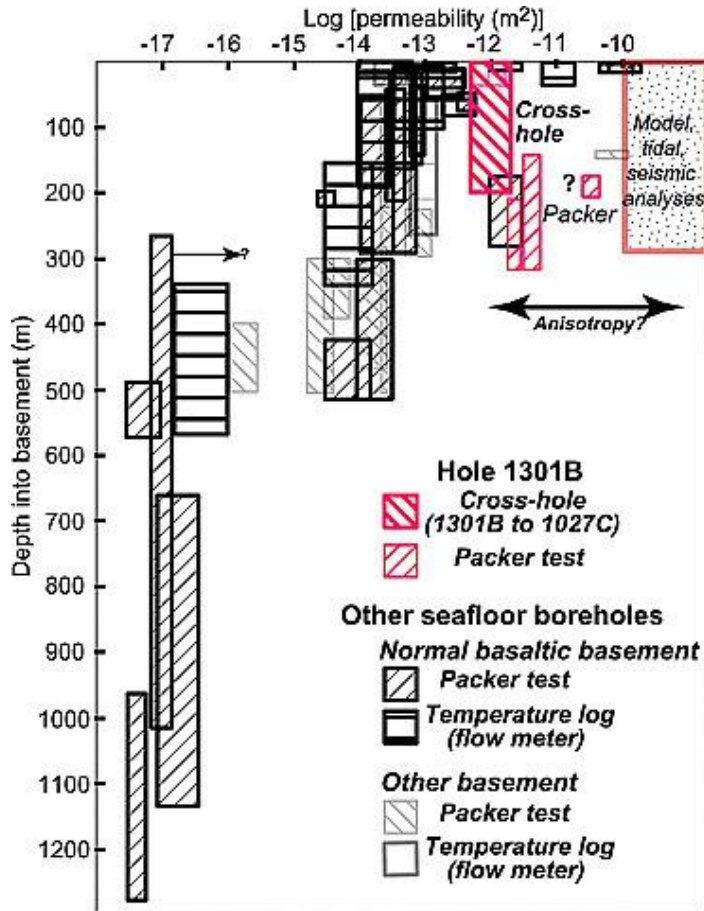


Figure 1.7. Global Permeability data set as a function of depth from packer and single-hole flow experiments by thermal logs Fisher et al., (2008).

CHAPTER 1. STATE OF THE ART

Figure-1.8 (Barreyre et al., 2018) illustrates the conceptual framework describing the variability of effective permeability of the discharge zone in layer 2A and 2B w.r.t the spreading rate. At slow spreading ridges, the upper crust is relatively thick and more tectonized by faults and fissures, leading to high permeability. On the contrary, at fast spreading ridges magmatic processes accommodate most of the plate spreading and the upper crustal structure therefore is less tectonized and frequently clogged by lava flows, which results in a lower permeability system.

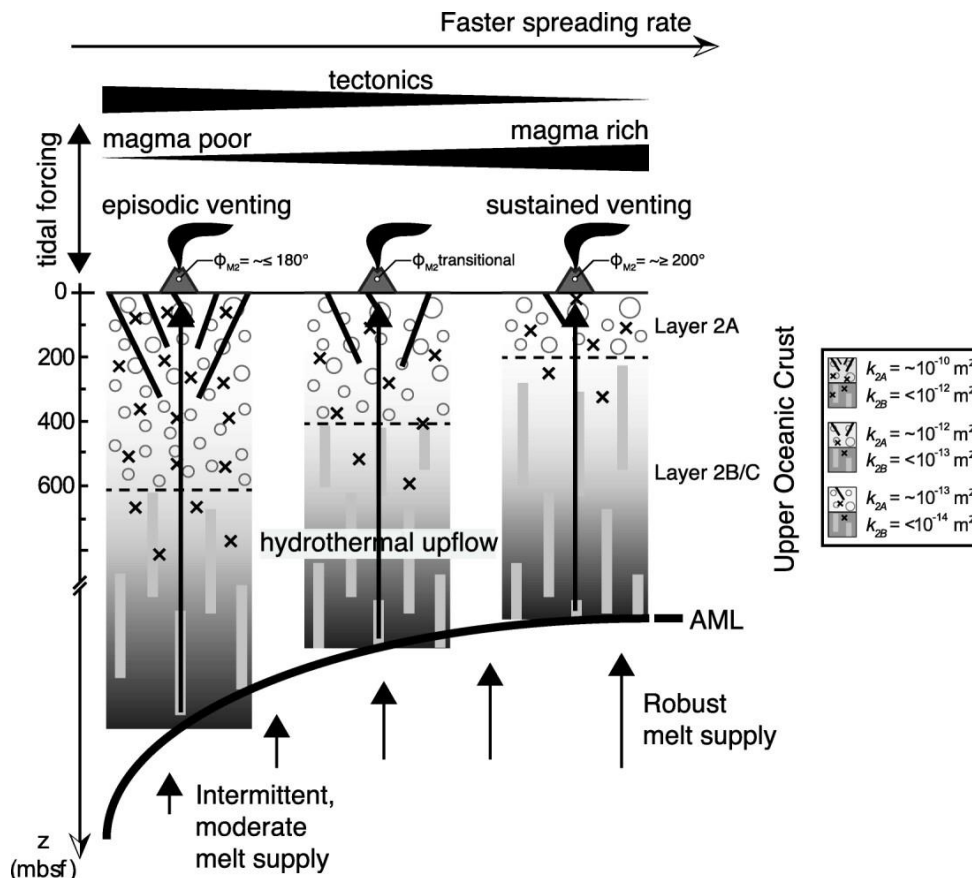


Figure 1.8. A conceptual model for changes in permeability layering in basalt-hosted hydrothermal systems in different spreading rate environments. The increase in permeability in layer 2A upflow zone with decreasing spreading rate is due to increasing tectonic processes. Figure taken from Barreyre et al., (2018).

1.2.3 Heat source: Magma chambers beneath MORs

Geochemical observations suggest that the majority of lavas erupted at MORs at all spreading rates have been modified from their original composition, suggesting that primary magma is modified by crystal fractionation, presumably in magma reservoirs within the crust

(Sinton & Detrick, 1992), which are called axial magma chamber (AMC). High-temperature hydrothermal activity on fast- and intermediate spreading ridge segments and at magmatically robust slow spreading segment centers is mostly driven by heat released from these AMCs. Most of the AMCs are detected by the presence of a low-velocity anomaly (LVA) zone in the mid-to-lower crustal layer or by a high-amplitude, sub-horizontal reflector corresponding to the roof of the AMCs detected in seismic reflection/refraction studies (e.g., Harding et al., 1993; Singh et al., 2006; Toomey et al., 1994; Vera et al., 1990), and in seafloor compliance studies (Crawford et al., 1999). The LVA zones are interpreted as crystal mush zone (Dunn et al., 2000) and the amount of melt and melt fraction is estimated by the percentage of decrease in seismic velocities (e.g., 26-60 m³ at the Axial Seamount in Juan de Fuca Ridge (JdFR) with melt fraction up to ~65%; Arnulf et al., 2018).

The shape and dimensions of the AMCs are best constrained on the fast-spreading ridges and some magmatically robust segments of intermediate spreading ridges. For example, At EPR between ~8°N to 10°N, the roof of the AMCs is located 1.2-2.4 km below the seafloor (bsf) and form 5- to 15- km long segments and coincide with fine-scale tectonic segmentation at the seafloor (Figure 1.9a; Carbotte et al., 2013). Recent studies also reveal multi-sill magma bodies or stacked magma lenses at these segments, which may result from porous flow and mush compaction. The deeper sub-magma bodies replenish the main shallower magma bodies and can be drained during eruptions (Figure 1.9b, c; Carbotte et al., 2021; Marjanović et al., 2014, 2018).

At slow and ultraslow spreading segments, the lithosphere is generally thicker and colder and hosts a deeper and more complex magma plumbing system (Cannat, 1993; Cannat et al., 1995; Sinton & Detrick, 1992). So far, LVAs and/or AMLs have only been found by seismic studies at the center of magmatically-robust segments of slow and ultraslow spreading ridges; for example at MAR Lucky Strike segment (Figure 1.10) (Combiér et al., 2015; Seher et al., 2010; Singh et al., 2006), the Reykjanes Ridge 57°N (Sinha et al., 1997), and the Southwest Indian Ridge (SWIR) segment 50°28'E (Jian, Chen, et al., 2017; Jian, Singh, et al., 2017). At Rainbow massif in MAR, seismically imaged reflectors have also been interpreted as magmatic sills (Canales et al., 2017). Rifting of the dome shaped volcanoes by axial graben faults in these areas suggests a non-steady state melt supply (Chen et al., 2021; Escartín et al., 2014; Klischies et al., 2019).

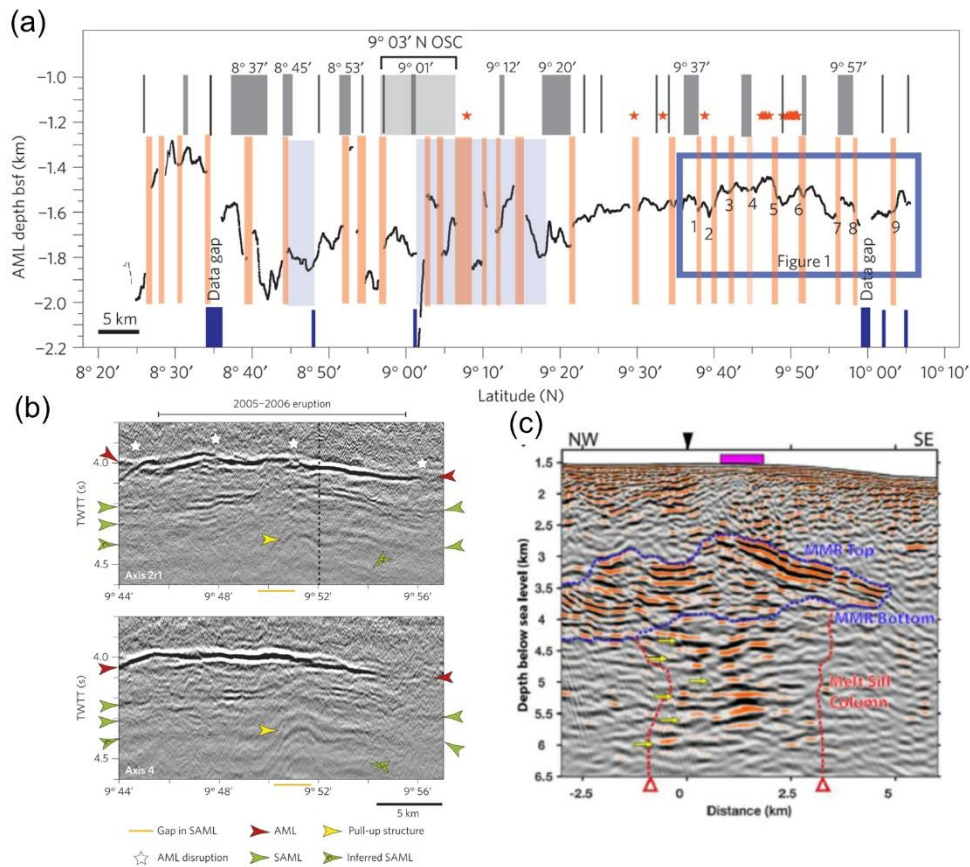


Figure 1.9. (a) Depth of the Axial melt lens (AML) identified below seafloor from seismic data at EPR between ~ 80 N to 100 N, variations coincide with fine-scale tectonic segmentation at the seafloor (Carbotte et al., 2013). Grey lines/bars: bathymetric discontinuities, Orange bars: magma lens disruptions beneath the axis, Red stars: hydrothermal vents. (b) & (c) Stacked magma bodies with AML and sub-AML (SAML) bodies imaged by seismic reflections at the EPR (Carbotte et al., 2020) and Axial Seamount, JdFR (Marjanović et al., 2014), respectively. MMR: Main magma reservoir.

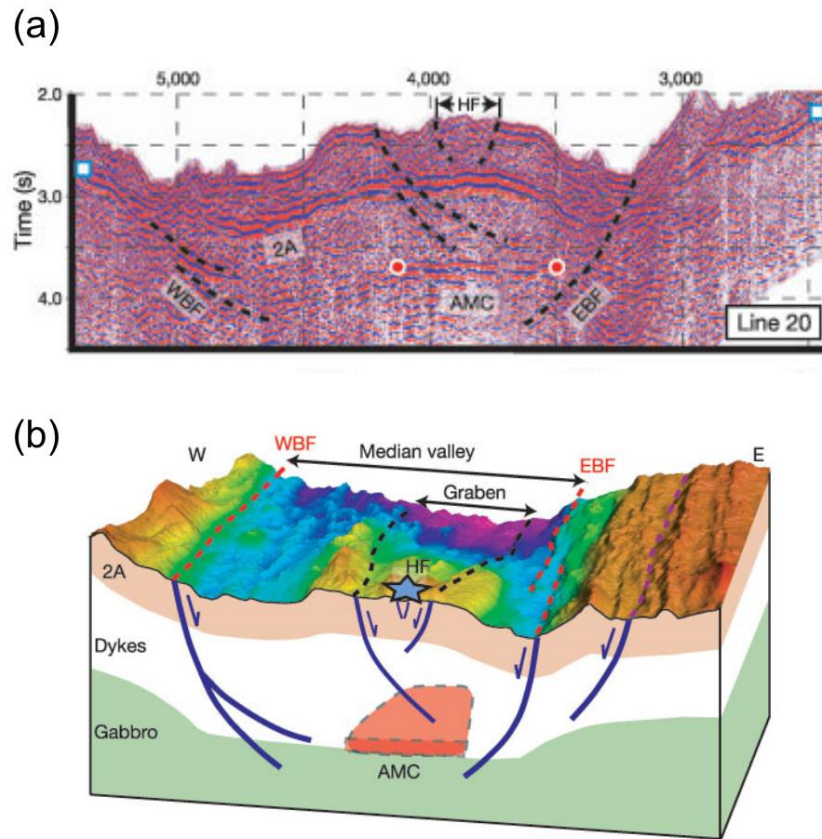


Figure 1.10. (a) Axial magma chamber (AMC) imaged by seismic reflections at the slow spreading MAR segment beneath Lucky Strike volcano (Singh et al., 2006). (b) Schematic 3D representation of the AMC and the crustal structure beneath the volcano based on seismic observations. EBF: Eastern Bounding Fault; WBF: Western Bounding Fault (Combiér et al., 2015).

Relationship between magma replenishment and hydrothermal heat flux

Magma replenishment is necessary to sustain high-temperature hydrothermal systems. Magmatic heat is transferred between the hydrothermal convection system and the roof of the AMCs through a thin thermal boundary layer. The depth of the AMC roofs is controlled by a balance between the frequency of magma injections and volcanic eruption, and the dynamics of hydrothermal convection. Fontaine et al., (2011) describe the interactions between a single, 2D hydrothermal cell (~400 m along-axis) and the underlying AMC, and constrain the dynamics of the thermal boundary layer and melt content of the AMC as a result of heat mining by the hydrothermal system. Considering realistic values for upper crustal permeability (10^{-14} m^2), depth and thickness of the AMC for a fast-spreading segment in a two-layer system (top layer with a hydrothermal circulation and a magmatic bottom layer with an emplaced AMC) (Figure 1.11a),

they show that the AMC will freeze in less than a few years or decades (Figure 1.11b), unless it is replenished by magma injections at regular intervals.

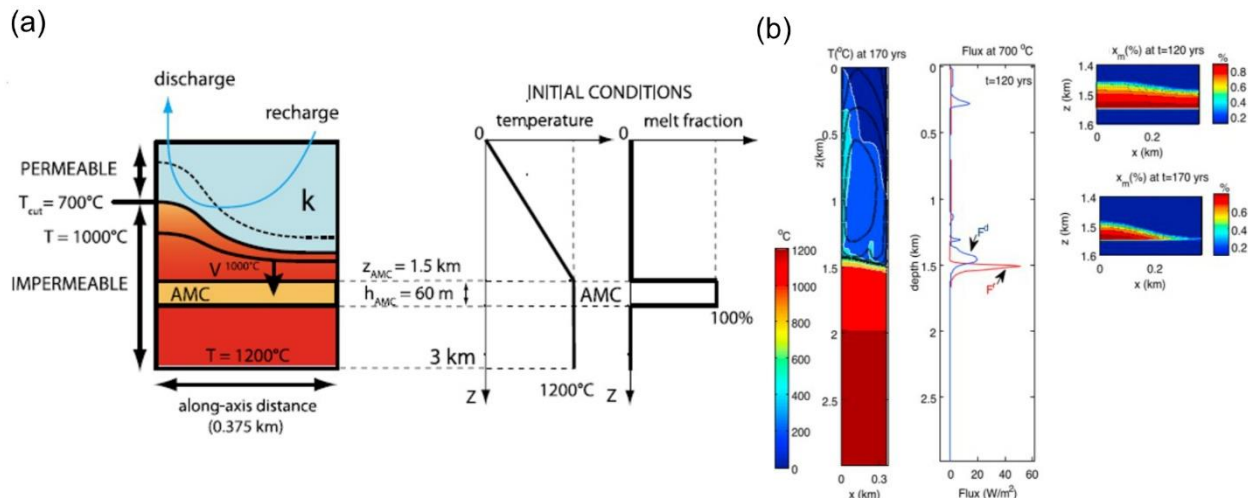


Figure 1.11. Hydrothermal heat extraction from the AMC. (a) Two-layer conceptual model with initial temperature and melt fraction conditions. Hydrothermal circulation is modelled for temperature $< 7000\text{ C}$ in the upper layer and the AMC is placed in the magmatic bottom layer. (b) Two-dimensional temperature and conductive heat flux distribution after a simulation time of 170 years for a coupled magmatic-hydrothermal model. The heat flux is maximum at the thermal boundary layer. Heat extraction is higher beneath the recharge leading to deepening of the isotherms and freezing of the AMC in the absence of magma replenishment. Right hand side smaller figures are the zoomed portion of the AMC with melt fraction after 120 years and 170 years, highlighting the freezing of the AMC. Figures taken from Fontaine et al., (2011).

1.2.4 Hydrothermal circulation models

Because direct measurements or sampling of the seafloor is difficult and expensive, the physical parameters of the hydrothermal convection system are best constrained indirectly from seismicity studies and through numerical models (see Section 1.3.1). Over the last few decades, complex numerical hydrothermal circulation models have been developed (e.g., Coumou et al., 2006; 2008; Fontaine & Wilcock, 2007; Jupp & Schultz, 2004; Wilcock, 1998). I focus here on the first-order physical properties of the hydrothermal system, as modelled in 3D by Coumou et al., (2008). Their model considers nonlinear temperature and pressure dependence of the fluid's properties for a single-phase fluid approximating seawater, as first introduced by (Wilcock, 1998) in a 2D model. Fluids heated up to $\sim 200^\circ\text{C}$ move down rapidly because their temperature-dependent density decreases only by 10% while viscosity decreases by one order of magnitude. Above 300°C both the density and the viscosity decrease substantially, and the fluids start to rise.

This model shows that pipelike upflow zones spaced at regular distances (~500 m) are developed (Figure 1.12a) after a short initialization period of the convection system, considering the above-described nonlinear temperature and pressure dependence of the fluid's properties. Within these pipes, upward discharge of hot hydrothermal fluids (~400⁰ C) occurs, forming the upflow/discharge zones. These discharge zones are surrounded by downflow zones (fluid temperature ranging from 100⁰ C to 300⁰ C; Figure 1.12b). The core of the discharge zone can reach up to 380⁰ C to 450⁰ C, while on the sides of the hot upflow zone low temperature venting occurs (200⁰ C to 250⁰ C) due to conductive cooling and entrainment of shallower fluid downflows.

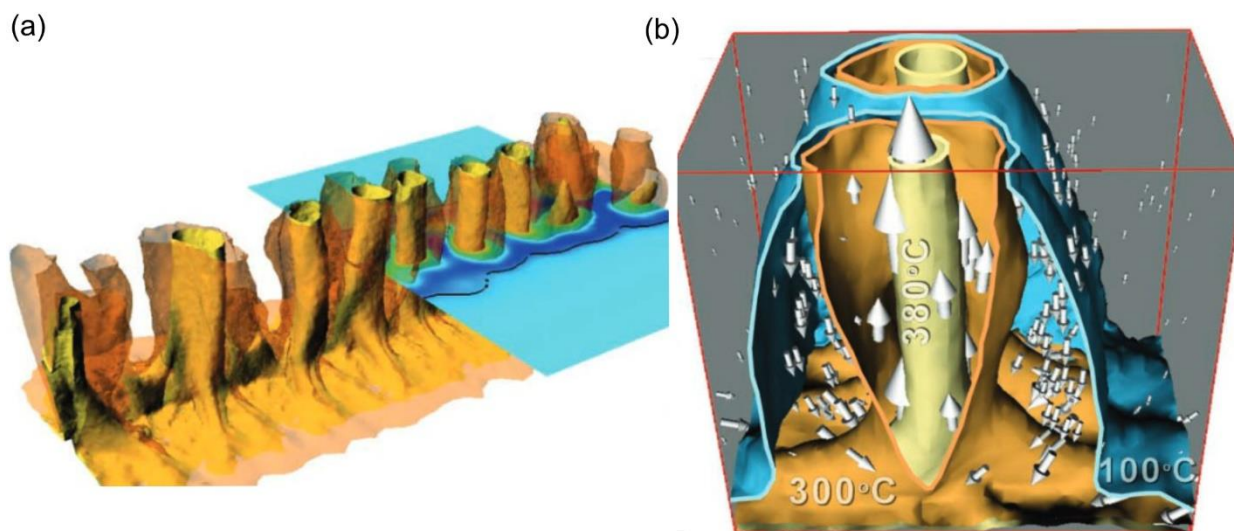


Figure 1.12. Hydrothermal fluid-flow structure after a simulation time of 100 years considering nonlinear temperature and pressure dependence of fluid's properties. (a) The 3D contours at 300⁰ C (brown) and 380⁰ C (yellow) isotherms form pipe-like upflow zones. (b) Cross-section through a thermal plume highlighting 100⁰ C (blue), 300⁰ C (brown), and 380⁰ C (yellow) isotherms and corresponding mass fluxes (white arrows) showing the downflow zone between 100⁰ C and 200⁰ C. Figures taken from Coumou et al., (2008).

1.3 Microseismic studies at Mid-Ocean Ridges

An earthquake is generated when the temperature of the crust is low enough to have brittle deformation and stress exceeds the rock strength. Seismicity observed at MORs is a common proxy to constrain the axial thermal regime. Studies conducted at different spreading segments show that earthquakes are associated with on-going magmatic, tectonic processes and hydrothermal activity

(e.g., Crawford et al., 2013; deMartin et al., 2007; Sohn et al., 1999; 2004; Wilcock et al., 2016). Depending on the spreading rate, magma supply and geological features of any region, the contribution of each of these processes on the overall seismic expression varies significantly. There are three main causes for MOR microseismicity: thermal contraction due to cooling by hydrothermal circulations, magma injection, and faulting.

We discuss the seismicity related to each of these processes (Sections 1.3.1 -1.3.3) using examples from two end-case geological settings: (i) Hydrothermal fields at magmatically robust fast/intermediate spreading ridge segments (9^o50'N EPR, Axial Seamount and Endeavour segment in the JdFR), and (ii) Hydrothermal fields at less magmatically active slow spreading segments (TAG & Rainbow hydrothermal fields, MAR). Lucky Strike's volcano and hydrothermal field in the MAR, which are the focus of this thesis, present at a magmatically robust slow spreading ridge segment center, lies between these two end-case scenarios.

Hydrothermal fields at magmatically robust fast/intermediate spreading segments

9^o50' N EPR hydrothermal field is one of the most extensively studied and monitored sites. Most of the volcanic and hydrothermal activity occurs within the axial summit trough (AST). Hydrothermal activity includes several focused high temperature vents located along the axis within the AST and in between there are regions of diffuse flow (Figure 1.13a; Von-Damm & Lilley, 2004). The AML is shallow, having been imaged at 1.2-2.4 km bsf (Carbotte et al., 2013).

Axial Seamount, on the intermediate spreading JdFR (46^o N) is the youngest of a series of seamounts influenced by the Cobb-Eickelberg hotspot (Chadwick et al., 2005). The summit of the volcano rises ~1000 m above the surrounding seafloor to ~1400 m below sea level and is marked by a horseshoe-shaped caldera that opens to the southeast. Beneath the volcano, the roof of a magma lens is imaged at 1.1-2.6 km bsf (Arnulf et al., 2018), similar to that of the North (9^o- 10^o N) EPR. Two outward dipping planes have been identified beneath the southern portion of the caldera which are inferred to be parts of a ring fault system and reactivated in response to the inflation and deflation of the magma chamber (Wilcock et al., 2016). The central caldera hosts three high temperature hydrothermal vent fields and several diffuse venting sites near the

southeastern caldera wall: the high temperature sites are named CASM at the northern end, ASHES at the southwestern caldera wall, and the international district (ID) at the south end (Figure 1.13b).

In contrast to the pronounced topographic high in Axial Seamount, Endeavour segment, located at the northern end of the JdFR (48° N), has a narrow rift valley with a volcanic high in the central third of the segment which is spilt by a steep axial rift. The central rift hosts five major hydrothermal vent fields and several diffuse venting fields (Figure 1.13c). Magma bodies have been imaged beneath all hydrothermal fields by seismic studies, which deepen from ~2.2 to ~3.3 km bsf from North to South (Ark et al., 2007; S. Carbotte et al., 2012).

Hydrothermal fields at less magmatically active slow spreading segments

The Trans-Atlantic Geotraverse (TAG) segment of the MAR (26.10° N) hosts one of the longest-lived MOR hydrothermal fields, which has been active, probably episodically, for the past ~140 k.y. (Claude Lalou et al., 1995). The high temperature venting is currently focused on the TAG mound, which is a massive sulfide deposit formed by deposition from the long hydrothermal activity. Hydrothermal circulation is situated on the hanging wall of an active, young detachment fault (Figure 1.13d). In the absence of seismically detected shallow crustal melt reservoirs, the detachment faulting process has been proposed to allow hydrothermal fluids to tap heat from a deep melt reservoir (~7-8 km bsf) near the crust-mantle interface to maintain the long-term high temperature hydrothermal system (deMartin et al., 2007).

The Rainbow massif sits in a non-transform discontinuity (NTD) on the MAR (36.2° N). The massif hosts an ultramafic-hosted hydrothermal system where high-temperature hydrothermal venting is currently going on through at least 10 active black smokers (Figure 1.13e). Seismically imaged multiple subhorizontal reflectors are interpreted to be intruded magmatic sills (most at 3-6 km bsf), which are probably feeding the high temperature hydrothermal system (Canales et al., 2017).

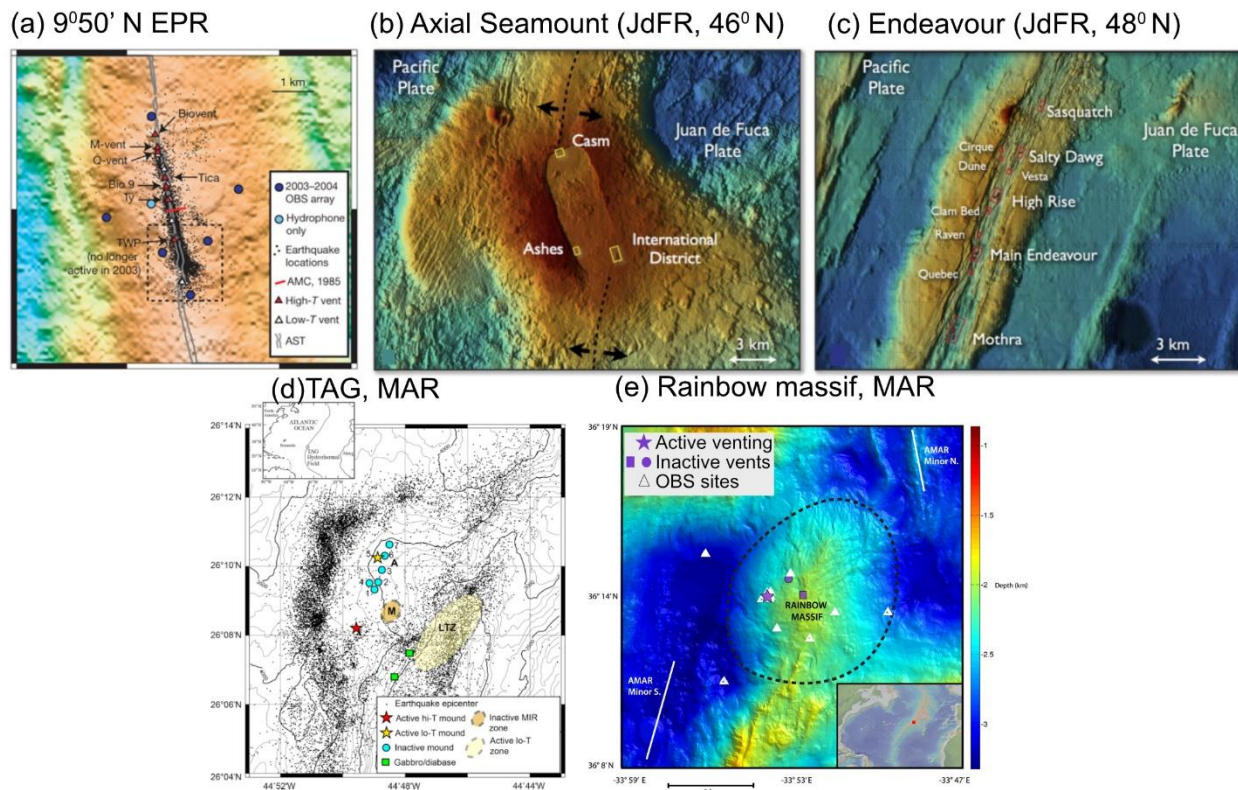


Figure 1.13. Bathymetric maps from (a) 9050'N EPR, (b) Axial Seamount, JdFR, (c) Endeavour segment, JdFR, (d) TAG, MAR (e) Rainbow massif, MAR showing the key features and hydrothermal fields. Figures taken from Tolstoy et al., (2008); Kelley et al., (2014); Humphris et al., (2015); Horning et al., (2018).

1.3.1 Seismicity due to thermal contraction in the hydrothermal downflow zone

One of the primary mechanisms proposed for observed microseismicity at MORs is the thermal contraction of rocks at the base of hydrothermal circulation, also called the hydrothermal cracking of rocks. Thermally induced microcracks form due to the accumulation of residual stresses at the grain scale, which is governed by thermoelastic properties (for example, thermal expansivity and elastic compressibility). At ocean spreading centers, anisotropic thermal contraction and different mineral grains generate larger residual stress compared to depressurization and therefore have a larger control on internal stresses of the environment (Demartin et al., 2004). Thermal contraction generates tensile cracks with strain discontinuities ($\Delta\epsilon$) normal to the horizontal axes because of the overburden ($\Delta\epsilon_{11} = \Delta\epsilon_{22}, \Delta\epsilon_{33} = 0$) (Figure 1.14; Sohn et al., 2004).

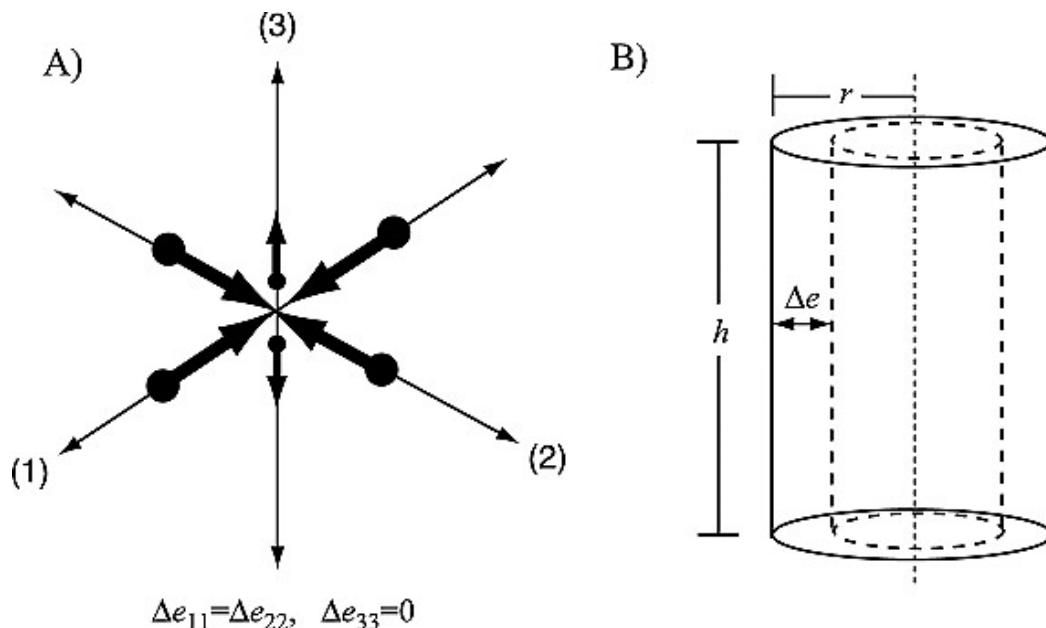


Figure 1.14. (A) Body force representation for a thermal cracking event. Contraction is uniform in all directions, but gives rise to (B) cylindrical source volume with horizontal strain due to overburden. Figures taken from Sohn et al., (2004).

As discussed in Section 1.2.1, thermal exchange between hydrothermal circulation and the magmatic heat source (AMC) occurs through the thermal boundary layer (TBL). In an ‘ideal’ hydrothermal system occurring in the brittle domain with steady heat extraction and homogeneous permeability, and the AMC in the viscous domain getting replenished at the appropriate time and space scale, this heat exchange would occur through the TBL and there would be no thermal cracking events. But most of the natural hydrothermal systems are dynamic with heterogeneously distributed and transient permeable channels and occasional melt injections above the AMCs. In this case, hydrothermal circulation may penetrate deeper to a previous inaccessible hotter domain by extensional cracking events making permeable pathways or by deepening of the cracking front in the absence of magma replenishment. Otherwise, melt injections can also occur occasionally directly into/above the TBL. In any of these scenarios, rapid cooling of the rocks can generate cracks triggering microearthquakes. Based on this proposed mechanism, the microseismicity cluster defines the bottom of the downflow zone of a hydrothermal circulation and it is inferred to indirectly constrain the hydrothermal flow geometry (Crawford et al., 2013; Sohn et al., 1999, 2004; Tolstoy et al., 2008). Hydrothermal system is a dynamic interface, with spatial and temporal changes in permeability and episodic melt injections, thus thermal contraction events due to these

CHAPTER 1. STATE OF THE ART

changes in the hydrothermal circulation occurs by enhanced local permeability and/or enhanced local cooling.

Most focal mechanisms softwares assume double-couple source mechanisms/shear movement, whereas thermal contraction generates tensile cracks (mode I type failure) and should be associated with changes in volume (e.g., Sohn et al., 2004). Therefore, calculating the focal mechanism for thermal contraction events assuming double-couple sources may give errors. There are also other practical problems associated with calculating focal mechanisms for thermal cracking events. First, almost all thermal cracking events are very small in magnitude ($M_L \leq 0$), which makes it difficult to pick a clear first polarity of an event. Second, in most of the deep-sea MOR settings, OBSs are deployed in a free-fall motion and therefore, the orientation of the horizontal components of the OBSs is unknown and horizontal amplitude ratios cannot be used to better constrain the focal mechanisms (Chapter 4 discusses the difficulty of orienting horizontal components on short period OBSs). Third, the number of the OBSs are usually limited at a time in all MOR experiments. Altogether, it is very difficult to get robust focal mechanism solutions for thermal cracking events.

At the $9^{\circ}50'N$ EPR fast spreading segment, a ~ 500 m wide band of seismicity was detected overlying the AMC (Tolstoy et al., 2008; Waldhauser & Tolstoy, 2011), which is interpreted as delineating the reaction zone of a hydrothermal circulation. Towards the south along the axis, this seismicity connects to a shallow cluster of seismicity near a fourth order discontinuity proposed to constrain a narrow downflow zone; and towards the north a broad, less pronounced seismic zone was identified as the upflow zone feeding the overlying high-temperature vents. The entire seismic expression along with the positions of the vents suggests an along axis hydrothermal circulation in one ~ 1.5 km long cell (Figure 1.15; Tolstoy et al., 2008).

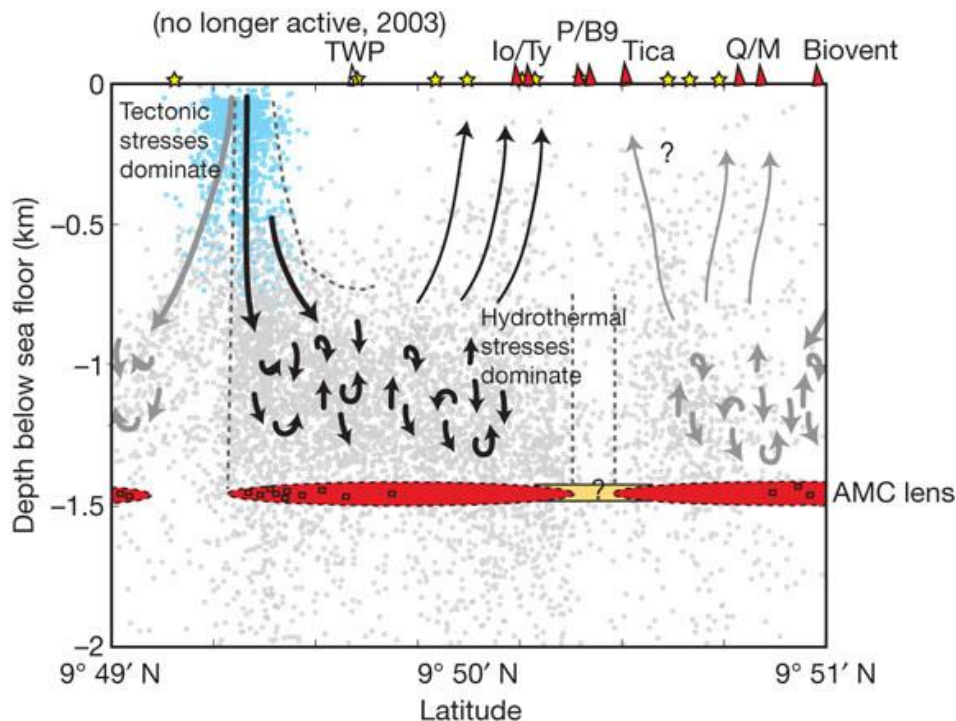


Figure 1.15. Schematic diagram of an along-axis hydrothermal circulation model beneath 9050'N EPR hydrothermal field based on microseismicity studies. Light grey dots illustrate the area where hydrothermal contraction dominates just above the AMC and Light blue dots illustrate the zone where tectonic stresses are likely to dominate. Yellow stars: high temperature vents, Red triangles: low temperature vents. Figure taken from Tolstoy et al., (2008).

Although seismicity at the Axial Seamount at the JdFR is mostly controlled by repetitive eruption events on a decadal scale (discussed in detail later), microseismicity after the 1998 eruption occurred at a steady rate, with small magnitude events ($M_w \sim 0$) beneath the Eastern hydrothermal vent fields in the southeast corner of the caldera at ~ 0.5 -1 km depth, above the crustal melt reservoir and (Sohn et al., 2004). This microseismic zone is proposed (Sohn et al., 2004) to define the reaction zone of hydrothermal circulation. The post-2015 eruption earthquakes in the same region also show a heterogeneous slip pattern with some having subvertical nodal planes (Figure 1.16a-3; Levy et al., 2018) and could be linked to the pathways of hydrothermal fluid beneath the eastern vent fields. Similarly, at the Endeavour segment in the northern JdFR, seismic epicenters cluster above the shallowest part of magma chamber with focal mechanism solutions suggesting thermal cracking events along with faulting (Ark et al., 2007; Wilcock et al., 2002).

CHAPTER 1. STATE OF THE ART

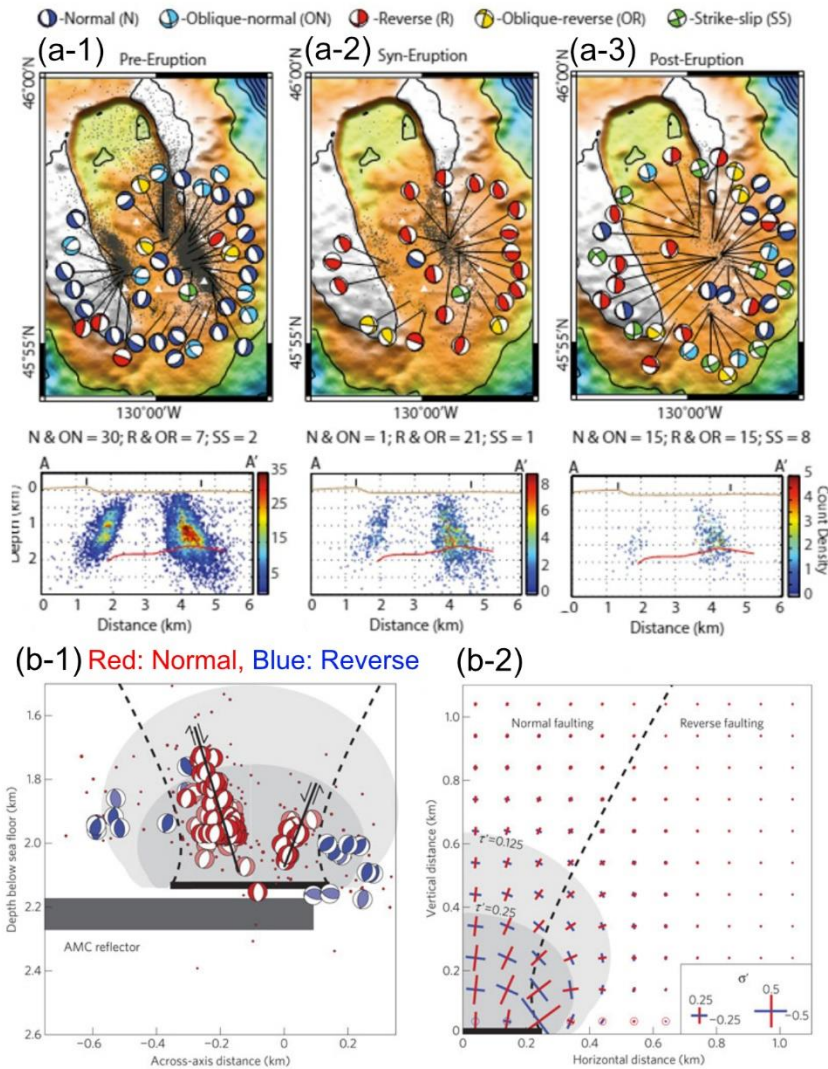


Figure 1.16. (a) Composite focal mechanism solutions and seismicity patterns (a-1) before, (a-2) during, and (a-2) after 2015 Axial Seamount eruption, color coded according to focal mechanism type shown at the top; adapted from Levy et al., (2018). Cross sections show earthquake density ($50 * 50$ m bins). (b) Cross-section of focal mechanisms and stress perturbations from injection of magma into a sill between main Endeavour and High Rise hydrothermal fields, Endeavour segment, JdFR; adapted from Wilcock et al., (2009). (b-1) hypocenters and focal mechanisms for earthquakes within 0.3 km across axis. Dark grey bar: Axial magma chamber, Black solid lines: inferred normal faults. (b-2) Stress perturbations above one side of a pressurized horizontal crack (0.5 km width). Red and blue lines: maximum compressional and extensional stress perturbations, shaded contours: maximum shear stresses.

At slow/ultraslow spreading segments, seismicity is mostly controlled by tectonic events along the large offset normal faults and detachment faults. Thermal contraction events have been reported only in the few existing magmatically rich segment centers (Crawford et al., 2013; Wolfe et al., 1995). However, at the Rainbow massif, part of the low magnitude persistent earthquakes

distributed in between seismically reflected sill bodies are interpreted to be generated by hydrothermal cooling along with other processes such as faulting and serpentinization (Figure 1.17b; Horning et al., 2018).

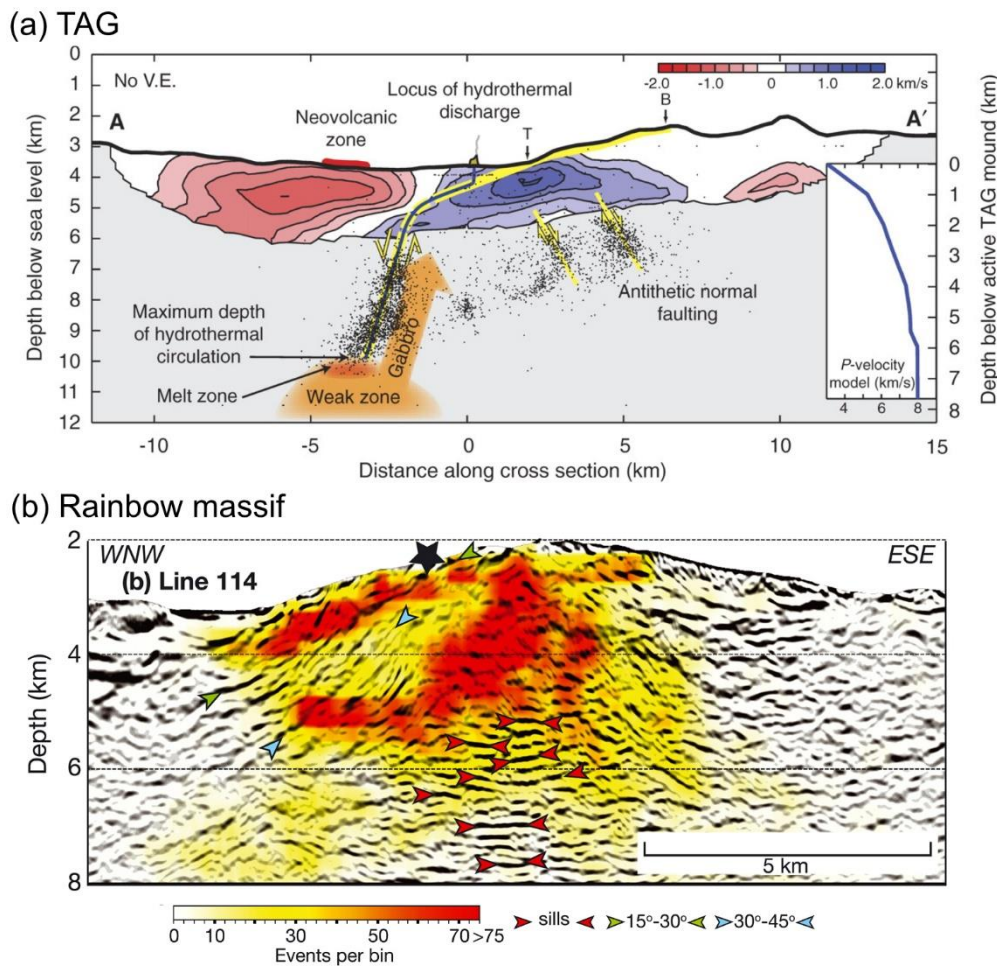


Figure 1.17. (a) Schematic model of crustal accretion, deformation and hydrothermal circulation at TAG, MAR showing earthquake locations, seismic velocity anomalies; adapted from deMartin et al., (2007). Maximum depth of hydrothermal circulation is inferred from the maximum hypocentral depth, focused along the detachment fault. (b) Microearthquake density plot along with multichannel seismic reflectors at Rainbow massif, MAR; adapted from Horning et al., (2018). Subhorizontal reflectors (red arrowheads) are interpreted as solidified magmatic sills, providing heat to the hydrothermal circulation. Event density is maximum just above these sill bodies.

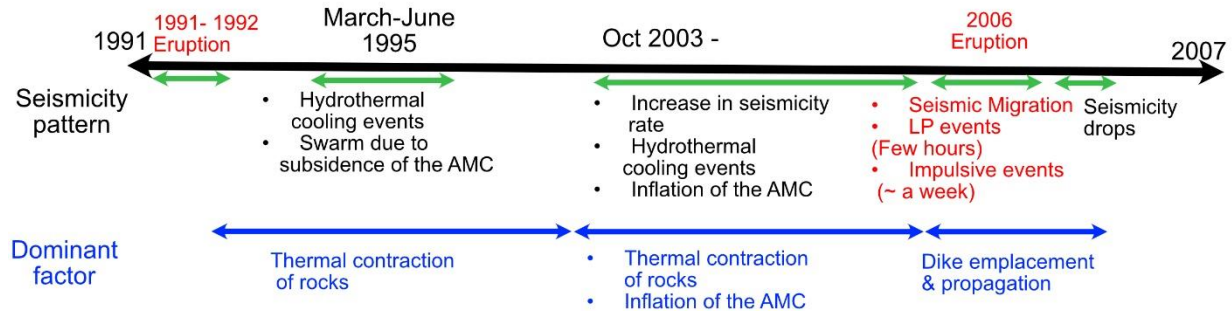
1.3.2 Seismicity related to magmatic processes

Injection of magma in the form of a dike/sill and its propagation is one of the major sources of seismicity in volcanically active areas. Intruded magma bodies generate compressional stress perturbations on the surrounding rocks and tensile stress at the dike/sill tips. Based on the phase in

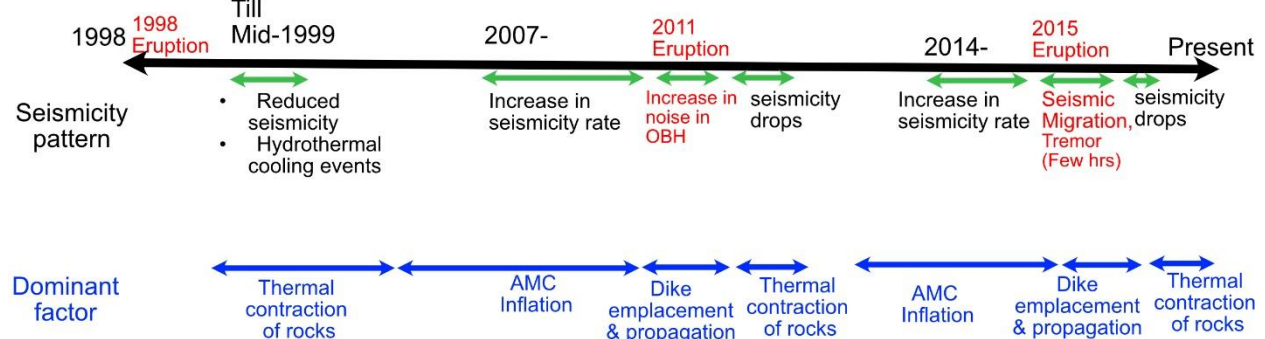
CHAPTER 1. STATE OF THE ART

a magma intrusion/eruption cycle, the seismicity rate, its distribution and focal mechanisms appear differently, which can be used to track the dike propagation and infer the stress state of the crust. On a long-term scale, monitoring of seismicity can also be used to predict future eruptions. At MORs, this has been illustrated by studies at the EPR, Axial Seamount, and Endeavour segment (Figure 1.18).

(a) 9°50' N EPR Seismicity cycle



(b) Axial Seamount Seismicity cycle



(c) Endeavour Seismicity cycle

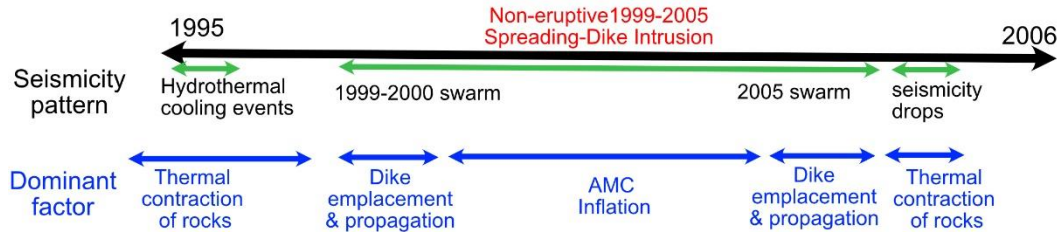


Figure 1.18. Seismicity cycles at (a) 9°50'N EPR, (b) Axial Seamount, JdFR, (c) Endeavour segment, JdFR based on compilation of different seismic studies (all citations referenced in section 1.3.2). Green arrows mark the time periods of seismic experiments conducted, and blue arrows mark the approximate time periods of inferred controlling factor on total seismicity.

Prior to eruptions, stress builds up in the crust as the magma chamber inflates, causing increase in seismic activities and seafloor inflation rate (R. P. Dziak et al., 2012; Sigmundsson et

al., 2015; Tan et al., 2016; M. Tolstoy et al., 2006; William S. D. Wilcock et al., 2016). At Axial Seamount, seismicity rate increased from <500 events/day to >2000 events/day leading up to onset of 2015 eruption (Figure 1.19a; Wilcock et al., 2016) and from ~100 events/day to >1000 events/day prior to the 2011 eruption (Dziak et al., 2012) (both cases on an average one year prior to the eruption). A similar trend of increase in seismicity rate was observed at 9°50' N EPR before the 2006 eruption (Tolstoy et al., 2006; Tan et al., 2016) and in Iceland (e.g., 2014 Bardarbunga eruption; Sigmundsson et al., 2015). Just prior to eruption, on a few hours' time scale, there are several precursors linked with initial subsurface magma movement such as: an increase in short-term noise on pressure recorders (Figure 1.19b; 2011 Axial Seamount eruption, Dziak et al., 2012), bursts of 7-10 Hz tremors (2015 Axial Seamount eruption, Wilcock et al., 2016) or long period ~1.6 Hz seismic events (2006 9°50' N EPR eruption, Tan et al., 2016). When the stress finally reaches a critical point in the magma reservoir, it leads to the actual diking event with lateral movement of magma and possible eruption. Individual diking events are short-lived (a few hours to days) and marked by intense migrating seismic swarms that track the propagation of magma (Figure 1.19c, d). Magma moving laterally out of the reservoir typically leads to seafloor deflation. The deflation event may be coincident in time with the seismic crisis (Figure 1.19a; 2015 Axial Seamount eruption), or a few hours delayed (Figure 1.19b; 1998 & 2011 Axial Seamount eruption). Both the 2015 Axial Seamount and the 2006 9°50' N EPR eruption coincided with thousands of impulsive events (short single-phase 22 Hz events), starting just after the seismic crisis and continuing for almost a month, until the volcano started to re-inflate; these events are suggested to be associated with the fresh lava reaching the seafloor (Tan et al., 2016; Wilcock et al., 2016). Following the eruptions, seismicity rates decrease dramatically (e.g., < 20 events/day within a month after the 2015 Axial Seamount eruption, Wilcock et al., 2016) as the magmatic event reduces the differential stress in the shallow crust and resets the stress environment (Dziak & Fox, 1999; Sohn et al., 2004; Wilcock et al., 2016). As discussed in Section 1.3.1, this is the period where thermal cracking events start to predominate the total seismicity, as cooling of intruded magma generates thermal contraction. The magma chamber gets replenished and re-inflated by influx of magma and stress again starts to build up, and the cycle continues.

CHAPTER 1. STATE OF THE ART

Levy et al., (2018) provides a detailed track of the stress pattern and sense of slip in pre, syn and post-2015 Axial Seamount eruption period (Figure 1.16a). In the pre-eruption period, as the magma chamber inflated leading up to the eruption, most events lying along outward dipping faults showed normal and oblique-normal slip patterns. During the dike emplacement and eruption phase, as the caldera floor subsided, the slip pattern changed, and the dominant focal mechanism observed was reverse and oblique-reverse. Finally, post-eruption seismicity showed a heterogeneous sense of slip (15 normal/oblique-normal, 15 reverse/oblique-reverse and 6 strike-slip events). While the authors do not give any specific reason for mixed focal mechanisms, it could be due to a mix of processes such as inflation of the replenishing magma chamber, residual dike-related thermal and mechanical stress, and hydrothermal cooling.

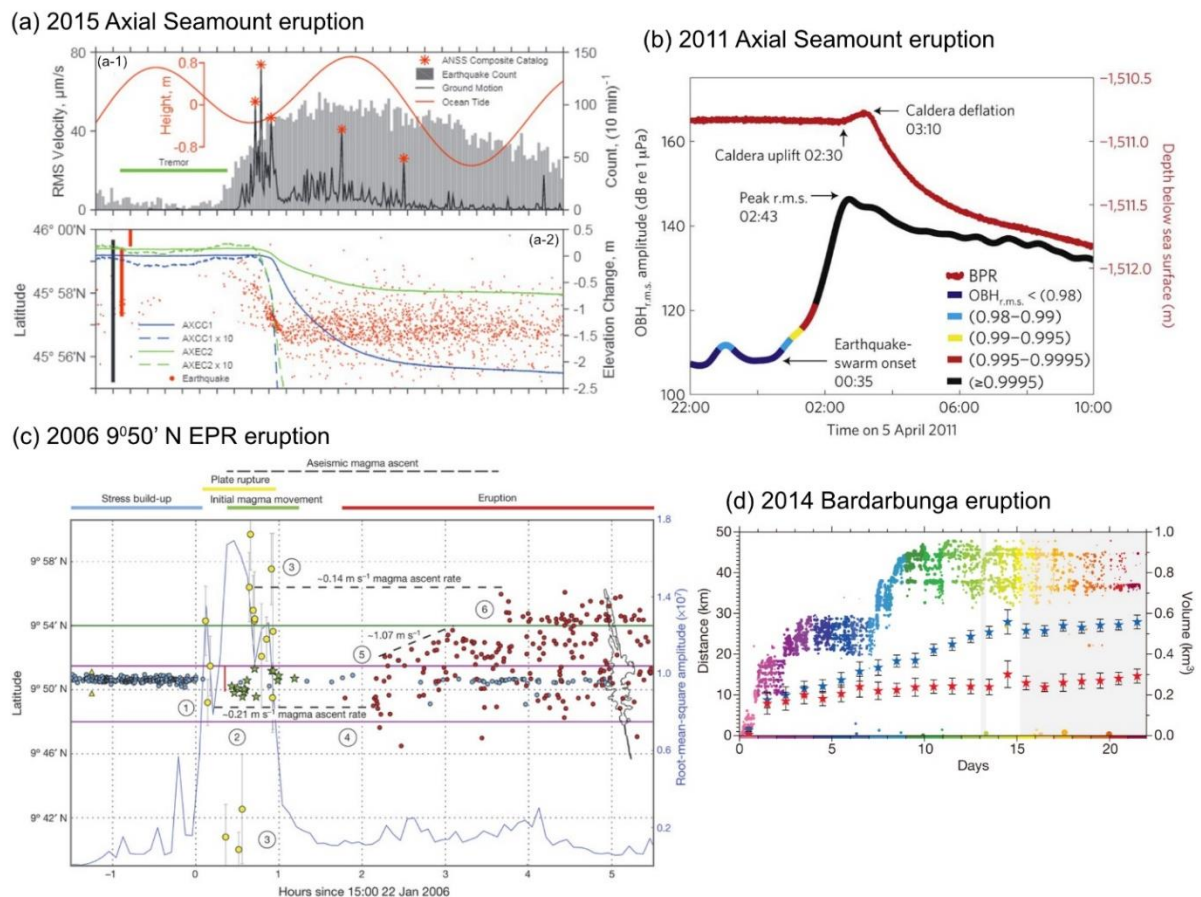


Figure 1.19. Chronology of different eruption events. (a) 2015 Axial Seamount eruption showing (a-1) histogram of earthquake counts and (a-2) along-axis migration of seismic swarm and change in seafloor elevation (Wilcock et al., 2016). (b) Increase in r.m.s amplitude in hydrophone and caldera deflation during 2011 Axial Seamount eruption (Dziak et al., 2012). (c) Temporal and along-axis progression of various seismic events during 2006 9050' N EPR eruption (Tan et al., 2016). (d) Along-axis migration of seismic swarm during 2014 Bardarbunga eruption, Iceland (Sigmundsson et al., 2015).

CHAPTER 1. STATE OF THE ART

Compared to the EPR and Axial Seamount, Endeavour segment has a deeper axial magma chamber and probably a lower magma supply rate (Carbotte et al., 2012). Nevertheless, the Endeavour segment exhibits elevated background seismicity, most likely due to stress associated with the reorganization of the plate boundaries near the unstable triple junction at the northern end of the JdFR (Dziak et al., 2011). The Endeavour segment has no historical record of eruptions, but it experienced a long non-eruptive spreading-dike intrusion event from 1999 to 2005, involving three major seismic swarms (Figure 1.18c; Weekly et al., 2013). The first swarm, in June 1999, started above the shallowest part of the imaged AMC and moved southward around ~12 km along-axis. This swarm is interpreted as a diking event beneath the ridge axis based on the seismic characteristics and increased CO₂ emissions from black smokers. It was followed by a shorter swarm in January 2000 at the southern end of the 1999 sequence, where the lithosphere may have undergone a ridge-normal extension in response to the previous dike propagation (Bohnenstiehl et al., 2004). In between 2003-2004, events between Main Endeavour and High Rise fields showed normal fault focal mechanisms on the axial valley graben faults and compressional mechanisms on either side of these faults, which can be explained by an inflating magma lens in the form of a narrow sill (Figure 1.16b; Wilcock et al., 2009). This indicates that, in 2003-2004, the segment was still in a magma inflation phase that probably started in 1999. In late January and February 2005, two complex swarms occurred at the northern end of the segment, both propagating towards the segment center. The seismicity in the vent field region increased from an average of 9 events/day to more than ~100 events/day during the swarm periods, then decreased to 15% of the pre-swarm level beneath the vent fields and almost ceased at both segment ends (Hooft et al., 2010; Weekly et al., 2013); similar to the post eruption phase at Axial Seamount (e.g., Dziak & Fox, 1999; Wilcock et al., 2016). Based on the observed seismicity pattern and a 4°C increase in diffuse vent temperature at Mothra field nearly 1.5 days after the main seismic swarm, the 2005 swarm period is interpreted as magma intrusion that terminated the 6-year spreading-diking event at the Endeavour segment and reset the stress level of the entire segment. The duration of the magmatic phase at the Endeavour segment is substantially longer with multiple diking episodes than that observed in any other observed ridge-spreading event, which has been explained as due to the large extensional stresses required to rupture thick lithosphere and the limited magma supply (Weekly et al., 2013).

At the slow spreading MAR's Lucky Strike segment, only one probable volcanogenic dike injection swarm has been detected (Dziak et al., 2004). The swarm period (~29 hours) was much shorter than any observed fast/intermediate spreading diking episodes. During the first hour, the seismicity rate detected by a remote hydrophone array rose from < 10 events/year to up to ~42 events/hour at the peak time and then declined rapidly to ~5 events/hour afterwards during the swarm. The swarm was accompanied by 3-20 Hz "intrusion tremor" but the seismicity showed no along-axis migration, nor was any evidence of a recent lava flow later detected (Dziak et al., 2004). The swarm was interpreted to be a discrete episode of dike emplacement related to upper crust construction in a slow spreading environment. In late September 2015, bottom pressure records showed a decrease in the seafloor pressure at the volcano summit (corresponding to a relative uplift ~1.5-2 cm), suggesting a seafloor inflation event which could be due to an episode of magma injection beneath the summit (Ballu et al., 2019). Changes in the seismicity pattern associated with this event are addressed in this thesis.

1.3.3 Seismicity related to tectonic processes

Tectonic processes play a much larger role in crustal accretion at slow and ultraslow segments than at fast and intermediate spreading ridges (Behn & Ito, 2008; Tapponnier & Francheteau, 1978). As a result, tectonic small- to moderate- earthquakes are abundant in slow/ultraslow spreading environments and dominate the overall seismic signature. However, tectonic seismicity varies depending on the mode of accretion. At symmetrically accreting slow spreading segments, an estimated 10-20% of the plate divergence is accommodated by the rift bounding normal faults, compared to ~50% to 100% at asymmetrically accreting ridge segments (with detachment faults). This difference in tectonic strain leads to a higher seismicity level in asymmetrical regions than symmetrical segments of slow/ultraslow spreading ridges (Escartín et al., 2008).

The spatial pattern of tectonic seismicity also differs significantly between symmetric and asymmetrically accreting ridge regions. At asymmetric regions, elevated seismicity is associated with detachment faults with deeper seismogenic depth beneath the neovolcanic zone than symmetrically accreting regions (deMartin et al., 2007; Parnell-Turner et al., 2017, 2020). For example, at TAG hydrothermal field a steady rate of seismicity (~80 events/day) was observed

during an 8-month microseismic experiment, with most of the events located along the young ocean detachment fault down to ~7-8 km bsf, where the fault sits directly beneath a neovolcanic zone sustaining a long-lived high temperature hydrothermal system (Figure 1.17a; deMartin et al., 2007). At symmetrical segments, tectonic events are mostly concentrated towards the segment ends and only a few, shallower (~5-6 km), tectonic events are located at the segment centers, where seismicity is mainly controlled by other processes like magmatism and hydrothermal contraction (e.g., Broken Spur hydrothermal field at 29° N MAR; Wolfe et., 1995).

1.3.4 Near seafloor hydrothermal circulations and related microseismicity

Apart from the primary hydrothermal circulation, intense discharge of hot hydrothermal fluids through focused high temperature vents creates local recharges of cold sea water entrained in the shallow sub-seafloor, known as secondary hydrothermal circulation. Local interactions between upflowing hot hydrothermal fluids and entrained cold sea water results in the formation of diffuse fluids along with mineral precipitation and the formation of a near-surface stockwork (Figure 1.20a). Diffuse vent regions also host a unique chemosynthetic microbial and hydrothermal fauna (Corliss et al., 1979; Cuvelier et al., 2009; Juniper et al., 1995).

The shallow region of the upflow zone was first described from ophiolites, but most direct evidence comes from ODP drilling (maximum depth 125.7 mbsf) at the TAG hydrothermal mound (Humphris et al., 1996; Humphris et al., 2015). The stratigraphical sequence of the upflow zone at TAG suggests that massive sulfides are present only in the first few meters, underlain by layers of breccias whose composition changes with depth. Up to 45 mbsf, the breccia layers are composed of pyrite clasts surrounded by a matrix rich in anhydrite (Figure 1.20b). Our understanding of the secondary hydrothermal system and the shallow portion of the upflow zone of the primary system is limited to these few drill cores and to numerical models (discussed later). This system can also be indirectly studied through the observation of shallow microseismicity, which has only been investigated beneath the TAG hydrothermal mound (Pontbriand & Sohn, 2014). Below, we discuss the possible source mechanisms for near seafloor microseismicity and how they can be used to constrain the secondary hydrothermal system and shallow portion of the discharge zone. These mechanisms include reaction driven cracking, collapsing bubbles and vibrations in the uprising fluids, and hydraulic fracturing.

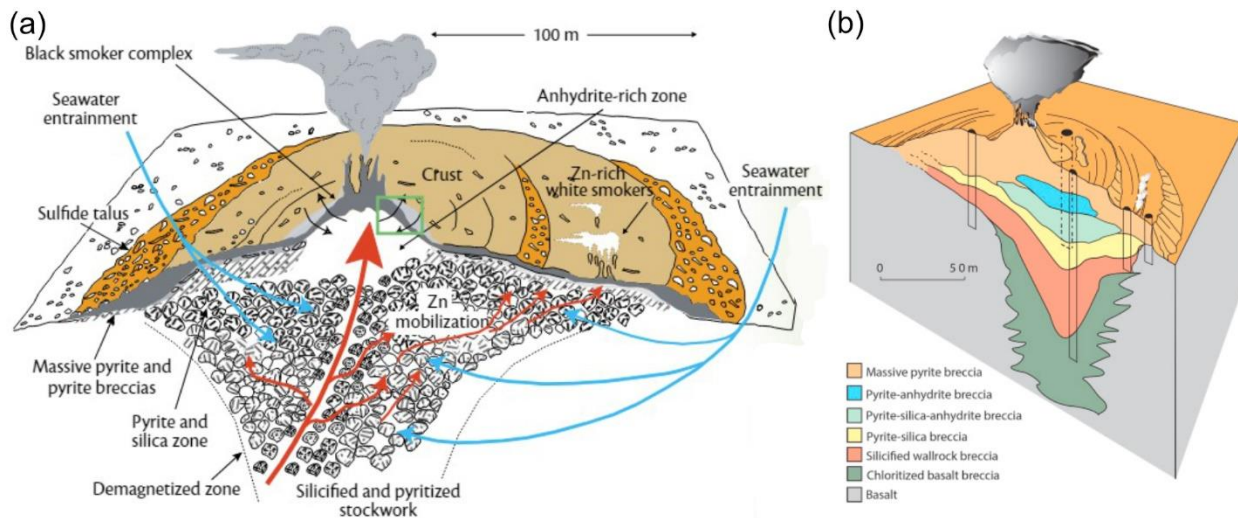


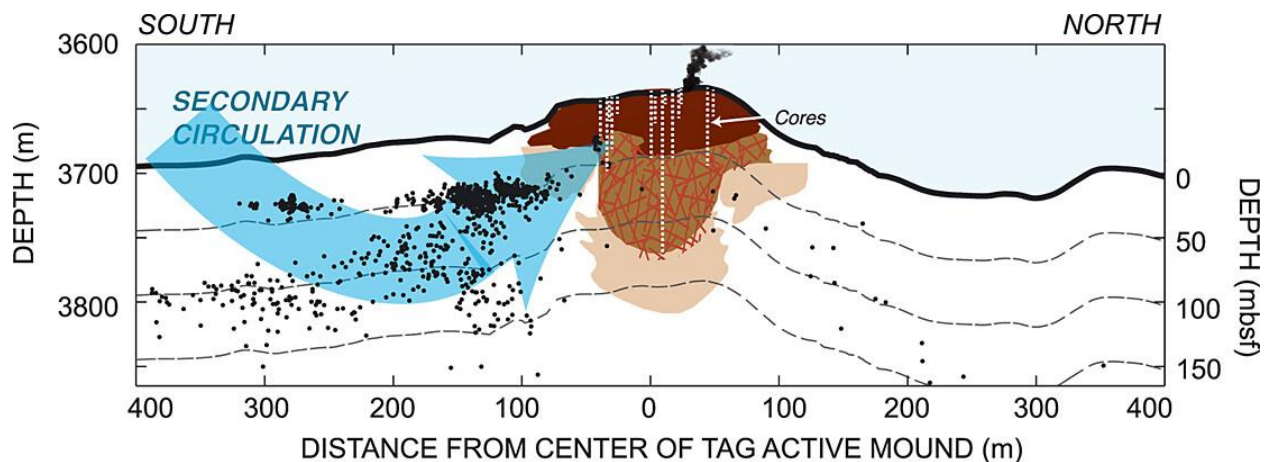
Figure 1.20. Cross-section of the TAG hydrothermal mound showing (a) dynamics of shallow secondary fluid circulation along with associated mineral precipitation, and (b) subsurface stratigraphy from drill holes of the ODP LEG 158; adapted from Humphris & Tivey, (2000); Tivey, (2007). (a) Venting from deep hydrothermal convection cell (red arrows) forming black smokers at the seafloor and mixing with the entrained cold sea water (blue arrows) in the subsurface leading to mineral precipitation. (b) Close to the surface above basaltic layer, the substratum is dominated by breccia followed by anhydrite in the shallower parts.

Reaction driven cracking

When the entrained seawater is heated, the first minerals to precipitate are anhydrite (CaSO_4) and barite (BaSO_4). Anhydrite is a retrograde soluble and continuously precipitates in pores and cracks when the entrained sea water temperature reaches $\sim 150^\circ\text{C}$ or more, either through conductive heating (Cooper et al., 2000) or mixing with hydrothermal fluids (Butterfield et al., 2004; Edmond, Measures, Mangum, et al., 1979). During periods of quiescence with weak hydrothermal upflow when the entrained sea water temperature is $< 150^\circ\text{C}$, anhydrite dissolves in sea water. Deposition and dissolution of anhydrite thus continuously occur beneath hydrothermal vents.

As the anhydrite is deposited in veins and pores, the solid volume of a hydrothermal deposit increases, leading to substantial increase in stresses and causing fractures in the host matrix. The hydrothermal mound cores collected during TAG ODP Leg 158 reveal complex, multistage fractures up to 45 cm in width (Humphris et al., 1996). Individual growth bands reflect sequential precipitation within cracks and repeated opening of fractures. The evidence of fracturing from ODP cores led to the idea of ‘reaction-driven cracking’ as a possible source mechanism for very shallow microearthquakes (Pontbriand et al., 2014) observed beneath the TAG hydrothermal

mound. These shallow microearthquakes are characterized by a short single phase (~1 sec) with no apparent S phase arrival. They cluster along the southwest corner of the active hydrothermal mound (Figure 1.21) and the clusters are oriented subparallel to fissure orientations, suggesting that the clusters occur in fissures where anhydrite is being actively deposited. From the depth of TAG shallow microseismicity, the maximum depth of entrained water is constrained to be ~125 mbsf, almost identical to the water entrainment depth inferred from ODP drilling. Based on mode-1 tensile cracking of a penny shaped fracture with nonzero strain only in the vertical direction (Figure 1.22a), Pontbriand et al., (2014) show the relationship between seismic moment of a reaction-driven cracking event and the required volume and stress drop of the source (Figure 1.22b), demonstrating that a source volume of $\geq 0.61 \text{ m}^3$ is sufficient to generate a microearthquake of $M_L = -0.95$ (the average magnitude in their catalog) if the stress drop is greater than or equal to the confining pressure of 39 MPa expected at a depth of 125 mbsf. Assuming anhydrite is precipitated in the secondary hydrothermal circulation system, the fluid flux there is $\sim 1.3\text{-}2.5 \text{ kg s}^{-1}$, which corresponds to a heat flux requirement of 0.8 to 3.6 MW, less than 1% of the total heat flux estimated for the TAG mound.



INTERNAL STRUCTURE OF DEPOSIT

- Sulfide deposition / Anhydrite-rich zone
- Anhydrite veins
- Alteration zone (e.g. Pyrite-silica breccia, silicified wallrock)
- Altered basalt

Figure 1.21. Shallow seismogenic zone beneath TAG active hydrothermal mound; adapted from Pontbriand & Sohn, (2014). The zone is focused to the south of the mound and < 150 m below the seafloor and likely marks a zone of reaction-driven cracking where secondary circulation enhances anhydrite precipitation.

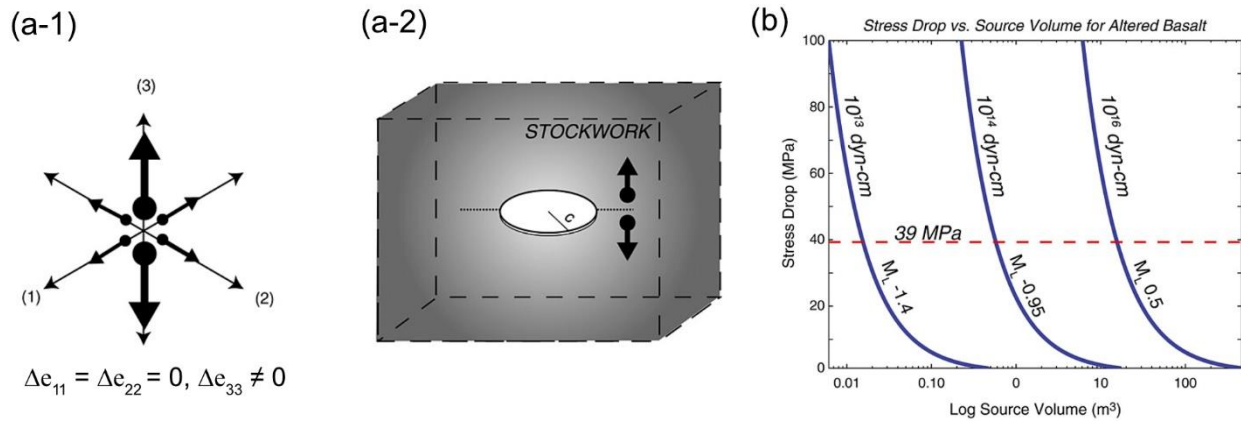


Figure 1.22. (a) Body force representation of mode I cracking and a horizontal penny-shaped opening in the vertical direction in response to anhydrite precipitation in shallow subsurface. (b) Relationship between stress drop, source volume and earthquake size in reaction-driven cracking model. Figures taken from Pontbriand & Sohn, (2014).

A few numerical models include mineral precipitation as a parameter while studying MOR flow dynamics. Lowell & Yao, (2002) show that anhydrite precipitation reduces permeability, and the recharge zone needs to be ~10-100 times larger than the discharge zone to maintain a steady flow rate on a long-term scale. Lowell et al., (2003) implement a two-loop model which includes the secondary hydrothermal circulation and a mixing zone between focused and diffuse flow (Figure 1.23), estimating that, if the permeability of the mixing zone and focus vent ranges between 10^{-12} - 10^{-11} m², the entrained seawater will be heated to $\geq 150^{\circ}$ C and anhydrite will precipitate in the mixing zone, forming a barrier between deep and shallow circulation systems (Figure 1.23b). In this case, low temperature diffuse fluid may occur next to focused high-temperature vents. The impermeable layer formed in the mixing zone by mineral precipitation focuses the upflow hydrothermal fluids below the seafloor, forming ‘pipe-like’ vein networks and producing high temperature focus vents which remain stable for thousands of years (Guo et al., 2020). The precipitation of anhydrite is therefore proposed to be a key mechanism for co-existing high temperature focus vents and low temperature diffuse flow observed at many hydrothermal systems.

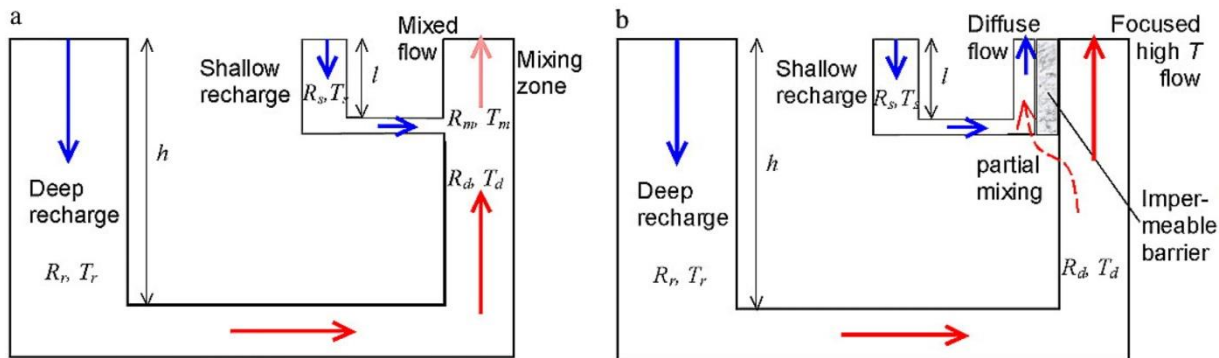


Figure 1.23. Two-loop models for seafloor hydrothermal circulation, adapted from Lowell et al., (2003). (a) Mixing of shallow and deep hydrothermal circulations. (b) Mineral precipitation in the mixing zone forming an impermeable layer and leading to co-existing focus vents and diffuse flow.

Collapsing bubbles and vibrating fluids

Collapsing bubbles and vibrating fluids are potential mechanisms for shallow microearthquakes associated with a hydrothermal system. These phenomena are typically observed in subaerial geothermal systems where there are large density changes associated with the phase transition from liquid to gas (Dawson et al., 2012; Kedar et al., 1996, 1998). Bubble collapse events are much more unlikely in deep hydrothermal systems such as TAG (3700 m bsl), because the volume changes associated with phase transition from liquid to gas is small at these depths. However, a bubble collapse might be possible in a shallow submarine hydrothermal system if it is saturated with gas such as CO_2 and the fluid is subcooled (Kedar et al., 1998; Leet, 1988).

Hydraulic fracturing

Hydraulic fracturing is another possible source mechanism for non double-couple mechanism events generated by hydrothermal circulation (Miller et al., 1998; Ross et al., 1996). Hydraulic fracturing occurs when the fluid pressure in the hydrothermal system exceeds the strength of the local host rocks. The maximum fluid pressure of the hydrothermal system can be constrained to be less than or equal to the buoyancy pressure. At TAG, the buoyancy pressure of the primary system (maximum convection depth 8 km bsl) is calculated to be in between ~ 5 and 18 MPa, which is much less than the confining pressure (39 MPa at a depth of 125 m). In addition, the shallow microseismicity was observed at the periphery of the mound, not directly beneath the high-temperature discharge zone. Therefore, hydraulic fracturing was not considered as a possible source mechanism for the observed shallow microseismicity.

1.4 A magmatically robust slow spreading segment center: The Lucky Strike volcano and hydrothermal vent field, MAR

Lucky Strike segment, at 37°N on the MAR (Figure 1.24a), is differentiated from many other slow-spreading segments by the presence of a large volcano at its center and a well-imaged axial magma chamber (AMC) underneath the volcano. The segment has a full spreading rate of ~20.3 mm/year (DeMets et al., 1994) and features the typical morphological and tectonic architecture of a slow spreading ridge in spite of its proximity to the Azores hotspot. The segment is characterized by a well-developed ~13-20 km wide axial valley, bounded by two major normal faults (Eastern and Western Bounding Faults, EBF and WBF). The axial valley gradually deepens from segment center (~2000 m) to segment ends (~3000 m).

The center of the segment is dominated by the 8 km wide, 15 km long and ~400 m high Lucky Strike volcano (Figure 1.24b). The volcano summit depression is surrounded by many high and low temperature vents and zones of diffuse flow over an area of ~1 km², constituting the Lucky Strike Hydrothermal Field (Figure 1.24b) (Barreyre et al., 2012; Escartin et al., 2015; Fouquet et al., 1995; Susan E. Humphris et al., 2002; Langmuir et al., 1997; Ondréas et al., 2009). The hydrothermal field and volcano region have been constantly monitored since 2007, as part of the long-term European Multidisciplinary Seafloor and water column Observatory (EMSO)-Azores. The detailed geological setting of the volcano region and hydrothermal field is covered in Chapter 2. Here I add relevant background about constraints on upper crustal velocity structure, effective permeability, and the hydrothermal reaction zone.

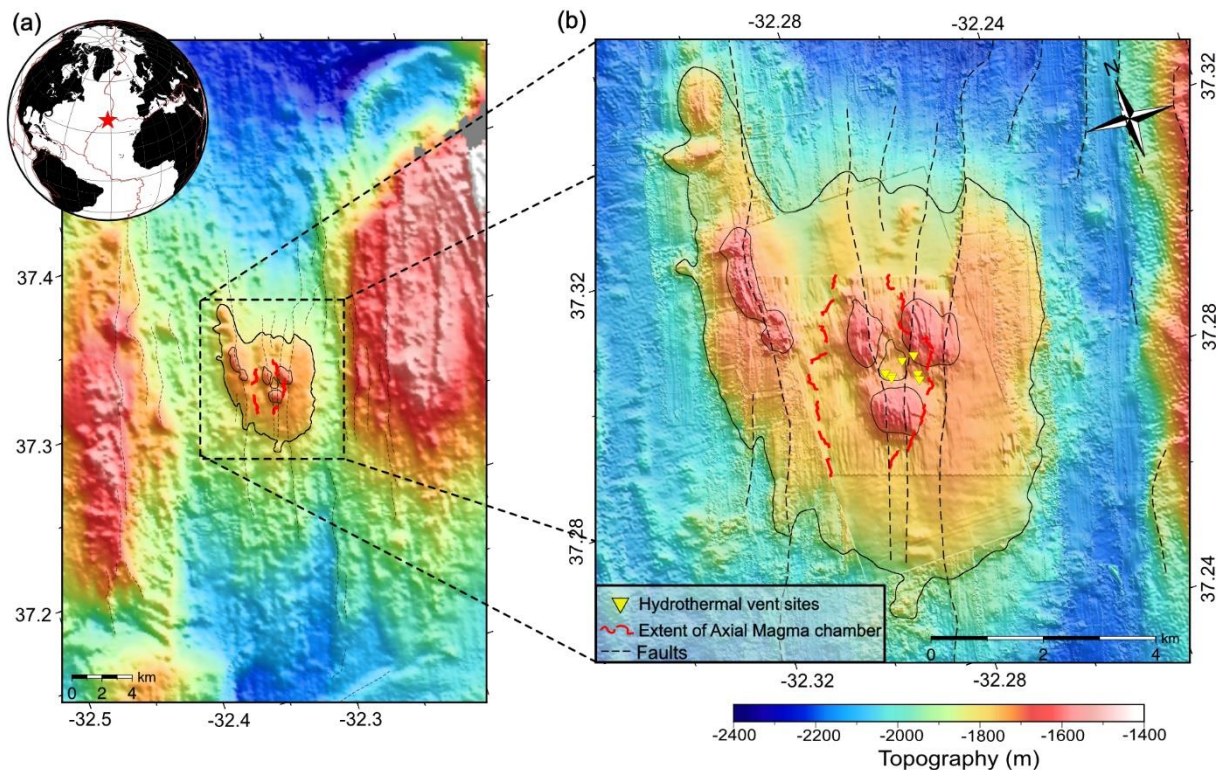


Figure 1.24. Overview maps of Lucky Strike volcano. (a) Segment scale. (b) Volcano scale. The solid black isocontours outline the volcano base (1900 m beneath sea floor (mbsf)), central fossil lava lake (1710 mbsf), its three surrounding peaks (1660 mbsf) and the western volcanic ridge (1660mbsf). Red dashed lines: Across-axis extent of the Axial Magma chamber (AMC) reflector (Combi^{er} et al., 2015; Singh et al., 2006), Black dashed lines: surface faults, Yellow inverted triangles: Hydrothermal vent sites.

Seismic structure of the upper crust beneath the LS volcano

The seismic crustal thickness of the Lucky Strike segment increases from ~ 5.5 km at the segment ends to ~ 7.5 km at the segment center, indicating melt focusing to the volcano region (Crawford et al., 2010; Seher et al., 2010) and the central volcano has significantly greater lateral P wave velocity structure than the surrounding axial valley floor with lowest values found beneath three central volcanic cones, which can be attributed to its more magmatic origin (Arnulf et al., 2014a). The uppermost crust is characterized by low velocities and a steep velocity gradient (up to 2.2 km/s increase in the first 300 mbsf), with crustal velocities reaching up to ~ 4.8 km/s at the base of Layer 2A (Figure 1.25; Arnulf et al., 2014a, b). The high velocity gradient in the shallow upper crust is interpreted as due to hydrothermal mineralization which seals pores and thin cracks. Seismic layer 2A is thick in the volcano region (up to ~ 700 -850 m, compared to 375 – 750m typical for slow spreading ridges), which is consistent with significant magmatism. Seismic reflection data imaged an axial magma chamber (AMC) 3- 3.8km beneath the volcano seafloor, spanning 2-3 km

across-axis (Combiér et al., 2015; Singh et al., 2006) and at least 5 km along-axis (Figure 1.10; Crawford et al., 2010). The AMC is underlain by a low-velocity zone, imaged using travelt ime tomography on ocean bottom seismic refraction data (Seher et al., 2010). The low-velocity zone is interpreted to be a hot domain with interstitial magma.

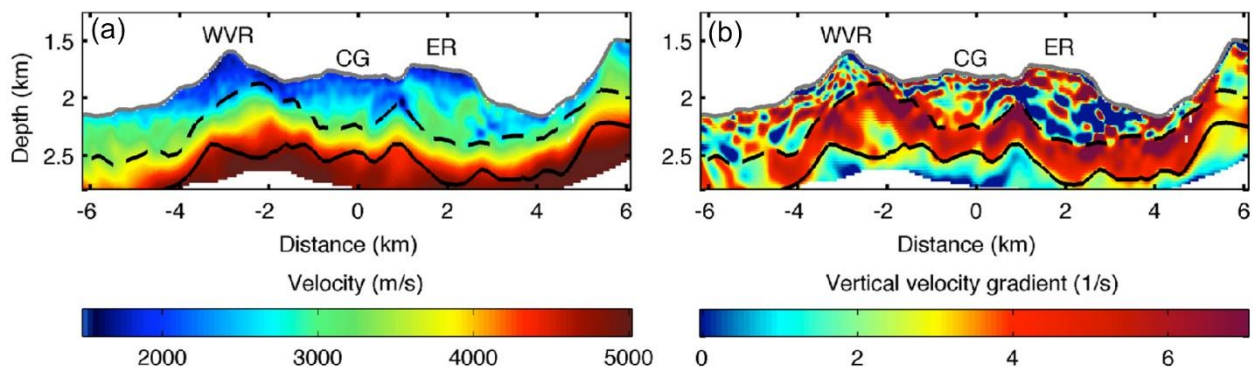


Figure 1.25. (a) Upper crustal velocity structure and (b) corresponding velocity gradient from Full waveform inversion model; adapted from Arnulf et al., (2014b). Black solid line and black dashed line mark the bottom and the top of the Layer 2A high velocity gradient zone. WVR: Western Volcanic Ridge, ER: Eastern Ridge, CG: Central Graben.

Monitoring constraints on effective permeability and seafloor vertical displacements

The long-term temperature records acquired as part of the EMSO-Azores experiment and historical measurements from the Lucky Strike hydrothermal field suggest that fluid discharge associated with the primary hydrothermal circulation at Lucky Strike has been stable over scales of 3 - 20 years (Barreyre et al., 2014a). The temperature records are primarily divided into 3 regimes based on measurement sites: the high-temperature regime (>190 °C) representing unmixed, primary hydrothermal fluid coming out of the black smokers, an intermediate regime (10 - 100 °C) associated with mixing of primary fluids with cold sea water, and a low temperature regime (<10 °C) representing the thermal boundary layer at the seafloor formed by diffuse discharge. There is a systematic and consistent coherency between exit-fluid temperatures at the high-temperature sites and tidal pressure, whose phase lag was used to estimate a high effective permeability (10^{-10} m²) in layer 2A shallow upflow zones, and upwelling of hydrothermal fluids is therefore suggested to be focused through permeable fissures and faults (Barreyre et al., 2014b; Barreyre & Sohn, 2016). Occasional episodic perturbations observed in high- and intermediate-temperature records are not correlated with the microseismicity (discussed below) and are most

likely generated by shallow, highly localized processes at the measurement sites that affect the mixing proportions of end member fluids.

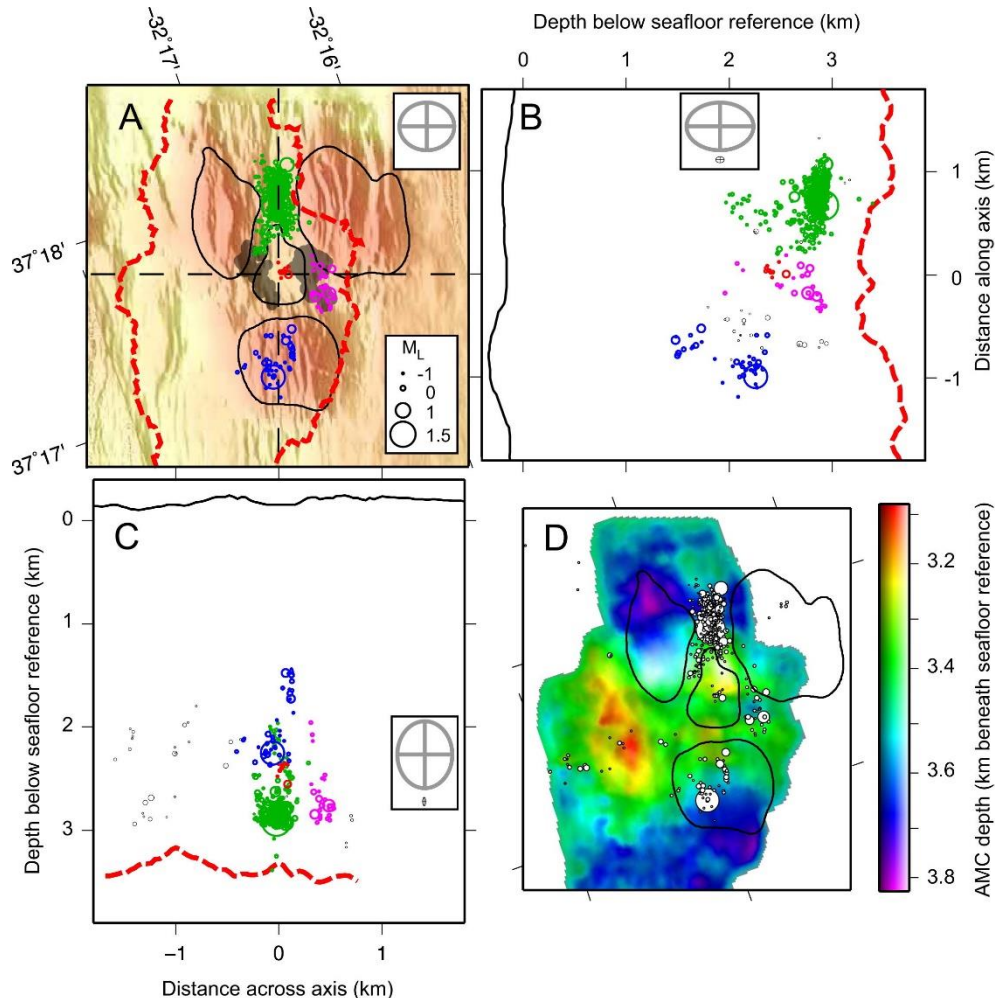


Figure 1.26. Hypocenters relocations from the year 2008-2009 beneath Lucky Strike volcano region; adapted from Crawford et al., (2013). Events are scaled by local magnitude and color coded by cluster; green: central graben north, blue: south peak, purple: east, red: summit depression. (a) Map view zoomed to summit depression and its three surrounding peaks shown by black isocontours. Red dashed lines: Across-axis extent of the Axial Magma chamber (AMC) reflector. (b) Along-axis cross section. (c) Across-axis cross section. (d) Map view of the AMC reflector, overlain by earthquakes and isodepth contour.

Tracking the hydrothermal reaction zone with seismicity and modelling

The seismicity beneath the volcano summit has been continuously recorded since 2007, using a network of 5 short period Ocean Bottom Seismometers (OBSs) with yearly redeployments (although there have not always been enough functioning instruments to continuously locate the events). Crawford et al., (2013) observed persistent microseismicity in the first 2 years of data (2007-2009), clustered in two main groups, one beneath the North of the hydrothermal field and

another beneath the peak just south of the field, with a clear depth limit over the AMC reflector (Figure 1.26). They and Fontaine et al., (2014) proposed that the source of these events is thermal contraction at the base of a hydrothermal convection cell and that these clusters thus represent the main hydrothermal heat extraction zones. The distribution of the main heat extraction zones indicates that the hydrothermal circulation at Lucky Strike is dominantly along-axis, similar to the proposed hydrothermal convection systems at fast/intermediate spreading segments. This interpretation is consistent with numerical models including a narrow along-axis high permeability zone, which supports a circulation with km-wide pipe-like upflow zones with recharge zones in between coinciding with observed seismicity clusters (Figure 1.27; Fontaine et al., 2014).

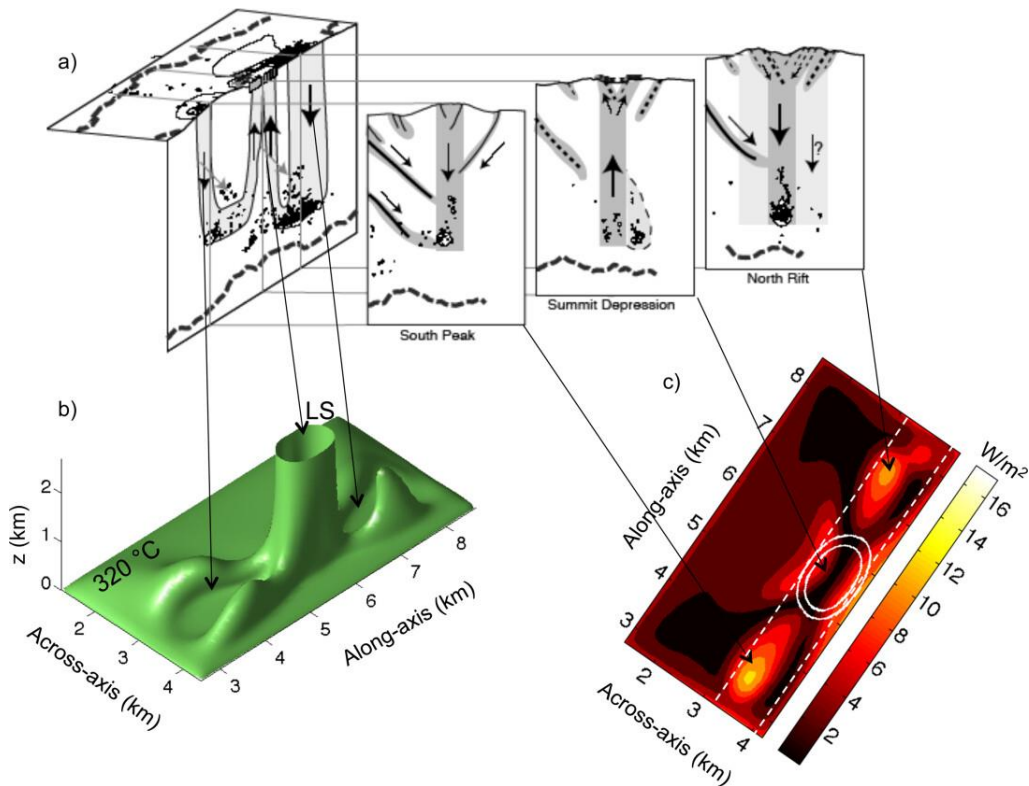


Figure 1.27. Conceptual model for hydrothermal convection beneath the Lucky Strike hydrothermal field; adapted from Fontaine et al., (2014). (a) Hydrothermal fluid pathways based on 2008-2009 hypocenters, suggesting an along-axis fluid flow. (b) The 3D 3200 C isotherm in the computing box forming a pipe at the center which corresponds to the upflow zone. (c) Heat extraction at the base of the box. The high heat extraction zones correspond to the downflow zones of the convection cells.

Chapter 2
Seismic constraints on hydrothermal
circulation and magmato-tectonic interactions
beneath Lucky Strike volcano, Mid-Atlantic
Ridge

2.1 Introduction

The Mid-Oceanic Ridge (MOR) system is the largest continuous feature on the surface of the earth and the major surface connection with the Earth's mantle. Hydrothermal activity at MORs controls lithospheric cooling by transferring most of the magmatic heat associated with crustal accretion (Lister, 1972; Lowell, 1995) and impacts thermal structure and associated subsurface processes such as magma replenishment, faulting, and diking. Two factors control the hydrothermal convection: the heat source driving the circulation and the crustal permeability steering it. Slow spreading ridges have a lower rate of magma supply than intermediate to fast-spreading ridges, leading to differences in the type of host rocks (Cannat et al., 1995), the interplay between magmatism and tectonic extension (Wilcock & Delaney, 1996), and hydrothermal activity (Lowell, 2010). Hydrothermal activity at a given slow spreading ridge location is not a steady state phenomenon, but shows repeated episodes of activation over the scale of thousands of years (Lalou et al., 1993; Lalou et al., 1995). It is speculated that hydrothermal processes are primarily magmatically controlled at fast-spreading ridges and more affected by tectonics at slow-spreading ridges, where they are driven by episodic magma emplacement in the shallow axial lithosphere (Humphris & Cann, 2000; Wilcock & Delaney, 1996).

Seismicity observed at MORs is a common tool to characterize subsurface magmato-tectonic activity, hydrothermal circulations, and the possible interactions between them. Episodic microseismicity at MORs has been interpreted to be driven by inflation/deflation of the magma chamber (Dziak et al., 2004; Wilcock et al., 2009) and by dike propagation (Dziak et al., 2012; Wilcock et al., 2016). Persistent microseismicity recorded in the vicinity of active vent fields at the EPR (Sohn et al., 1999; Tolstoy et al., 2008), Juan de Fuca (Ark et al., 2007; Sohn et al., 2004) ridges, and at the Lucky Strike volcano in the Mid-Atlantic Ridge (Crawford et al., 2013), has been interpreted as caused by thermal contraction of rocks at the base of the hydrothermal circulation zone. Microseismicity recorded within the upper few hundred meters below the TAG (Trans-Atlantic Geotraverse) vent field, has been interpreted as reaction-driven cracking in response to anhydrite precipitation in the shallow substratum (Pontbriand & Sohn, 2014).

CHAPTER 2. HYDROTHERMAL MICROSEISMICITY

Studying hydrothermal circulation at slow-spreading ridges is particularly challenging because the location and size of the magmatic heat source, and the geometry of hydrothermal fluid pathways are in most cases poorly constrained. The Lucky Strike segment on the Mid-Atlantic Ridge (MAR) differs from many other slow-spreading ridge segments by the presence of a large volcano at its center and of a well-imaged axial magma chamber (AMC) lying 3-3.8km beneath the volcano seafloor (Combié et al., 2015; Singh et al., 2006). The Lucky Strike volcano also hosts one of the largest known deep sea hydrothermal fields (Barreyre et al., 2012; Escartin et al., 2015; Fouquet et al., 1995; Susan E. Humphris et al., 2002; Langmuir et al., 1997; Ondréas et al., 2009). Using a 2007-2009 local seismicity network, Crawford et al., (2013) identified microseismicity clusters which they interpreted as due to thermal cracking in the deep regions of hydrothermal cells. They also documented a period of higher seismic activity in the second half of 2009. The distribution of the microseismicity clusters indicated that, contrary to what had previously been hypothesized for slow-spreading ridges, the hydrothermal circulation geometry at Lucky Strike is dominantly along-axis. This is consistent with numerical modelling results that predict nested pipe geometry of upflow/discharge zones, surrounded by downflow/recharge zones, controlled by dominantly along-axis distribution of magmatic heat and a narrow along-axis high permeability zone (Coumou et al., 2009; Fontaine et al., 2014).

We present 12 years (2007-2019) of seismicity recorded in the Lucky Strike volcano region by a seafloor seismological network as part of the European Multidisciplinary Seafloor and water column Observatory (EMSO)-Azores, using yearly redeployments of ocean bottom seismometers (OBSs). This long-term dataset gives us a unique opportunity to constrain the spatial distribution and temporal variation of seismic activity beneath a mid-ocean ridge volcano, and to address the following questions: was the microseismicity reported by (Crawford et al., 2013) persistent over the following 10 years? If so, did the seismicity clusters interpreted as due to hydrothermally induced thermal contraction in the base of hydrothermal downflows move and/or change shape over that period? Did other higher seismic activity periods occur? Does the thermal contraction interpretation hold for this longer record? And what do these characteristics tell us about the respective roles of magmatic and tectonic processes in controlling hydrothermal circulation patterns in the Lucky Strike volcano?

2.2 Geological context

The Lucky Strike volcano lies at the center of the ~65 km long Lucky Strike segment, MAR, ~300 km southwest of the Azores Islands. The segment has a full spreading rate of ~20.3 mm/year (DeMets et al., 1994) and features the typical morphological and tectonic architecture of a slow spreading ridge, with a ~13-20 km wide axial valley that gradually deepens from segment center (~2000 m) to segment ends (~3000 m; Detrick et al., 1995). The seismic crustal thickness increases from ~5.5 km at the segment end to ~7.5 km at the segment center, indicating melt focusing to the volcano region (Crawford et al., 2010; Seher et al., 2010).

Lucky Strike volcano lies in the axial valley, rising ~400 m from the valley floor, and is cut by numerous along-axis oriented faults (Figure 2.1a). The summit has three ~100 m high local peaks surrounding a depression containing recent lava flows and which is interpreted as a fossil lava lake (Fouquet et al., 1995; Humphris et al., 2002; Ondréas et al., 2009). The depression is a part of a recent axial graben that dissects a volcanic cone to the north, forming the two northern local peaks; the southern local peak is another, more recent, volcanic cone (Ondréas et al., 2009). The summit depression is surrounded by many high and low temperature vents (Figure 2.1c) and by zones of diffuse flow constituting the Lucky Strike hydrothermal field (Barreyre et al., 2012; Escartin et al., 2015). Detailed imagery and in-situ observations of the hydrothermal field reveal extensive diffuse venting, with an estimated total heat flux of ~200-1000 MW (Barreyre et al., 2012). Exit-fluid temperature records from vent sites of the Lucky Strike hydrothermal field show that the temperature of the fluid discharge associated with the primary hydrothermal circulation at Lucky Strike has been stable over the past 12 years; except for episodic perturbations which are not correlated with microseismic activity, indicating that they are generated by shallow processes at the measurement sites (Barreyre et al., 2014a). The observed phase relationship between the tidal pressure and exit-fluid temperature requires a high effective permeability (10^{-10} m²) in the upflow zone (Barreyre et al., 2014b; Barreyre & Sohn, 2016), and upwelling of hydrothermal fluids is therefore suggested to be focused through the permeable fissures and faults.

Seismic reflection/refraction data imaged an axial magma chamber (AMC) 3- 3.8 km beneath the volcano seafloor (Figure 2.1b), spanning 2-3 km across-axis (Comber et al., 2015;

Singh et al., 2006) and at least 5 km along-axis (Crawford et al., 2010). The AMC is underlain by a low-velocity zone, imaged using traveltimes tomography on ocean bottom seismic data (Seher et al., 2010). The low-velocity zone is interpreted to be a hot domain with interstitial magma. Synthetic Ocean Bottom Experiment (SOBE) and 3D traveltimes tomography of seismic streamer data (Arnulf et al., 2014a) suggest that seismic layer 2A is thick in the volcano region (up to ~700-850 m), with relatively lower seismic velocities than the typical layer 2A velocity structure observed beneath the axial valley.

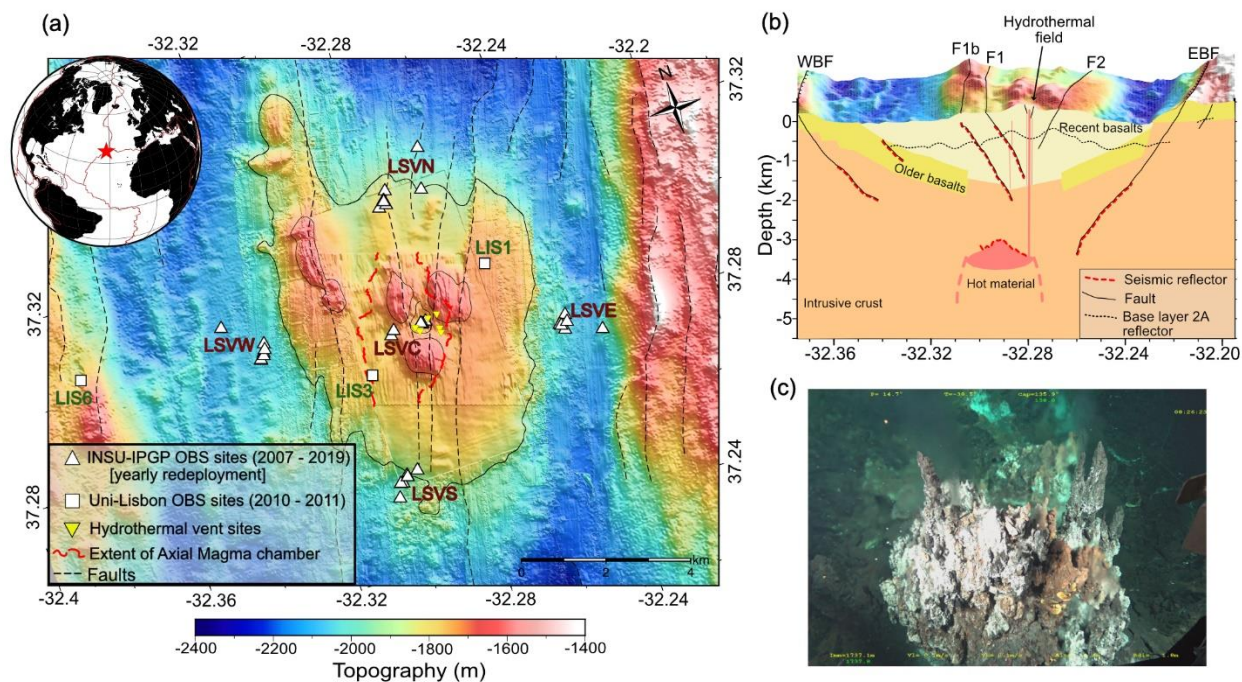


Figure 2.1. Overview of Lucky Strike Volcano, Mid-Atlantic Ridge. (a) Map view: The solid black isocontours outline the volcano base (1900 m beneath sea floor (mbsf)), central fossil lava lake (1710 mbsf), its three surrounding peaks (1660 mbsf) and the western volcanic ridge (1660 mbsf). Red dashed lines: Across-axis extent of the Axial Magma chamber reflector (AMC; Combier et al., 2015; Singh et al., 2006). Black dashed lines: surface faults, Yellow inverted triangles: Hydrothermal vent sites, White triangles: INSU IPGP OBS deployment sites, White squares: University of Lisbon OBS deployment sites. (b) Cross-sectional view with main faults and the 2006 AMC reflector based on seismic observations (Modified after Combier et al., 2015). Depth is referenced to the average seafloor reference depth (bsfr, 1.9km). WBF: Western Boundary Fault, EBF: Eastern Boundary fault. (c) Field photograph of one of the vent sites (Tour Eiffel) of the Lucky Strike Hydrothermal Field.

2.3 Method

2.3.1 Data acquisition and processing

As part of the EMSO-Azores observatory, five ocean bottom seismometers (OBSs) have been deployed around the Lucky Strike volcano summit since 2007, using repeated yearly redeployments (Figure 2.1a and Table S2.1). Each year's deployment usually consists of five INSU-IPGP short period OBSs (SPOBSs) containing a 3-component geophone (Sercel L28) and a hydrophone (High Tech-90-U). During the first 3 deployments (2007-2010) and in 2018-2019, the southern OBS (LSVS) was a broadband instrument with a 3-component Trillium T240 seismometer and a differential pressure sensor. In 2010-2011, three additional SPOBSs from the University of Lisbon (Figure 2.1a) were also deployed. All the OBSs except the 3 from the University of Lisbon have a sampling rate of 62.5 sps with a cut-off frequency at ~25 Hz. The University of Lisbon instruments have a sampling rate of 100 sps and a cut-off frequency at ~40 Hz. We processed the data for time periods when data were recovered from at least 4 OBSs (Table S2.1).

The internal clocks of the OBSs were synchronized on deployment and recovery and the timestamps were corrected by assuming a linear drift between the synchronizations. The final clock offset was verified and, in 5 cases, corrected, by plotting the change in the earthquake location time residuals over time after deployment. The local events have significant energy at the cut-off frequency for the INSU-IPGP OBSs and so the datalogger's last digital filter stage's impulse response is visible on the data. This last stage was a zero-phase filter, whose acausal response makes it difficult to precisely pick the first arrival's time and polarity. We therefore converted the data to the equivalent minimum phase filter response using a Finite Impulse Response (FIR) correction (Scherbaum & Bouin, 1997). The broadband OBS data was filtered with a 2-pole high-pass filter at 4.5 Hz to match the SPOBS data.

Events were detected using a standard short-period average/long-term average (STA/LTA) algorithm, then P and S arrival times and waveform amplitudes were automatically picked using a Kurtosis-based picker (Baillard et al., 2014). A new Python version of the Kurtosis picker was developed for the 2010-2011 data in order to handle the different sampling rates of the INSU-IPGP

and University of Lisbon OBSs (<https://github.com/WayneCrawford/pspicker>). The use of a different picker may result in different waveform amplitudes which may lead to different magnitudes and moment magnitude. The phases from events picked by at least 4 OBSs were then manually corrected and only those events were used further.

2.3.2 Earthquake Locations

In this study, we incorporate only events originating within the OBS network, heretofore "volcano events". We located the earthquakes using a grid search algorithm within the NonLinLoc (NLLoc) location software (Lomax et al., 2000) and a 3D seismic P-wave velocity model (Figure 2.2).

The 3D velocity model was obtained by combining two different 3D models derived from active seismic data: 1) the full waveform inversion (FWI) of seismic streamer data ('AA model'; Arnulf et al., 2014b) and 2) the travel time tomography of OBS data ('TS' model; Seher et al., 2010). This composite model (hereafter referred to as AA_TS) combines the FWI model in the upper crust (0-4 km bsl) with the tomography model from 6-12 km bsl, using a 2 km linearly interpolated buffer zone in between (Figure 2.2a, c). Arnulf et al., (2014b) observed that the TS model overestimates upper crustal velocities because of the lack of shallow turning rays combined with the smoothing used to stabilize the travel time tomography inversion. The AA model only extends 5 km along-axis (Figure 2.2b) and so we expanded it to the 20 km along-axis dimension of the AA_TS model using the average AA model value at each depth and across-axis location (Figure 2.2b).

We calculated V_s for our model using a constant V_p/V_s of 1.93. The average RMS residual is minimum for $V_p/V_s = 1.93$ (Figure S2.1b) and a modified Wadati diagram (Chatelain, 1978) using the 3D model indicates a V_p/V_s of 1.91 ± 0.09 (Figure S2.1a). The modified Wadati diagram has high uncertainty because the OBSs are at nearly the same distance from most epicenters, causing similar phase arrival offsets at all OBSs for volcano events.

We compared the locations obtained with the AA_TS composite model with those obtained using Seher et al.'s (2010) 3D tomography model ('TS model') and a 1D model used in Crawford

et al., (2013). The ‘TS’ tomography model gives smaller RMS residuals (Figure 2.2d) but most of the events are located below the AMC (Figure S2.2) due to higher upper crustal velocities (Figure 2.2c). The 1D model of Crawford et al., (2013) yields locations about 0.5 km shallower and with a narrower vertical range than those obtained with the AA_TS model, probably because of a sharp velocity gradient at 2-3 km bsfr (beneath seafloor reference depth = 1.9 km) in the 1D model (Figure 2.2c), which forces locations toward that depth range. The earthquakes located using the AA_TS model were relocated using the Double-Difference Hypocenter algorithm (Waldhauser & Ellsworth, 2000) (Supplementary Text S2.1 and Figure S2.3, S2.4).

To estimate how much network-based bias could affect or contribute to event locations, we compared station delays for each deployment year (Figure S2.5, Supplementary text S2.2), and we estimated the effect of picking errors using a derived bootstrap inversion (Baillard et al., 2015) for a selection of events from several deployments (Figure S2.6, Supplementary text S2.2). To estimate the effect of any change in upper crustal structure during the experiment, we performed synthetic tests in which we increased/decreased the upper crustal velocity by 15% of its original value (Figure S2.7, Supplementary text S2.2). Each of the above-mentioned variables (network-based bias, picking errors, change in upper crustal velocity structure) could generate a 100-300 m shift (Supplementary text S2.2).

2.3.3 Magnitude of completeness and b-value estimation

Earthquake local magnitudes (M_L) were calculated in the HYPOCENTER program (Lienert et. al, 1986; Lienert and Havskov, 1995), using the custom scale defined in Crawford et al., (2013). We estimated the magnitude of completeness (M_c) using the stability of the b-value as a function of cutoff magnitude (Woessner & Wiemer, 2005). The b-value at each step was estimated using the Maximum Likelihood (MLE) method (Aki, 1965) and we then defined M_c as the minimum magnitude for which $|b_{\text{avg}} - b| < \delta b$, where b_{avg} is the arithmetic mean of the successive cutoff magnitudes and δb is the b-value uncertainty calculated using the criterion defined in Shi & Bolt, (1982). The number of OBSs and their orientations were not the same each year, which could affect the completeness of the earthquake catalog. We therefore calculated M_c and b-values for each deployment year separately (Figure S2.8).

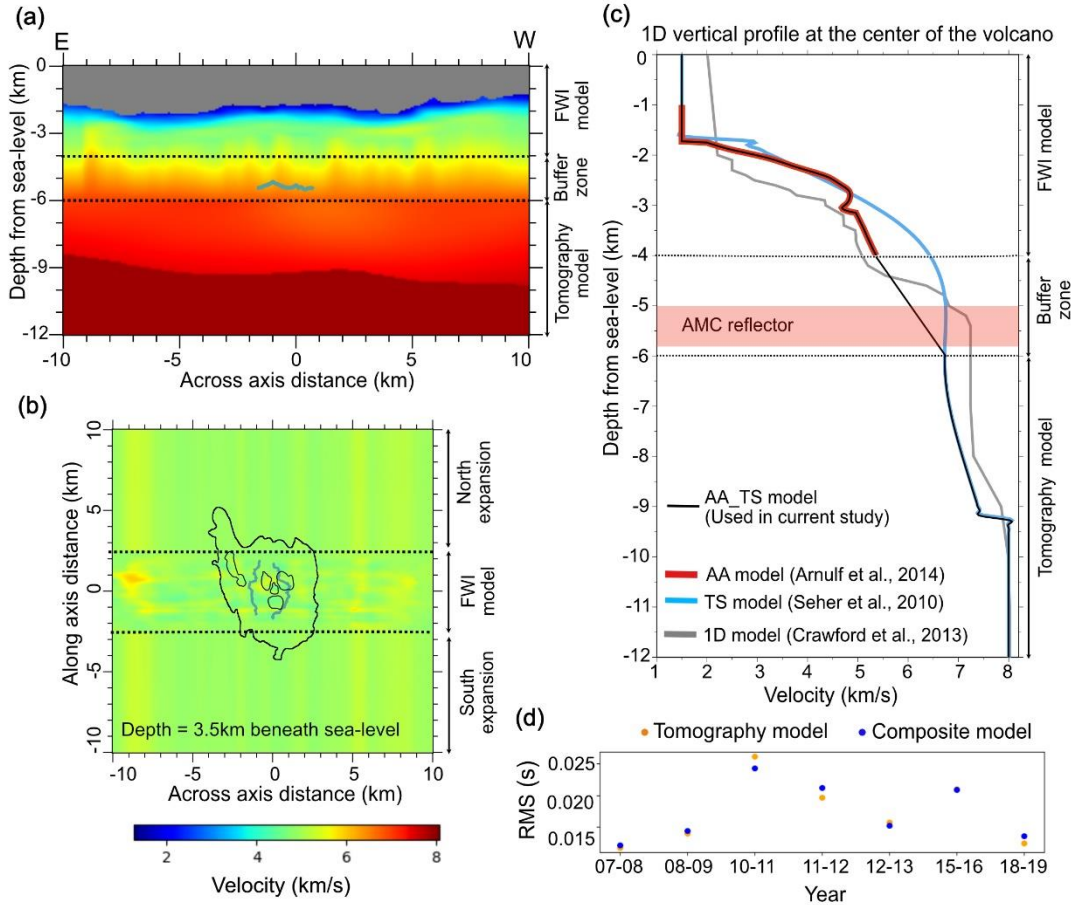


Figure 2.2. 3D seismic P-wave composite (‘AA_TS’) velocity model used for earthquake locations along (a) an across-axis vertical section through the center of the volcano (b) a horizontal section 3.5 km below sea level. The black isodepth contours are the same as in Figure 2.1 (volcano base, western volcanic ridge, lava lake and its three surrounding peaks). Grey lines mark the extent of the axial magma chamber. (c) Comparison of 1D vertical velocity profiles for different velocity models at the center of the volcano. The “buffer zone” in (a) and (c) contains a linear vertical velocity gradient from the FWI model (Arnulf et. al, 2014b) to the 3D tomography model (Seher et. al, 2010). (d) Comparison of average RMS residuals for the tomography model and the composite (AA_TS) models for each deployment year.

2.3.4 Focal Mechanisms

We used the first motion algorithm FOCMEC (Snook et al., 2003) to calculate focal mechanisms of events in the year 2010-2011, for which we had 8 working OBSs. INSU-IPGP OBSs and University of Lisbon OBSs have opposite vertical polarities, which we verified using teleseismic events and we accounted for in calculating the focal mechanisms. Using the following criteria: ≥ 5 first motion P-wave arrival polarities, $< 10\%$ weighted fraction of misfit polarities and ≥ 4 P to S amplitude ratio pairs, we obtained 18 focal mechanisms out of 217 events detected in

that year (Table S2.2). FOCMEC assumes double-couple source mechanisms for events while calculating focal mechanisms. So, the focal mechanism solution given by FOCMEC for an event generated by thermal contraction/expansion may be in error.

2.4 Results

We show results for the 5 time periods when data was available from at least 4 OBSs (Figure 2.3): 2007-07-22 to 2009-07-27, 2010-10-14 to 2011-12-31, 2012-07-17 to 2013-05-31, 2015-04-22 to 2016-05-26 and 2019-02-01 to 2019-06-14. Only 4 OBSs were operational in 2012-2013 & 2019 (Table S2.1). 8 OBSs operated in 2010-2011, and 5 during the other studied periods (Table S2.1). The magnitude and moment calculated for the 2010-2011 events are not exactly equivalent to the rest of the dataset because of the use of a different picker program (see the Method section).

We define Higher Seismic Activity (HSA) periods as those when the seismicity rate is at least twice the average rate (Figure 2.3c). The average seismicity rate beneath the volcano region is 8.6 events/week overall, and most local magnitudes (M_L) are between -1 and 0 (Figure 2.3a). Several HSA periods are associated with the occurrence of higher magnitude events ($M_L > 0.8$; light blue lines in Figure 2.3a). In the following sections, we describe the temporal and spatial variations of seismicity beneath the volcano in three time periods, each comprised of several consecutive or non-consecutive successful (i.e., at least 4 working OBSs) deployments: 2007-2009, 2010-2013 (with a data gap from 2012-01-01 to 2012-07-16), and 2015-2019 (with a long data gap from 2016-05-27 to 2019-01-31).

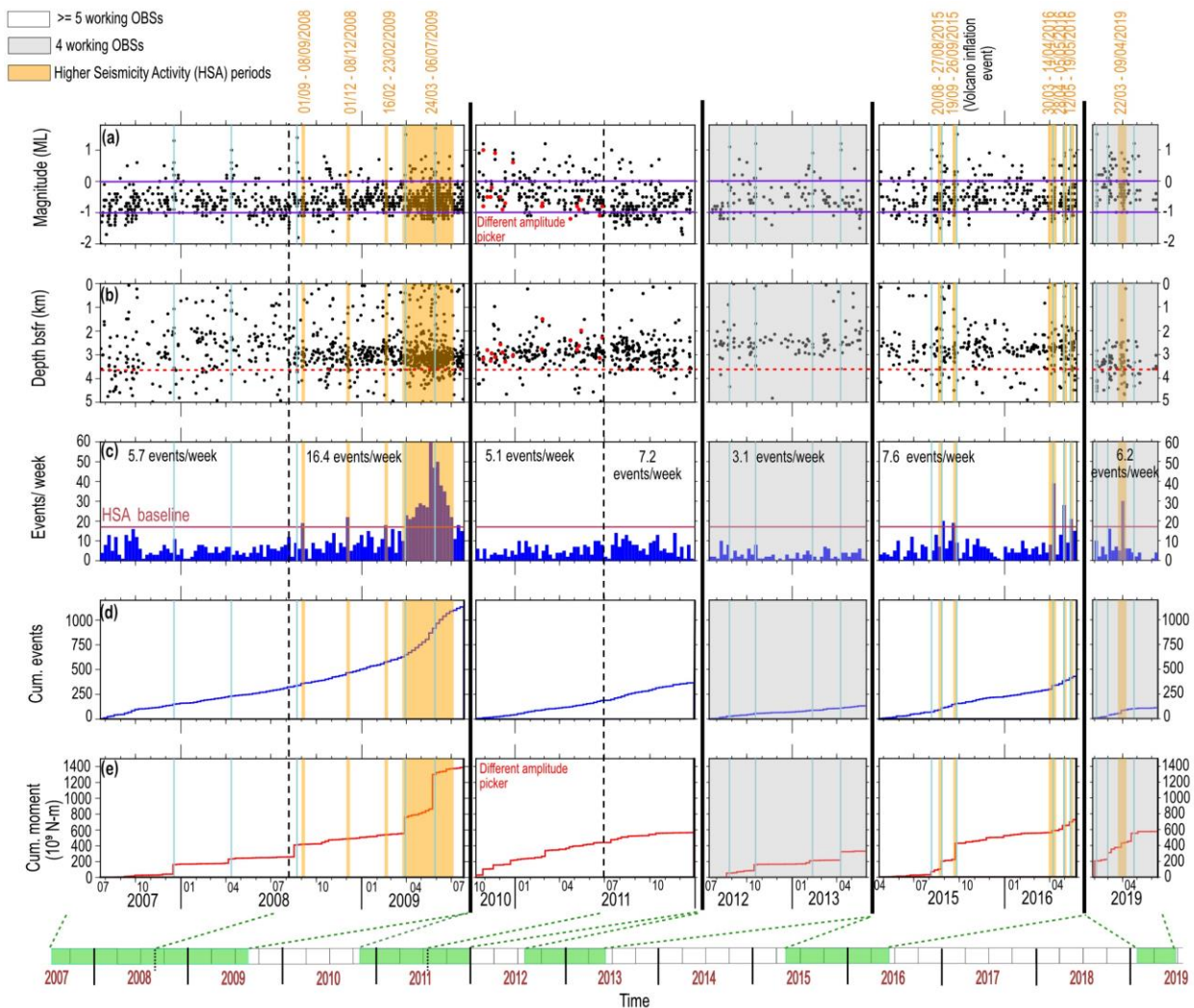


Figure 2.3. Temporal distribution of seismicity beneath Lucky Strike volcano, 2007-2019. On the bottom time scale, green color filled time periods correspond to those considered in this study: i.e., with ≥ 4 working OBSs (grey background marks periods with only 4 working OBSs). Thick black vertical lines mark data discontinuity in time. Dashed vertical black lines correspond to maintenance cruises and separate consecutive deployments. Orange background marks Higher Seismicity Activity (HSA) periods and light blue vertical lines mark the occurrence of higher magnitude events ($ML > 0.8$). An event of volcano inflation detected using bottom pressure probes, occurred in late September 2015 (Ballu et al., 2019). (a) Local magnitude. Values for the 2010-2011 period were obtained with a different picker and are not directly comparable. Red dots represent the magnitudes of the events for which focal mechanisms were obtained in the 2010-2011 period (Figure 2.8). (b) Event depths (referenced to avg. sea floor reference depth of 1.9km). Red dashed line at 3.6 km bsfr marks average depth of AMC reflector. Scattering in 2007-2008 is probably due to poorer seafloor coupling during that deployment. Red dots represent the depth of the events for which focal mechanisms were obtained for the 2010-2011 period (Figure 2.8). (c) Events per week. The horizontal line is the threshold value for defining HSA periods. (d) Cumulative number of events for each period. (e) Cumulative seismic moment for each period.

2.4.1 Earthquake magnitude distribution

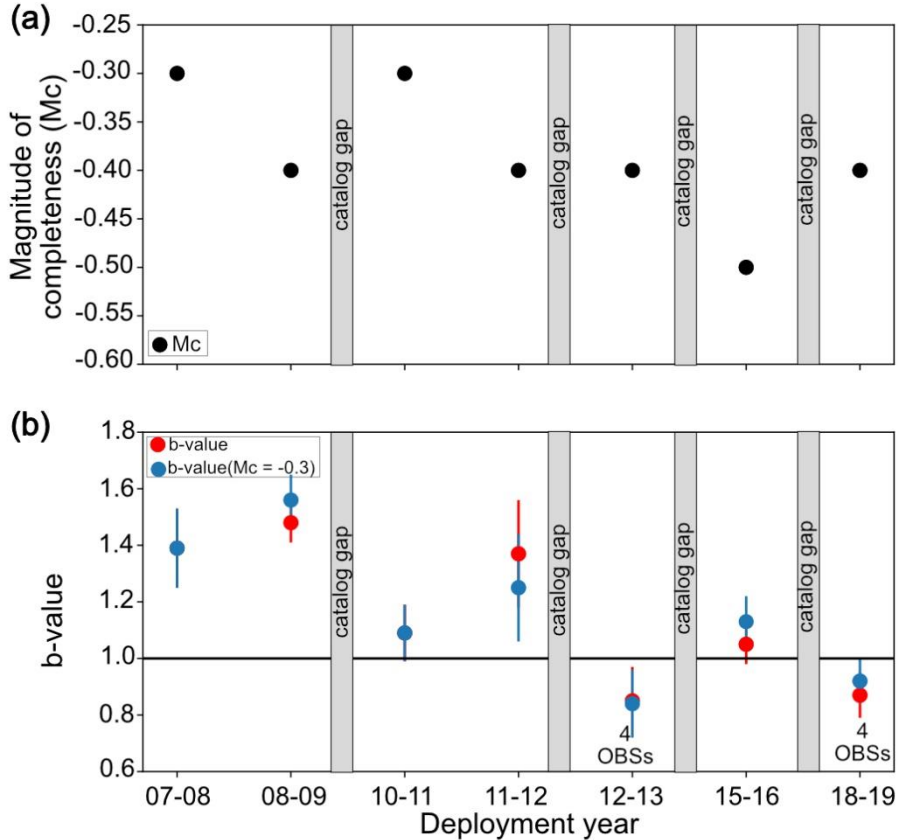


Figure 2.4. Magnitude of completeness (M_c) and b -value estimation for seismicity recorded beneath the Lucky Strike volcano, 2007-2019. In each deployment year, M_c and b -value are estimated by MLE method (Figure S2.8). Gray boxes represent data discontinuity between two non-consecutive deployments (non-green periods in the bottom scale of Figure 2.3). (a) M_c value for each deployment year. (b) B -value estimated for different deployment years using that year's M_c (red dots) and a global M_c value (-0.3) for the entire catalog (blue dots). The global M_c is defined as the highest M_c of all deployments. Black horizontal line represents the standard b -value (1.0). B -value is < 1.0 for two deployments when there were only 4 working OBSs.

The magnitude of completeness (M_c) of the volcano events varies between -0.5 and -0.3 for different deployment years (Figure 2.4a, S2.8). We calculate M_c value for each deployment year separately and take the highest M_c value of calculated of all the deployment years as the global M_c for the entire 12-year catalog. For each deployment, we calculate the b -value using: 1) the M_c value computed using the corresponding year's catalog (red dots in Figure 2.4b) 2) the global M_c of the entire catalog ($M_c = -0.3$) of all years (blue dots in Figure 2.4b): both values are within each other's error limit. The b -value varies between 0.85 and 1.48 over the different deployment periods (Figure 2.4b). It is > 1.0 for all but 2 years (2012-2013 and 2018-2019), which is typical of volcanic regions with strong heterogeneities, thermal gradients, high pore pressures

and extensive fracture (Wiemer & Wyss, 2002). The two years with b-value <1.0 (2012-2013 and 2018-2019), correspond to networks with only 4 working OBSs and we believe these low values are probably an artifact of the network size, as a 4-station network will probably miss more small events than a network with more stations.

2.4.2 Temporal variation in seismicity rate, magnitude and depth

The 2007-2009 seismicity record (covering two consecutive deployments) has already been described in Crawford et al., (2013). Magnitudes of most of the events in this period are in the M_L range of -1 to 0 (Figure 2.3a), with 5 higher magnitude events ($M_L > 0.8$; light blue lines in Figure 2.3a). There is a wavy variation in lowest magnitudes of the events detected with a periodicity of ~ 1 year (May-August 2008, April-July 2009 periods in Figure 2.3a), that probably corresponds to periods during which other sources of seismic signal were quieter. Most of these other sources are whale songs that are detected in the 20-30 Hz band at which local events have maximum energy, and therefore it is difficult to see small magnitude events in the periods of abundant whale songs (mostly between November to March). During the first deployment (2007-2008), the depth distribution of the events seems very scattered (Figure 2.3b), probably because of high pick errors due to bad coupling of the instruments to the seafloor (the instruments had a supplementary floatation that was removed in following years). In the 2008-2009 record, the depth distribution is more clustered with most events located 2.0-3.5 km beneath the seafloor reference depth (bsfr = 1.9 km) and few (7% of total events at < 1 km bsfr) close to the seafloor (Figure 2.3b). We detect 4 HSA periods in the 2008-2009 record: 3 are only 1-week long and one lasts ~ 13 weeks, from end of March to Early July 2009 (Figure 2.3c). This is the longest HSA period recorded during the entire experiment, with a seismicity rate that reached up to fifty events/week in end of May 2009 (Figure 2.3c). This HSA period includes two higher magnitude events ($M_L = 1.7$ & 1.8 ; light blue lines in Figure 2.3a), marking sharp jumps in cumulative magnitude moment curve (Figure 2.3e), with the first one defining the beginning of the HSA period (Figure 2.3c) and the second one in the middle, after which the seismicity rate slowly declined (Figure 2.3c).

The 2010-2013 period consists of three deployments: two consecutive ones in October 2010 to June 2011 and July 2011 to December 2011, then another from July 2012 to May 2013 (Table S2.1). The magnitudes of most of the events in this period remain in the M_L range of -1 to

0 (Figure 2.3a). Until the end of 2011, events are mostly located in the 2.0-3.5 km bsfr range (Figure 2.3b). In July 2012 to May 2013, they are mostly focused in the upper limit of this range (~2.2 km bsfr) with almost no events just above the AMC reflector (Figure 2.3b). Overall, event locations show less vertical variation throughout this period than in 2007-2009. This 2010-2013 record has no detected HSA periods (Figure 2.3c). The July 2012 to May 2013 record is particularly quiet (Figure 2.3c, d), with a seismicity rate of only 3.1 events/week, yet it does include several higher magnitude events which are relatively evenly spaced throughout that time period (light blue lines in Figure 2.3a, e).

The seismicity rate is back up to the pre-2012 average in the April 2015 to June 2019 period (covering two non-consecutive deployments: April 2015 to May 2016 and February 2019 to June 2019). Magnitude of most of the events are in the M_L range of -1 to 0 (Figure 2.3a). Wavy variations in magnitudes observed in earlier periods are also seen in the entire 2015-2016 period (Figure 2.3a), with smaller magnitude events ($M_L < -1.0$) detected probably during periods (July-September 2015, April-May 2016) during which other sources of seismic signal (whale songs primarily), were quieter. In the April 2015 to May 2016 deployment, five HSA periods are detected, which are confined to two time intervals: August-September 2015 and April-May 2016 (Figure 2.3c). The August-September 2015 interval has two HSA periods (6-7 days each; two orange bands in August-September 2015 in Figure 2.3c). There is one higher magnitude event ($M_L = 1.0$) occurring ~15 days prior to the first HSA, and two other higher magnitude events, one at the end of each HSA period ($M_L = 1.2$ & 1.5 ; light blue lines in Figure 2.3a). The April-May 2016 interval has 3 consecutive HSA periods: each 7-10 days long (three orange bands in April-May 2016 in Figure 2.3c). There are three higher magnitude events in this interval, one in each HSA period ($M_L > 0.8$; light blue lines in Figure 2.3a). The events in these HSA periods vary more in depth than the events outside the HSA periods, which are concentrated within the ‘standard’ 2.0-3.5 km bsfr range (Figure 2.3b).

After a ~3 years gap, the average seismicity in the 4-month long 2019 seismicity record is similar to that in 2015-2016 and an HSA period of ~18 days occurs in March-April 2019 (Figure 2.3c). The average event depth in this 4-month record is significantly greater than in previous years (Figure 2.3b), with most events between ~2.5 and 5 km bsfr. Although there were only 4 months

of recording and fewer earthquakes than in the 2015-2016 record (Figure 2.3d), the cumulative moment reached almost the same value (Figure 2.3e) because of several higher magnitude events, indicating a similar amount of energy release in a shorter time frame.

CHAPTER 2. HYDROTHERMAL MICROSEISMICITY

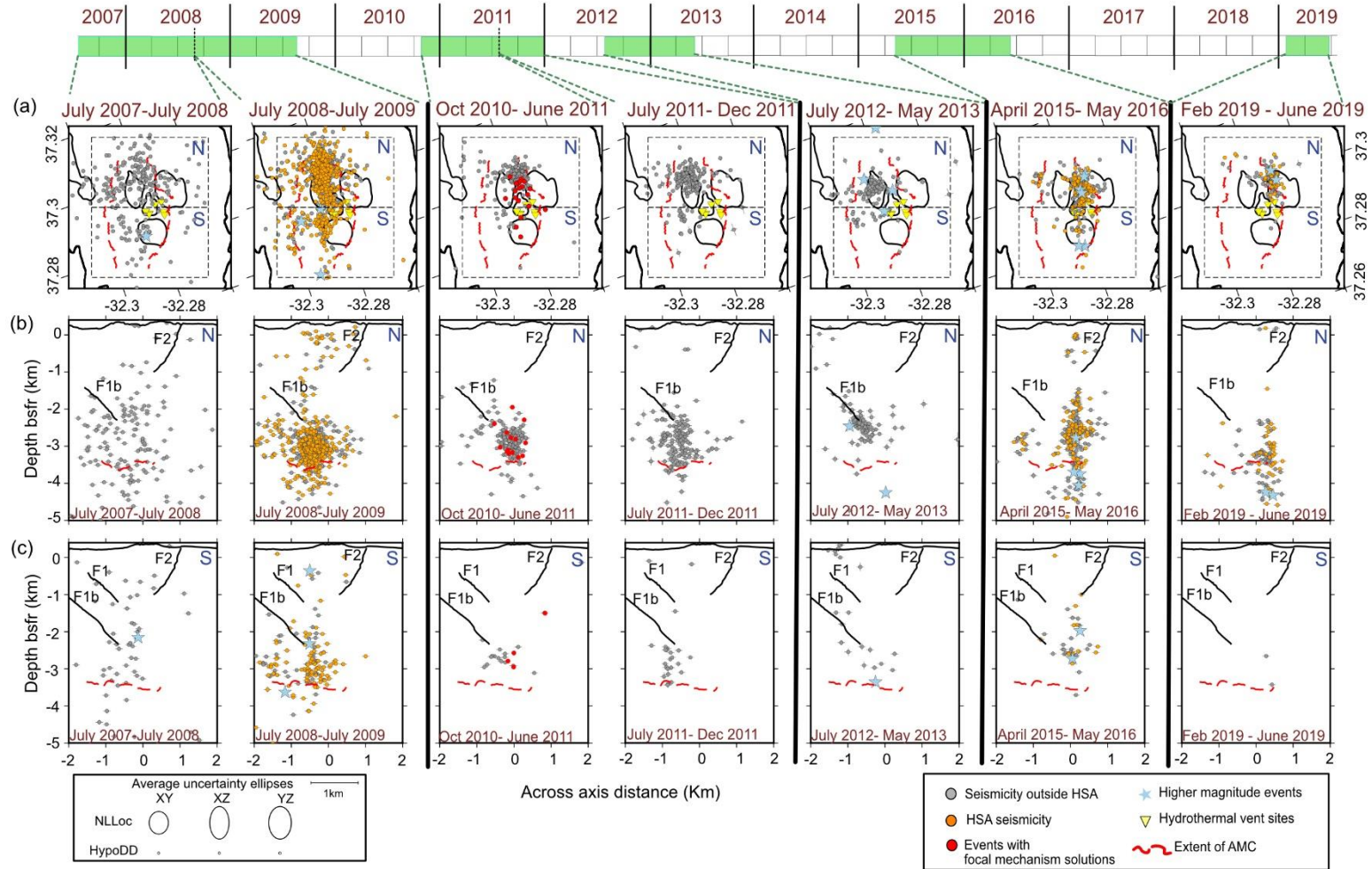


Figure 2.5. Spatial distribution of seismicity recorded beneath the Lucky Strike volcano, plotted for each successful deployment year (i.e., 4 or more recording OBSs). Thick black lines mark data discontinuity in time (same as Figure 2.3). Grey circles represent background seismicity (events outside HSA periods), orange circles represent events from HSA periods, and light blue stars are higher magnitude events marked as light blue lines in Figure 2.3. Red circles in the 2010-2011 record are the events for which focal mechanisms were obtained (Figure 2.8). (a) Map view. Black isocontours outline the lava lake and its three surrounding peaks. Red dashed lines mark extent of the AMC, yellow inverted triangles mark hydrothermal vent sites. Extent of vertical cross sections in (b) and (c) are indicated by black dashed boxes. (b) Across-axis cross section in North of hydrothermal field marked as N in (a). The depth is referenced beneath seafloor reference depth (bsfr) 1.9km and red dashed line marks the roof of the AMC in North box. The black lines are fault reflectors (Combiér et al., 2015). (c) Across-axis cross section in South of hydrothermal field marked as S in (a), same scale and symbols as in (b). Red dashed line marks the roof of the AMC in South box.

2.4.3 Spatial variation in seismicity

In the 2007-2009 record (two consecutive deployments), most of the volcano events are clustered north-northwest of the hydrothermal field (Figure 2.5a and S2.9a). The events from the 2007-2008 deployment appear more scattered, probably because of the poor coupling issue mentioned before. Most of the events in the 2008-2009 record are in the depth range of 0-1.4 km above the AMC and do not align to the seismically imaged faults (Figure 2.5b, c). There are no significant differences in event location in the 2008-2009 record, before and during the HSA periods, with most of the events located in a patch above the AMC (Figure 2.5a and S2.10). The April-June 2009 HSA period also has another seismic cluster south of the hydrothermal field, where seismicity had previously been quite low (Figure 2.5a, c, S2.10). In the north-northwest cluster, some events in the 2008-2009 period are very shallow (< 1 km bsfr; Figure 2.5b). The first higher magnitude event occurred at beginning of the April – June 2009 HSA period ($M_L > 1.7$; light blue lines in Figure 2.3) is located just to the south of the north-west volcanic cone (light blue star in Figure 2.5a) and at a depth of 2.4 km bsfr at the deepest portion of the F1b fault (light blue star in Figure 2.5c). The second higher magnitude event occurring in the peak period of the April – June 2009 HSA is located further south (~ 1 km south of the southern volcanic cone, light blue star in Figure 2.5a), at a ~ 0.350 km bsfr depth (light blue star in Figure 2.5c). A few events from the 2008-2009 record are located beneath the AMC reflector, mostly during the April-June 2009 HSA period (Figure 2.5b, S2.12). These deep events are located well within the lateral bounds of the AMC reflector (Figure 2.5b, S2.12), but their depth distribution is within the depth uncertainty of the events above the AMC (Figure S2.13), so all these events could be above the AMC.

In the 2010-2013 record (three deployments, the first two consecutive), there are very few shallow events (< 1 km bsfr) or events beneath the AMC reflector (Figure 2.5b), and seismicity is almost absent to the south of the hydrothermal field (Figure 2.5a, c). Overall, seismicity is mostly confined to depths of ~ 2.0 and 3.5 km bsfr, between the deepest portion of the F1b fault reflector and the AMC reflector (Figure 2.5b), and the spatial extent of the seismicity is confined to a smaller zone than the 2007-2009 seismicity (Figure 2.5a). In the July 2011 to December 2011 record, the mean locus of the seismicity cluster is ~ 600 m to the west of the mean locus of the seismicity recorded during the October 2010 to June 2011 deployment (Figure 2.5a, S2.9b), to just beneath the north-west peak of the volcano (Figure 2.5a, 2.6b, 2.6d). This shift is unlikely to be due to

changes in the network configuration between the two deployments (Supplementary text S2.2, Figure S2.5). Following a data gap of ~7 months, in the July 2012 to May 2013 record, the mean locus of the seismicity remained beneath the north-western peak (Figure 2.5a). There are almost no events just above the AMC during this time and the events align along the F1b fault (Figure 2.5b).

In the 2015-2016 record, after a long (June 2013 to April 2015) data gap, the mean locus of the seismicity had shifted eastward (~800 m east of the 2012-2013 mean locus of the seismicity; Figure 2.5a, S2.9c) and was focused just beneath and north of the hydrothermal field, and along the eastern edge of the AMC reflector (Figure 2.5a, 2.5b, 2.6c, 2.6d). The events cluster in a subvertical, pipe-like pattern that extends from ~1 km below the AMC reflector up to ~2 km bsfr depth, with a few events occurring <1 km below the seafloor (Figure 2.5b). Events located below the AMC reflector are very close to/outside the eastern edge of the AMC reflector (Figure 2.5b, S2.12). HSA events have the same pipe-like clustering pattern as the events outside the HSA periods (Figure 2.5b, S2.11). On 27th August 2015 (during the first HSA period in the August-September 2015 interval; Figure 2.3c), 6 events occurred within 30 minutes, with the first event ($M_L=1.2$) just below the edge of the AMC and the last two events very close to the seafloor (Figure 2.7). A similar upward migration pattern was observed on 10th September 2015 (between the two HSA periods in the August-September 2015 interval; Figure 2.3c), but all the events then were very small (Figure 2.7). Out of the three higher magnitude events occurring the August-September 2015 interval (light blue lines in Figure 2.3a), the first two are located in the main cluster of seismicity north of the hydrothermal field (light blue stars in Figure 2.5a), both below the AMC (Figure 2.5b), and the third one is located beneath the southern volcanic cone (Figure 2.5a), at ~2 km depth above the AMC (Figure 2.5c). In the April-May 2016 interval containing 3 HSA periods, higher magnitude events have same pattern: the first two are in the main seismicity cluster north of the hydrothermal field (light blue stars in Figure 2.5a), one above and one below the AMC (Figure 2.5b) and the third higher magnitude event is beneath the southern volcanic cone (Figure 2.5a, 2.5c).

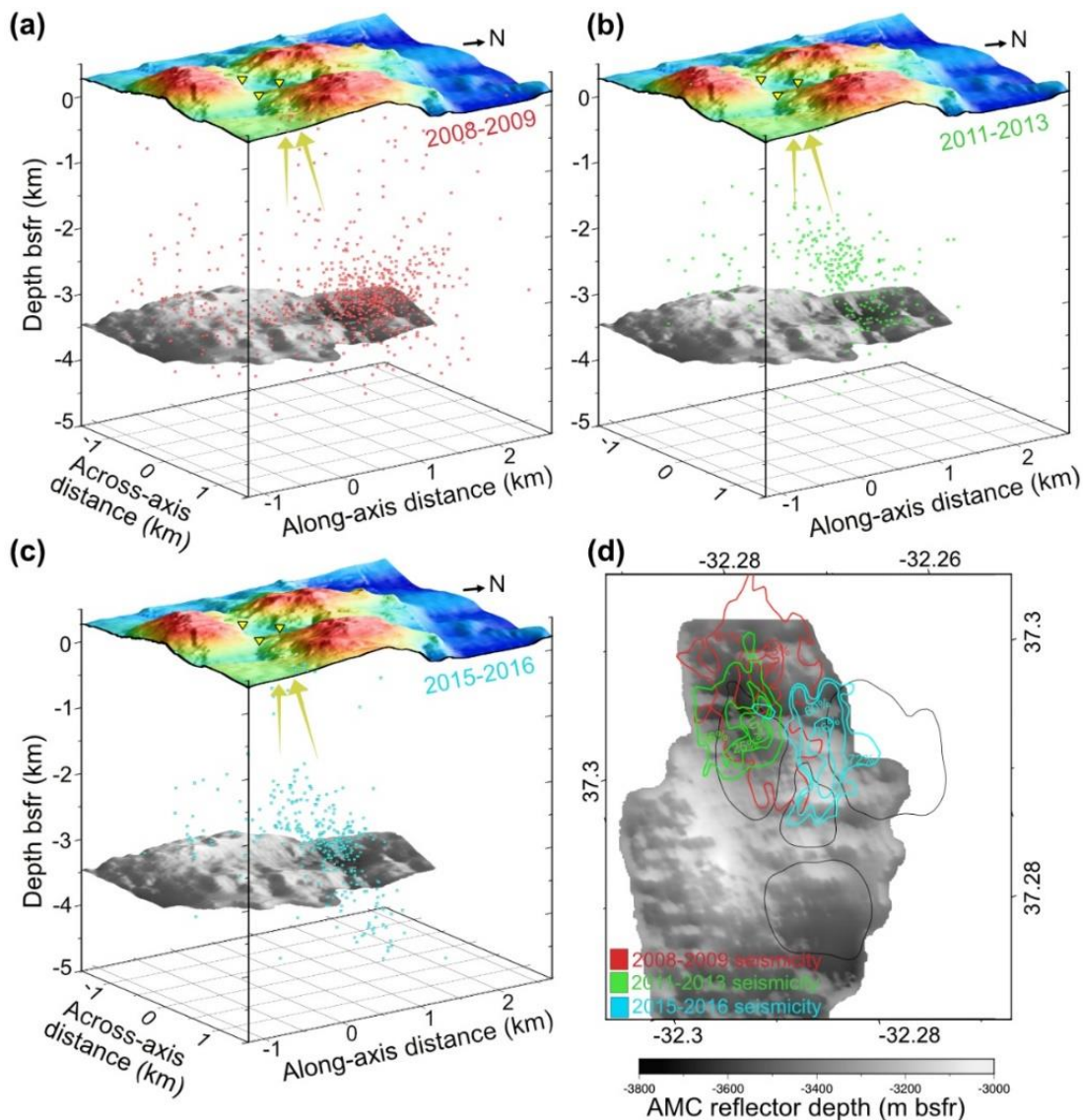


Figure 2.6. Spatial shifts in the Lucky Strike volcano seismicity with time. (a), (b) & (c) are 3D representations of the recorded seismicity in 2008-2009, 2011-2013 & 2015-2016 respectively. Yellow inverted triangles on the topographic map represent approximate location of hydrothermal venting sites. Gray surface is the roof of the AMC reflector (Combier et al., 2015; Singh et al., 2006). Yellow arrows mark upflow zone of the hydrothermal circulation. (d) Spatial shift of seismicity on the map view. Black isodepth contours are the same as in Figure 2.1 (lava lake and its three surrounding peaks). The contours lines represent the percentage of total events occurring inside it in the respective time period, color coded with time and plotted on the top of the AMC reflector. Outer most contour in each time period contain 61% (2008-2009 period), 56% (2011-2013) and 72% (2015-2016) of total events recorded in that period respectively. More detailed contours from each time period are shown in Figure S2.9.

CHAPTER 2. HYDROTHERMAL MICROSEISMICITY

After a gap of ~ 3 years, we had a short successful deployment (i.e., at least 4 working OBSs; Table S2.1) from February-June 2019. In this 4-month long seismicity record, the main seismicity cluster is smaller and restricted to the north-northeast region of the 2015-2016 seismicity cluster, along the Eastern boundary of the AMC (Figure 2.5a). Most of the events are distributed from ~ 1 km beneath the AMC to ~ 1.5 km above it (Figure 2.5b). The distribution of event locations in the single recorded HSA period (Figure 2.3c) is similar to the events outside the HSA period. Two higher magnitude events ($M_L > 1.0$; light blue stars in Figure 2.5a) are located below the AMC depth (Figure 2.5b). There is almost no seismicity south of the hydrothermal field (Figure 2.5c).

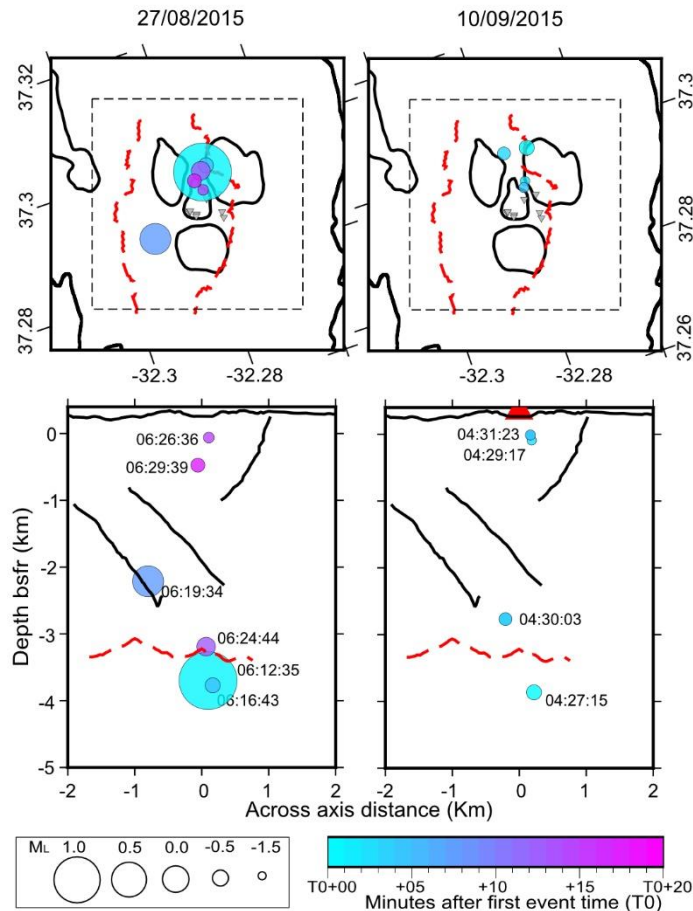


Figure 2.7. Upward migration events observed on 27/08/2015 and 10/09/2015. Events are scaled according to magnitudes and color coded according to time.

2.4.4 Focal mechanisms

Of the 18 events from the 2010-2011 deployment for which we could determine focal mechanisms, assuming these are double couple events (see Method), 9 had thrust, 7 normal

faulting and 2 strike/slip faulting mechanisms (using the classification proposed by Frohlich, (2001)). These solutions may be in error if the events are generated thermal contraction/expansion mechanisms since we have assumed double couple events. These events are scattered throughout the period of 2010-2011 deployment (red dots Figure 2.3a) and their depths are in the same range as most of the events present in the main cluster of seismicity (red dots in Figure 2.3b). Most of these events are located to the north of the hydrothermal field (red dots in Figure 2.5a; Figure 2.8a) and within 1km above the AMC along the downward continuation of the F1b normal fault, like most of the 2010-2011 events (red dots in Figure 2.5b, c). There is no obvious pattern observed in the source properties of these events, and none of them have mechanisms consistent with the seismically observed normal faults (Figure 2.8b, c, & d).

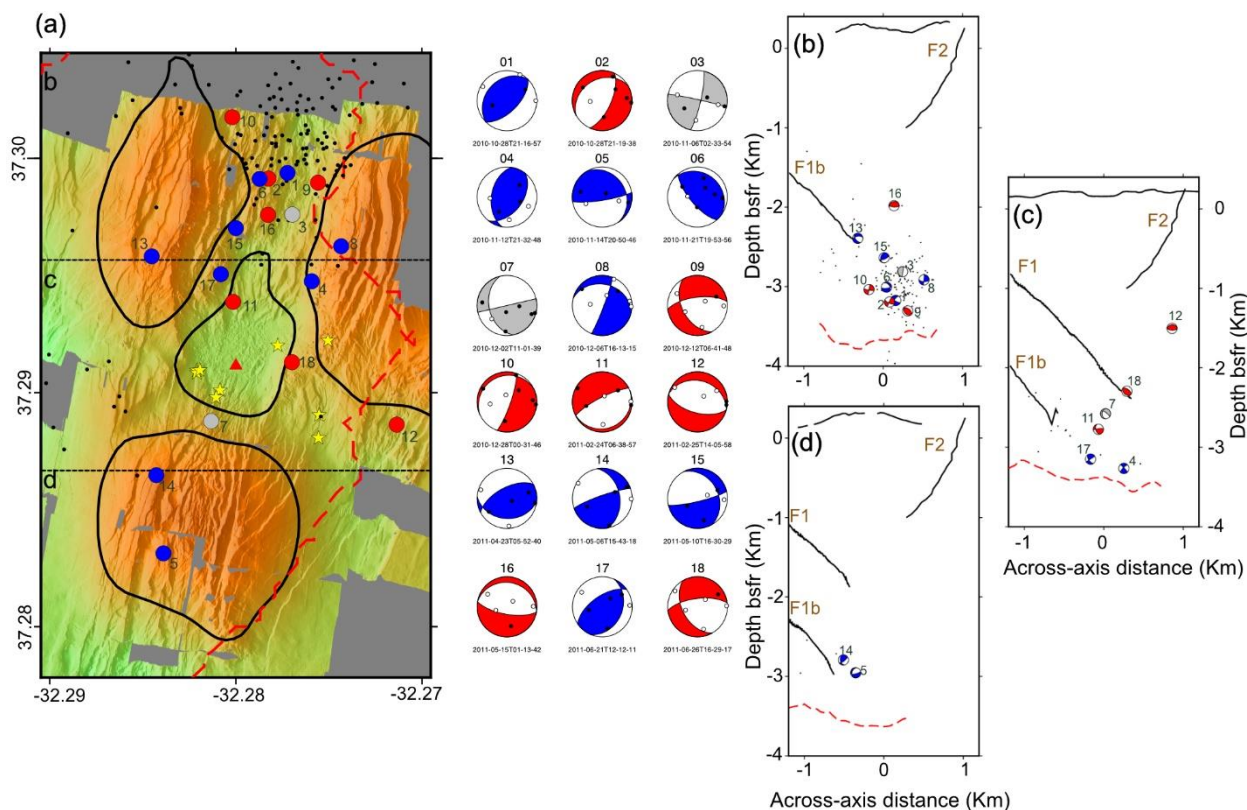


Figure 2.8. Focal mechanism solutions for 18 events (red dots in Figure 2.3, 2.5) from the 2010-2011 record. (a) Events are numbered chronologically, and color coded in red for normal faulting, blue for thrust faulting and grey for strike-slip/intermediate slip mechanisms. Small black dots represent rest of the events recorded that year. Small circles within the focal mechanism spheres indicate compressional (black) and extensional (white) recorded phases. (b), (c) and (d) are three cross-sections along the 3 boxes shown in map view. Red dashed line: the AMC reflector, black lines: reflectors associated with faults (Combi^{er} et al., 2015).

2.5 Discussion

Our study of the Lucky Strike volcano 2007-2019 microseismicity record shows persistent microseismicity in the M_L range -1.0 to 0 (Figure 2.3a), with an average seismic rate of ~8 events/week (Figure 2.3c). Most seismic events cluster beneath the volcano summit, north of the hydrothermal field (Figure 2.5a) and between ~2 km bsfr and the 3-3.8 km bsfr AMC reflector. The locus of the main seismicity cluster shifted by several hundred meters at least twice between 2007 and 2019 (Figure 2.5a, 2.6d, S2.9). Several higher seismicity periods (seismicity rates > 18 events/week, Figure 2.3c) are often associated with higher magnitude ($M_L > 0.8$) events (Figure 2.3a, e). Focal mechanisms could only be determined for the 2010-2011 deployment: they show a mix of normal, thrust, and strike-slip source mechanisms, assuming they are double-couple events (Figure 2.8). In the following sections, we discuss the possible sources of the recorded microseismicity, the origin of the spatial shifts of the main seismicity clusters and of the HSA periods, and the consequences of these interpretations in terms of how the Lucky Strike hydrothermal system works and interacts with magmatic and tectonic processes.

2.5.1 Sources of seismicity

Based on the spatial distribution of the events and on their depth distribution relative to the AMC, Crawford et al. (2013) favored thermal contraction at the base of hydrothermal circulation as the primary source of the persistent microseismicity observed in 2007-2009 beneath the Lucky Strike volcano summit region. They proposed that the hydrothermal circulation feeding the Lucky Strike vent field is primarily along-axis, with most heat being extracted to the north of the field. This along-axis circulation model was supported by numerical modelling including an along-axis high permeability zone (F. J. Fontaine et al., 2014) reproduces heat extraction highs/down flow zones coinciding with the 2007-2009 seismicity clusters north and south of the hydrothermal field and a heat extraction low/upflow zone beneath the vent field.

We also observed persistent microseismicity over our 12-year measurement period, focused in the same narrow along-axis region. Most of the events still occur north to northwest of the hydrothermal field (Figure 2.5a) and mostly just above the AMC reflector (Figure 2.5b), and M_L is similarly low (mostly between -1 and 0; Figure 2.3a). This longer catalog supports the

hypothesis that processes at the base of hydrothermal circulation are the major sources of seismicity in the Lucky Strike volcano region. These processes may be primarily related to thermal contraction of previously hot domains, as proposed by Crawford et al. (2013), with the main seismicity cluster north and northwest of the hydrothermal field representing the principal domain of hydrothermal heat extraction.

However, there are significant changes in the seismicity distribution over this period that suggest other, more punctual, processes that can rapidly modify hydrothermal circulation. In a steady-state end-member scenario (Figure 2.9a, b), where the hydrothermal circulation occurs at a steady rate in a brittle crust with a homogeneous permeability (both temporally and spatially) and with a magmatic heat source in the viscous domain which is replenished at the appropriate time and space scale, there would be no temperature change in the hydrothermal domain and thus there would be no thermal cracking events. In this context, tectonic extension and occasional diking should be the main sources of seismicity. These processes do not explain the persistent microseismicity that we observe in the Lucky Strike region. Frequent thermal contraction events indicate that the hydrothermal system mines heat from rock domains that were previously preserved or subjected to weak hydrothermal circulations. This could happen if magmatic replenishment does not keep up with hydrothermal heat extraction, in which case the base of the hydrothermal system will move down into previously impermeable hot rocks (Figure 2.9c). Fontaine et al., (2011) calculated that this downward migration should have a rate on the order of 1 m/year for the Lucky Strike system. In this context, the domain subjected to thermal cracking should be immediately above the AMC. Instead, we observe that thermal cracking events occur over a range of depths and that the main locus of seismicity changes, both laterally and in depth, over time. We propose that the hydrothermal circulation domain is itself a dynamic interface, controlled by spatial and temporal changes in permeability and by episodic melt injections. A melt injection into the hydrothermal circulation domain (Figure 2.9d) will lead to enhanced thermal cooling generating thermal cracks. Lateral variations in the permeability of the hydrothermal domain, as suggested by studies of the tidal modulation of venting temperatures at Lucky Strike (Barreyre & Sohn, 2016), will lead to locally thicker thermal boundary layers (TBL; Figure 2.9e) over regions with a lower permeability. When tectonic faulting or cracking in these regions restores higher local permeabilities, hydrothermal circulation will penetrate into previously inaccessible

domains, thinning the TBL and generating thermal cracks. This spatial and temporal variation in the permeability of the hydrothermal domain depends on other tectonic and volcanic processes. Stress perturbations induced by the AMC dynamics (Bohnenstiehl & Carbotte, 2001; Wilcock et al., 2009) due to decrease/increase in the magma chamber volume by hydrothermal heat extraction/episodes of magma replenishment will perturb the crustal stress field which in turn will affect the permeability in the hydrothermal domain. Similarly, tectonic cracking due to extension may also locally increase or decrease the hydrothermal domain permeability. Overall, the crustal stress field is dynamic due to a complex mix of volcanic, hydrothermal, and tectonic processes. It is therefore plausible that the observed seismicity traces the changes in the dynamic hydrothermal circulation domain.

We could only calculate focal mechanisms for the 2010-2011 catalog, and they show a mix of normal, reverse, and strike-slip faulting mechanisms (Figure 2.8, Table S2.2), none of which fit with the expected motion at local normal faults. In the 2012-2013 record, the seismicity rate is lower than any other period (Figure 2.3c), and the events appear to be aligned along the trace of the normal fault F1b (Figure 2.5b). We do not have focal mechanisms for these 2012-2013 events, yet because they share the characteristics of the persistent seismicity in the other years (small magnitudes, similar depth and map distribution), we propose that these events are also dominantly due to thermal and reaction-induced cracking, in this case probably following tectonic events opening new permeable pathways near the F1b normal fault.

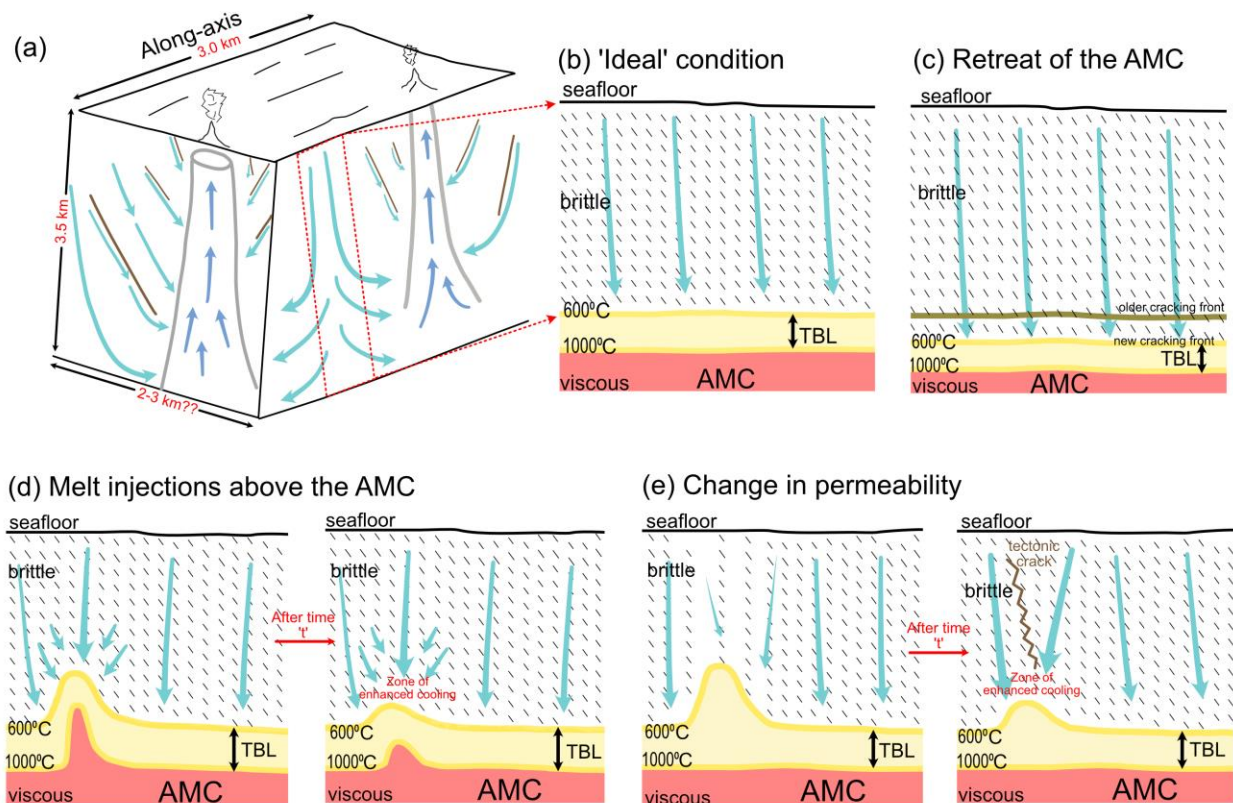


Figure 2.9. (a) 3D schematic hydrothermal circulation model. Light blue and dark blue arrows mark the hydrothermal downflows and upflows respectively in the brittle regime, brown lines are the faults. The scales marked are approximation for the Lucky Strike hydrothermal circulation model. (b-e) Modes of hydrothermal circulation focused only to the downflow region. Dashed lines in the brittle domain denote permeability (dense dashed lines: enhanced permeability, less dashed lines: lower permeability), TBL: thermal boundary layer between the AMC (in viscous domain) and hydrothermal system (in brittle domain). (b) Ideal hydrothermal circulation with uniform permeability and steady rate hydrothermal circulation. (c) Deepening of the cracking front to a hotter domain of rocks due to absence of magma replenishment. (d) Melt injections above the AMC leading to local enhanced thermal cooling. (e) Region with lower permeability corresponds to a thicker TBL which is then restored by tectonic cracking making permeable pathways and leading to local enhanced thermal cooling.

Thermal contraction events are expected to result primarily from tensile cracks (mode I type failure, non double-couple origin; Sohn et al., 2004), so the double-couple focal mechanisms we calculated using the FOCMEC software may be in error. That said, similarly varied double-couple focal mechanisms have been determined in other mid-oceanic ridge settings including Endeavour segment (Wilcock et al., 2002) and Axial seamount (Levy et al., 2018; Sohn et al., 2004) in the post-eruption periods, when the dominant observed seismicity is interpreted as due to thermal contraction. So, whether the events we determined focal mechanisms for are indeed double-couple or not, the variability observed in our limited period of focal mechanisms supports

the interpretation of these events as associated to hydrothermal cooling. The hydrothermal contraction or expansion events (non double-couple origin) are being triggered, or triggering other possible seismogenic events such as extensional cracking and melt injections above the AMC (double-couple origin). As these processes are not mutually exclusive, it may prove difficult, even with data recorded by a larger instrumental network, to precisely tell the source mechanism of each event.

Microseismicity occurring beneath hydrothermal fields present at fast/intermediate spreading segments have higher seismicity rate compared to our observed seismicity beneath the Lucky Strike hydrothermal field (~8 events/week; Figure 2.3c): seismicity beneath the 9°50'N EPR hydrothermal field has a rate of ~234 events/week, (Tolstoy et al., 2008); while beneath main Endeavour field, the seismicity rate is ~63 events/week, (Wilcock et al., 2009). This difference could be due to the combination of higher melt influx and faster spreading rates in those areas enhancing thermal cooling and tectonic cracking. But the magnitude range of these events remains more or less same as the Lucky Strike seismicity record (M_L range: -1.0 to 0, Figure 2.3a): Tolstoy et al., (2008) have reported seismicity beneath the 9°50'N EPR field with local magnitudes ranging between -1.8 and 1.4 ($M_c = -0.5$); at Axial Seamount post-1998 eruption seismicity has magnitude (M_w) range in between -1.3 and 0.7 (Sohn et al., 2004); and at Endeavour segment M_L range is between 0.5 to 2.5 (Wilcock et al., 2009).

2.5.2 Shifts of the seismicity clusters with time and HSA periods

In the previous section we interpret that the persistent microseismicity recorded at Lucky Strike volcano traces complex tectonic, hydrothermal and possibly magmatic (diking) processes leading to and accompanying the progression of hydrothermal cooling. Based on this interpretation, the location of the principal seismicity clusters, and the intensity of the microseismic activity (> 18 of event/week, HSA periods) can then be used to track these enhanced cooling domains through time during the 2007-2019 survey.

We document two shifts of the mean locus of the principal seismicity cluster. The first shift occurs in Early to Mid-2011: the mean locus of the principal seismicity cluster in map view shifts ~600 m to the West (Figure 2.5a, 2.6d, S2.9b), but the vertical seismicity distribution does not

change (Figure 2.5b, 2.6b). The second shift, occurring in the catalog gap of June 2013 to April 2015, corresponds to a map change of mean locus of the principal seismicity cluster by ~800 m eastward, to the eastern edge of the AMC reflector (Figure 2.5a, 2.6d, S2.9c). The vertical seismicity distribution also changes from a patch above the AMC to a pipe-shaped pattern that extends down to ~1 km below AMC depth (Figure 2.5b, 2.6c).

Variables such as network-based biases, picking errors or change in shallow velocity structure may individually cause 100-300 m shifts (Method section, Figure S2.5, S2.6 & S2.7). A fortuitous combination of these variables could account for the first shift (Early to Mid-2011), that coincided with the yearly redeployment of the OBSs. If this shift is real, however, it occurred in a matter of just 15 days. The second shift is most likely real: it is too large (~800 m in map view; Figure 2.5a, 2.6d) to be a relocation artefact, and it corresponds to a clear change of the seismicity distribution from a patch above the AMC to a pipelike pattern. Unfortunately, this shift occurred during the catalog gap of June 2013 to April 2015 so that it is not possible to tell when exactly and how fast it happened.

We observe one prominent HSA period (April-June 2009, seismicity rate > 18 events/week; Figure 2.3c) and two other time intervals containing several short consecutive HSA periods: August-September 2015 (2 HSA periods; Figure 2.3c), and April-May 2016 (3 HSA periods; Figure 2.3c). The 2009 HSA period was the most intense: it lasted ~13 weeks. The seismic rate in the pre-HSA period (August 2008 – March 2009) was ~9 events/week, building up to > 20 events/week in April-May 2009 and finally culminating in the beginning of June 2009 with seismicity rate > 50 events/week (Figure 2.3c). The spatial distribution of the seismicity during this 2009 HSA period did not differ from that of the whole 2007-2009 period (mostly clustered north-northwest of the hydrothermal field in a patch 0 to ~1.4 km above the AMC reflector; Figure 2.3b, 2.5b). This HSA period started with a higher magnitude event ($M_L = 1.7$), and culminated in June after another higher magnitude ($M_L = 1.8$) event (light blue lines Figure 2.3a). The first higher magnitude event was located just south of the northwest volcanic cone in the map (light blue star in Figure 2.5a) and at the deepest portion of the F1b fault reflector (light blue star in Figure 2.5c). The second higher magnitude event occurred further south (~1 km south of the southern volcanic cone; light blue star in Figure 2.5a) and very close to the seafloor (~0.35 km bsfr; light blue star in

Figure 2.5c). Based on these observations, we interpret both the higher magnitude events as probably tectonic in origin and propose that these events helped open enhanced permeability channels for downgoing hydrothermal fluids in 2007-2009 seismogenic domains.

The 5 HSA periods that occurred in August-September 2015, and April-May 2016 were shorter-lived (~7-10 days each, Figure 2.3c), with a spatial distribution of events that did not differ from that of the whole 2015-2019 period (mostly clustered north-northeast of the hydrothermal field in a dike-like pattern that extends down to ~1 km below AMC depth; Figure 2.3b, 2.5b, 2.6). The August-September 2015 interval had two HSA periods (seismicity rate ~20 events/week; Figure 2.3c) and three higher magnitude events ($M_L > 1.0$; light blue lines in Figure 2.3a), with the first two in the main seismicity cluster north of the volcano, both below the AMC reflector depth (light blue stars in Figure 2.5a, 2.5b) and the third one beneath the southern volcanic cone, above the AMC reflector depth (light blue stars in Figure 2.5a, 2.5c). The April-May 2016 interval had three HSA periods (seismicity rate ~30 events/week, Figure 2.3c), and three higher magnitude events ($M_L > 1.0$; light blue lines in Figure 2.3a) which had same distribution as the previous interval: first two in the main north cluster (light blue stars in Figure 2.5a, 2.5b) and the third one beneath the southern volcanic cone (light blue stars in Figure 2.5a, 2.5c). The first upward migration sequence observed in the first HSA period of the August-September 2015 interval (Figure 2.7) could suggest a dike injection, but the intensity and magnitude of these events is much lower than that of seismic events interpreted as due to dike propagations at Axial seamount (Dziak et al., 2012; Wilcock et al., 2016) and Iceland (Sigmundsson et al., 2015), and no evidence of a sea floor eruption was observed at Lucky Strike during the 2009-2019 yearly site submersible surveys. A seafloor inflation event interpreted as being due to a magmatic injection event at AMC or greater depths was recorded in late September 2015 (Ballu et al., 2019), at the end of the second HSA period of the August-September 2015 interval (Figure 2.3a), and another upward migration sequence, with yet smaller magnitude events was observed earlier in September 2015 (Figure 2.7).

We had only 3 working OBSs from July 2014 to April 2015, too few to locate seismic events, but the total number of triggers detected by these 3 OBSs was similar to that of other deployments, with no indication of a seismic swarm period that could have been caused by a dike injection (Figure S2.14). We also looked into the hydroacoustic monitoring record for the Northern Mid-

Atlantic area, available for July 2012 – July 2014 (Perrot, 2012) . This experiment was designed to detect comparatively larger magnitude events on a much bigger scale and the horizontal uncertainty given by this method is high (~4 km). All the events detected in the Lucky Strike segment by this experiment were scattered with only two uncorrelated events detected inside the volcano area (Figure S2.15), and there was no swarm-like pattern as observed before during a magma intrusion event in 2001 (Dziak et al., 2004).

It thus appears that there is no conclusive evidence for a significant dike injection event that might have caused the change to a dike like seismicity pattern sometime during the June 2013 to April 2015 data gap. Yet, this change, the upward propagation sequences in August and September 2015, and the seafloor inflation event in late September that same year, suggest a change in the tectono-magmatic activity of the volcano compared to the pre-June 2013 period. This change may have involved the injection of small dikes at depth next to the eastern edge of the AMC. It might also be due to local extensional tectonics opening new pathways for downgoing hydrothermal fluids in the eastern AMC region.

2.6 Conclusions

1. 12 years of microseismicity record beneath Lucky Strike volcano from 2007 to 2019 reveal steady and continuous low magnitudes (M_L between -1 and 0) seismicity in the north-northwest of the hydrothermal field and above the AMC reflector. We propose that the hydrothermal circulation domain is a dynamic interface, with spatial and temporal changes in permeability and possibly episodic melt injections, and that the microseismicity is due to processes occurring at depth in hydrothermal downflow regions. These processes would include thermal cracking, tectonic cracking, and also possibly the injection of small dikes.
2. The observed microseismicity would thus track the progression of domains of enhanced hydrothermal heat extraction where the rocks are not yet fully cooled. The rates of seismicity (5 to 50 events /week, ~8 events/week on average) are lower than observed for similar events at EPR and Axial Seamount and this may be because of the slower spreading rates and lower melt fluxes at the Lucky Strike volcano.

3. There were at least two shifts of the main seismicity clusters in our 12-year seismicity record. The first shift occurring in July 2011, if not an artifact, could have been caused by small tectonic events creating local enhanced permeable pathways. The second shift of ~800 m eastward, along with a change in seismicity pattern from a patch above the AMC to a more vertically aligned structure, occurred sometime in June 2013 – April 2015. This is the first reported observation of a spatial shift of this scale in a Mid-Ocean ridge setting. It marks a clear change in the tectono-magmatic activity of the volcano compared to the pre-June 2013 period.
4. Several (7 days to 13 weeks-long) periods of Higher Seismic Activity occurred over the experiment, the longest and most intense being the March-June 2009 HSA period. This HSA period appears to have been triggered by higher relative magnitude tectonic events, which may have opened more permeable pathways for hydrothermal downflow. Five shorter higher seismicity periods occurred in August-September 2015 and in April-May 2016 might similarly have been triggered by tectonic cracking.

Supplementary materials

Supplementary text S2.1 Earthquake relocation in HypoDD

We relocated events with horizontal and depth errors < 1 km and RMS residual < 50 ms, using Double-Difference Hypocenter (HypoDD) algorithm (Waldhauser & Ellsworth, 2000) in python module HypoDDpy (Krischer, 2015). The relocation was done using both catalog P & S picks, and cross-correlation using a correlation coefficient cut-off value of 0.6. We performed relocation using both conjugate gradient or least square method (HypoDD LS), and singular value decomposition (HypoDD SVD) method. By HypoDD SVD method, we were losing almost 50% of the events. We therefore used HypoDD LS method for relocation for all years (Figure S2.3). Figure S2.4 compares the earthquake relocations and their uncertainties using different methods for the deployment year 2015-2016, which shows that relocations obtained from HypoDD LS and HypoDD SVD method do not differ from each that much.

Supplementary text S2.2 Tests on event locations

Network-based biases/ Station delays

The first shift in the main seismic cluster was observed in mid-July 2011 when it shifted ~ 600 m towards West (Figure 2.5a). It coincided with the timing of the yearly redeployment of the OBSs which raised the question whether this shift was due to the change in the OBS network. Moreover, there were 3 additional OBSs from university of Lisbon in 2010-2011 with different sampling rates (100 sps). So initially, we located the events from 2010-2011 with just 5 INSU-IPGP OBSs, but the locations did not change significantly than when located with 8 OBSs (Figure S2.5b). We then looked into the station delays, which reflect the crustal structure just below the stations, from both the deployments 2010-2011 and 2011-2012. The East OBS (LSVE) station delay was higher (~ 0.0008 s) in 2011-2012 compared to the previous deployment (Figure S2.5a). Therefore, we relocated 2011-2012 events using the LSVE station delay from 2010-2011. The new locations in 2011-2012 moved ~ 200 m towards the 2010-2011 locations, but not entirely (Figure S2.5c, d). So, the network-based bias might change the event locations but does not account for the complete shift which was observed in mid-July 2011.

Derived Bootstrap Inversion

We performed a derived bootstrap inversion in order to check the effect of picking biases. Here we take an event from the center of each seismic cluster (Figure 2.6d) and randomly add an error (always less than the phase uncertainty) to each phase pick and then relocate the event. We performed it for 100 iterations for one event from each seismic cluster, and each time new location shifts (100-300 m) are much less than the actual shifts observed, which suggests that picking biases cannot account for the complete shifts observed (Figure S2.6).

Change in velocity structure

We used a 3D seismic velocity model for earthquake locations. But we used the same velocity model throughout the 12 years of experiment span. The upper crustal beneath the volcano region is highly fractured, and recrystallisation and precipitation of hydrothermal fluids along these fractures and reorganization of the hydrothermal pathways may change the upper crustal velocity structure. To see the effect of change in velocity structure, we used a synthetic dataset with 392 events at the center of the volcano from the seafloor till 3.5km bsf, located 500m apart. We changed the original 3D velocity model by 15% reducing and 15% increasing the upper crustal velocity w.r.t the original AA_TS model (Figure S2.7a), calculated the phase traveltimes, and relocated the events with the modified velocity models. When the traveltimes were calculated with 15% reduced model, the events are concentrated towards the center and shallower as the original model has higher velocity (Figure S2.7b1, b2). But when the traveltimes were calculated with 15% increased model, the events are located deeper and moved North-East (Figure S2.7c1, c2). Ideally, the events should be deeper and move away equally in all directions. But the movement in North-East might be because the North and East OBSs are closer compared to the South and West OBSs, and therefore have a larger effect on the locations. In any case, the shifts observed with the changed velocity models are smaller than the actual shifts.

CHAPTER 2. HYDROTHERMAL MICROSEISMICITY

Table S2.1. Overview of the OBS data

Year	Duration of deployment	No. of OBSs worked	Duration of data processed	Comment
2007-2008	2007/07/22 - 2008/08/10	5	All	Poor seafloor coupling
2008-2009	2008/08/15 - 2009/09/02	5	All	--
2009-2010	2009/09/03 - 2010/10/09	3	All	4 OBSs recovered, one was very noisy
2010-2011	2010/10/11 - 2011/07/05	8	All	3 additional U. Lisbon OBSs
2011-2012	2011/07/11 - 2012/07/15	5	2011/07/11-2011/12/31	2 OBSs did not work after 2011/12/31
2012-2013	2012/07/18 – 2013/08/29	4	2012/07/18- 2013/05/31	One OBS did not work after 2013/05/31
2013-2014	--	--	--	No OBS recorded data
2014-2015	2014/07/20 – 2015/04/16	3	All	Only 3 OBSs recovered
2015-2016	2015/04/22 – 2015/05/26	5	All	--
2016-2017	2016/08/31 – 2017/07/12	1	--	Only 1 OBS deployed
2017-2018	2017/07/14 – 2018/08/11	3	--	One OBS did not work, another was not time synchronized
2018-2019	2018/08/15 – 2019/06/14	4	2019/02/14– 2019/06/14	2 OBSs partially worked

CHAPTER 2. HYDROTHERMAL MICROSEISMICITY

Table S2.2. Focal Mechanism solutions

Ev	Time		Longitude	Latitude	Depth bsf	Focal mechanism			M _L	Picks
#	yyyymmdd	hhmmss	(°)	(°)	(km)	Strike	Dip	Rake		#
1	20101028	211657	-32.2772	37.2993	3.17	45	60	90	-0.8	5
2	20101028	211938	-32.2785	37.2991	3.19	240	29	-58	1.0	7
3	20101106	023354	-32.2769	37.2976	2.81	13	81	03	-0.5	6
4	20101112	213248	-32.2759	37.2947	3.26	189	47	69	-0.5	6
5	20101114	205046	-32.2838	37.2831	2.95	81	81	70	-0.2	5
6	20101121	195356	-32.2787	37.2991	3.10	307	20	78	0.9	7
7	20101202	110139	-32.2813	37.2887	2.57	257	90	50	-0.5	7
8	20101206	161315	-32.2743	37.2962	2.91	283	30	-9	-0.9	7
9	20101212	064148	-32.2755	37.2989	3.30	151	48	-31	-0.7	6
10	20101228	003146	-32.2801	37.3017	3.03	245	14	-45	0.6	8
11	20110224	063857	-32.2801	37.2938	2.77	68	12	-85	-0.8	7
12	20110225	140558	-32.2713	37.2886	1.50	285	30	-90	-0.7	5
13	20110423	055240	-32.2845	37.2958	2.39	242	61	73	-1.2	6
14	20110506	154318	-32.2842	37.2864	2.79	350	41	12	-0.8	6
15	20110510	163029	-32.2800	37.2970	2.63	332	31	-17	-0.9	5
16	20110515	011342	-32.2782	37.2975	1.98	280	20	-90	-0.6	5
17	20110621	121211	-32.2808	37.2950	3.14	23	33	62	-1.1	6
18	20110626	162917	-32.2769	37.2912	2.29	151	48	-31	-0.8	6

Supplementary figures

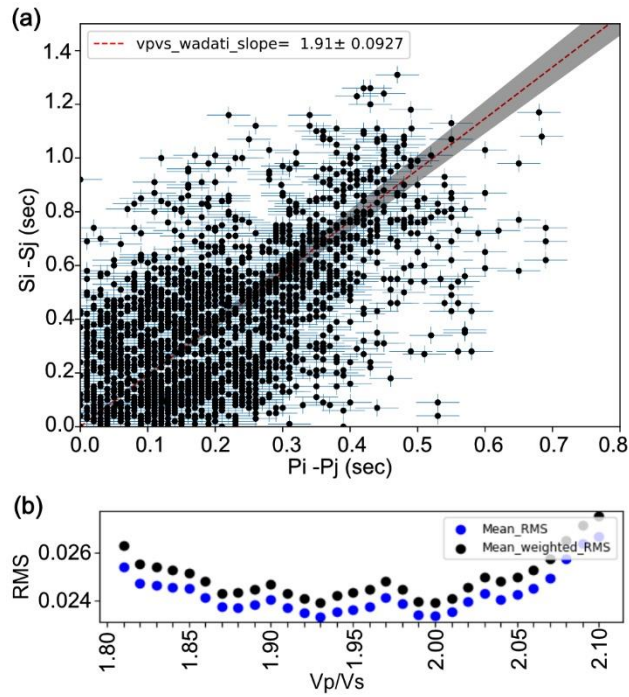


Figure S2.1. Estimation of Vp/Vs . (a) Vp/Vs calculation using a modified Wadati diagram (Chatelain, 1978). (b) Vp/Vs value vs. average RMS residual of all events. Blue dots represent the average RMS values and black dots represent the average RMS weighted over the number of P and S phase picks.

CHAPTER 2. HYDROTHERMAL MICROSEISMICITY

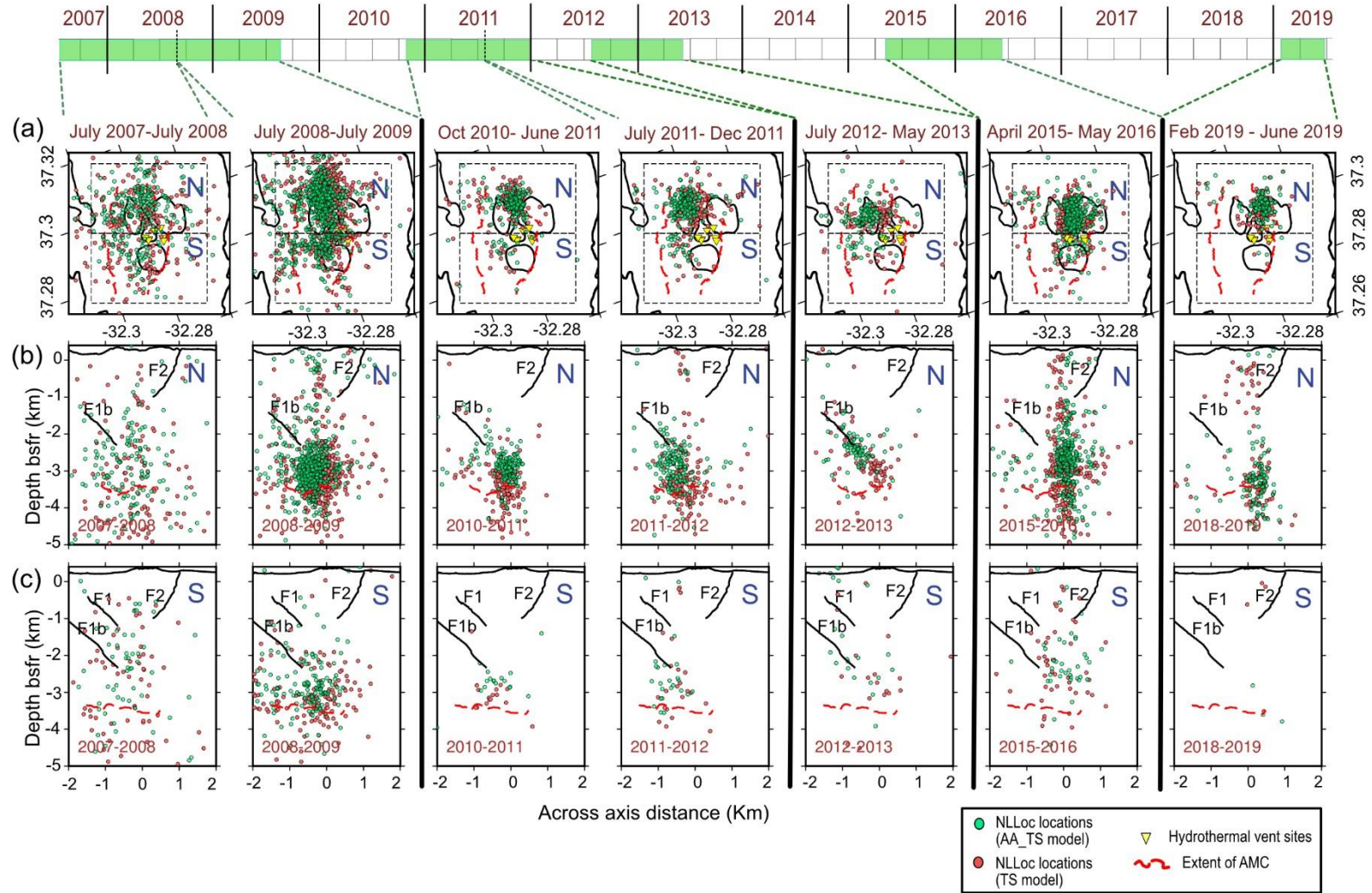


Figure S2.2. Comparison of locations obtained using composite (AA_TS) model (Green circles) and TS model (Red circles) in NLLoc. Scale and symbols same as Figure 2.5.

CHAPTER 2. HYDROTHERMAL MICROSEISMICITY

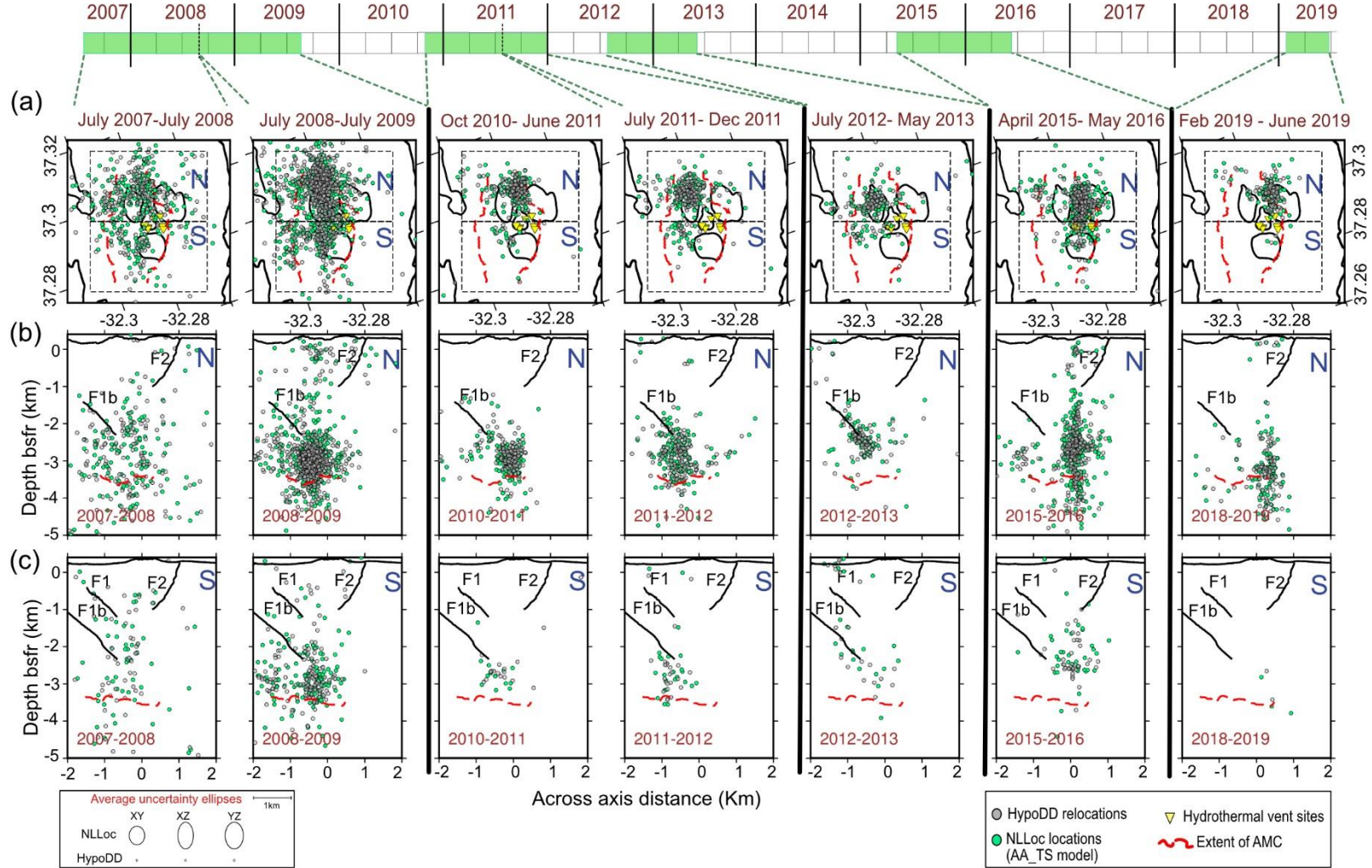


Figure S2.3. Comparison of locations obtained using NLLoc (Green circles) and HypoDD LS method (Grey circles) using composite (AA_TS) model. Scale and symbols same as Figure 2.5.

CHAPTER 2. HYDROTHERMAL MICROSEISMICITY

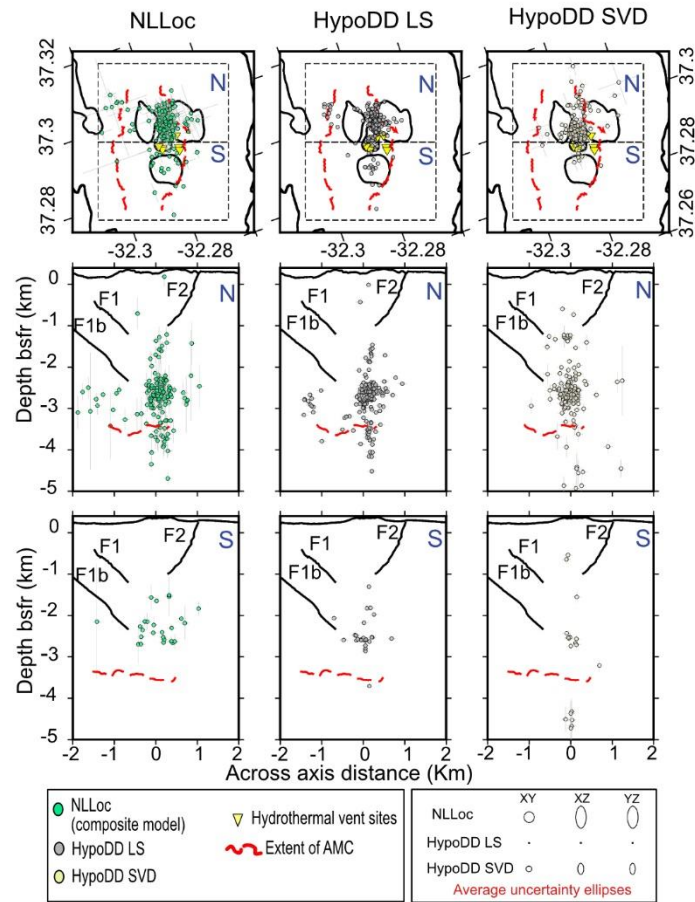


Figure S2.4. Comparison of locations obtained using NLLoc, HypoDD LS and HypoDD SVD method for the deployment year 2015-2016.

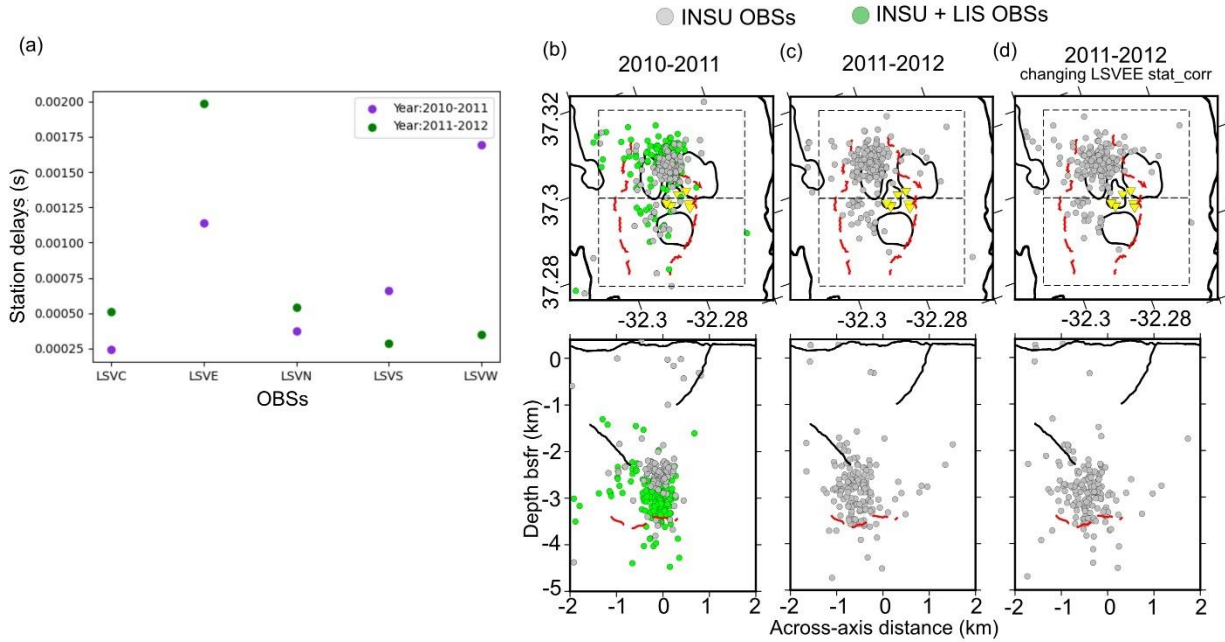


Figure S2.5. Effect of station delays/network-based biases on event locations. (a) Comparison of station delays in the deployment year 2010-2011 (purple) and 2011-2012 (green). (b) Original event locations in 2010-2011 located with just INSU OBSs (gray dots) and with both INSU and university of Lisbon OBSs (green dots). (c) Original event locations in 2011-2012. (d) Event locations in 2011-2012 after changing LSVEE OBS station delays.

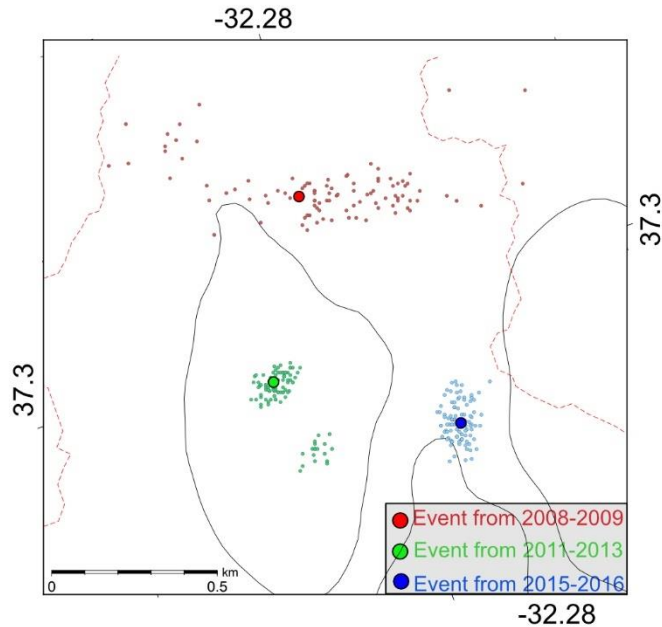


Figure S2.6. Derived bootstrap inversion result for an event from each seismicity cluster in 2008-2009 (red), 2011-2013 (green) and 2015-2016 (blue). Big circle is original event location in each cluster and small dots are locations from 100 iterations after adding a random picking error in the original event phases.

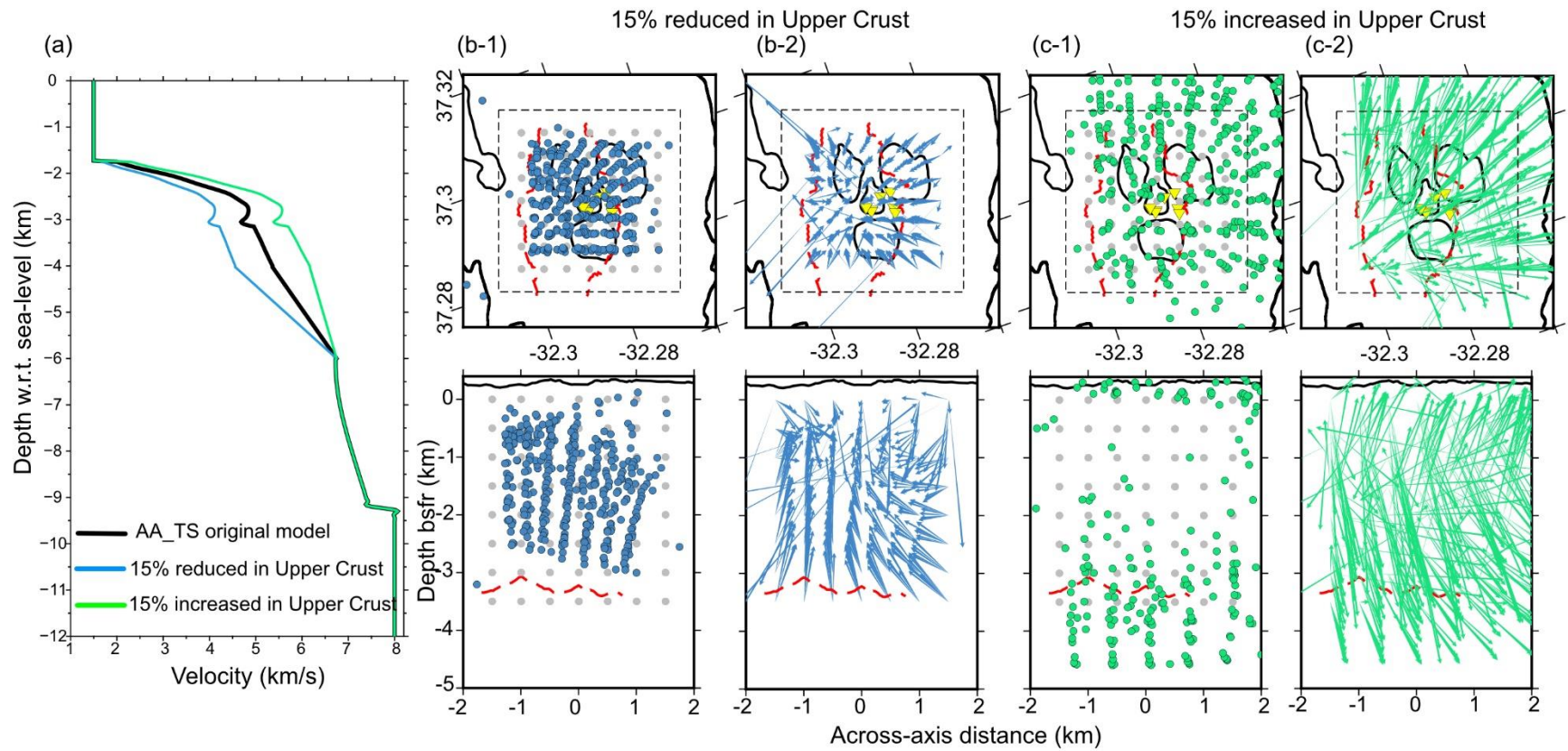


Figure S2.7. Test on event locations with change in velocity structure. (a) AA_TS model (black line) at the center of the volcano, and velocity models with 15% reduction (blue line) and 15% increase (green line) in the upper crust. (b-1) Event locations with 15% reduced velocity model. Gray dots: synthetic events, blue dots: relocated events and (b-2) Relative movement of the events after reducing velocity. (c-1) Event locations with 15% increased velocity model. Gray dots: synthetic events, green dots: relocated events and (c-2) Relative movement of the events after increasing velocity.

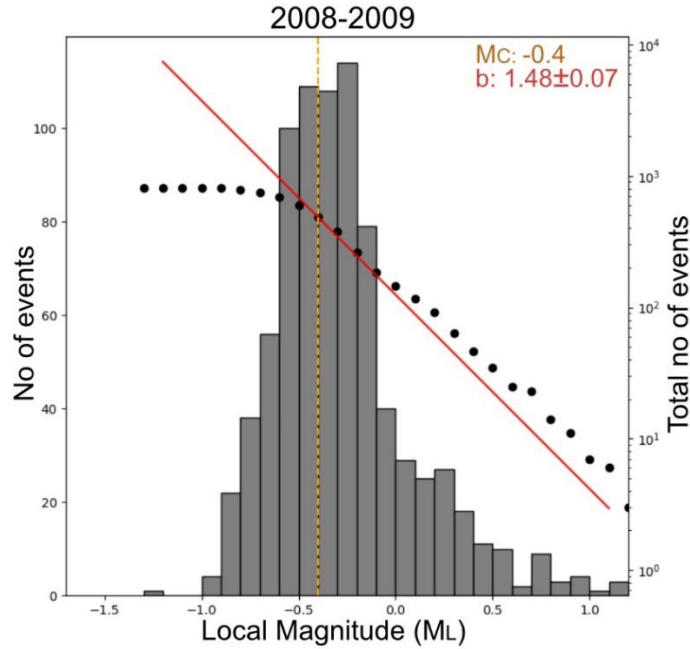


Figure S2.8. (a) Histograms of local magnitudes for 2008-2009 catalog (left Y axis). Cumulative number of earthquakes (black circles, right Y axis) as a function of local magnitude. Magnitude completeness (M_c) is determined as -0.4 (dashed orange line), resulting in a b -value of 1.48 (slope of the red line). M_c and b -value for other deployment years are obtained using the same method.

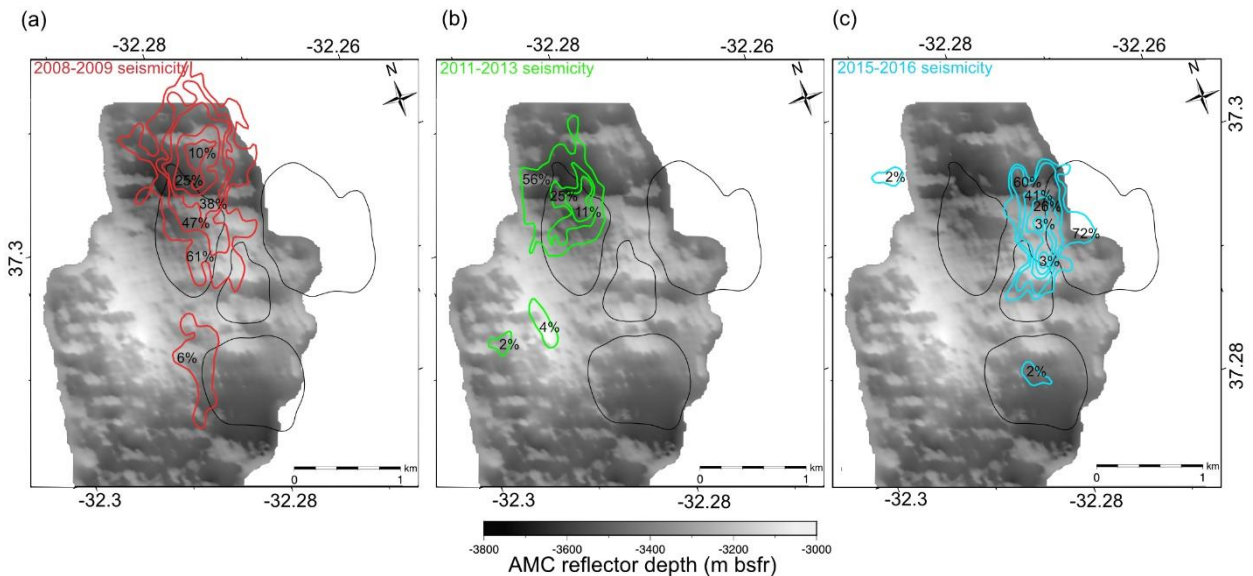


Figure S2.9. Event density maps for 3 time periods: (a) 2008-2009, (b) 2011-2013 & (c) 2015-2016. Gray surface is the roof of the AMC reflector (Combi \acute{e} r et al., 2015; Singh et al., 2006). Black isodepth contours are the same as in Figure 2.1 (lava lake and its three surrounding peaks). Each contour represents percentage of total events from the respective time periods located inside it.

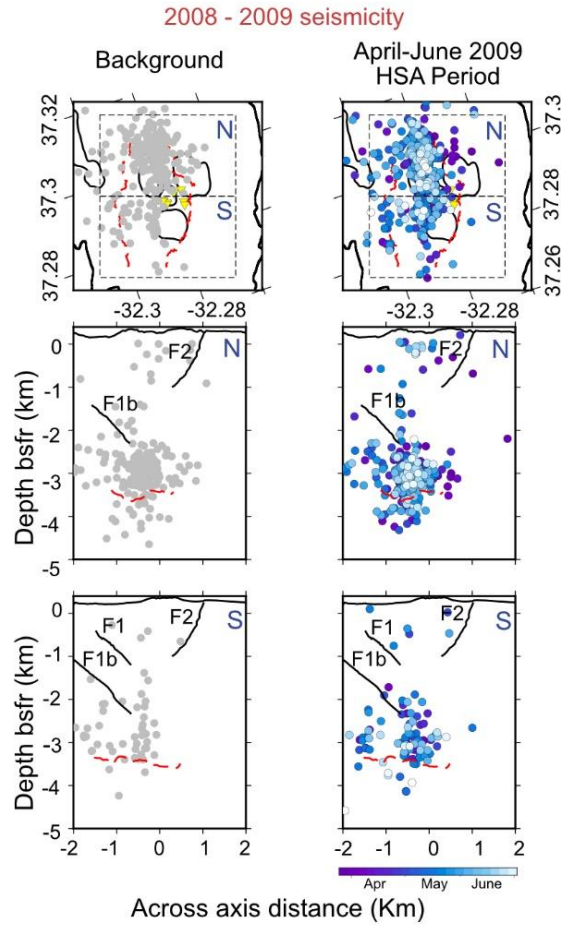


Figure S2.10. 2008-2009 seismicity locations plotted separately for background events (those outside HSA period) and April-June 2009 HSA period. Events of the HSA periods are color coded with time.

CHAPTER 2. HYDROTHERMAL MICROSEISMICITY

2015 - 2016 seismicity

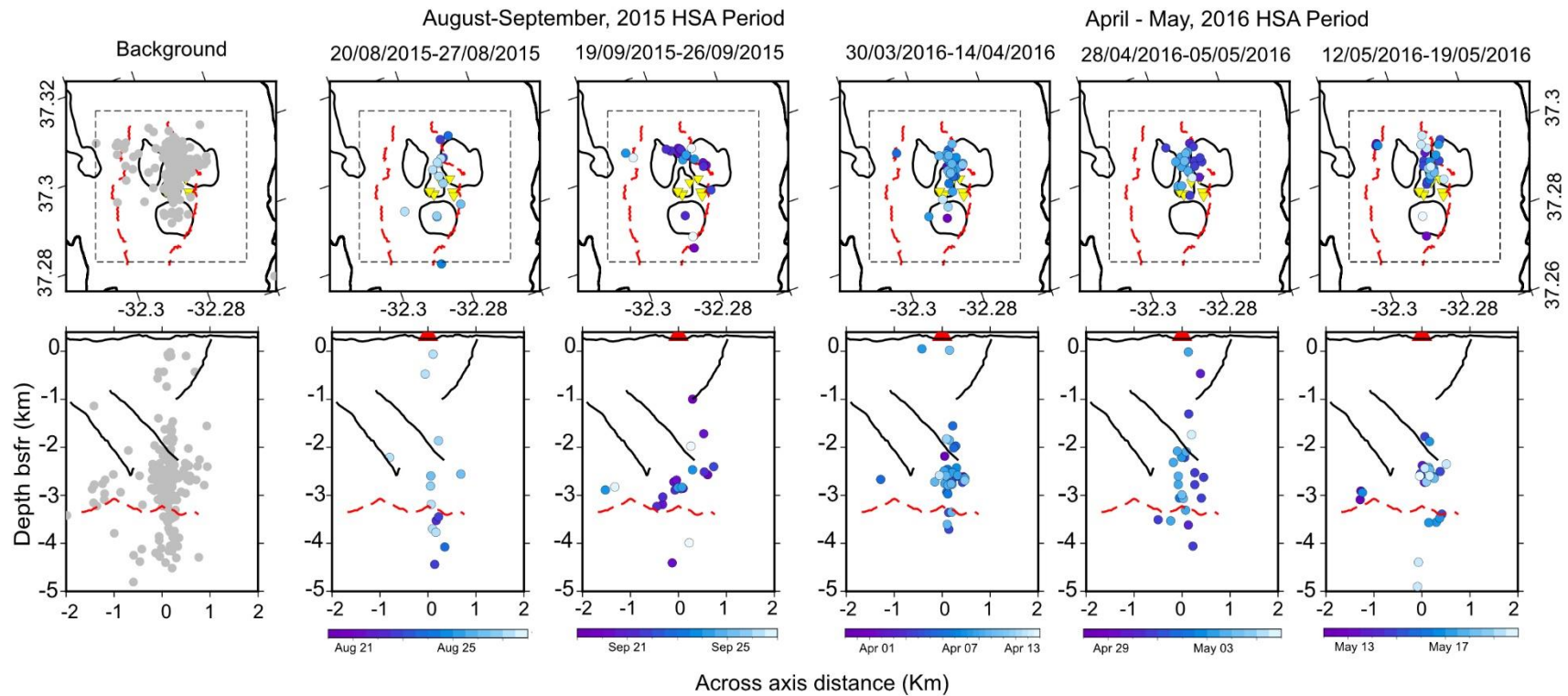


Figure S2.11. 2015-2016 seismicity locations plotted separately for background events (events outside HSA periods), 2015 and 2016 HSA periods. Events of the HSA periods are color coded with time separately for each swarm period.

CHAPTER 2. HYDROTHERMAL MICROSEISMICITY

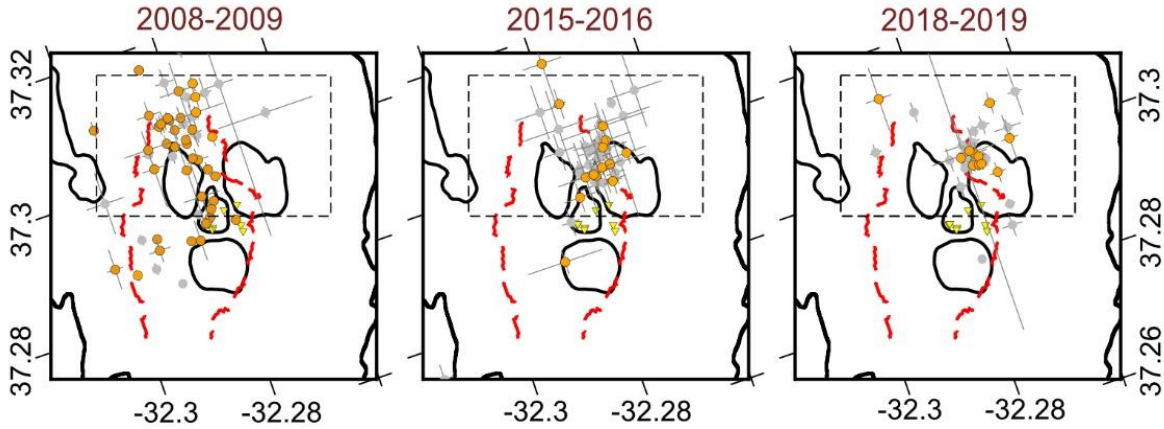


Figure S2.12. Spatial locations of events which are located below the AMC reflector depth in the deployment years 2008-2009, 2015-2016 and 2018-2019. Scale and symbols same as Figure 2.5. Error bars show horizontal location uncertainties calculated in NLLoc using composite (AA_TS) model.

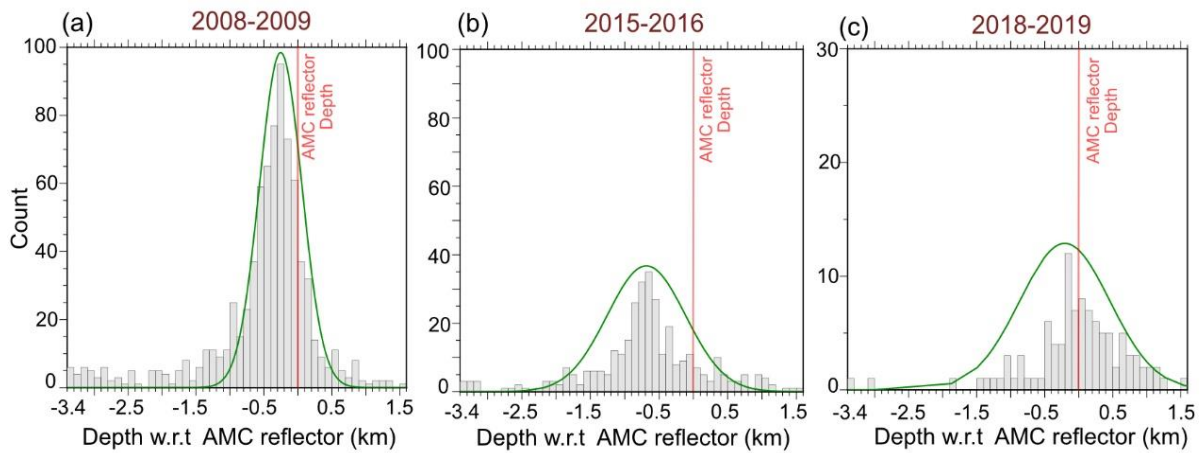


Figure S2.13. Depth distribution of NLLoc event locations (all events) for the year (a) 2008-2009, (b) 2015-2016 and (c) 2018-2019. Depths are w.r.t the mean AMC reflector depth (3.4 km). Green curve represents depth uncertainty at the most common event depth for each dataset.

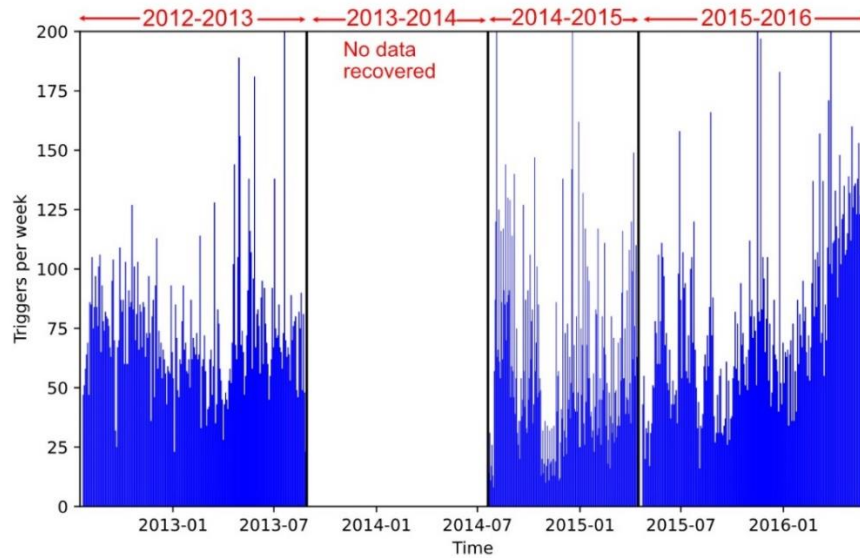


Figure S2.14. Number of triggers detected by 3 OBSs (east, south and west OBSs) from July 2012 – May 2016 covering 3 deployments (2012-2013, 2014-2015 & 2015-2016). In 2014-2015, triggers rate is similar to other years, giving no indication of possible magma injections.

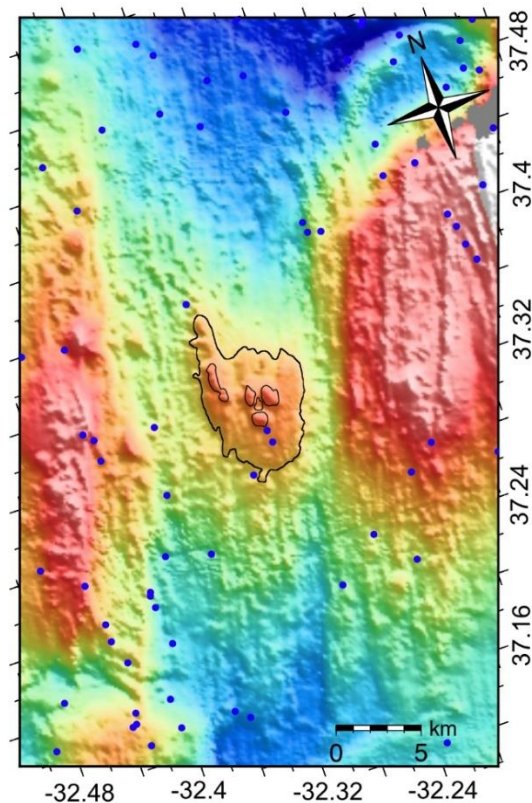


Figure S2.15. Seismicity detected near the Lucky Strike segment from July 2012 – July 2014 as part of the hydroacousting monitoring of Northern Mid-Atlantic ridge (Perrot, 2012). At the center, black isodepth contours are the same as in Figure 2.1 (volcano base, western volcanic ridge, lava lake and its three surrounding peaks). Blue dots are the seismic events.

Chapter 3

Detection of near-seafloor microseismicity beneath Lucky Strike vent field, Mid-Atlantic Ridge using a hydrophone array

3.1 Introduction

Hydrothermal circulations at Mid-Ocean Ridges (MORs) transport magmatic heat (Lister, 1972; Lowell, 1995) and chemicals (Elderfield & Schultz, 1996) between the solid Earth and the ocean. MOR hydrothermal systems usually consist of several sites, each with focused hydrothermal vents, often at temperatures $>300^{\circ}\text{C}$ and a wider domain of low temperature diffuse vents. Intense discharge of high temperature fluids through the focused vents creates local entrainment of cold seawater into the shallow sub-seafloor. The cold seawater mixes with the primary hydrothermal fluids (Butterfield et al., 2004; Edmond, Measures, Mangum, et al., 1979), or is conductively heated (Cooper et al., 2000), both processes creating low temperature diffuse fluids. The diffuse vents extend over a larger and more scattered area, and host a unique chemosynthetic microbial and hydrothermal fauna (Corliss et al., 1979; Cuvelier et al., 2009; Juniper et al., 1995). This entrained circulation also leads to mineral precipitation, forming large hydrothermal deposits.

Our current understanding about near-seafloor secondary circulation and shallow upflow primarily comes from a few short drill cores recovered at Trans-Atlantic Geotraverse (TAG) hydrothermal field at Mid-Atlantic Ridge (Humphris et al., 1996; Humphris et al., 2015), and various analytic and numerical models (Guo et al., 2020; Lowell et al., 2003; Lowell & Yao, 2002). However, the geometry and subsurface extent of the secondary circulation system remains largely unknown. Pontbriand and Sohn, (2014) constrained this secondary system beneath the TAG sulfide mound, by characterizing shallow microearthquakes which were located by a small ~ 200 m aperture short-period Ocean Bottom Seismometer (OBS) network. These microearthquakes are proposed to have been triggered by reaction-driven cracking in response to anhydrite precipitation in the secondary circulation system (Pontbriand & Sohn, 2014).

The Lucky Strike hydrothermal field, located at the center of Lucky Strike volcano, Mid-Atlantic Ridge, is one of the largest known deep sea hydrothermal fields (Barreyre et al., 2012; Fouquet et al., 1995; Susan E. Humphris et al., 2002; Langmuir et al., 1997; Ondréas et al., 2009). The hydrothermal system has been sustained over thousands of years (Sánchez-Mora et al., 2022) by extracting heat from an axial magma chamber (AMC), detected in 2005 at $\sim 3\text{-}3.8$ km beneath

the seafloor by a multichannel seismic reflection/refraction study (Combier et al., 2015; Singh et al., 2006). A volcano-scale OBS network (described in Chapter 2) identifies seismicity clusters, ~1.4 - 0.5 km north of the main hydrothermal field and ~2.0 – 3.5 km beneath the seafloor, which are interpreted as markers of enhanced hydrothermal cooling and alteration at the base of the hydrothermal cells (Crawford et al., 2013; Chapter 2 of this thesis). Based on the location of the main seismicity cluster(s) (base of hydrothermal downflows) and hydrothermal vent field (upflow/discharge zones), the volcano-scale hydrothermal circulation at Lucky Strike is proposed to be dominantly along-axis. This interpretation is supported by numerical models incorporating a narrow along-axis high permeability zone and higher magmatic heat flux (Fontaine et al., 2014).

The Lucky Strike hydrothermal system comprises at least 18 documented vent sites (Barreyre et al., 2012), with several black smokers and a wider domain of diffuse venting at each vent site. The vent sites are clustered in two major zones, east and west of the hydrothermal field and the axial graben faults appear to act as permeable pathways for the ascending fluids which create these two clusters of outflow zones (Barreyre et al., 2012; Humphris et al., 2002). A two-layer hydrothermal circulation model has been proposed based on the tidal variability of vent temperature records (Barreyre et al., 2018), and on Full Waveform Inversion (FWI) of active seismic data (Arnulf et al., 2014b) which reveals an extensively faulted, more permeable, upper layer. The widespread diffuse flow in the vicinity of the focused vents, indicating conductive heating of the entrained seawater in the secondary circulation layer, has been documented by a study of dive videos and photomosaics of the seafloor (Barreyre et al., 2012).

The Tour Eiffel (TE) site is one of the largest Lucky Strike vent sites, located in the southeast corner of the hydrothermal field, extending over ~ 24 m * 20 m area. The site is dominated by a massive ~15 m high sulfide edifice, bearing several high temperature vents and surrounded by diffuse flow areas. The total heat flux, including both discrete and diffuse venting, from the Tour-Eiffel vent site is estimated to be $\sim 19.88 \pm 2.88$ MW, with more than 95% of the heat coming from diffuse venting (Mittelstaedt et al., 2012). A recent conceptual geological model was developed for the fluid dynamics in the shallow portion of the upflow zone for the TE site based on geological mapping and on time-series of diffuse fluid temperature and chemistry (Wheeler, 2021). Numerical models including anhydrite precipitation for the shallow upflow zones (upper 100 m;

Wheeler, 2021) show that formation of low permeability zones by mineral precipitation may affect the geometry of fluid flow in the shallow subseafloor, facilitating an extended area of diffuse venting ($< 80^{\circ}\text{C}$) and the formation of small-scale (meter wide) secondary cells, with cold fluids inflowing on one side of the low-permeability areas, and moving back up to the seafloor at some distance from the focused high temperature vent. Such low temperature diffuse vents and small-scale secondary cells may prevail at ‘mature’ sites such as Tour Eiffel, where a complex widely distributed shallow permeability structure exists.

Here we present ~one year of near-seafloor seismicity recorded near the Tour Eiffel vent site of the Lucky Strike hydrothermal field, using a small-aperture hydrophone network consisting of 4 hydrophones, deployed as part of the European Multidisciplinary Seafloor and water column Observatory (EMSO)-Azores. All of the hydrophones are connected to the same datalogger, allowing precise differential timing of earthquake arrivals. This small aperture network detected several types of events, including whale songs, and earthquakes originated outside the network, and at depths/elevations greater than the few hundred meters that are the scope of this study. We therefore developed criteria based on waveform characteristics, number of phases and frequency spectra to select only shallow microearthquakes. The location of these shallow microearthquakes is not well constrained because of the limited number of instruments and the poorly resolved shallow upper crustal velocity structure. Nonetheless, we provide here a first order picture of shallow microearthquake locations in the vicinity of the Tour Eiffel vent site and discuss their possible source mechanisms.

3.2 Method

3.2.1 Experimental setup

In order to record very small microearthquakes potentially associated with the near seafloor upflow of the hydrothermal fluids and mineral precipitation, a small-aperture, single datalogger hydrophone network has been deployed since 2016 as part of the EMSO-Azores observatory in the vicinity of two active hydrothermal vent sites: Tour Eiffel and Montségur (Figure 3.1). Here we report analyses and results from the first two consecutive deployments spanning from 2016-09-10 to 2017-09-25 (380 days). After each deployment, the data acquisition system was recovered

CHAPTER 3. NEAR-SEAFLOOR MICROSEISMICITY

and reset, but the hydrophones were not moved from their positions except H-3 (central hydrophone, Figure 3.1; moved no more than a few decimeters). The hydrophone network consists of 4 HTI04 hydrophones connected by ~100 m cables to a single datalogger (collectively called ‘HydrOctopus’) on one of the EMSO-Azores sea monitoring nodes (SEAMON-East), in the southeast corner of the volcano region. The network array aperture is ~150 m and the sampling frequency of the hydrophones is 250 sps, with an effective high-frequency cut-off at ~100 Hz.

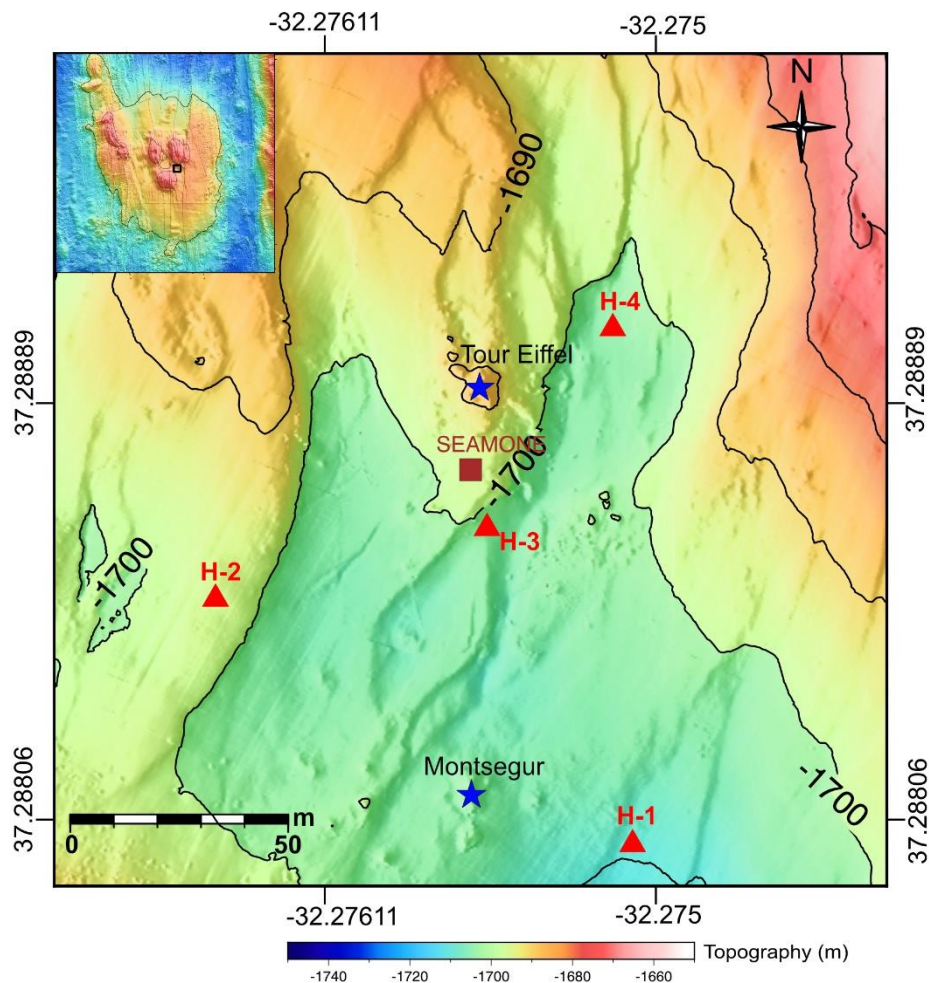


Figure 3.1. Overview map of the HydrOctopus array. Red triangles: hydrophones, Brown square: SEAMON-East (one of the Sea Monitoring nodes of the observatory), Blue stars: Hydrothermal vent sites, Black lines: Isocontours. Inset map: localization of the experiment on Lucky Strike volcano (the color bar does not correspond to the inset map).

3.2.2 Events detection and classification

As this was the first analysis of HydrOctopus data, we evaluated the data quality using Probabilistic Power Spectral Density (PPSD) analysis, compared with existing OBS hydrophone data from the primary OBS network (Figure 2.1; Figure S3.1). Only one OBS (C-OBS) worked during the first deployment (2016-09 to 2017-07) and its data quality was bad (Figure S3.1a). For the second deployment (2017-07 to 2017-09), out of 4 OBSs we had data only from the northern OBS (heretofore ‘N-OBS’) with good data quality (Figure S3.1b), working throughout the entire period of HydrOctopus (central-OBS data quality was bad and not time synchronized, East & South OBS worked only partially when the HydrOctopus was working). The 50th percentile PPSD of all hydrophones in the HydrOctopus are the same in both the deployments, indicating good data quality in all hydrophones (Figure S3.1). It is also similar to that of N-OBS in the lower frequency range (up to ~20 Hz; the effective OBS high-frequency cut-off is ~25Hz). Therefore, only the N-OBS from the second deployment was used to compare the waveform characteristics of the HydrOctopus-detected events.

Events were detected with a standard short-period average/long-term average (STA/LTA) algorithm (Figure 3.2). We adapted the STA/LTA parameters to detect very small, short duration events (STA/LTA > 2.2 for window lengths of 0.2 s and 10 s respectively). Events detected with all 4 hydrophones were selected for further analysis. Pontbriand & Sohn, (2014) characterized subseafloor shallow microearthquakes originated within the TAG hydrothermal mound as extremely short (< 1 s) waveforms with apparent lack of S arrivals, and with a nondouble couple origin. With that idea, we put a filter to select events with maximum energy observed within 1 second of the event’s first phase arrival time (Figure 3.2). The hydrophones also recorded more than 60,000 whale songs. The whale songs repeated at 12-15 s intervals and have a spectral peak between 20 and 30 Hz (Figure S3.2). Using these criteria, we removed the whale songs (Figure 3.2). We then manually classified the rest of the events based on waveform duration, number of phases and frequency spectrum. We identified 4 types of events: shallow events, deeper events in the volcano, deeper events outside the volcano (at the Lucky Strike segment ends, mostly) and unclassified events, that include ship noise (Figure 3.2). The waveform characteristics of each type of events are discussed in the results section (the corresponding catalogs will also be made available). We then focused further analysis on shallow events.

Relative P phase arrival times were calculated using phase cross-correlation. Assuming the trigger time given by STA/LTA method to be the direct P arrival time at the H-3 hydrophone (center of the network, Figure 3.1), we cross-correlated the H-3 waveform with the rest of the hydrophones and calculated the pick-correction time for the highest cross-correlation coefficient. The pick-correction time was then added/subtracted from the H-3 hydrophone P arrival time to calculate the P arrival times at the other hydrophones. We also tried the same approach taking the trigger time in H-1 hydrophone as the reference and cross-correlating it with the other hydrophones: it does not affect the results.

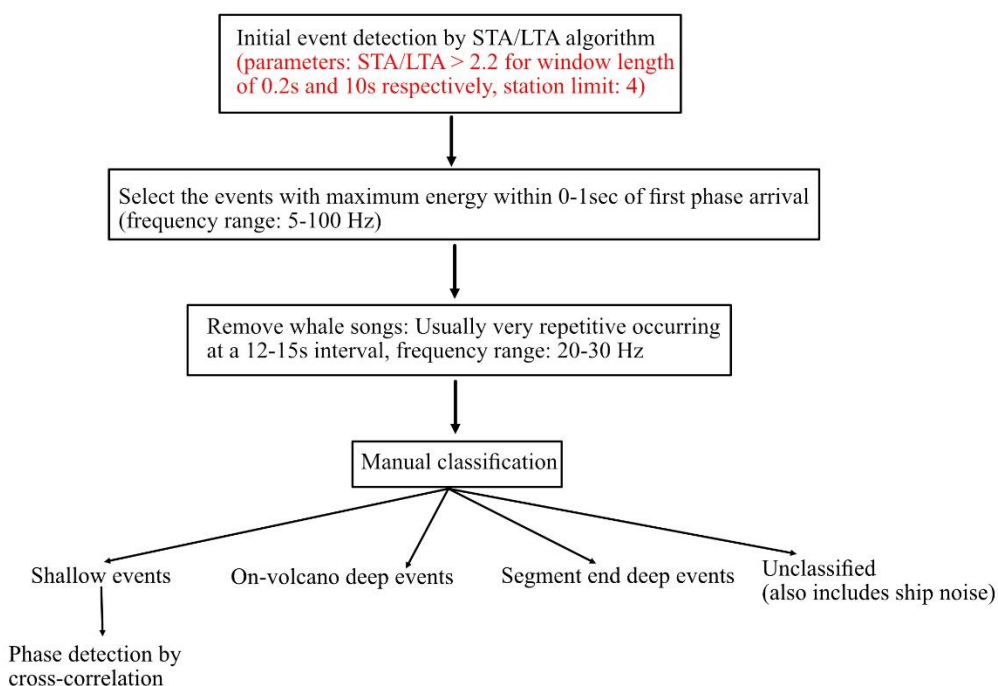


Figure 3.2. Schematic representation of steps adapted to detect shallow events.

3.2.3 Magnitude calculation

We did not have good quality OBS data for the duration of the HydrOctopus deployment. Also, shallow events that had been detected in the HydrOctopus, were only detected in the OBS's hydrophone channel and not its vertical seismometer channel (discussed later). We therefore used the catalog of deeper on-volcano events recorded by the primary OBS network (374 events recorded April 2015 and May 2016) to initially establish a relationship between the amplitude on the hydrophone channel (pressure scale) and the amplitude on the vertical channel (displacement scale), using the south station (LSVSI) (Figure S3.3). We verified that the OBS hydrophone and

HydrOctopus channels had the same response using PPSD analysis (Figure S3.1b). Using the established relation, we then converted the amplitude in the HydrOctopus hydrophone channels to approximate displacement and calculated the local magnitudes with the custom scale defined in Crawford et al., (2013).

3.2.4 Shallow earthquake locations

Earthquake locations were estimated using a grid search algorithm within the NonLinLoc (NLLoc, Lomax et al., 2000) software over a 1 km^3 cubic grid from the center of the hydrophone network with 10 m node spacing. Since the subseafloor shallow upper-crustal velocity structure is not well constrained, we tested different shallow velocity models, with subsurface P-wave velocities at the seafloor ranging from 1.5 km/s to 3.2 km/s and velocity gradients ranging from 0 to 3.6 (km/s)/km, and then selected a model that yielded minimum RMS error and minimum horizontal and vertical standard deviations for the event locations (Figure S3.4). Note that models with very high starting velocity and high velocity gradient yield low standard deviations in the event locations, but in those cases, events are clustered at one depth very close to the seafloor, which is most probably an artefact. This is also true for models with low starting velocity and high velocity gradient (Figure S3.4). Following our analysis, we decided to use a velocity model with a very low P-wave velocity of 1.5 km/s at the seafloor (seawater P-wave velocity) and a rather high velocity gradient of 2.6 (km/s)/km, leading to a P-wave velocity of 4.1 km/s at the base of the model at 1 km beneath the sea floor. This model has lower velocity than the velocity model used in Pontbriand & Sohn, (2014) for TAG shallow event locations (starting seafloor velocity of 2.5 km/s and velocity gradient of 1.5 (km/s)/km) because all of our models starting with seafloor starting velocity $> 1.6 \text{ km/s}$ clustered events at a single depth very close to the seafloor.

Since this was the first time HydrOctopus data were analyzed, we tested for possible error in the correspondence between data channels and the actual hydrophone locations at the seafloor. To do so, we located events and calculated the mean RMS using each possible location for each data channel. All of the other configurations have higher mean RMS than the expected configuration (Figure S3.5), suggesting that the initial configuration is correct. Mean RMS values are lower for the configurations when the center hydrophone (H-3) position is fixed and only the positions of the other hydrophone channels are swapped.

3.3 Results & Discussion

3.3.1 Events classification

Based on the waveform duration, number of phases and frequency spectrum, we classified all events detected by the HydrOctopus network (except whale songs) into 3 major categories. Type-1 events have very short durations (~ 1 s) with one detectable phase (direct P) on all 4 hydrophones (Figure 3.3a, 3.3c, S3.6). Type-2 events are ~ 3 s and have 2 phases separated by ~ 2.25 - 2.3 s (Figure 3.4a, d). Based on the water column thickness (1.7 km) in this region and the acoustic water velocity (1.5 km/s); the two-way P-wave traveltime in the water column is ~ 2.26 s. Therefore, the first phase and second phases in type-2 events are the direct P phase and the water reflected P phase (PwP) from sea surface, respectively. We also verified this by autocorrelating the event waveform with an inverted and 2.26 s delayed waveform. Type-3 events are very long (>15 s) with direct P and PwP phase, and a long coda after the PwP arrival (Figure 3.5a, d).

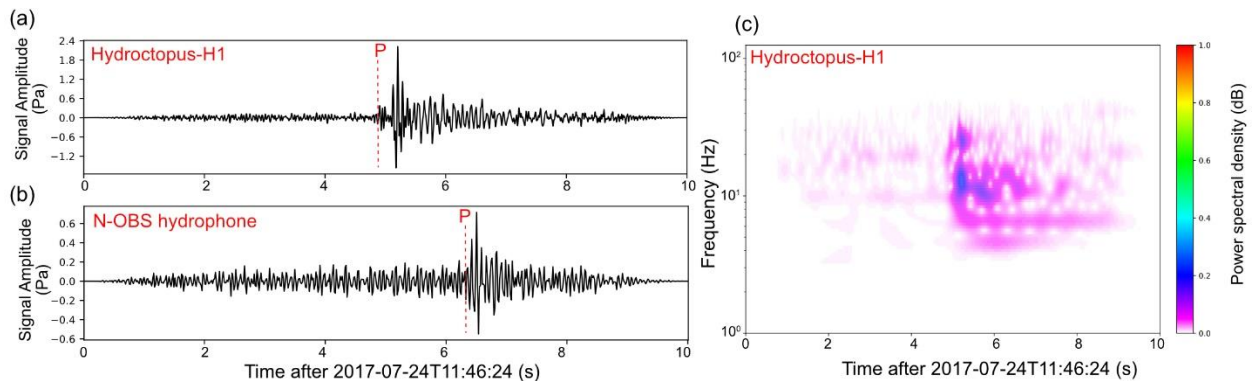


Figure 3.3. Example of a shallow (type-1) event waveform on (a) HydrOctopus hydrophone and (b) N-OBS hydrophone. (c) Frequency spectrum of HydrOctopus hydrophone waveform. Waveform patterns in the rest of the HydrOctopus hydrophones and N-OBS channels are shown in Figure S3.6.

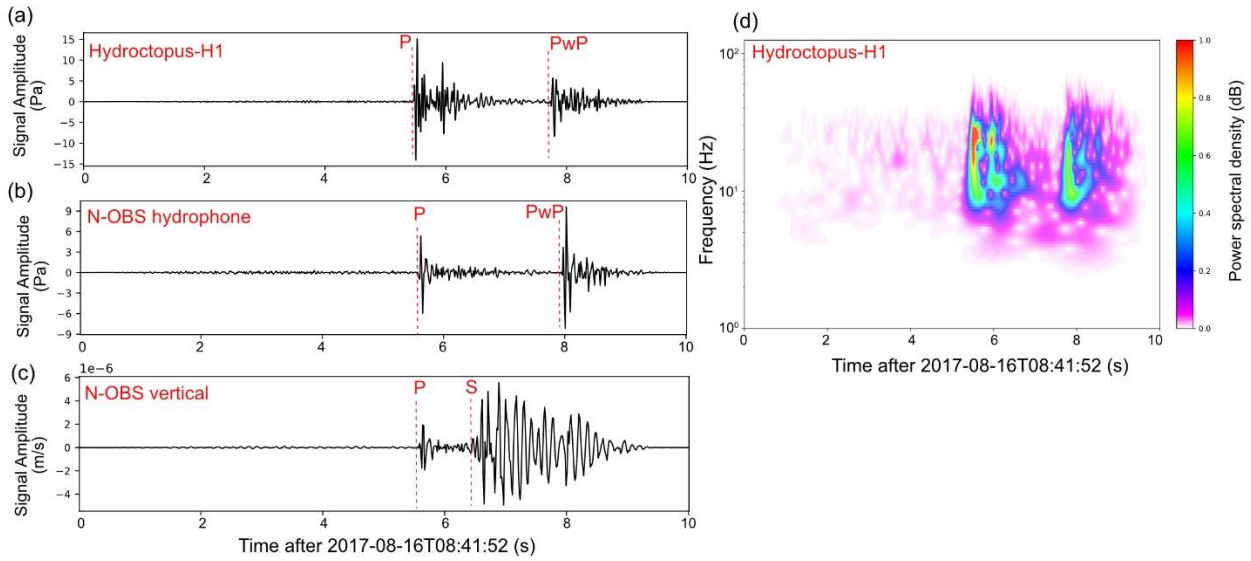


Figure 3.4. Example of an on-volcano deep (type-2) event waveform on (a) HydrOctopus hydrophone, (b) N-OBS hydrophone and (c) N-OBS vertical channel. (d) Frequency spectrum of HydrOctopus hydrophone waveform.

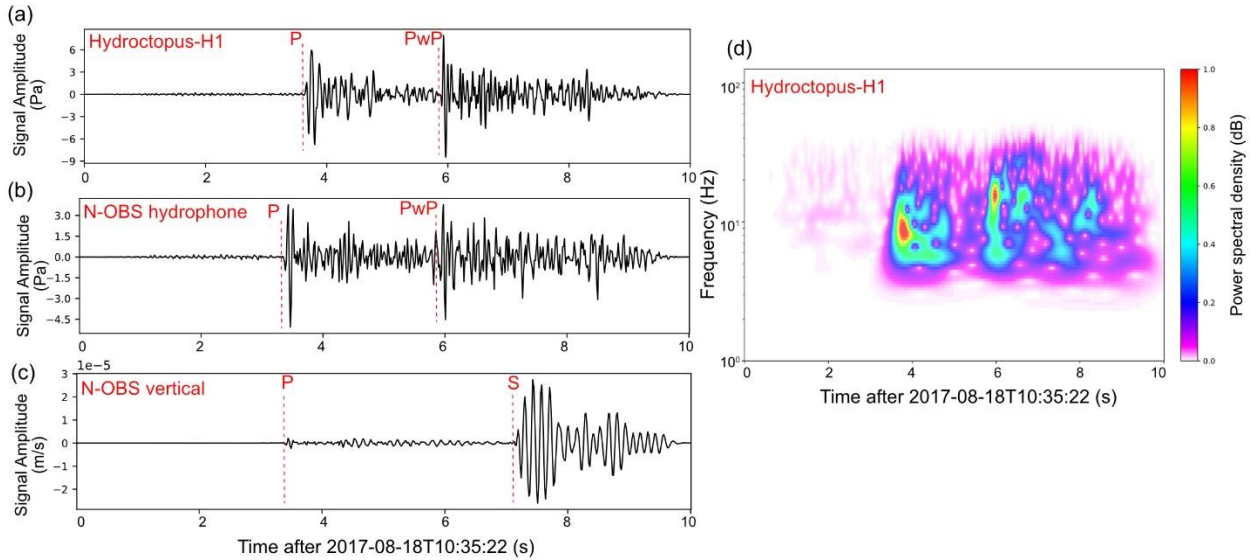


Figure 3.5. Example of a segment end/off-volcano deep (type-3) event waveform on (a) HydrOctopus hydrophone, (b) N-OBS hydrophone and (c) N-OBS vertical channel. (d) Frequency spectrum of HydrOctopus hydrophone waveform.

We then looked for all 3 types of event waveform patterns in the vertical channel and the hydrophone channel of the N-OBS (consisting of a 3-component Sercel L-28 geophone and a HiTech HT-90-U hydrophone), working during the second deployment and which was deployed ~3.5 km from the hydrophone network. In the vertical channel of the N-OBS, type-2 events have both direct P and S phases with an S-P traveltime difference of ~0.8 s (Figure 3.4c). In the hydrophone channel of the N-OBS, they have P and PwP phase separated by ~2.3 s with the P

arrival slightly after that on the HydrOctopus hydrophones (Figure 3.4b). Type-3 events have direct P and S phases with a S-P traveltimes difference of ~ 3.6 s on the vertical channel (Figure 3.5c), and P and PwP phases in the hydrophone channel of the N-OBS (Figure 3.5b). The absolute average time difference between the first P phase in the HydrOctopus and the N-OBS for type-3 events is ~ 1.1 s. Based on the S-P traveltimes difference observed in the OBS seismicity catalog, which is recorded by the primary network of short period OBSs in the Lucky Strike region (Chapter 2 of this thesis), we recognized type-2 events as on-volcano deeper events (originated mainly on the top of the AMC and interpreted as related to hydrothermal cooling and alteration processes, see Chapter 2), and type-3 events as segment end/off-volcano deeper events.

Only the type-1 events with local magnitudes > -2.0 are identified on the hydrophone channel of the N-OBS, with the first P arrival arriving ~ 1.54 s later than on the HydrOctopus hydrophones (Figure 3.3b). These events are very difficult to identify on the vertical channel of the N-OBS, probably because of their low energy (Figure S3.6b). A delay time of ~ 1.54 s in the first P phase of the N-OBS compared to the HydrOctopus hydrophones is consistent with if the events are indeed very shallow (< 200 mbsf) and originated in the vicinity of the HydrOctopus. To determine this, we took synthetic events located at a range of depths (0 - 1000 m) and at a horizontal distance of 10 m from the center of the HydrOctopus network and calculated the P travel time difference between the HydrOctopus hydrophone and the N-OBS hydrophone as a function of event depths (Figure S3.7). This shows that the ~ 1.54 s delay corresponds to event depths of less than 200 mbsf. We, therefore, consider type-1 events as very shallow events because of their short durations in both HydrOctopus and N-OBS hydrophones, lack of PwP phase, and the P arrival delay at the N-OBS.

We identified 740 shallow events, 1089 on-volcano deep events, and 988 segment end events in the September 2016 - September 2017 HydrOctopus record (Figure 3.6). Very few shallow events were detected between November 2016 and March 2017 when whale songs were abundant. A similar effect, to a lesser extent, is visible for on-volcano deeper events (Figure 3.6b).

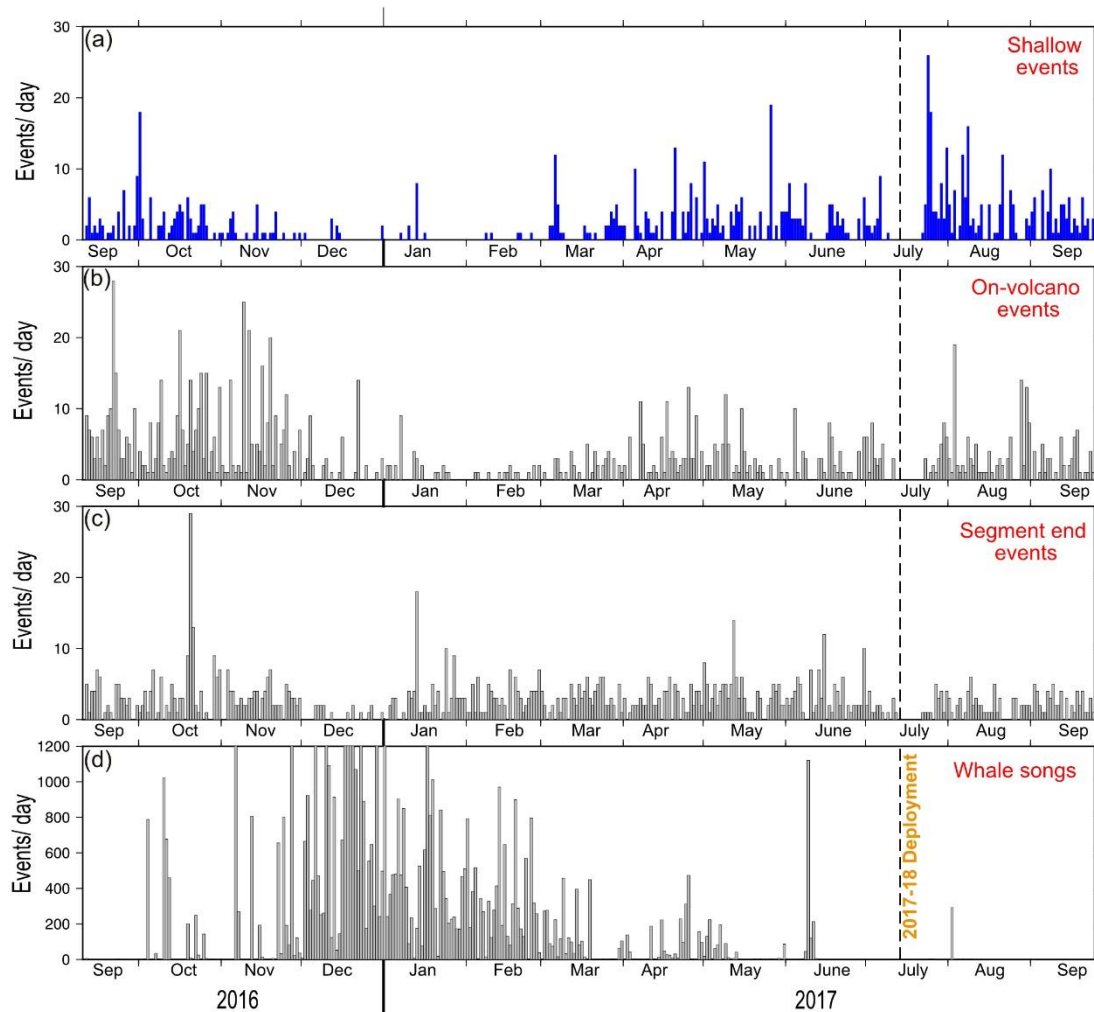


Figure 3.6. Temporal distribution of (a) shallow events (type-1), (b) on-volcano deep events (type-2), (c) segment end deep events (type-3), and (d) whale songs. Number of on-volcano deep and segment end deep events are not accurate as some of them might have been excluded by the shallow event selection approach.

3.3.2 Shallow event characteristics

There were 740 very small shallow events detected with local magnitudes (M_L) ranging between -4.0 and -0.5 in September 2016 - September 2017 (Figure 3.7a). The average local magnitude of these shallow events is ~ -2.48 . Shallow events appear to occur persistently throughout the year (if we exclude the November 2016 to March 2017 period when whale songs obscured the record) with a seismicity rate of ~ 3 events/day (Figure 3.7b). Only one significant swarm-like period is observed in Mid-July 2017 for almost 2 days with a seismicity rate > 20 events/day. Cumulative moment release of all events is really small and is around $5.2 \cdot 10^9$ N-m (Figure 3.7d), which is equivalent to one event of local magnitude $M_L \sim 0.45$. The contribution of

the shallow events in total seismic release is really small. There is only one comparatively big event ($M_L = 0.04$) in the beginning of May 2017.

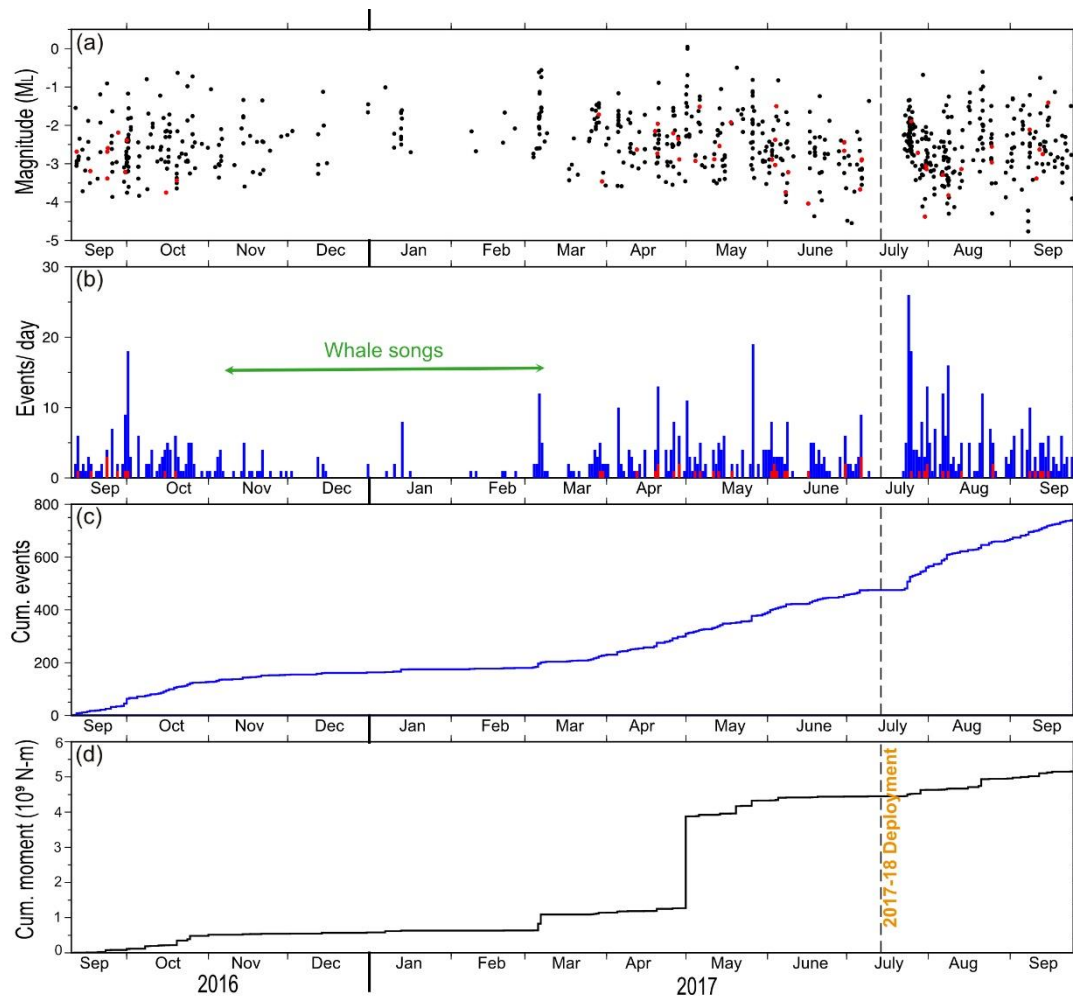


Figure 3.7. Temporal distribution of shallow seismicity located in the vicinity of Tour Eiffel hydrothermal vent site, Lucky Strike hydrothermal field. Dashed line corresponds to 2017-2018 maintenance cruise and separates consecutive deployments. (a) Local magnitudes. Black dots are the events detected outside the network; red dots are the events located inside the network. (b) Events/day. Green arrow marks the approximate time period of abundant whale songs when shallow events could not be detected. Blue bars correspond to all shallow events, red bars correspond to the events located inside the network. (c) Cumulative number of all shallow events, and (d) Cumulative seismic moment of all shallow events.

3.3.3 Event Locations

Since there are only 4 hydrophones and the shallow upper crustal velocity structure is not well known, event locations are not well constrained by the 4 direct P arrivals. The mean rms of all events is less than 10 ms, but the average event location uncertainties are high: ~ 232 m vertically and ~ 178 m horizontally (this is, however, in the same range as the TAG shallow

CHAPTER 3. NEAR-SEAFLOOR MICROSEISMICITY

microseismicity catalog, whose uncertainties were ~ 187 m vertically and ~ 200 m horizontally; Pontbriand & Sohn, 2014). Most of the events are located outside the HydrOctopus network and seemingly randomly scattered horizontally (Figure 3.8a) although there is a small cluster southeast of the Montségur site, including some “large” events with $M_L > -1.0$, and another small cluster in the North, in the vicinity of the Sintra and Y3 vent sites. Most events have depths < 300 m bsfr (Figure 3.8b, c). The scatter of the events appears to be real, as relocations done for all other hydrophone configurations are clustered in geometric forms related to the positions of the changed stations and with significantly higher mean RMS (Figure S3.5).

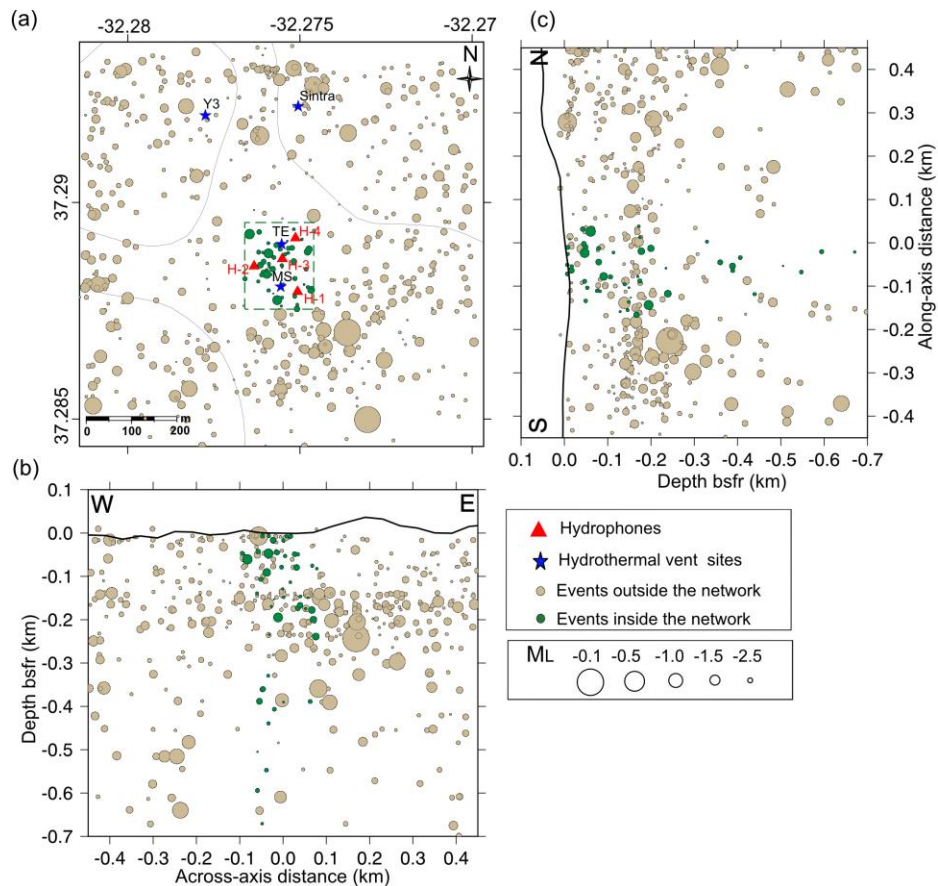


Figure 3.8. Spatial distribution of shallow seismicity in the vicinity of Tour Eiffel hydrothermal vent site, Lucky Strike hydrothermal field. Green dashed rectangle represents the area of the HydrOctopus network, and the events located inside it are marked as green dots (red bars in Figure 3.7b). Light brown dots represent the rest of the events located outside the network. All the events are scaled according to their local magnitude. (a) Map view. Partial black solid isocontours outline the central lava lake, north-western and southern volcano peak. Red triangles: hydrophones, Blue stars: Hydrothermal vent sites (TE: Tour Eiffel, MS: Montsegur). (b) Across-axis cross section through the center of the hydrophone network. Depth is referenced beneath seafloor reference depth (bsfr) 1.7 km. (c) Along-axis cross section.

Only 76 events (~10% of total shallow events) of the 12-month catalog were located inside the network (Figure 3.9a). The average horizontal and vertical uncertainties of these 76 events are ~210 m and ~214 m respectively. All these events are very small ($M_L < -1.5$) and most of them are within 200 m of the sea floor (Figure 3.9b, c). We observe no specific clustering of these events (Figure 3.7, 3.9).

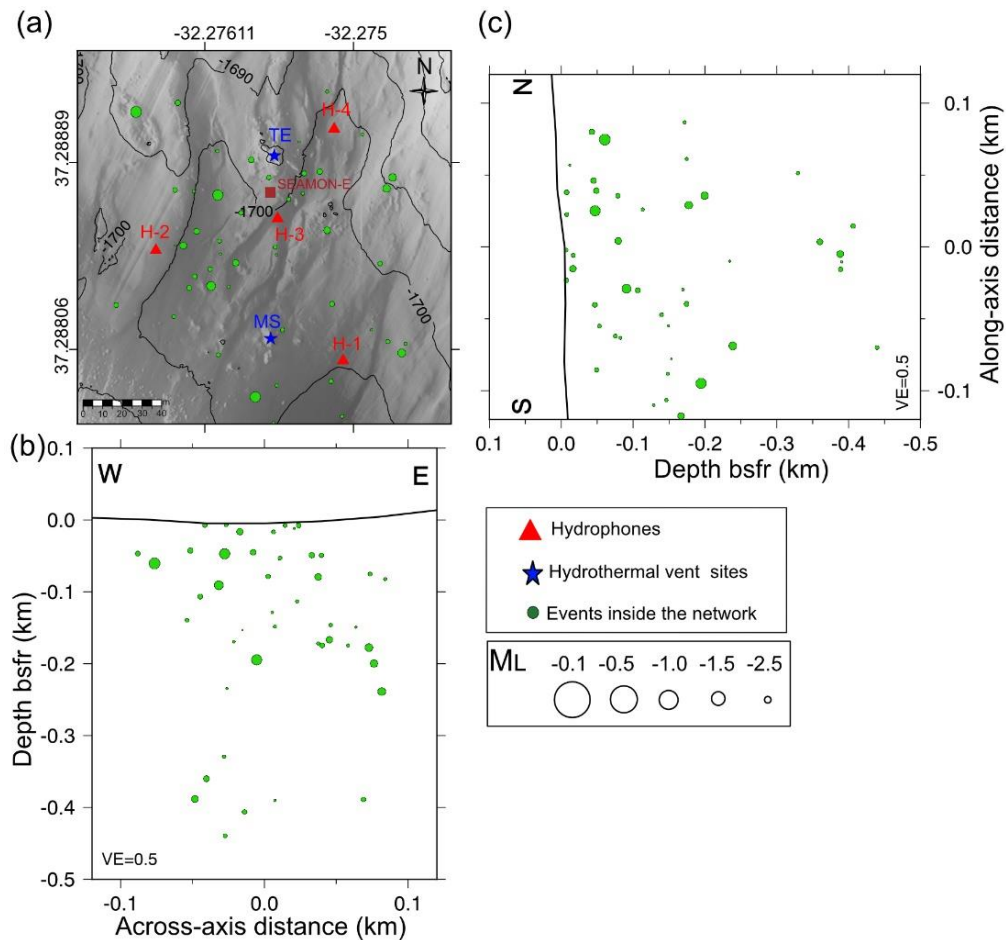


Figure 3.9. Spatial distribution of shallow seismicity located inside the HydrOctopus network (Green dashed box in Figure 3.8). Events are marked at green dots. All the events are scaled according to their local magnitude. (a) Map view. Red triangles: hydrophones, Blue stars: Hydrothermal vent sites (TE: Tour Eiffel, MS: Montsegur), Brown square: SEAMON-East (one of the Sea Monitoring nodes of the observatory). (b) Across-axis cross section through the center of the hydrophone network. Depth is referenced beneath seafloor reference depth (bsfr) 1.7 km. (c) Along-axis cross section.

3.3.4 Potential source mechanisms

Here we discuss various possible source mechanisms for shallow microearthquakes, focusing on these events that are located within the HydrOctopus network. The 740 shallow microearthquakes (average $M_L = -2.48$) detected in September 2016 - September 2017 represent a

seismicity rate of ~3 events/day (Figure 3.7). The number of shallow events, and their magnitudes, are much smaller than those observed beneath the TAG hydrothermal mound (~ 243 events/day with average $M_L = -0.95$). The TAG mound is a much larger hydrothermal site than Tour Eiffel (diameter ~200 m, Humphris et al., (2015); Humphris & Kleinrock, (1996); whereas that of TE is ~20 m), with a significantly higher estimated heat flux (~1 GW for the TAG mound, Wichers et al., (2005); ~20 MW for TE, Mittelstaedt et al., (2012)).

One of the mechanisms discussed in Pontbriand & Sohn, (2014) for the generation of secondary-circulation seismicity is reaction-driven cracking in response to anhydrite precipitation. Anhydrite is precipitated from the entrained seawater at a temperature of ~150⁰ C or more, either through conductive heating or mixing with hydrothermal fluids, and dissolves in seawater below 150⁰ C in response to cooling. Anhydrite precipitation is proposed to play a key role in coexisting high-temperature focused vents and low-temperature diffuse flow (Guo et al., 2020; Lowell et al., 2003). The continuous precipitation of anhydrite in veins and cracks leads to an increase in volume which causes fractures in the hot matrix and generates microearthquakes. As most of the shallow microearthquakes are located in a depth range of 150-250 m beneath the sea floor in our observation near TE (Figure 3.8, 3.9), we believe that anhydrite precipitation could also be a plausible source mechanism for these earthquakes, in which case their depth limit would define the maximum seawater entrainment depth in the hydrothermal upflow domain.

Diffuse fluids sampled at the TE hydrothermal vent site in 2017, 2018 and 2019 show no chemical evidence for anhydrite precipitation (Wheeler et al., submitted), which supports a low rate of seismicity originated from anhydrite precipitation. If we further explore the anhydrite precipitation hypothesis, following the relation demonstrated for a penny shaped fracture with only vertical strain (Pontbriand & Sohn, 2014), a minimum source volume of ~0.007 m³ is required to generate an average earthquake with $M_L = -2.48$ for a stress drop equivalent or greater than the confining pressure (Supplementary text S3.1). Assuming all 740 events (seismicity rate ~3 events/day) to be originated by precipitation, anhydrite would precipitate with an annual volume between 0.32 m³ and 1.277 m³ (Supplementary text S3.1), against 27 m³ to 51³ below TAG (Pontbriand & Sohn, 2014).

Hydraulic fracturing and collapsing bubbles are other potential mechanisms for generating shallow microearthquakes in hydrothermal systems (Dawson et al., 2012; Kedar et al., 1996, 1998; Miller et al., 1998). These are not likely to be the cause of the observed shallow seismicity. Hydraulic fracturing occurs when the fluid pressure exceeds the strength of the host rocks or the confining pressure. The fluid pressure of the hydrothermal system is less than or equal to the buoyancy pressure of the hydrothermal circulation (Cann & Strens, 1989). Since the maximum depth of the primary hydrothermal system is constrained at ~2.5-3 km bsf (Crawford et al., 2013, Chapter-1 of this thesis), the buoyancy pressure is estimated at ~10-15 MPa (Supplementary text S3.1). This is significantly less than the estimated 22 MPa confining pressure at 200 m depth below seafloor at the TE site (Supplementary text S3.1). The buoyancy pressure of shallower, secondary circulations will be even smaller. It is therefore not possible to have shallow microearthquakes generated by hydraulic fracturing. The arguments developed by Pontbriand & Sohn, (2014) against an origin of the TAG microearthquakes by vibrating or collapsing gas bubbles also apply to TE: such bubbles would form in uprising end-member fluids and would thus not cause microseismicity in areas of diffuse venting; they would also have to be unreasonably large to generate the observed seismic frequencies.

3.4 Summary

1. In this work, we attempted to detect near seafloor seismic events in the vicinity of the Tour Eiffel hydrothermal vent site, Lucky Strike hydrothermal field using a small aperture, temporally synchronized hydrophone network (HydrOctopus). Since this was the first time HydrOctopus data were analyzed, we developed a systematic approach to detect shallow events based on waveform durations, number of phases, and frequency spectrum.
2. We detected 740 near seafloor seismic events with a seismic rate of ~3 events/day and local magnitudes ranging from -4 to -0.5 in September 2016 - September 2017. These shallow events are characterized by short duration (<1 s) with only a direct P phase. The apparent lack of PwP phase is probably due to the very small energy release by these events. At the N-OBS station (located ~3.5 km north of the HydrOctopus network), these events were only seen on its hydrophone channel (and only those with $M_L > -2.0$), with the P arrival ~1.54 s after the HydrOctopus arrivals, consistent with a shallow source near to the HydrOctopus.

3. On-volcano deep and segment end/off-volcano events have very clear P and PwP phases separated by ~2.25-2.3 s. In the N-OBS vertical channels, they have both P and S phases. In the absence of an OBS working at the same time, the apparent lack of PwP phase in the hydrophone can be used as a criterion to identify shallow events.
4. The event locations are not very well constrained, probably because of the limited number of hydrophones and use of a simplified velocity model. However, tests based on network configurations confirms that the scattered event locations represent the true event distribution.
5. Most of the events are present within ~150-250 m beneath the sea floor. As a preliminary interpretation, we consider these events to have originated as a result of reaction driven cracking in response to anhydrite precipitation. Further analyses are needed to improve the locations and to infer source mechanisms.

Supplementary materials

Supplementary text S3.1

Reaction driven cracking:

If we consider a penny shaped fracture for reaction driven cracking in response to anhydrite precipitation with only vertical nonzero strain ($\Delta e_{11} = \Delta e_{22} = 0, \Delta e_{33} \neq 0$; same model as described in Pontbriand & Sohn, (2014)), the moment tensor of this source in an isotropic medium is

$$M = -V \begin{pmatrix} \lambda \Delta e & 0 & 0 \\ 0 & \lambda \Delta e & 0 \\ 0 & 0 & (\lambda + 2\mu) \Delta e \end{pmatrix} \quad (1)$$

Where λ and μ are lamé parameters. Taking the scalar moment tensor as $M_0 = \frac{1}{\sqrt{3}}(M:M)^{1/2}$, it can be calculated from equation-1 as

$$M_0 = \frac{\Delta e V}{\sqrt{3}} \sqrt{2\lambda^2 + (\lambda + 2\mu)^2} \quad (2)$$

Taking the relationship between stress drop and strain for a penny-shaped crack ($\Delta \sigma = \frac{7\pi}{16} \mu \Delta e$), the relationship between seismic moment and volume & stress drop of a penny shaped source is given by

$$V\Delta e = \sqrt{3}M_0 \frac{7\pi}{16}\mu \left[\sqrt{2\lambda^2 + (\lambda + 2\mu)^2} \right]^{-1} \quad (3)$$

For our shallow microseismicity catalog, the average local magnitude is -2.48 which corresponds to a seismic moment $M_0 = 2.13 \times 10^5$ N-m. The confining pressure at TE region (1700 mbsf) is ~22 MPa. For a stress drop greater than or equal to the confining pressure, following equation 3, we calculate that a source volume of ~0.007 m³ (20 cm sides for the case of a cube) is sufficient to generate an average magnitude event.

Anhydrite precipitation:

The hypothesis of reaction driven cracking assumes that the size of each event is directly related to the incremental volume of the anhydrite deposited. Taking an average magnitude earthquake ($M_L = -2.48$) and for a stress drop ranging between the confining stress (22 MPa) and 100 MPa, it corresponds to a volume change between 0.35 cm³ and 1.4 cm³ respectively. Assuming all the shallow events (total number 740) occur by anhydrite precipitation, taking a seismicity rate of ~3 events/day, we will get an annual volume change of between 0.32 m³ and 1.277 m³.

Hydraulic fracturing:

The maximum fluid pressure achieved by a hydrothermal system is less than or equal to the buoyancy pressure. The buoyancy pressure (Cann & Strens, 1989) at a depth z of the hydrothermal system is calculated as $\Delta p = gz(\rho_{sw} - \rho_{ht})$, where ρ_{sw} and ρ_{ht} are the density of the seawater and hydrothermal fluid respectively, and g is the gravitation constant. The maximum depth of volcano-scale hydrothermal circulation beneath the Lucky Strike region is ~2.5 – 3.5 km. Taking $\rho_{ht} \sim 615$ kg/m³ (Bischoff & Rosenbauer, 1985) and $\rho_{sw} \sim 1041$ kg/m³, the buoyancy pressure of the primary circulation system beneath Lucky Strike region is ~ 10 – 15 MPa.

Supplementary figures

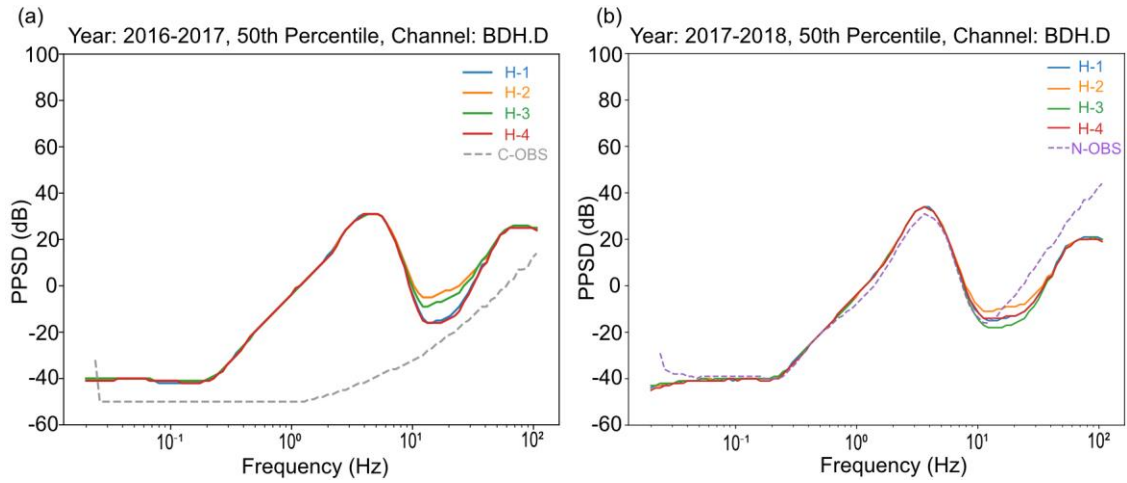


Figure S3.1. Probabilistic Power Spectral Density (PPSD) analysis for all HydrOctopus hydrophones and existing OBS hydrophone channel for (a) 2016-2017 and (b) 2017-2018 deployments. C-OBS: Central OBS, N-OBS: North OBS. Data quality in C-OBS from 2016-2017 deployment was bad.

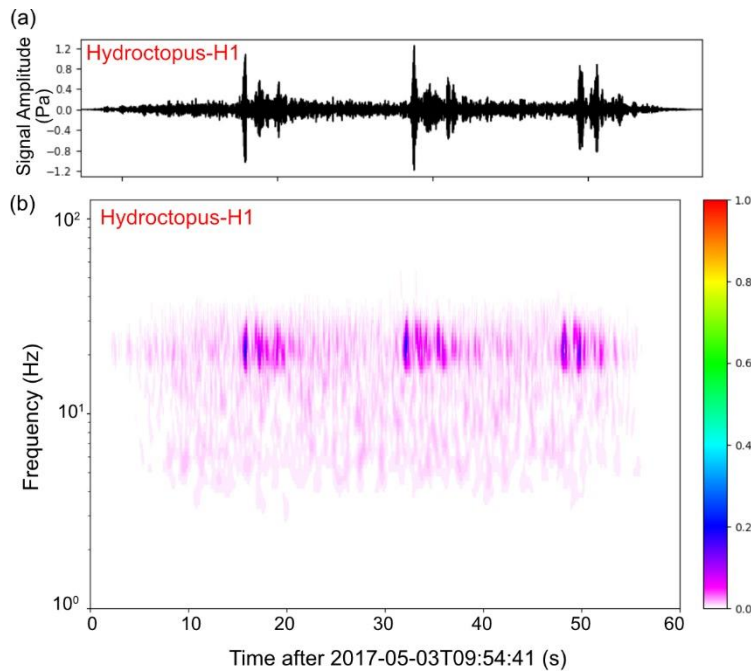


Figure S3.2. Example of whale songs. (a) Waveforms on one of the HydrOctopus hydrophone, and (b) corresponding frequency spectrum.

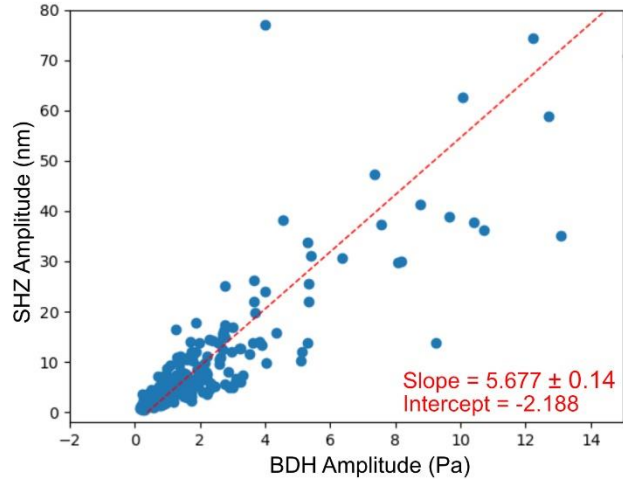


Figure S3.3. Relationship established between hydrophone channel amplitude (pressure) and OBS vertical channel amplitude (displacement) using deeper on-volcano events catalog (374 events recorded between April 2015 – May 2016) recorded by the primary OBS network (South-OBS), in order to calculate local magnitudes using hydrophone amplitude.

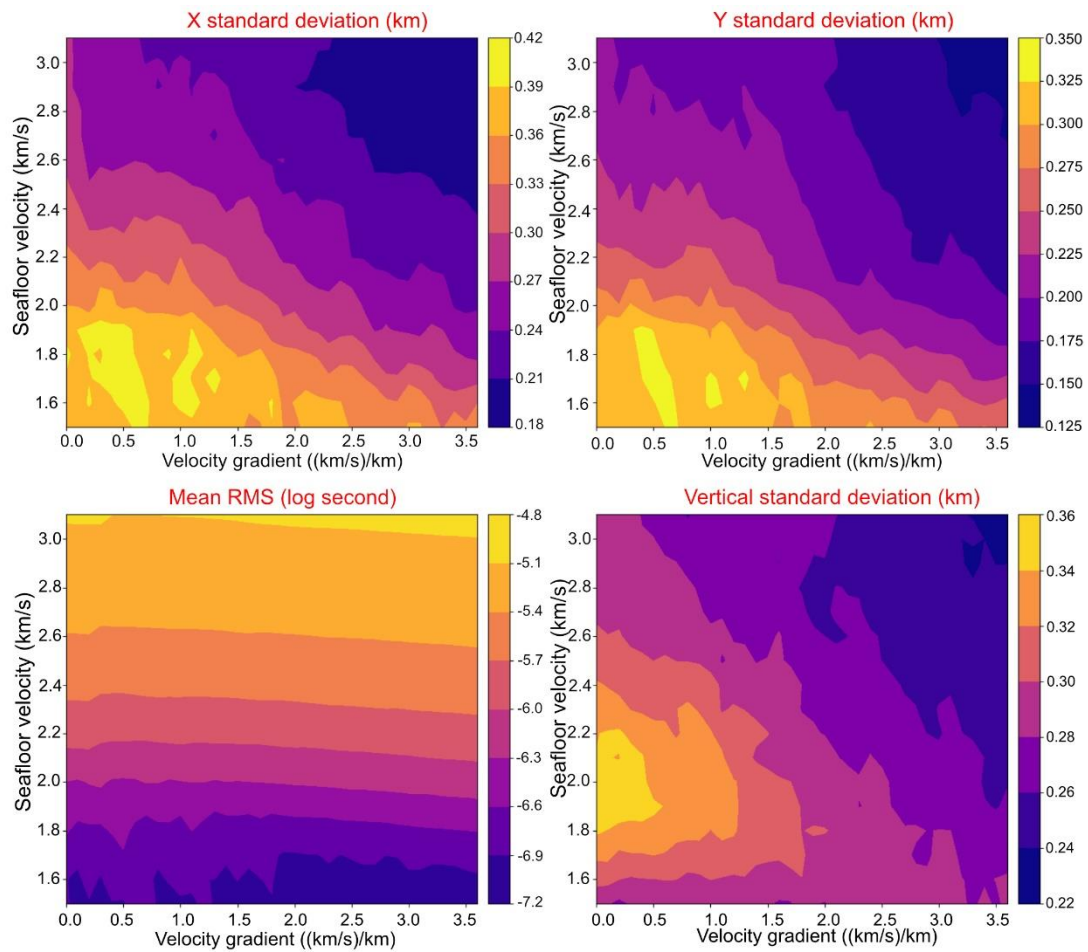


Figure S3.4. Horizontal and vertical standard deviation, and Mean RMS values for all shallow upper crustal velocity models with seafloor starting velocity ranging from 1.5 km/s to 3.2 km/s and velocity gradient ranging from 0 to 3.6 (km/s)/km.

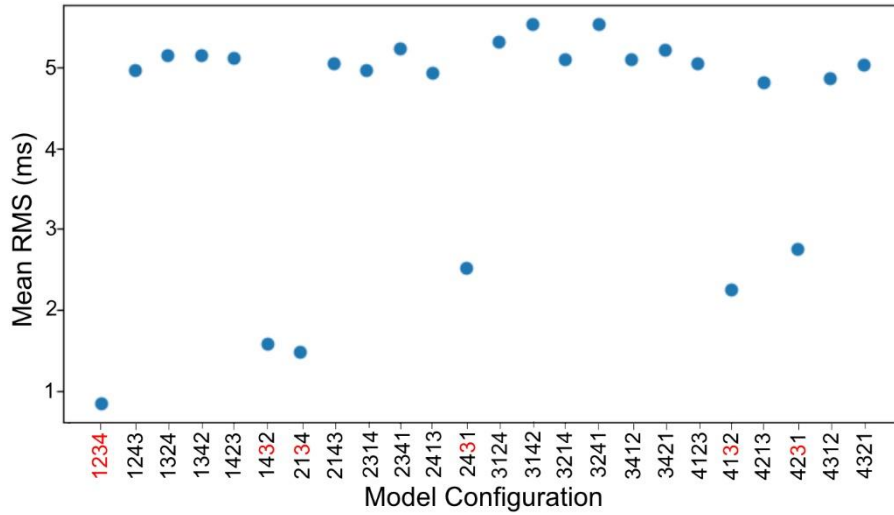


Figure S3.5. Mean RMS values for all possible HydrOctopus model configurations. Red letters indicate the expected configuration (red '1234') and configurations in which the position of the central hydrophone is unchanged (red '3'). The numbering corresponds to the hydrophone no. in the HydrOctopus network (1: H-1 hydrophone and so on). Mean RMS is minimum for the expected configuration and is also relatively low when the central hydrophone (3) is kept in its original position.

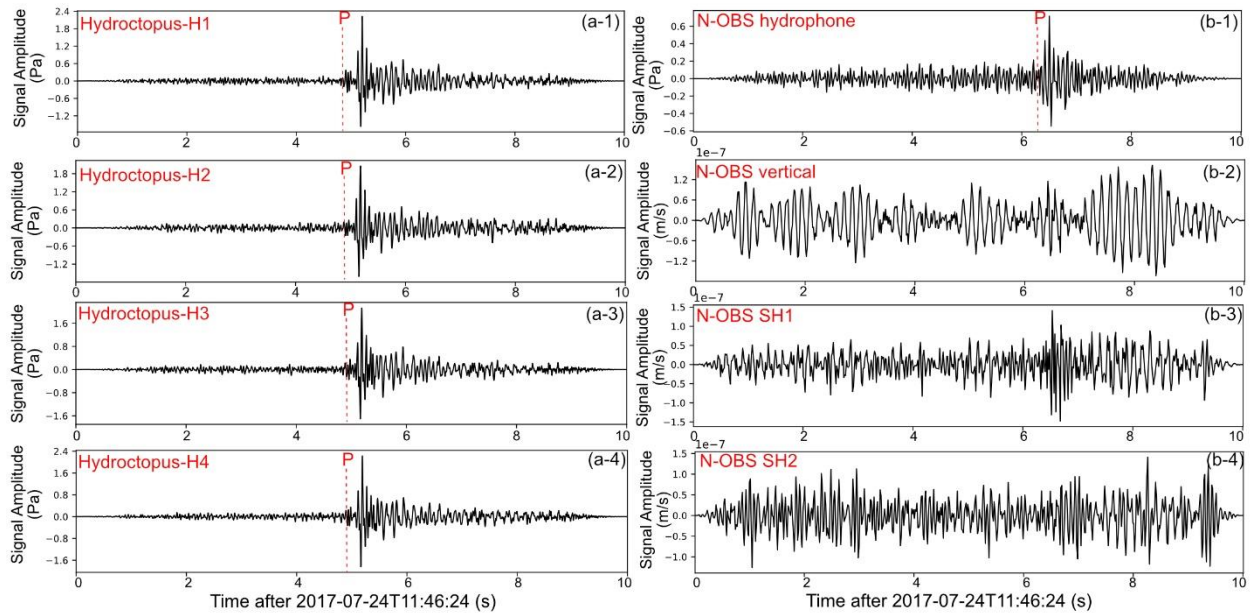


Figure S3.6. Example of a shallow event waveform on (a1-a4) all HydrOctopus hydrophones, and on (b1-b4) all N-OBS channels.

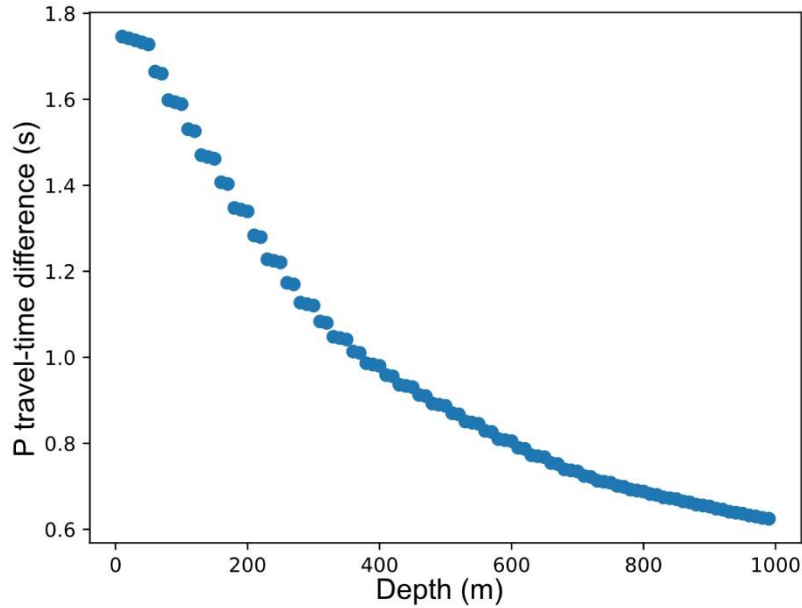


Figure S3.7. P travel time difference between the HydrOctopus hydrophone and N-OBS hydrophone as a function of depth (0-1000 m) of the events. The spatial positions of the events were kept the same (at 10 m distance from the center of the HydrOctopus network). A delay time of ~ 1.54 s in the N-OBS hydrophone compared to HydrOctopus hydrophone would correspond to an event depth of < 200 m.

Chapter 4
Orientation of horizontal components of short
period OBSs using P wave polarization

4.1 Introduction

The three-dimensional seismological wave field provides important information about the source and propagation of seismic waves. A properly oriented field is useful to determine focal mechanisms for earthquake source investigations, and to separate wave types for various studies such as receiver functions, waveform tomography and SKS splitting. Seismometers generally output three channels: one oriented vertically (named Z), one oriented N-S (named N) and the other oriented E-W (named E). However, Ocean bottom seismometers (OBSs) are generally deployed to seafloor in free-fall motion and their horizontal sensors are rarely geographically oriented.

There are various established methods to retrieve the orientation of the horizontal channels. Active sources such as air guns and explosions have been used to determine the orientation of horizontal channels (Duennebieer et al., 1987), but are not available for all OBS deployments. Ambient noise cross-correlation has also been implemented to orient OBSs (Xu et al., 2020; Zha et al., 2013). Analysis of wave arrival polarity (P, S and Surface waves, and Receiver functions) is another commonly used method to determine the correct orientations of horizontal sensors (Doran & Laske, 2017; Janiszewski & Abers, 2015; Lim et al., 2017; Scholz et al., 2016; Stachnik et al., 2012; Xu et al., 2020; Zhu et al., 2020). Grigoli et al., (2012) retrieved relative sensor orientations using a linear least-square inversion method, but this method requires a neighboring station of known absolute orientation. Other methods include ship noise analysis (Trabattoni et al., 2019), whale songs analysis or use of co-oriented sensors such as calibrated compass, gyrocompass, and north-finding sensors (Liu et al., 2014). All these methods have been successfully implemented to orient the horizontal channels of broadband OBSs (BBOBSs) with different levels of accuracy depending on the site and the OBS array, but most of them do not work for short period OBSs (SPOBSs). SPOBSs cannot use teleseismic waveforms because of their limited sensitivity to long period energy and retrieving surface waves from local seismicity is difficult because of the small source-receiver distance. As the accuracy of ship noise analysis depends on the number of well-located passing boats with a strong enough signal, it is difficult to use this technique in many marine settings.

Here we present and evaluate a technique to orient the horizontal channels of SPOBSs using P-wave polarization from local earthquakes, modified from the P-Pol algorithm of Scholz et al., (2016), which is itself based on previous P wave polarization techniques (Fontaine et al., 2009;

Schulte-Pelkum et al., 2001). This method uses principal component analysis of 3 component seismograms to determine the particle motion directions of first P wave arrival in 2D and 3D, and then determines the orientation angle by calculating the difference between real back-azimuths, calculated from the event and OBS positions, and measured back-azimuths based on the observed P wave polarity. We present here a modified version of this method which can use the local P-wave arrival from local seismicity recorded by SPOBSs. We tested the technique on 4 different types of SPOBSs and 1 type of BBOBSs deployed in various marine environments, and on one land geophone network. We show that the technique can provide reliable orientations in some cases, but in many cases the orientations are not reliable, apparently related to local structure beneath the station. We propose criteria to determine if orientations are reliable.

4.2 Dataset

We initially analyzed datasets from SPOBSs deployed on Lucky Strike volcano, Mid-Atlantic Ridge as part of the European Multidisciplinary Seafloor and water column Observatory (EMSO)-Azores, and off-shore Mayotte island in the Indian Ocean (Table 4.1, Figure 4.1). From the EMSO-Azores data, we used one year of data recorded between April 2015 - May 2016. The 5 OBSs here are INSU-IPGP SPOBSs and have three-component Mark Systems L-28 geophone sensors (single-sided connection) with a high-pass corner frequency of 4.5 Hz and a High Tech-90-U hydrophone. From the Mayotte dataset, we analyzed 19 SPOBSs from 3 deployments: 12 stations (MO*) used INSU-IPGP SPOBSs with the same specifications as the EMSO-Azores OBSs and the other 6 stations (IF*) used Sercel MicroOBS SPOBSs with OYO Geospace GS-11D geophones with a high-pass corner frequency of 4.5 Hz. We then expanded our study to publicly available datasets from Axial seamount (Juan de-Fuca Ridge), Trans-Atlantic Geotraverse (TAG) and Rainbow hydrothermal fields (Mid-Atlantic Ridge), using in total 4 different types of SPOBS deployed in 5 different marine settings (Table 4.1, Figure 4.1). At the Axial seamount summit region, a network of OBSs is installed within the southern half of the caldera as part of Ocean Observatories Initiative (OOI) cabled array network. Out of these OBSs we tested, 4 stations use Guralp CMG-6TF SPOBSs (1 Hz) and the other two use CMG-1T BBOBSs. The TAG network used 13 short period 4-component OBSs using Geospace Technologies GS-11D geophones (4.5 Hz) and one HTI-90-U Hydrophone. From the MARINER experiment conducted at the Rainbow hydrothermal field, we have analyzed data from 13 SPOBSs containing Sercel L-28 (4.5 Hz) geophones with differential connections. Finally, we used this method on data from one land

CHAPTER 4. ORIENTATION OF SPOBSs

geophone network: the Berkeley Geysers network (BG) deployed in the Northern California region. Their sensors have changed over time: we did P-Pol estimation for seven OYO GS-11D (4.5 Hz) sensors for consistency with the most common SPOBS corner frequencies.

The BG and OOI network stations were oriented *in situ* upon deployment, and we were able to obtain the orientation of some of the Mayotte stations using ship noise (by Richard Dreo, doctoral student, IPGP): we used these values to ground-truth our results.

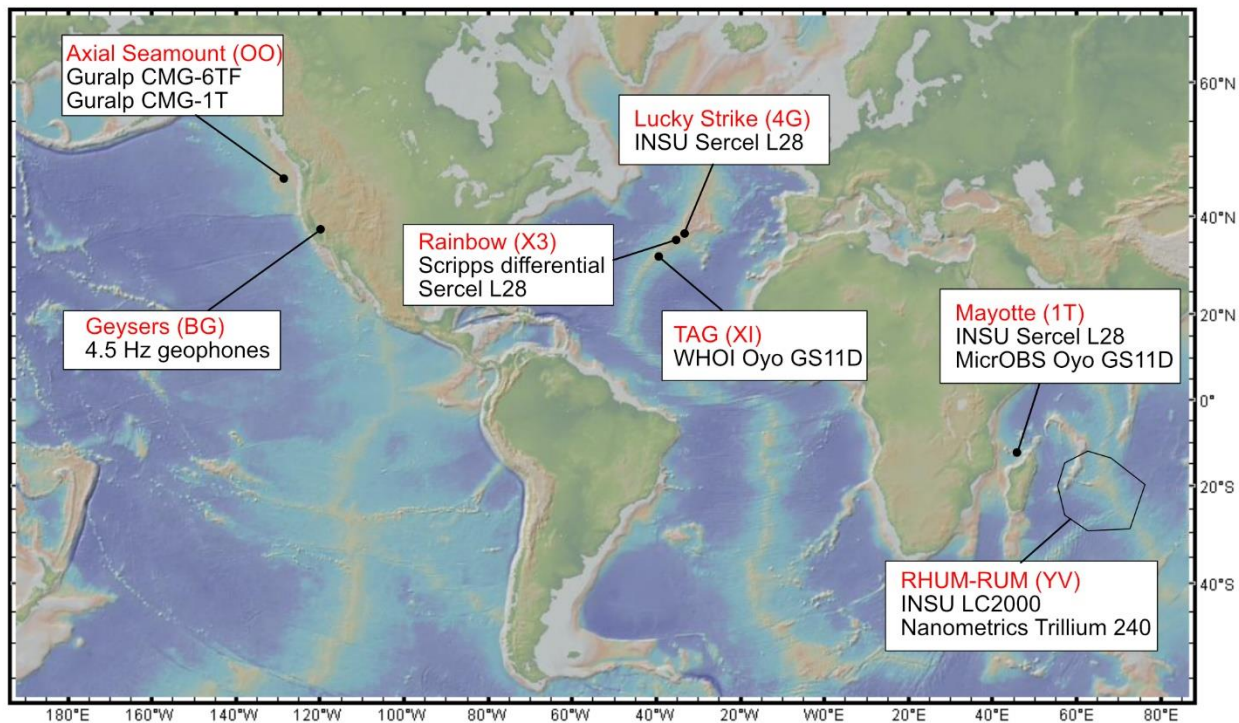


Figure 4.1. Overview map of the dataset and their instrument specification used in this study.

CHAPTER 4. ORIENTATION OF SPOBSs

Table 4.1. Instrument specifications for dataset used in this study.

Site (Network)	OBS type	No of OBSs	Type of instrument	Sensor specification	Sampling frequency (sps)	Cut-off frequency (Hz)	Time period
Lucky Strike (4G)	SPOBS	5	INSU	Sercel L-28 geophones, single sided connections	62.5	4.5	04/2015-05/2016
Mayotte (1T)	SPOBS	12	INSU	Sercel L-28 geophones, single sided connections	125	4.5	05/2019-09/2019, 10/2020-01/2021
		6	MicROBS	Oyo Geospace GS-11D geophones	250	4.5	05/2019-06/2019
TAG (XI)	SPOBS	13	WOODSHOLE	Oyo Geospace GS-11D geophones	100	4.5	06/2003-03/2004
Rainbow (X3)	SPOBS	13	SIO	Sercel L-28 geophones, differential connections	200	4.5	05/2013-01/2014
Axial Seamount (OO)	SPOBS	4	GURALP	CMG-6TF	200	1	2015 onwards
	BBOBS	2	GURALP	CMG-1T	40	360 s	2015 onwards
Geysers (BG)	Geophone	7		OYO GS - 11D 4.5 Hz sensors	500	4.5	2011-2020

4.3 Methodology

This method is based on particle motion analyses of the first P wave arrivals (P-Pol) implemented by Scholz et al., (2016). P waves are elliptically polarized waves in the direction of propagation in the absence of anisotropy and dipping discontinuities.

Non-orientated OBSs normally use “1” and “2” instead of “N” and “E” in to name their two horizontal channels. “1” and “2” have the same relative orientation as “N” and “E” (“1” is 90⁰ counterclockwise from “2” when viewed from above). For the vertical channel, geophones normally use ‘3’ instead of ‘Z’ as geophones commonly have inverse polarity (a positive signal corresponds to a downward motion). In this chapter we use ‘1’ (N*), ‘2’ (E*) for the non-orientated N and E channels respectively, and ‘3’ for the vertical channel with opposite polarity.

For each event recorded at the station, the orientation angle can be calculated as:

$$orient = (BAZ_{expected} - BAZ_{measured} + 360^0) \bmod 360^0 \quad (1)$$

Where *mod* is the modulo operator, $BAZ_{expected}$ is the clockwise angle at the station along the great circle path between the source and receiver, and the apparent back-azimuth ($BAZ_{measured}$) is the clockwise angle from the station’s ‘1’ (N*) component to the direction of maximum particle motion (Figure 4.2a). The apparent back-azimuth is calculated both in 3D by principal component analyses (PCA) of a 3D data covariance matrix comprised of the East, North and Vertical component of an event, and in 2D by PCA of a data covariance matrix of the horizontal components only. The apparent incidence angle is calculated from the PCA of the radial and vertical components.

Since short period OBSs are insensitive to teleseismic arrivals, we used the P wave arrivals of local events located within the seismic network. Use of local events presents two main issues: 1) The event location uncertainty is often significantly high compared to the event-station distance and thus $BAZ_{expected}$ has significant uncertainty; 2) Local seismicity is often clustered w.r.t the station position and it is therefore difficult to get an ideal distribution of $BAZ_{expected}$. Getting consistent results for a small range of back-azimuth angles is not a validation for the orientation of the horizontal components. We modified the method of Scholz et al., (2016) to account for the uncertainties in back-azimuth when calculating the component orientations. The back-azimuth

uncertainty (BAZ_{uncert}) is calculated as half of the horizontal angle between the event uncertainty ellipse (in 2D) or ellipsoid (in 3D) and the station position (Figure 4.2b). It can vary greatly between events depending on the event distance, event location error ellipse size and orientation (Figure S4.1).

The averaged station orientation is calculated by taking the circular mean of all the P-Pol measurements for that station. The circular mean error is calculated as defined in Scholz et al., (2016)

$$Error_Orient_{circmean} = 2 \sqrt{2(1 - R)}. 180^\circ / \pi \quad (2)$$

Where R is defined as

$$R = \frac{1}{N} \sqrt{\left(\sum_{i=1}^N \cos(orient_i)\right)^2 + \left(\sum_{i=1}^N \sin(orient_i)\right)^2} \quad (3)$$

The accuracy of the measurement is controlled by the degree of rectilinearity ($CpZ = 1 - \beta_2/\beta_1$ and $CpH = 1 - \epsilon_2/\epsilon_1$). CpH and CpZ are equal to 1 for pure linear polarization and 0 for circular polarization. β_i and ϵ_i are the eigenvalues of 2D PCA of radial and vertical components, and 2D PCA of horizontal components respectively and respect $\beta_1 > \beta_2$ and $\epsilon_1 > \epsilon_2$.

For each P-Pol measurement, the data was preprocessed in ObsPy module. After instrument correction, mean and trend were removed and a Hanning taper was applied. For local events, the time window length to isolate clean first P wave arrival was set to 0.3 sec, which were filtered in two different frequency bands (5 - 10 Hz, 7 - 10 Hz) to check the frequency dependency of the results. P-Pol calculation was done only for those events which had $BAZ_{uncert} \leq 30^\circ$. For teleseismic events, we set the time window length was 25 sec and the frequency band to 0.07 - 0.10 Hz, as in Scholz et al., (2016). Individual P-Pol results were retained only if the following criteria were met: SNR (Signal to Noise ratio) ≥ 10 , CpH and $CpZ \geq 0.9$.

Figure 4.2c, d shows an example of individual P-pol measurement of a local event ($M_1 = 2.7$) from the OOI dataset recorded in a SPOBS (AXAS1) at Axial Seamount. The event-station $BAZ_{expected}$ is 25.2° based on the event catalog. The data was filtered in the 7 - 10 Hz frequency band and then $BAZ_{measured_3D}$ and $BAZ_{measured_2D}$ were calculated to be $187.2^\circ \pm 1.7^\circ$ and $185.9^\circ \pm 12.6^\circ$ from the 3D and 2D PCAs respectively (Figure 4.2d). Following equation 1, the orientation

angle of the ‘1’ (North) component of the SPOBS is $198^{\circ} \pm 1.7^{\circ}$ (From 3D measurement) and $199.3^{\circ} \pm 12.6^{\circ}$ (From 2D measurement) with respect to the geographic North, calculated from this single event.

We verified our algorithm by calculating the orientation of BBOBSs using teleseisms from the RHUM-RUM experiment which duplicates the results from Scholz et al., (2016) (Figure S4.2).

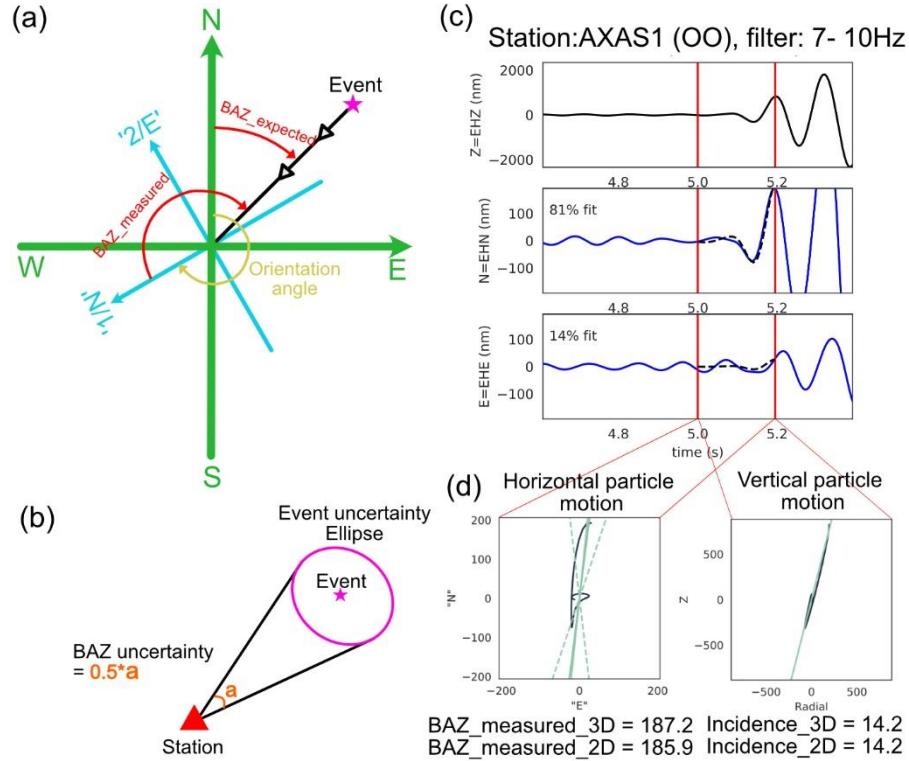


Figure 4.2. (a) Principle of P-Pol method. Green arrows: Geographic N-S & E-W, Blue arrows: ‘1’ (North) and ‘2’ (East) orientation of a sensor, Black vector: Event direction. (b) Schematic representation of calculation of BAZ uncertainty from event uncertainty ellipse. (c) P-Pol measurement of a local event recorded at AXAS1(OO): 3 channel waveforms with redlines marking P-Pol time window. (d) Horizontal and vertical particle motion for the same event.

4.4 Results

We determined orientation using the P-Pol technique using local seismic events for the 6 aforementioned networks. For the Axial Seamount OBSs, which have lower corner frequencies, we also determined orientation using teleseismic events. Overall, we obtained two categories of results from the local P-Pol calculation: 1) The $BAZ_{measured}$ varied linearly with $BAZ_{expected}$ with a slope = 1 (Figure 4.3a-1), giving the same orientation angle for significantly different $BAZ_{expected}$ (Figure 4.3a-2), as we had expected. 2) The $BAZ_{measured}$ was approximately constant for different values of $BAZ_{expected}$, (Figure 4.3b-1) which gave linearly increasing

orientation angle w.r.t the $BAZ_{expected}$. In the second case, the orientation angle is unidentifiable using local P-Pol (Figure 4.3b-2). Below we summarize results from each geological setting.

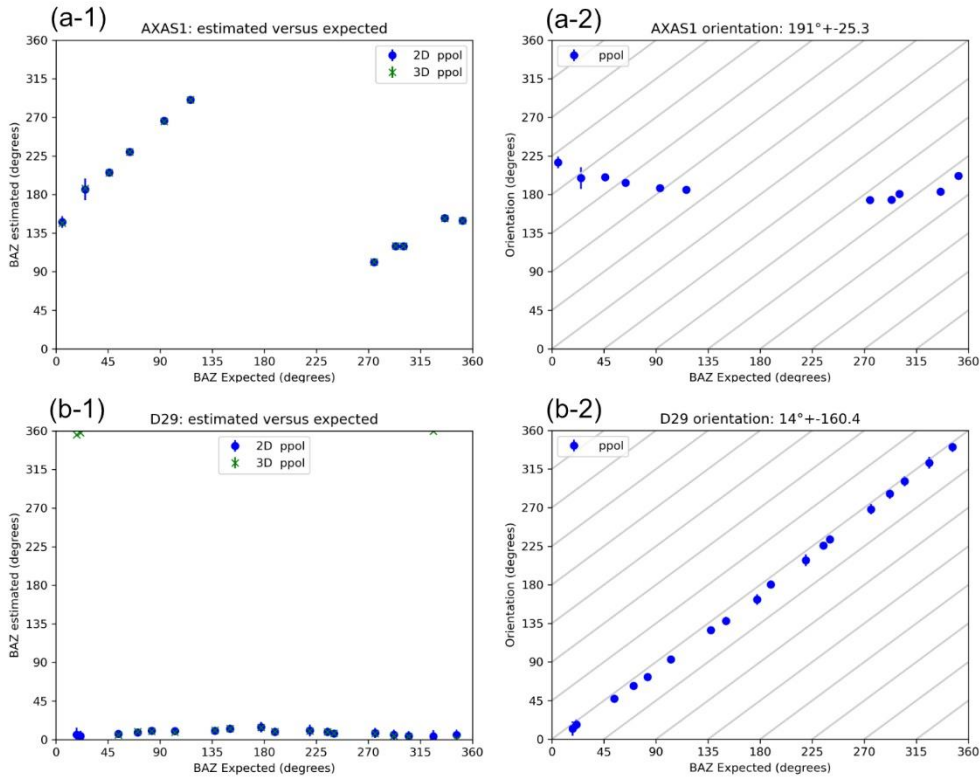


Figure 4.3. Categories of results obtained from local P-Pol measurement. (a-1) Linearly increasing $BAZ_{measured}$ with increase in $BAZ_{expected}$, and thus giving (a-2) a constant orientation angle with $BAZ_{expected}$. (b-1) Constant $BAZ_{measured}$ with increase in $BAZ_{expected}$, and thus giving (b-2) a linearly increasing orientation angle with $BAZ_{expected}$.

4.4.1 Lucky strike volcano

At the Lucky Strike volcano in the Mid-Atlantic Ridge, 5 SPOBSs were deployed surrounding the volcano region (Figure S4.3a) and most of the local seismicity occurs within the summit zone. As a result, the $BAZ_{expected}$ range for each SPOBS was limited. For all SPOBSs, we got a nearly constant $BAZ_{measured}$ irrespective of the $BAZ_{expected}$ values, and thus a linearly dependent or unidentifiable orientation angle for the horizontal components (Figure S4.3b-1 to b-5).

4.4.2 Offshore Mayotte

The seismicity is also clustered offshore Mayotte and it was therefore difficult to get an ideal distribution of back-azimuths for P-Pol calculation for all SPOBSs (Figure 4.4a). Out of 12

INSU SPOBSs (MO*) from two deployments, we got good orientation results (constant orientation estimate) for 7 SPOBSs with a limited $BAZ_{expected}$ coverage (Figure 4.4b-1 to 4.4b-7). Out of these 7, orientation results for 5 INSU SPOBSs (MO*H) from one deployment agrees well with the orientation obtained from ship noise analysis (By Richard Dreo, doctoral student, IPGP; Table 4.2). Rest 4 SPOBSs gave a linearly dependent orientation estimate (Figure S4.4a-1 to a-4), and for one SPOBS (MOCA) which was deployed at the center of the seismic zone, the events were noisy to get a good P-Pol measurement.

Out of 6 MicroOBS SPOBSs (IF*), 5 showed linearly dependent orientation estimate w.r.t the $BAZ_{expected}$ (Figure S4.4a-5 to a-9) and the last one (IF1A), deployed at the same position as MOCA, was non-orientable due to low SNR.

Table 4.2. Orientation results for Mayotte OBSs

OBS Name	OBS Type	Orientation from local P-Pol ('N')	Orientation from ship noise ('N')
MOAH	SPOBS	$284^0 \pm 25^0$	303^0
MOBH	SPOBS	$68^0 \pm 116^0$	150^0
MODH	SPOBS	$109^0 \pm 23^0$	106^0
MONH	SPOBS	$67^0 \pm 120^0$	66^0
MOSH	SPOBS	$14^0 \pm 28^0$	31^0

4.4.3 TAG hydrothermal field

At TAG hydrothermal field, 13 SPOBSs were deployed surrounding the active hydrothermal mound in 3 successive circular rings (Figure S4.5a) and most of the earthquakes occurred on the hanging wall of a detachment fault (deMartin et al., 2007). We calculated the P-Pol calculation for 6 of the SPOBSs (for the remaining 7, there was either no data or too noisy data on one or more components). We got good $BAZ_{expected}$ coverage for all 6 stations, however all of them showed linearly dependent orientation estimates (Figure S4.5b-1 to b-6).

4.4.4 Rainbow hydrothermal field

At Rainbow hydrothermal field, 13 SPOBSs were deployed in 3 successive circular rings, similar to TAG (Figure 4.5a) (Horning et al., 2018). We got a good estimation of orientation angle for only one SPOBS (OBS47) (Figure 4.5b-1). OBS54 gave good orientation result for estimated back-azimuths between 225° and 330° , but the orientation angle linearly increased at other back-azimuths (Figure 4.5b-2). 8 other SPOBSs gave linearly dependent orientation estimate (Figure S4.6), while for the remaining 3 one of the component's data was missing/noisy.

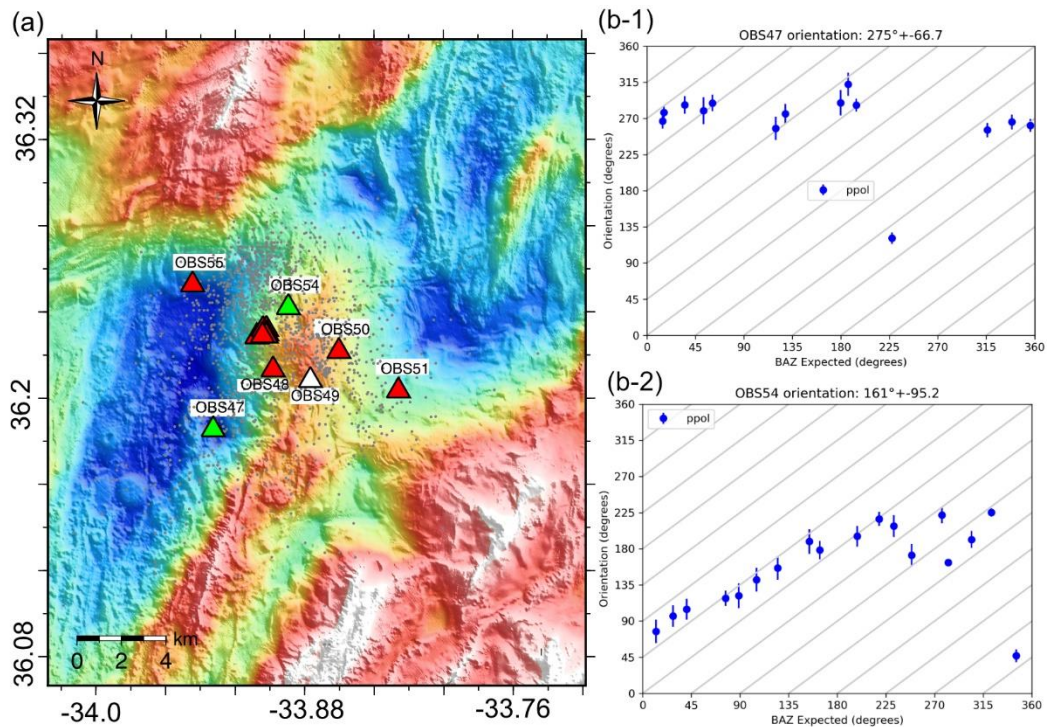


Figure 4.5. P-Pol result for Rainbow hydrothermal field. (a) Event station map. Green triangles: Stations with good orientation result. Red triangles: Stations with bad orientation result, white triangles: No orientation. Gray dots: events used. (b-1 & b-2) Individual good P-Pol result (Green stations only).

4.4.5 Axial Seamount

The 4 SPOBSs and 2 BBOBSs at the Axial seamount were deployed with remotely operated vehicles and therefore their orientations were previously known (Figure 4.6a, Table 4.3). We initially estimated the orientation of all 6 OBSs using local events. The orientation of the horizontal sensors for both the BBOBSs was well recovered using the P-Pol technique with local events (Figure 4.6b-1 & b-2). Out of 4 SPOBSs, 2 (AXAS1, AXEC1) had good estimated orientation angles, but 180° opposite the metadata value. The remaining 2 SPOBSs (AXAS2,

CHAPTER 4. ORIENTATION OF SPOBSs

AXEC3) showed very scattered results (Figure 4.7a-1 to a-4). Since these SPOBSs had lower frequency cut-offs (1 Hz), we were able to use teleseismic events to estimate their orientation as well. Using teleseismic events, we got good orientation estimation for all 4 SPOBSs (Figure 4.7b-1 to b-4) and 2 BBOBSs (Figure 4.6c-1 & c-2), but again 180° deviated for all SPOBSs from metadata orientation (Table 4.3). There is a 180° ambiguity in P-pol measurements on horizontal sensors, which is resolved using the vertical motions, so a wrong polarity on the vertical sensor would give a 180° error on the $BAZ_{measured}$. We checked P-arrival polarities for all BBOBSs and SPOBSs using a teleseismic event (27.838N, 140.493E) in the teleseismic P-pol frequency range, but both BBOBSs and SPOBSs appear to have same first P wave polarity (Figure S4.7). We think that the SPOBSs might have deployed pointing ‘South’ or there might have been some error with the orientation geometry of the SPOBSs which was not considered in the metadata.

Table 4.3. Orientation results for Axial seamount OBSs

OBS Name	OBS Type	Metadata Orientation (‘N’)	Orientation from local P-Pol (‘N’)	Orientation from teleseismic P-Pol (‘N’)
AXAS1	SPOBS	0^0	$191^0 \pm 25^0$	$182^0 \pm 16^0$
AXAS2	SPOBS	0^0	$73^0 \pm 117^0$	$185^0 \pm 24^0$
AXEC1	SPOBS	128^0	$309^0 \pm 64^0$	$309^0 \pm 22^0$
AXEC3	SPOBS	35^0	$220^0 \pm 120^0$	$214^0 \pm 26^0$
AXEC2	BBOBS	0^0	$357^0 \pm 43^0$	$3^0 \pm 6^0$
AXCC1	BBOBS	0^0	$360^0 \pm 21^0$	$357^0 \pm 8^0$

CHAPTER 4. ORIENTATION OF SPOBSs

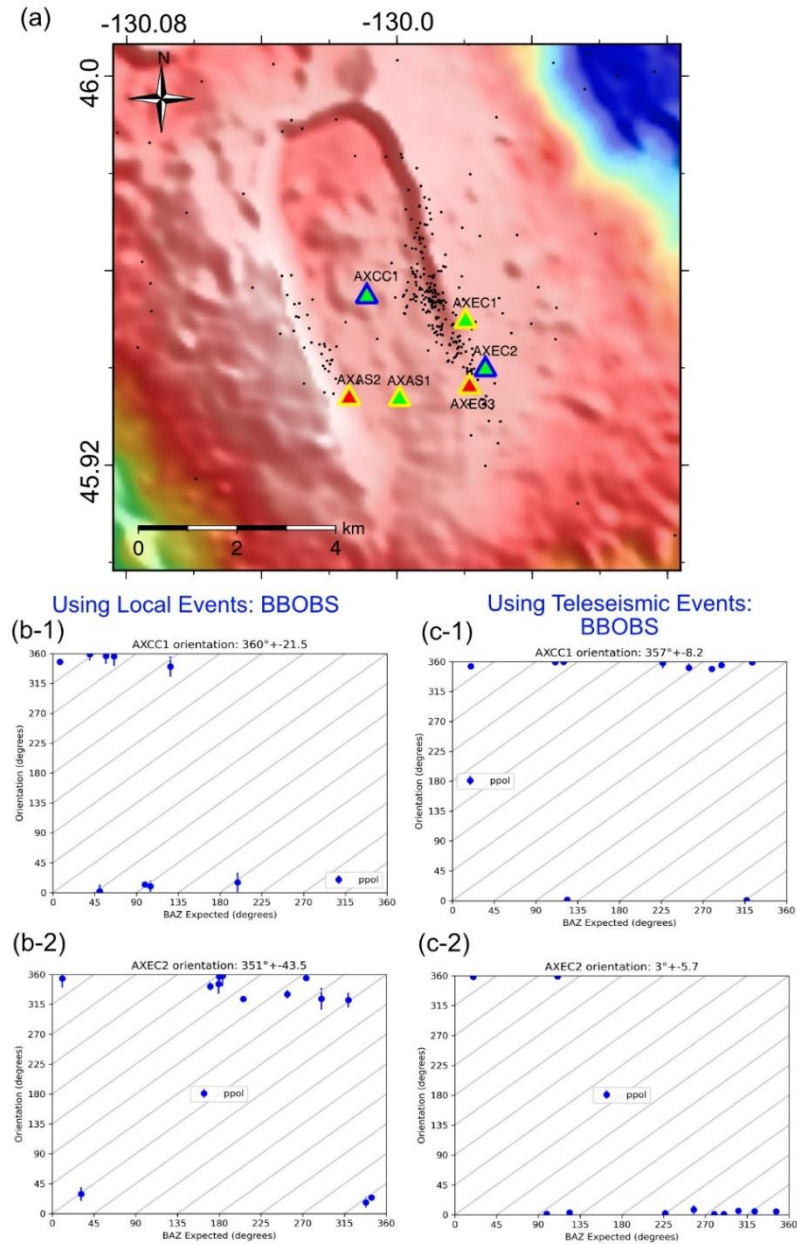


Figure 4.6. P-Pol result for Axial Seamount. (a) Event station map. Blue outlined triangles: BBOBSs, Yellow outlined triangles: SPOBSs. Green filled triangles: Stations with good orientation result. Red filled triangles: Stations with bad orientation result. Black dots: events used. (b-1 & b-2) Individual P-Pol result for BBOBSs using local events. (c-1 & c-2) Individual P-Pol result for BBOBSs using teleseismic events.

CHAPTER 4. ORIENTATION OF SPOBSs

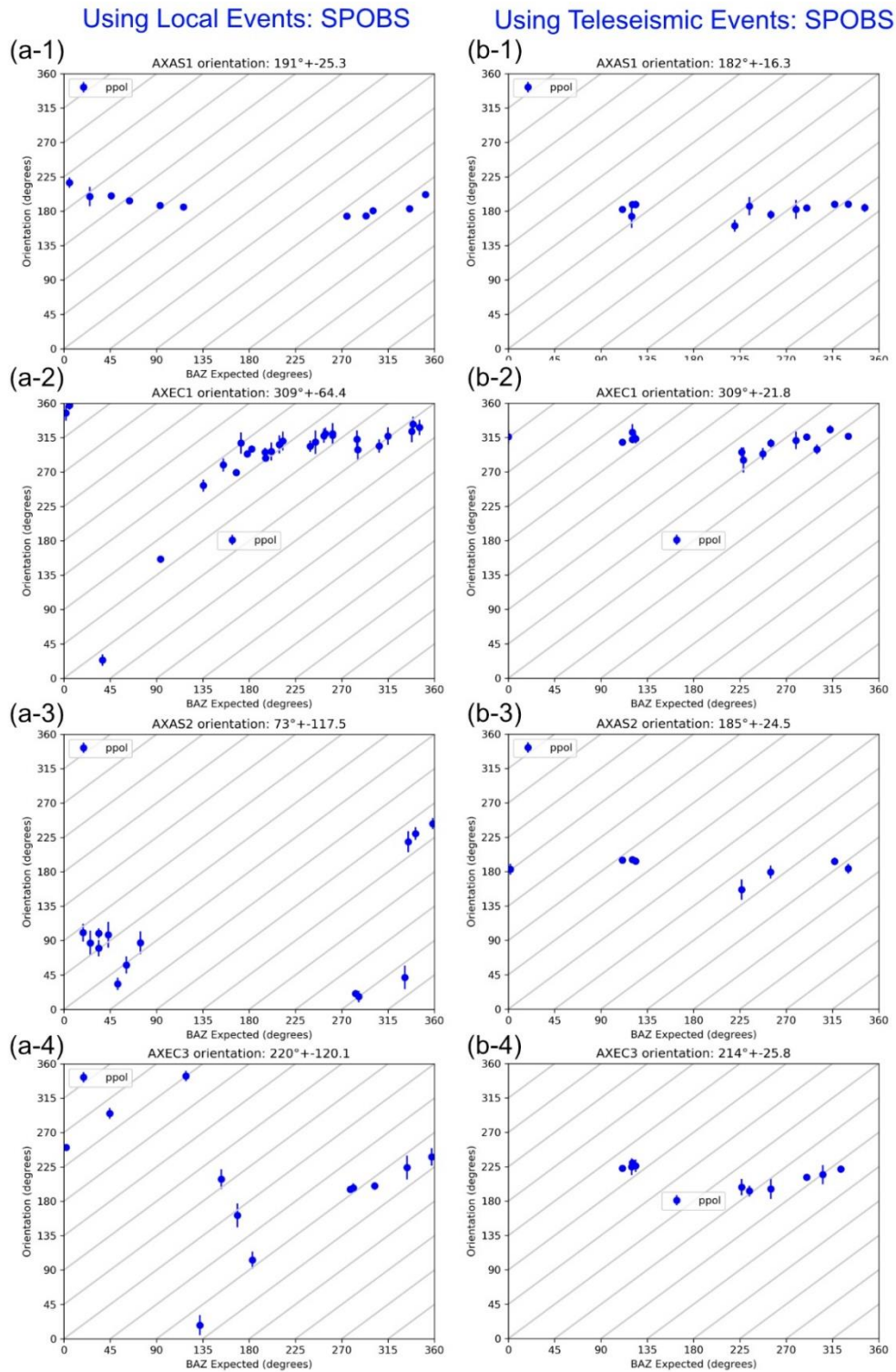


Figure 4.7. P-Pol result for Axial Seamount SPOBSs. (a-1 to a-4) Individual P-Pol result using local events. (b-1 to b-4) Individual P-Pol result using teleseismic events.

4.4.6 Geysers land network

We applied the P-Pol technique to short-period land stations from the Berkeley Geysers network. Of 7 sensors we tested, we obtained consistent orientation angles for 5 stations (Figure 4.8b-1 to b-5) but linearly dependent orientation estimate for the other rest 2 stations (Figure S4.8).

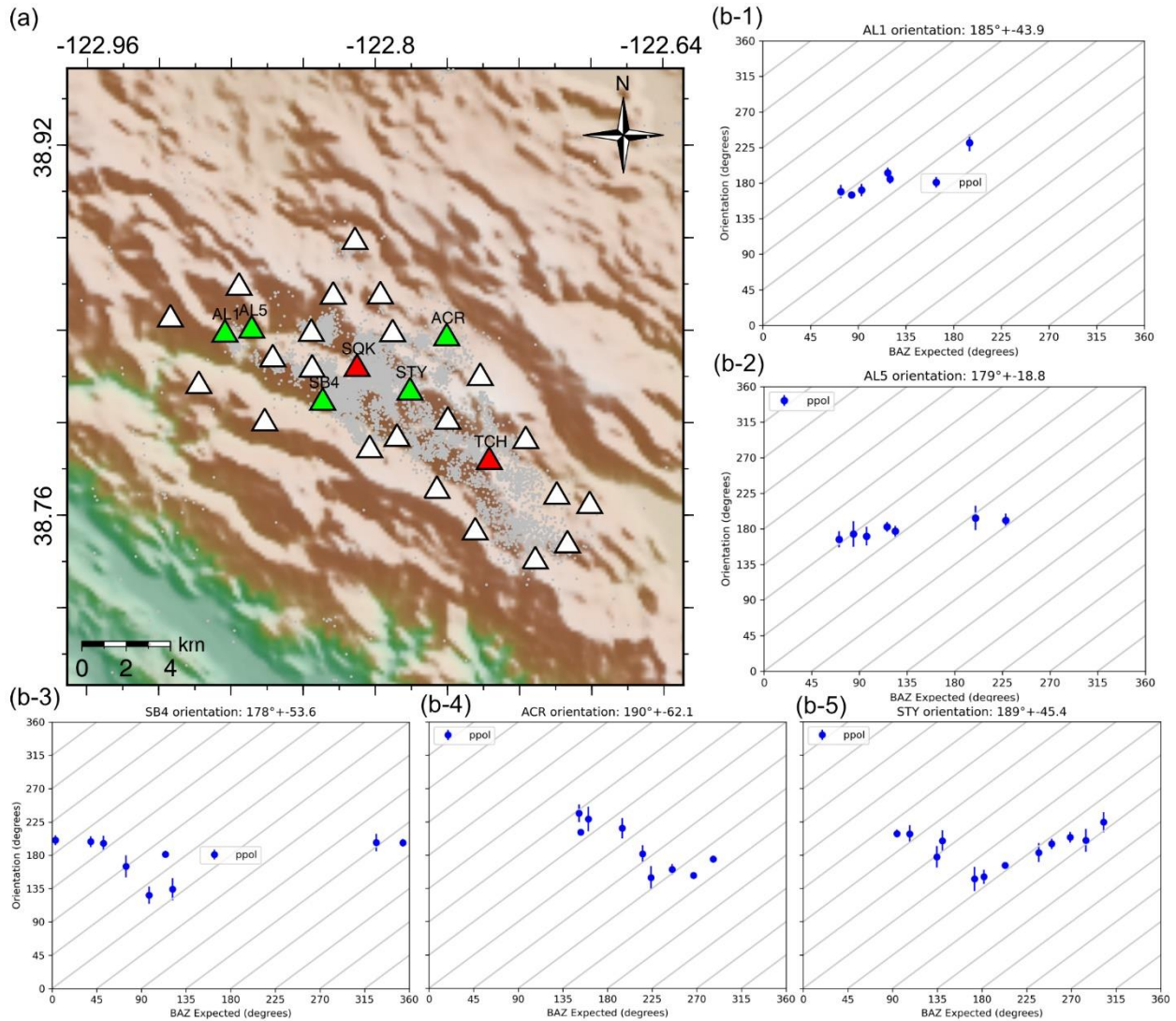


Figure 4.8. P-Pol result from Geysers network. (a) Event station map. Green triangles: Stations with good orientation result. Red triangles: Stations with bad orientation result, white triangles: No orientation measured. Gray dots: events used. (b-1 to b-5) Individual good P-Pol result (Green stations only).

4.5 Discussion

We calculated orientations using P-pol versus expected BAZ of local earthquakes for a total of 48 short-period and 2 broad-band stations including 7 land stations, for which we obtained reliable orientation angles for 11 SPOBSs, 5 land short-period geophones and 2 BBOBSs. 16 of these stations (9 SPOBSs, 5 land short-period geophones and 2 BBOBSs) had known orientations, all of which agreed with the P-pol results. For rest of the SPOBSs, the technique indicated a constant $BAZ_{measured}$, corresponding to a linear increase in estimated orientation angle with increase in $BAZ_{expected}$.

The constant $BAZ_{measured}$ obtained for most SPOBS stations could be due to instrument bias, event bias or because of near subsurface structures. The INSU OBSs tie all geophone negative pins to ground, which could allow crosstalk between sensor channels, but SIO SPOBSs which have differential connections, have the same problem. There could also be instrument structural bias such as preferential sway in instrument and/or sensor gimbals giving constant back-azimuths. But it seems highly unlikely to have the same bias in all 4 types of SPOBSs we tested, and even if there was a physical bias, we would expect to see a 180° flip in estimated orientation over the 360° range of event back-azimuths. We also rule out event location bias because event locations in most of the networks we used are well-constrained, with more than 5 stations. It is important to note that the P-pol method worked for teleseismic events on all OBSs in the Axial Seamount network, whereas it produced the constant $BAZ_{measured}$ for two of these same stations using local events. We discuss below the possible effect of subsurface structures in getting constant back-azimuths from P wave polarization.

4.5.1 Effect of surface structures

Many of the networks we studied are in volcanic regions with many reflectors and near-surface reflectors, which may bias the arrival direction. At Mayotte, the 7 SPOBSs with good estimation (green diamonds, Figure 4.4) were deployed away from the main volcanic ridge. At the Rainbow hydrothermal field, the SPOBS (OBS47) with good orientation estimation was in a deeper region, farther from the active hydrothermal venting area (Figure 4.5). OBS54 from the same region also showed good estimation of orientation for $BAZ_{measured}$ from $225\text{-}330^\circ$, which traveled through comparatively thick sediments. At Axial Seamount, the best local seismicity-

based orientation result was obtained for the SPOBS (AXAS1) in the middle of the caldera, whereas the SPOBSs located near the caldera walls AXAS2 and AXEC3 have inconsistent orientation using local events (Figure 4.6a, 4.7). Even on the land-based Geysers network, the inconsistent-orienting geophones seem to align along an NW-SE axis in the middle of the network, while the geophones present in the outer line of the network have good orientation estimates (Figure 4.8). These observations in different settings suggest that subsurface structure affects the P-wave arrival first arrival direction, giving near-constant estimated back-azimuths. On the other hand, some of the SPOBSs, like MONE from Mayotte and OBS56 from Rainbow were situated in thick sediment regions, yet gave inconsistent orientations. So, there could also be some instrumental bias as well as near subsurface structures.

4.6 Conclusion

1. We evaluated the P-wave polarization method to get the orientation of SPOBSs using local earthquakes. In most of the cases, P-wave arrivals on SPOBSs give a constant back-azimuths, regardless of the true direction to the event. This phenomenon persists on all 4 types of SPOBSs deployed in different marine settings as well as on some land geophones.
2. Since P-Pol method gives a constant back-azimuth using local events, orientation angle should be obtained for a wide array of events, and constant orientation angles obtained from a short range of back-azimuth events should not be validated.
3. We hypothesize that the phenomenon of constant back-azimuth may be due to local subsurface structures which could be affecting the P-wave arrival direction. Further work (e.g., forward modelling) is needed to give a conclusive opinion.
4. A station exhibiting this phenomenon may be unusable for any kind of analysis which relies on the 3D wave field but could provide useful information about near-subsurface structures.

Data acknowledgement

Station inventory files and earthquake waveforms for Axial Seamount, TAG and Rainbow were obtained from FDSN with network codes OO, XI and X3 respectively. Local seismicity catalog for Axial Seamount was taken from <http://axial.ocean.washington.edu/> (Wilcock et al., 2016) and

the broadband catalog was downloaded from USGS. TAG seismicity catalog was obtained from Robert Sohn, WHOI. Rainbow seismicity catalog was obtained from <https://www.marine-geo.org/index.php> (Sohn et al., 2020). Waveform data, catalog, and station inventory for Geysers network were accessed through the Northern California Earthquake Data Center (NCEDC), doi:10.7932/NCEDC. The Mayotte and Lucky Strike data is in the French RESIF data center <https://seismology.resif.fr/>.

Supplementary Figures

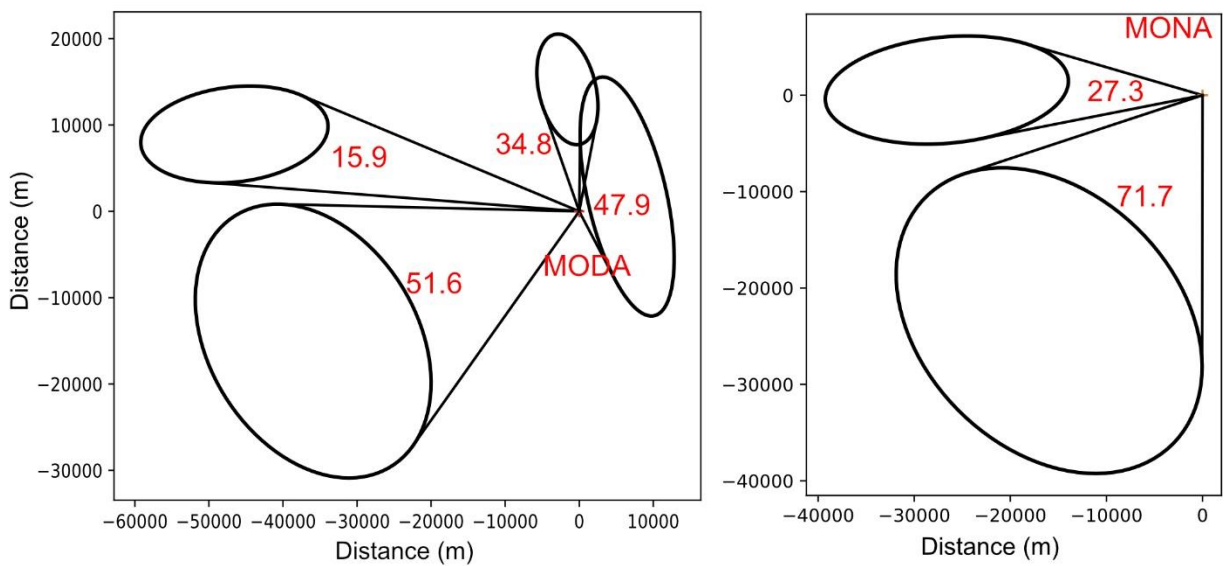


Figure S4.1. Examples of BAZ uncertainty calculations based on location uncertainty ellipses for 2 Mayotte SPOBSs.

CHAPTER 4. ORIENTATION OF SPOBSs

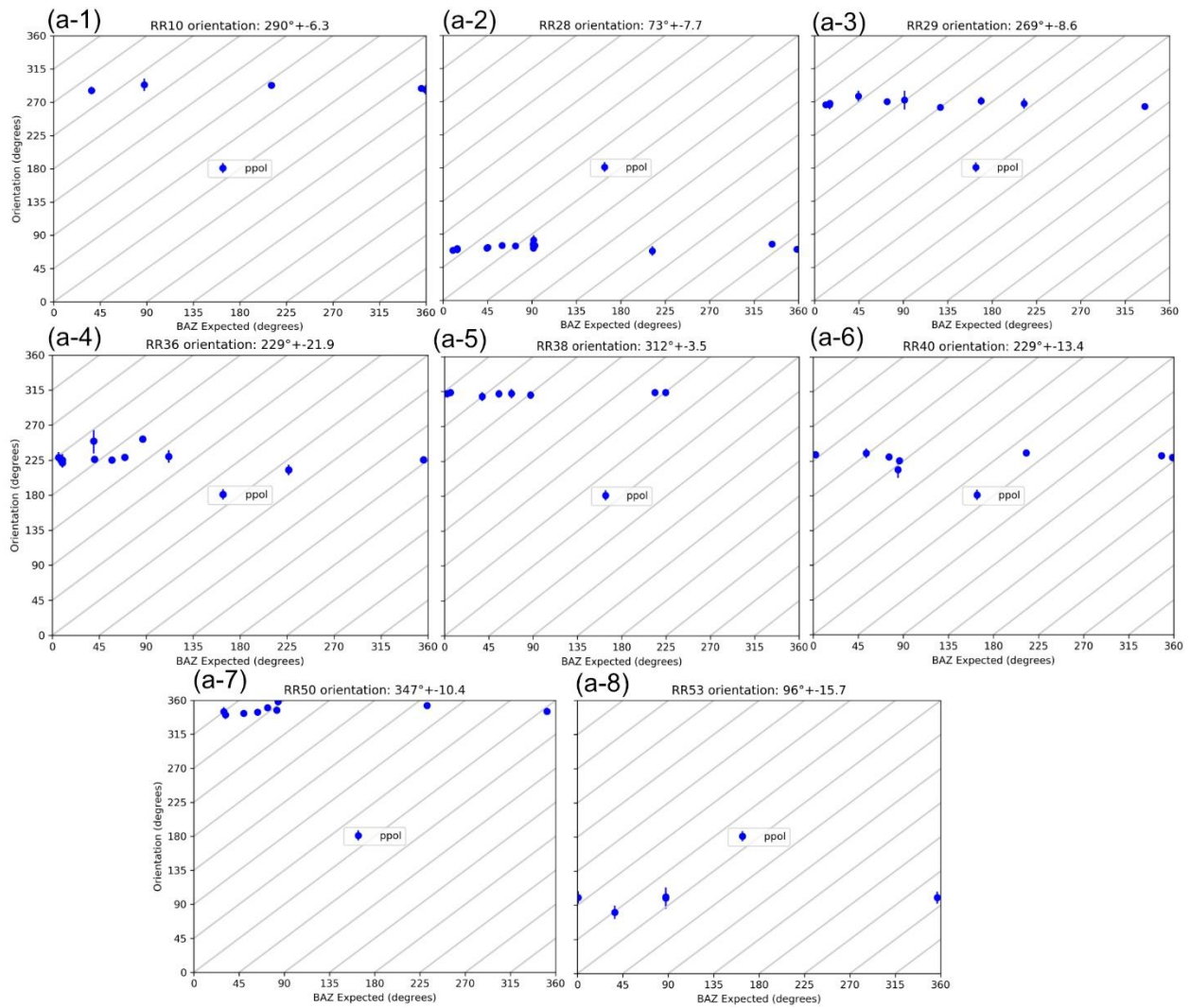


Figure S4.2. (a-1 to a-8) Individual P-Pol result from RHUM-RUM experiment using teleseisms.

CHAPTER 4. ORIENTATION OF SPOBSs

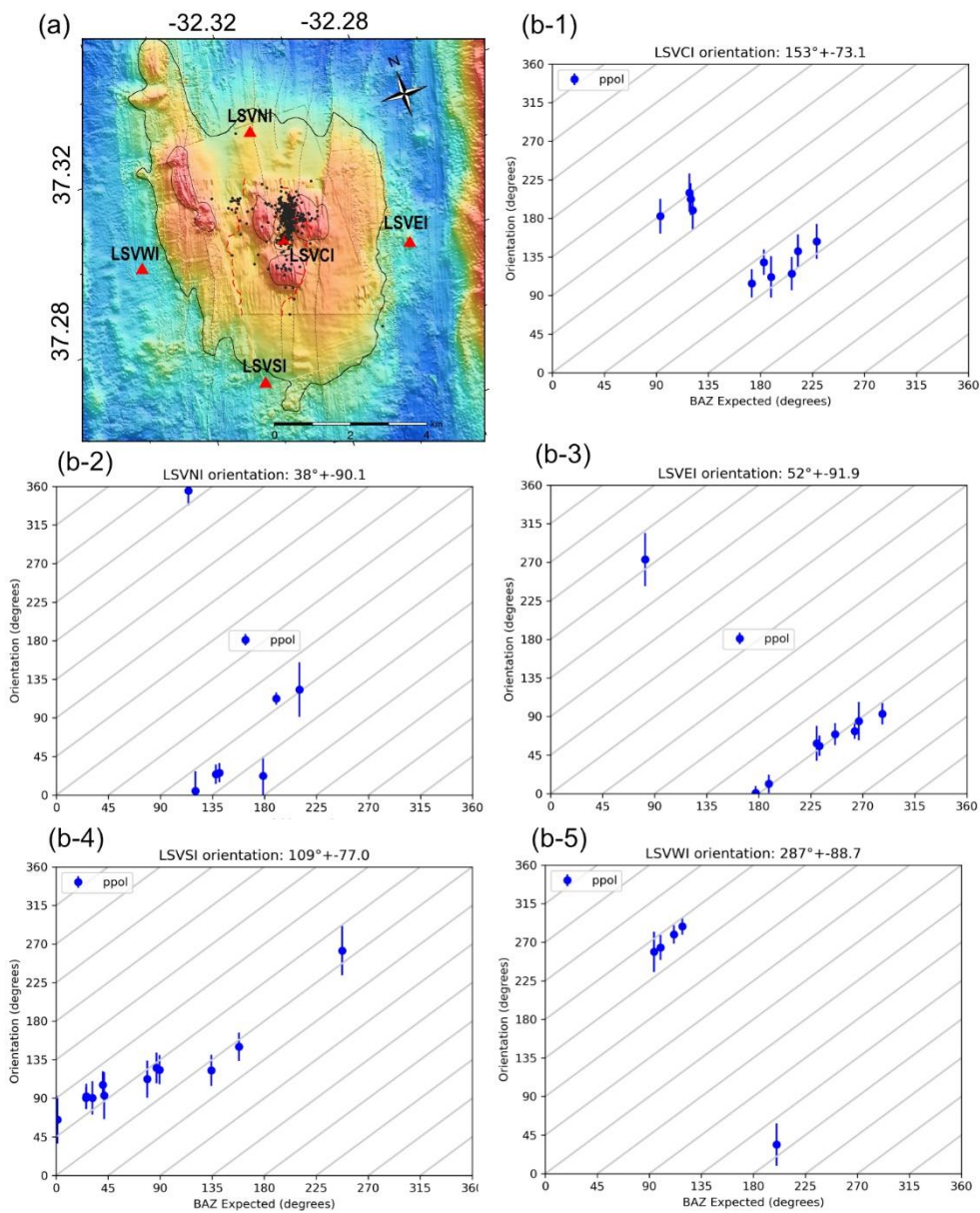


Figure S4.3. P-Pol result from Lucky Strike volcano. (a) Event station map. Red triangles: Stations with bad orientation result, Black dots: events used. (b-1 to b-5) Individual P-Pol result showing linearly increasing behavior.

CHAPTER 4. ORIENTATION OF SPOBSs

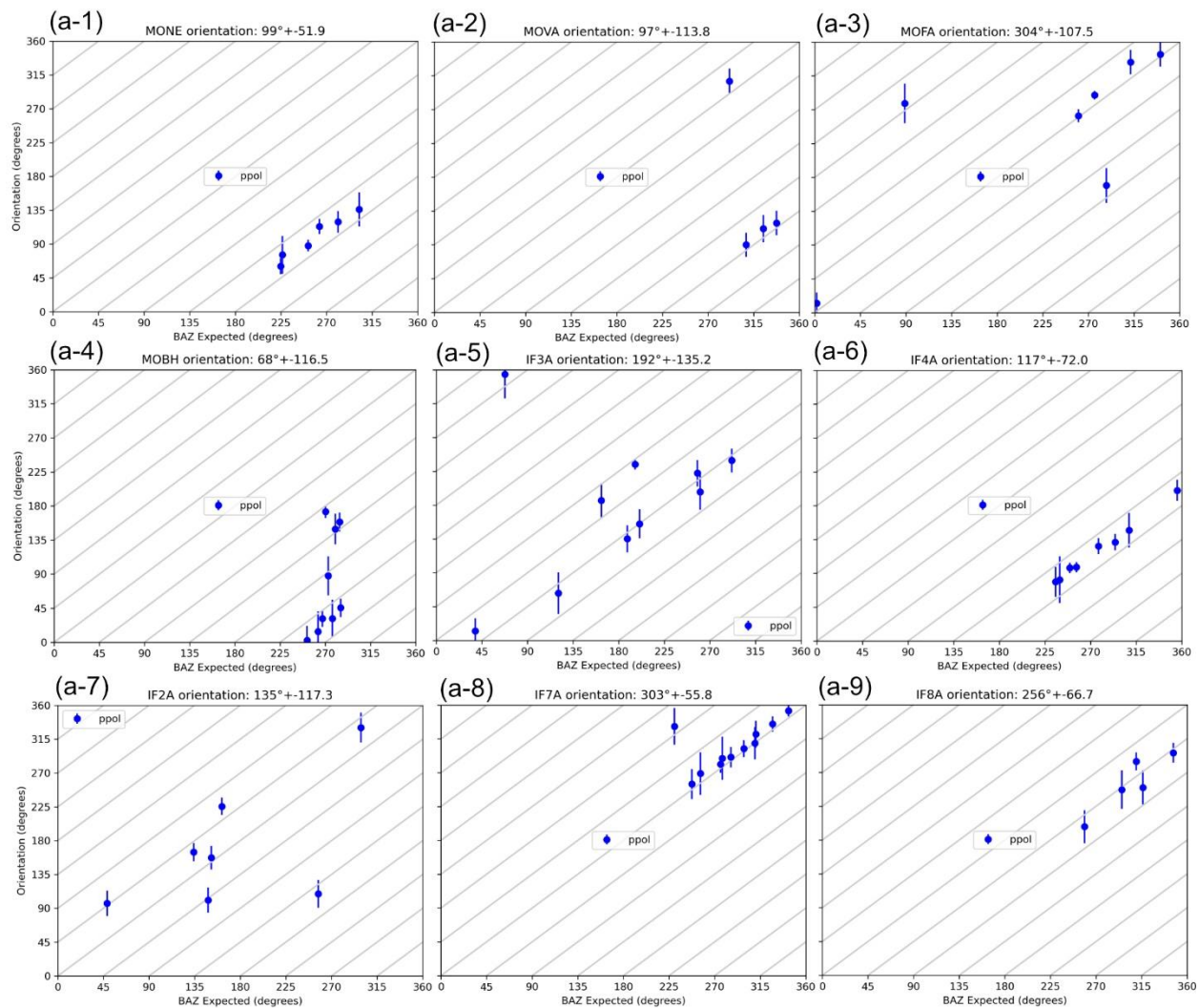


Figure S4.4. (a-1 to a-9) Individual P-Pol result from Mayotte stations (Red triangles in Figure 4a) showing linearly increasing behavior.

CHAPTER 4. ORIENTATION OF SPOBSs

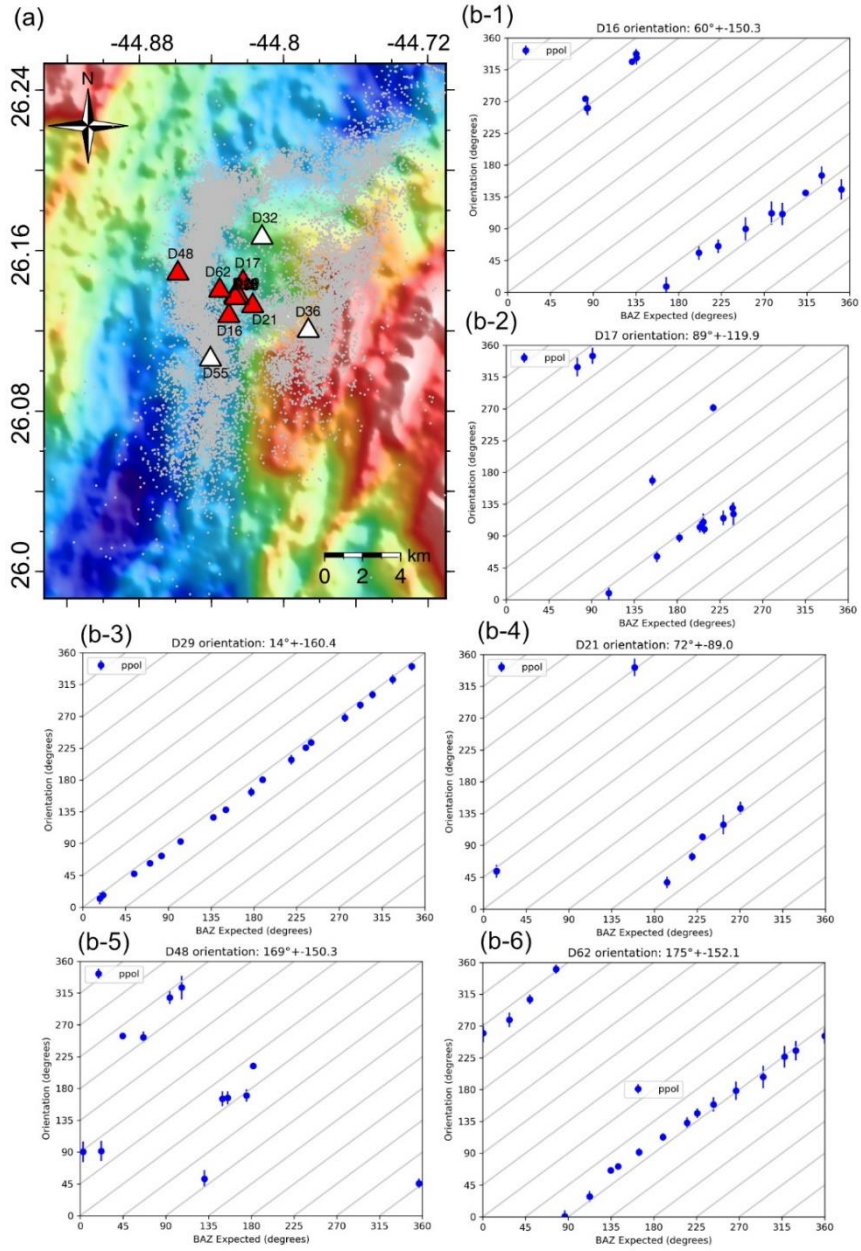


Figure S4.5. P-Pol result from TAG. (a) Event station map. Red triangles: Stations with bad orientation result, White triangles: No orientation, Gray dots: total events used. (b-1 to b-6) Individual P-Pol result showing linearly increasing behavior.

CHAPTER 4. ORIENTATION OF SPOBSs

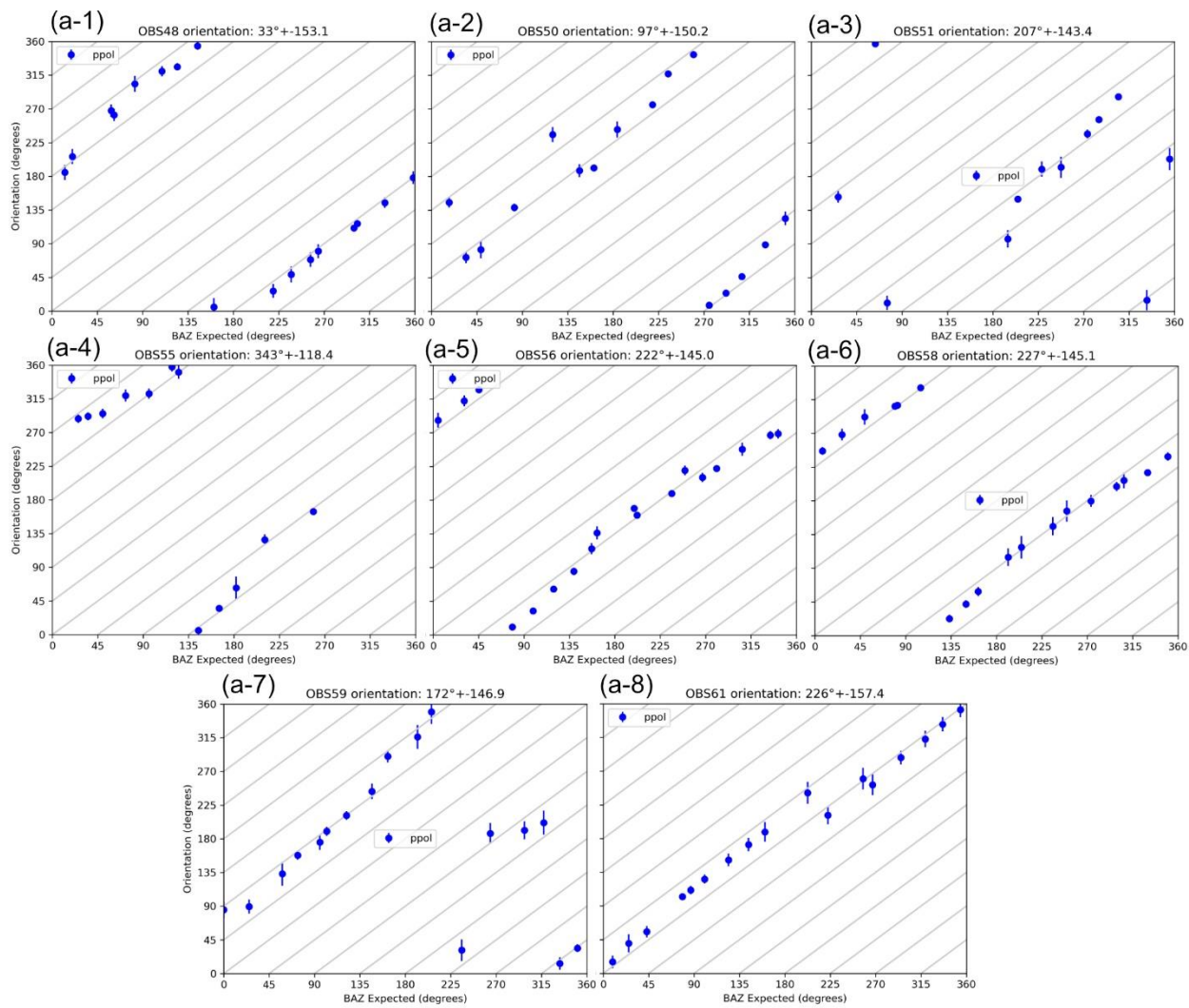


Figure S4.6. (a-1 to a-9) Individual P-Pol result from Rainbow hydrothermal field (Red triangles in Figure 5a) showing linearly increasing behavior

CHAPTER 4. ORIENTATION OF SPOBSs

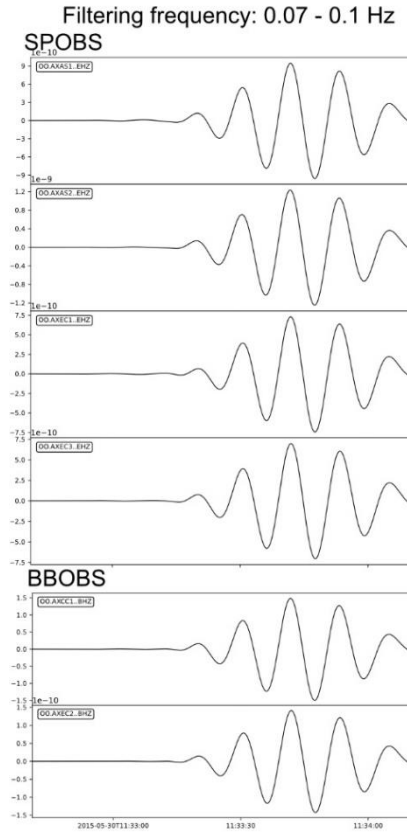


Figure S4.7. Polarity of first P wave arrival of a teleseismic event in SPOBSs and BBOBSs (OO network) in teleseismic P-Pol frequency range (0.07 – 0.1 Hz).

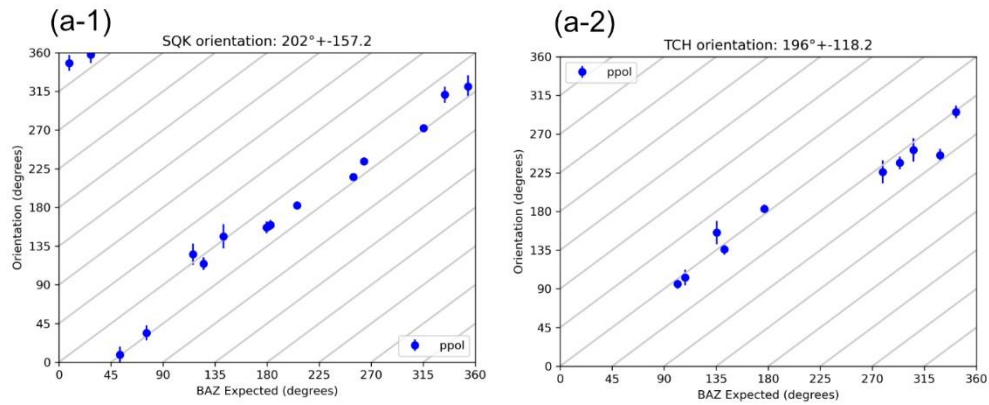


Figure S4.8. (a-1 to a-2) Individual P-Pol result from Geysers (Red triangles in Figure 8a) showing linearly increasing behavior.

Chapter 5

General conclusions and future perspectives

5.1 Conclusions

In this thesis, I have studied the spatiotemporal characteristics of microseismicity beneath the Lucky Strike volcano and hydrothermal field, Mid-Atlantic Ridge (MAR) to understand the hydrothermal circulation and magmato-tectonic interactions in a magmatically robust slow spreading segment center.

In our 12-year seismicity record by the Ocean bottom Seismometer (OBS) network from 2007 to 2019, we observed persistent microseismicity located in a narrow along-axis bin north to northwest of the hydrothermal field and mostly 0-2 km above the Axial Magma Chamber (AMC) reflector, with local magnitudes (M_L) between -1 and 0. The events showed mixed focal mechanisms with normal, thrust and strike/slip faulting patterns and their positions change over the 12 years of the seismicity record.

Over the 12 years of our experiment, there were at least two shifts of the main seismicity cluster. The first shift (occurred in July 2011) was ~600 m, and the vertical distribution of the seismicity remained the same during and after this shift. This shift could possibly be an artefact, achieved by a fortuitous combination of network-based biases, picking errors and/or change in shallow crustal velocity structure. If real, this shift could have been caused by small tectonic events creating local permeable pathways. The second shift, ~800 m eastward, to the eastern edge of the AMC reflector, occurred in a catalog gap between June 2013 and April 2015. The shift is too large to be explained by any combination of the above network-based biases. Furthermore, the vertical seismicity distribution changed from a relatively flat patch above the AMC to a vertical pipe-shaped pattern. This shift is most likely driven by recent melt injections in the eastern edge of the AMC.

We observed one intense and longer higher seismic period in April-June 2009. The April-June 2009 period lasted ~13 weeks (seismicity rate > 50 events/ week during the peak time) and started with a higher magnitude event ($M_L = 1.7$) and culminated in June after another higher magnitude ($M_L = 1.8$) event. We propose that both of the higher magnitude events were tectonic in origin and led to opening of local permeability channels for downgoing hydrothermal fluids,

CONCLUSIONS & PERSPECTIVES

resulting in vigorous hydrothermal heat extraction and higher seismicity. We also observed 5 shorter higher seismicity periods (~7-10 days each, seismicity rate 20-30 events/week) occurred during two time intervals: August-September 2015, and April-May 2016. The events in these periods formed a pipe-like pattern between 1 km below the AMC reflector and close to the seafloor, as did the events in the whole 2015-2019 period. In August-September 2015, we also observed two groups of upward migration sequences, but the intensity and magnitude of their events were much smaller than any other dike injection phenomena reported in other mid-ocean ridge settings. There is no conclusive evidence that a significant dike injection event occurred during the June 2013 and April 2015 seismological data gap, but the change in the seismicity pattern, the eastward shift, the upward propagation sequences in August and September 2015 and a seafloor inflation event in late September 2015 suggested by geodesy measurements suggest a change in the tectono-magmatic activity of the volcano. This change may have involved small dike injections at depth next to the eastern edge of the AMC or local extensional tectonic events creating new pathways for downgoing hydrothermal fluids in the eastern AMC region.

We propose that processes occurring at the base of the hydrothermal circulation are the major source of seismicity beneath the Lucky Strike volcano region and that the hydrothermal circulation domain is a dynamic interface, controlled by spatial and temporal changes in permeability and probable episodic melt injections. The seismological events may be caused by thermal contraction of rocks during rapid cooling, possibly combined with tectonic events related to plate spreading and episodic melt injections. These processes are not mutually exclusive: thermal contraction leading to an initial set of cracks could facilitate local fluid circulation, leading to a progression of thermal contraction into the surrounding rocks. Thus, the shifts in seismicity clusters track the progression of enhanced heat extraction zones in the lower part of the hydrothermal downflow zone. The rate of seismicity (~8 events/week on average) is lower than that observed for hydrothermal systems on the East Pacific Rise and at Axial seamount on the Juan de Fuca Ridge, which may be because of the Lucky Strike segment's lower spreading rate and probable lower melt influx.

CONCLUSIONS & PERSPECTIVES

Moving to an individual hydrothermal vent site scale, I focused on the detection of near seafloor microseismicity near the Tour Eiffel hydrothermal vent site, using ~1 year of hydrophone data recorded by a small array of hydrophones (called the 'HydrOctopus'). I selected near-seafloor events based on waveform durations, number of phases and frequency spectra. The near seafloor events are very short (< 1 s) with only a direct P phase. The lack of a visible PwP phase in the shallow events is probably due to their very small energy release/shallow depth. We detected 740 shallow events (seismicity rate of ~3 events/day) with local magnitudes between -4 and -0.5 between September 2016 and September 2017. The event locations are not well constrained due to the limited number of stations/phases and our need to use a simple shallow upper crustal velocity model. The events are mostly scattered over the measurement area and only ~10% of the events are located inside the network. The events have a depth limit of ~150-250 m beneath the sea floor and we interpret them as being due to reaction driven cracking in response to anhydrite precipitation in the secondary hydrothermal circulation. The seismicity rate is ~80 times lower than that observed for near-seafloor seismicity at the TAG hydrothermal mound (Pontbriand & Sohn, 2014), which is consistent with the chemical evidence for limited to absent anhydrite precipitation recorded in the Tour Eiffel diffuse vent fields.

In the third part of my thesis, I presented and evaluated the P-wave polarization (P-Pol) method to orient the horizontal components of Short Period Ocean Bottom Seismometers (SPOBSs) using local seismicity. In most cases, P wave arrivals on SPOBSs give a constant back-azimuth regardless of the true direction of events and this phenomenon exists on 4 different types of SPOBS we studied using data from different marine environments as well as some stations in one land geophone network we studied. We hypothesize this phenomenon of constant back-azimuths to be an effect of local subsurface structures. Because of this issue, the P-pol orientations using local earthquakes should only be validated if the source events have a wide range of back-azimuths and the apparent orientation is consistent over these back-azimuths. Moreover, a station exhibiting constant apparent back-azimuth may be unusable for 3D wave field analysis but could provide important information about local subsurface structures.

5.2 Future perspectives

- I. This thesis provides a well constrained seismicity catalog for a slow spreading environment, which can be used further for various other analyses. For example, this catalog can be utilized to examine the 3D spatial and temporal patterns in the frequency-magnitude distribution of the earthquakes (e.g., Bohnenstiehl et al., 2008). In chapter-2, I only discussed M_c and b-value distribution to compare events from different deployments. Analyses focusing on spatial relative changes in b-value may provide more detailed information on subsurface fracture distributions, stress conditions, and hydrothermal fluid pathways.
- II. This thesis focuses only on seismic events occurring within the volcano region at the segment center. The primary OBS network also records events occurring off-volcano, mainly at the segment ends for which a seismicity catalog has already been made during this thesis. Provided a reasonable segment scale crustal velocity model, the location and magnitude of events could be properly constrained and provide information on segment end deformation and segment-scale crustal accretion. A short deployment of Portuguese OBSs at the southern end of the segment in 2007 could be used to help calibrate the velocity model/locations.
- III. I provide a preliminary analysis of near seafloor seismicity detection using a hydrophone network, which can be greatly improved and further analysed. In my thesis, I manually selected shallow events, which is a bit tedious. In the future, this one-year shallow seismicity catalog could be used as a training dataset for any automated technique. In subsequent deployments, we also have data available at 4000 sps which can be used to check if 250 sps is sufficient to detect shallow events, or if more shallow events can be detected beyond 100 Hz.
- IV. For the P-Pol orientation analysis, we hypothesize that local subsurface structures can affect the P-wave arrival direction and can give constant back-azimuths. An analysis based on forward modelling should give further insights. If it were to be true, the P-Pol method can be modified to study local subsurface structures.

Appendix A
Data processing

A.1 FIR correction

The cut-off frequency for INSU-IPGP SPOBSs is ~ 25 Hz at which the local events have significant energy. So, the impulse response of the data logger's last digital filter stage (a zero-phase filter) makes it difficult to precisely pick the first phase arrival time and its polarity. Therefore, initially the data was converted to equivalent minimum phase using a Finite Impulse Response (FIR) correction (Figure A1; Scherbaum & Bouin, 1997).

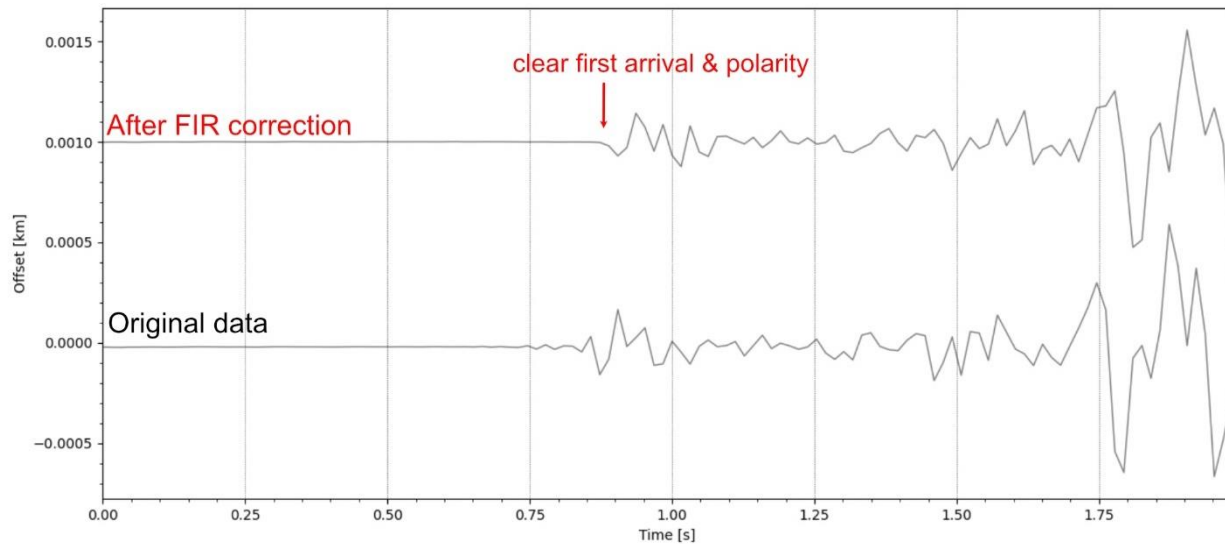


Figure A1. Example of a FIR corrected waveform.

A.2 Data Quality

Data quality on each channel of all OBSs were assessed by Probabilistic Power Spectral Density (PPSD) analysis. Normally, P phases were picked on the vertical channels and S phases were picked on both horizontal channels. In case vertical channel data is noisy, we picked P phase on either of the horizontal channels. Here I have shown 50th percentile of PPSDs for all channels of all OBSs in every deployment (Figure A2).

A.3 Time drift correction

We verified and corrected (if needed) the clock offset in all OBSs by plotting the change in earthquake location time residuals over time after deployment. Corrections were made for the center OBS in 2011-2012 deployment by -1.2 s, the East-OBS in 2012-2013 deployment by -1.3 s, the North-OBS in 2018-2019 deployment by -1.2 s, and two of the University of Lisbon OBSs in 2010-2011 deployment (LIS1: 0.9 s, LIS3: -1.2 s; Figure A4).

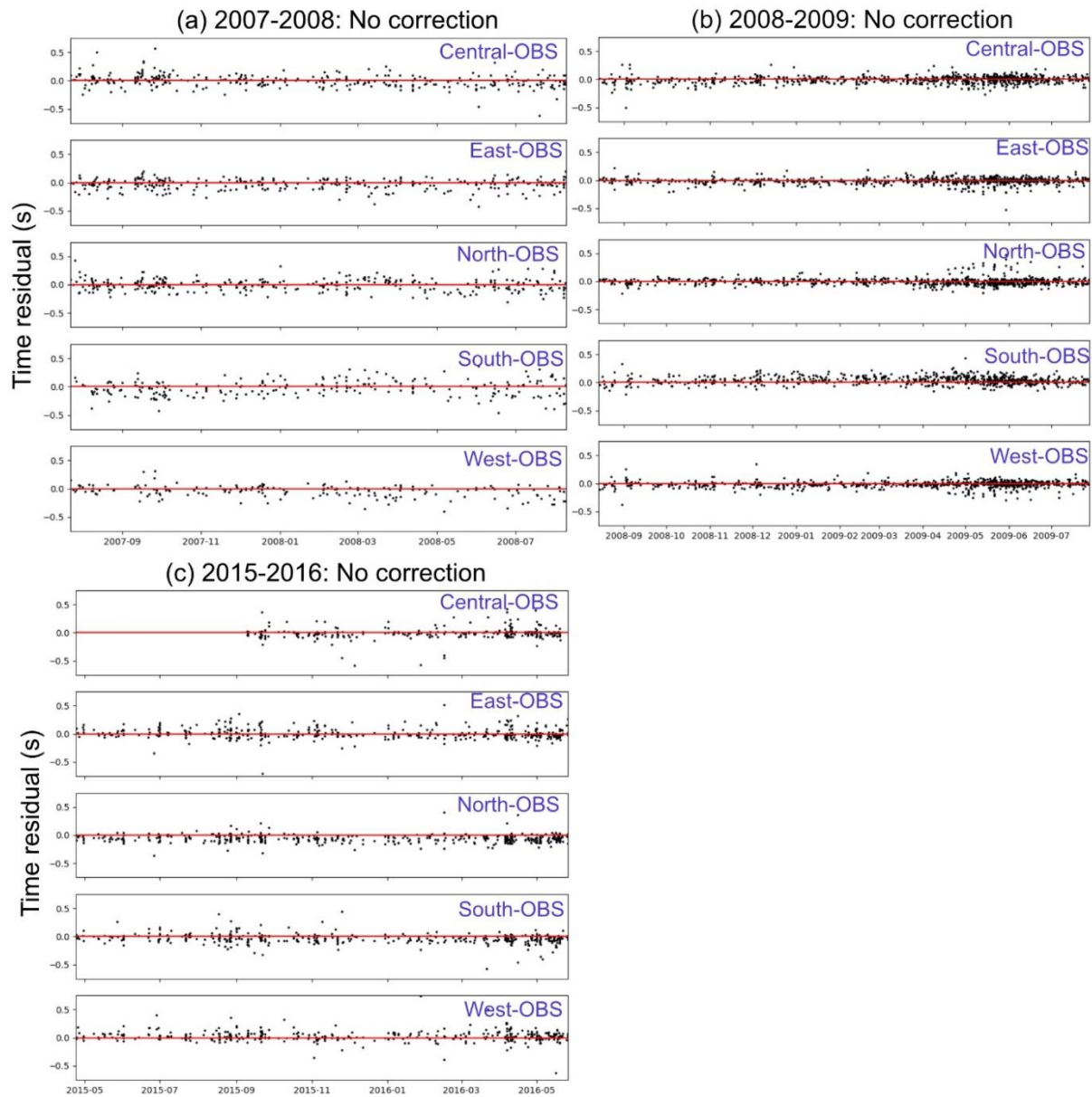
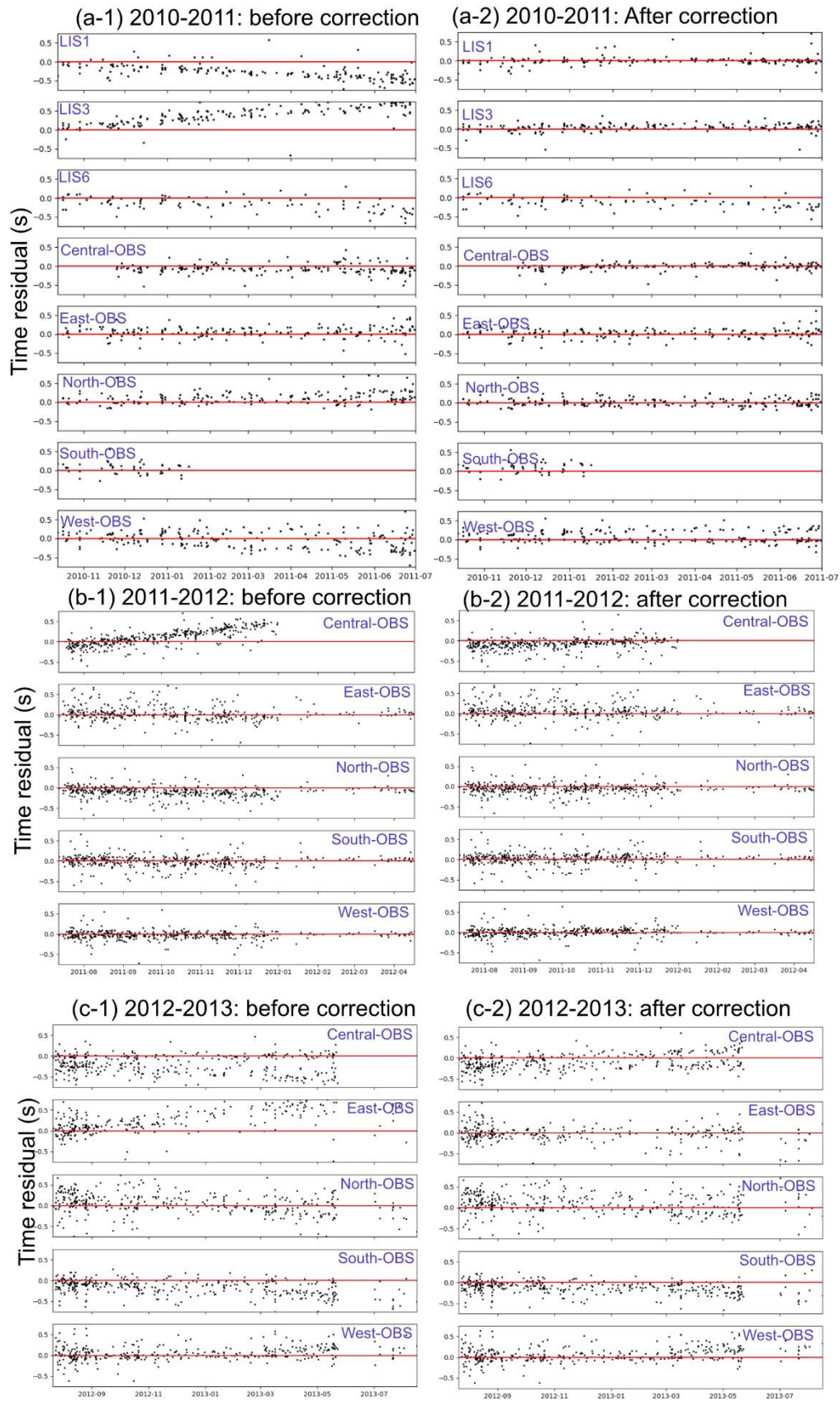


Figure A3. Time drift estimations for the deployments for which no corrections were required.

APPENDIX A. DATA PROCESSING



APPENDIX A. DATA PROCESSING

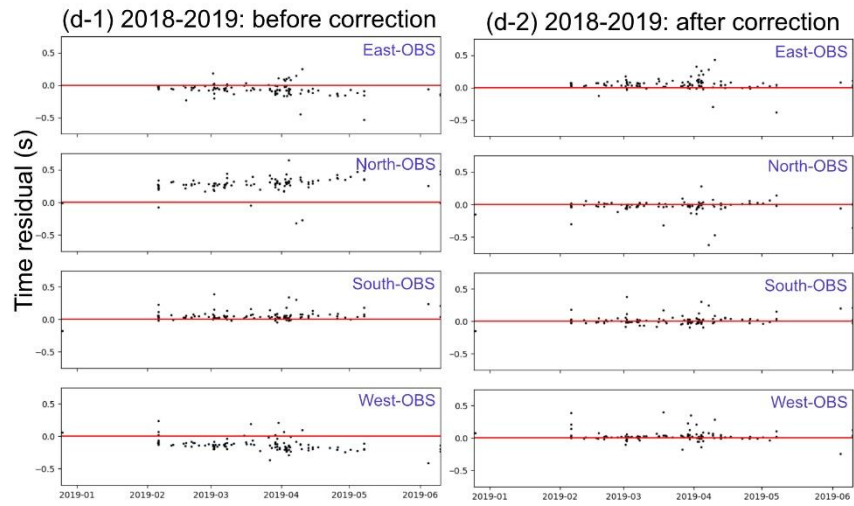


Figure A4. Time drift estimations for the deployments for which corrections were made for one or more OBSs. Offset values are mentioned in the text above.

A.4 Magnitude of completeness (M_C) and b -value estimation

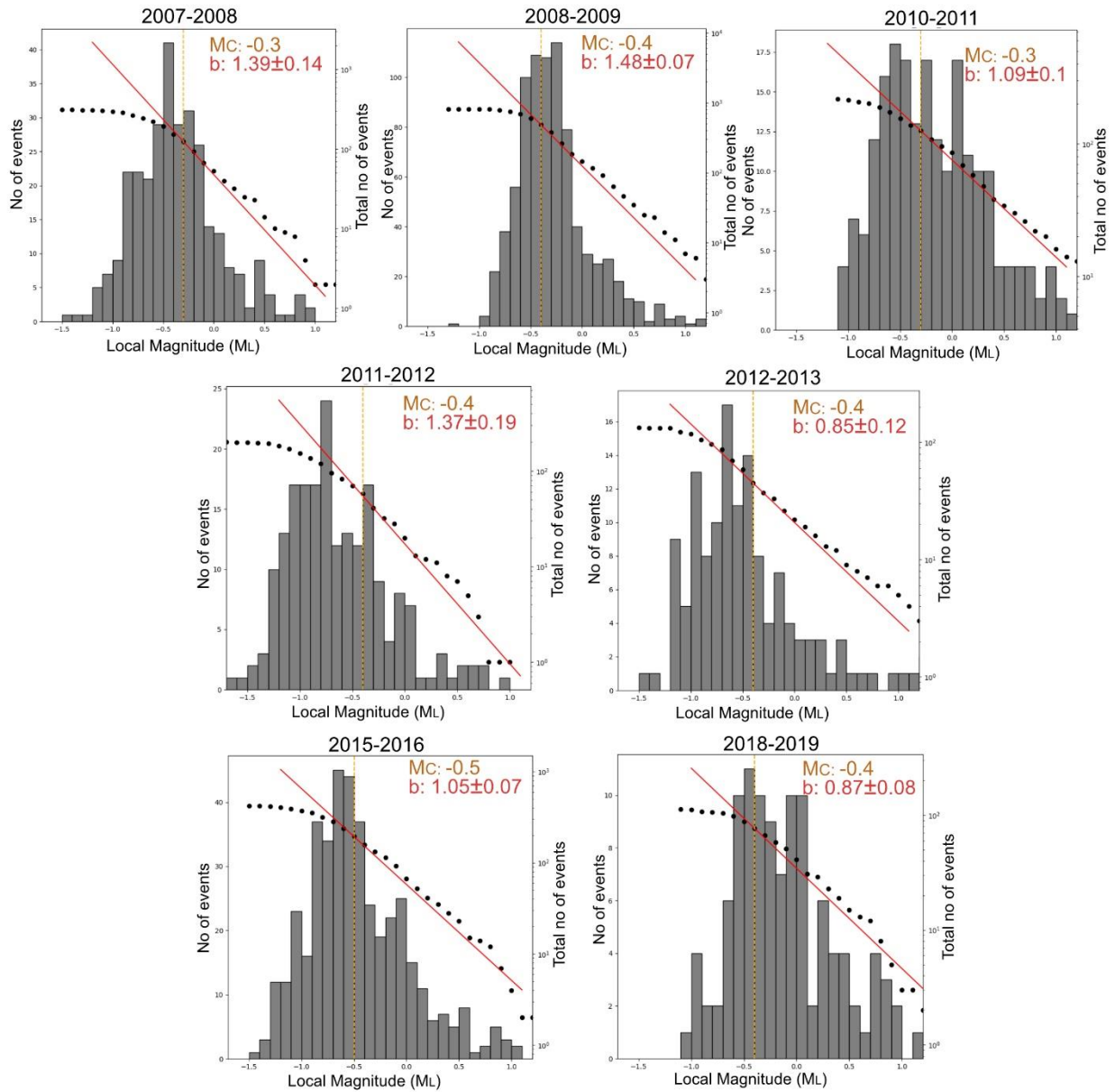


Figure A5. Calculation of magnitude of completeness and b -value for each deployment.

A.5 Estimation of V_p/V_s (segment scale)

In Chapter-2, I have calculated V_p/V_s using just ‘volcano’ events. Here I have shown V_p/V_s calculation for the entire segment using both ‘volcano’ events and segment end events (Figure A6). Since the velocity structure is different for segment center (volcano region) and segment end, we cannot use the same velocity model for earthquake locations.

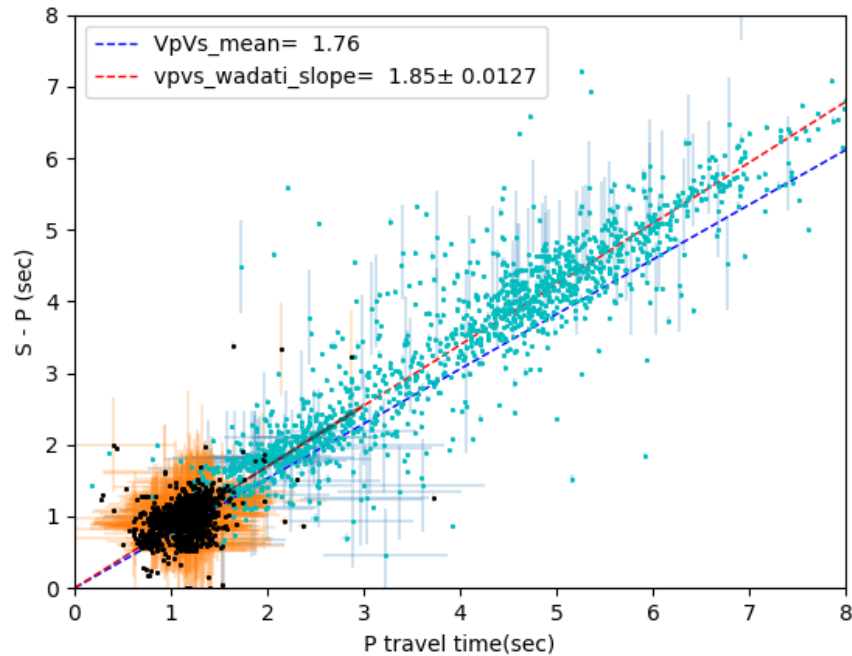


Figure A6. V_p/V_s calculation for the entire segment using Wadati diagram using both ‘volcano’ events (black dots) and segment end events (sky-blue dots). Blue dotted line is the V_p/V_s value calculated as the mean of V_p/V_s calculated from individual event. Red dotted line is V_p/V_s value calculated as slope of the line fitting through the events.

A.5 Earthquake locations in NLLoc

The location of an earthquake is characterized by its hypocenter i.e., the spatial position (x , y , z) and the origin time (t_0) at which the energy is released from a seismic event. Location of an earthquake is a non-linear inverse problem where the travel times of seismic waves depend non-linearly both to the hypocenter and the velocity model. In grid search location technique, which is a non-linear earthquake location method, the misfit function between observed and predicted arrival times of the seismic phases $i = 1$ to N is defined in L2 norm as:

$$E = \sum_{i=1}^N e_i^2 = \sum_{i=1}^N (t_{obs}^i - t_{pre}^i)^2$$

Where e_i is the time residual for one seismic phase. The predicted arrival time is given by:

$$t_{pre}^i = T^0 + t_{model}^i + t_{corr}^i$$

Where T^0 is the origin time, t_{model}^i is the travel-time table value, and t_{corr}^i is the sum of travel-time corrections. The least square solution of the time residual equation corresponds to the minimum misfit function, and it then updates the initial location. The grid search method calculates a global minimum misfit over a model grid.

We have adopted above-described grid location method using the location software NonLinLoc (NLLoc, Lomax et al., 2000). Following the algorithms in Tarantola & Valette, (1982), NLLoc calculates the maximum likelihood origin time from the observed and predicted travel times and thus it reduces the 4D problem of location to a 3D search of x , y , z in space. The model parameters are given by a probability density function (PDF). The NLLoc grid search algorithm systematically determines the posterior probability density function or the misfit function over a 3D (x , y , z) spatial grid. The maximum likelihood (or minimum misfit) point of the complete, non-linear location PDF is selected as an ‘‘optimal’’ hypocenter. Instead of normal grid search method, NLLoc also uses an oct-tree sampling technique where it sub-divides the initial grid with minimum misfit to multiple smaller grids (8) and calculates the individual PDFs in smaller grids. It iterates the division until a threshold of the grid size is reached and thus provides the location in higher resolution.

A5.1 NLLoc programs and control file

Here the main programs of NLLoc and the most useful statements of the control file have been summarized. For a detailed description, refer to the NLLoc software guide (<http://alomax.free.fr/nlloc/>).

A5.1.1 Vel2Grid:

Given a velocity model (1D/3D), Vel2Grid produces a 3D model Grid containing velocities and other model specifications.

Control statements:

1. **VGOUT**: Specifies the path for output Velocity grid.
2. **VGTYPE**: Specifies the wave type
3. **VGGRID**: Describes the Grid. Model grid is centered around each station.
e.g., VGGRID xNum yNum zNum xOrig yOrig zOrig dx dy dz gridType
For a 2D Grid: xnum = 2 and xorig = 0 (CAN NOT BE NEGATIVE).
For a 3D Grid, xorig and yorig can be negative.
4. **LAYER**: Describes the velocity model. NLLoc always uses a left-handed coordinate system (Positive X: East, Positive Y: North and Positive Z: Down). The velocity model should start from the sea level. In STATION0.HYP, depths are the bottom of the layer while in NLLoc it is to the top of the layer.

A5.1.2 Grid2Time:

It calculates the travel time at each grid of the model.

Control statements:

1. **GTFILES**: Specifies the path for input and output
2. **GTMODE**: Type of time grid. It cannot be 3D if xnum in VGGRID line is 2.
3. **GTSOURCE**: Specifies the stations positions.
e.g., GTSRCE label LATLON latSrce longSrce zSrce elev
Z = zSrce - elev (Not sure how useful!)

A.5.1.3 NLLoc:

It performs the earthquake location using the travelttime grid models.

Control statements:

1. **LOCFILES**: Specifies Input and output file path
2. **LOCHYPOUT**: Specifies Output file type.

3. LOCSEARCH: Specifies Search method
4. **LOCGRID**: Describes the search grid. It must be ALWAYS inside the intersection of model grids centered around each station. The origin point here is taken from the coordinate origins described in TRANS statement.
5. LOCMETHOD: Specifies Location method.
6. LOCGAU: Specifies Gaussian model error.
7. LOCPHASEID: Phase Identifier mapping.
8. LOCDELAY: Specifies phase time delays.

A5.1.4 General control statements

1. TRANS: Sets the geographic transformation.

A5.2 Location using 1D velocity model

The 1D velocity model is taken from Crawford et al., (2013) which was calculated using VELEST software. But instead of defining the base at sea floor level, the model starts at sea level. The Vp/Vs ratio is taken as 1.83 (taken from Crawford et al., (2013)) and all the densities are taken from Carlson & Raskin, (1984). As mentioned in Chapter-2, we later calculated Vp/Vs value by modified Wadati diagram using just volcano events. The final Vp/Vs value adopted was 1.93 for volcano events.

A5.2.1 Using 2D travel time grid

For a 2D travel time grid, the velocity model grid and location search grid are defined as following. Earthquake locations are show in Figure A7.

```
GTMODE GRID2D
```

```
VGGRID 2 60 60 0.0 0.0 0.0 0.5 0.5 0.5 SLOW LEN
```

```
LOCGRID 400 400 200 -10 -10 0.0 0.05 0.05 0.05 PROBDENSITY SAVE
```

A5.2.2 Using 3D travel time grid

In order to compare with the result from a 3D velocity model, location is also done using a 3D travel time grid keeping the model grid same as the 3D velocity model (Figure A8).

```
GTMODE GRID3D
```

```
VGGRID 1281 1281 801 -16.0 -16.0 0.0 0.025 0.025 0.025 SLOW LEN
```

APPENDIX A. DATA PROCESSING

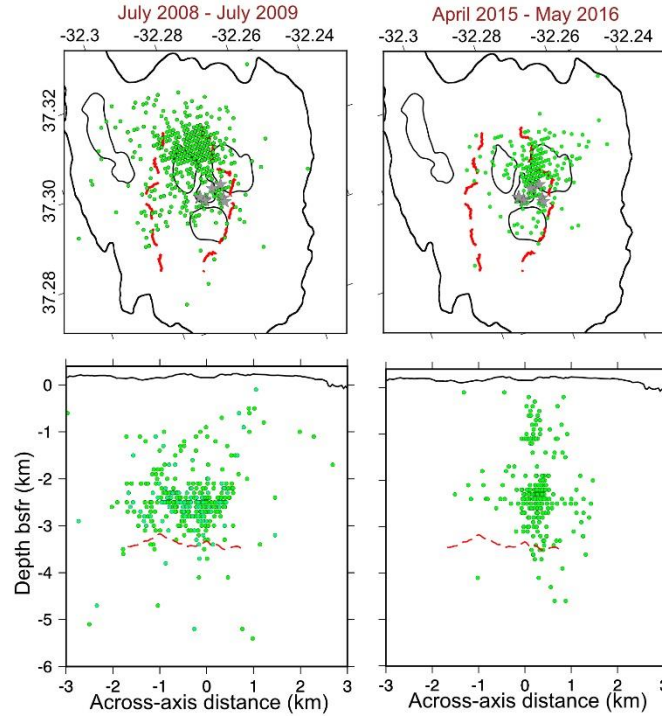


Figure A7. Earthquake locations using 1D velocity model, 2D travel time grid for two deployments (2008-2009 & 2015-2016).

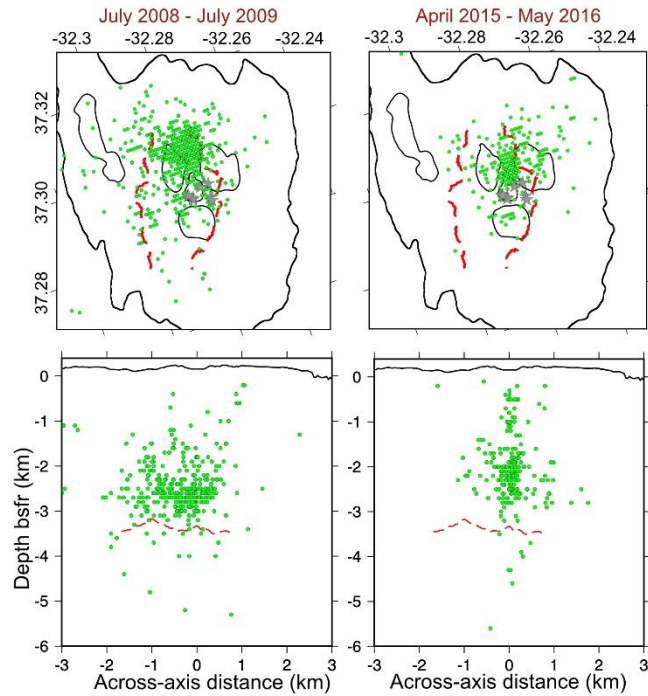


Figure A8. Earthquake locations using 1D velocity model, 3D travel time grid for two deployments (2008-2009 & 2015-2016).

A5.2.3 Encountered problems

1. While calculating 2D travel time grid where $xNum = 2$ (in VGGrid line), $xOrig$ and $yOrig$ can not be NEGATIVE. I initially thought that model origin point is taken from the TRANS statement and since it is at the center, I used to start the model with negative $XOrig$ and $YOrig$. In that case it gives depths either at the bottom of the model or clustered at two different depths. But 2D grids are centered around the stations. And the search grid (LOCGRID line) must be inside the intersection of all stations model grid.
2. Comparing the location from HYPOCENTER and NLLoc: Initially the STATION0.HYP file used in HYPOCENTER had the station locations relative to the seafloor (defined 2000 m below the sea level). But the traveltime grid model in NLLoc was relative to the sea level. So, there was 2 km discrepancy in depth between two methods which I thought to be a problem of NLLoc. Later I changed the STATION0.HYP station locations and made all the depths w.r.t the sea level.

A5.3 Location using 3D velocity model

As mentioned in Chapter-2, we used a 3D velocity model as the final model for earthquake locations. The final 3D model (AA_TS) was obtained by combining 2 different models derived from active seismic data: 1) the full waveform inversion (FWI) of seismic streamer data ('AA' model; Figure A9b; Arnulf et al., 2014b) and 2) the travel time tomography of OBS data ('AA' model; Figure A9a; Seher et al., 2010). Here I only discuss how a 3D model can be incorporated into NLLoc.

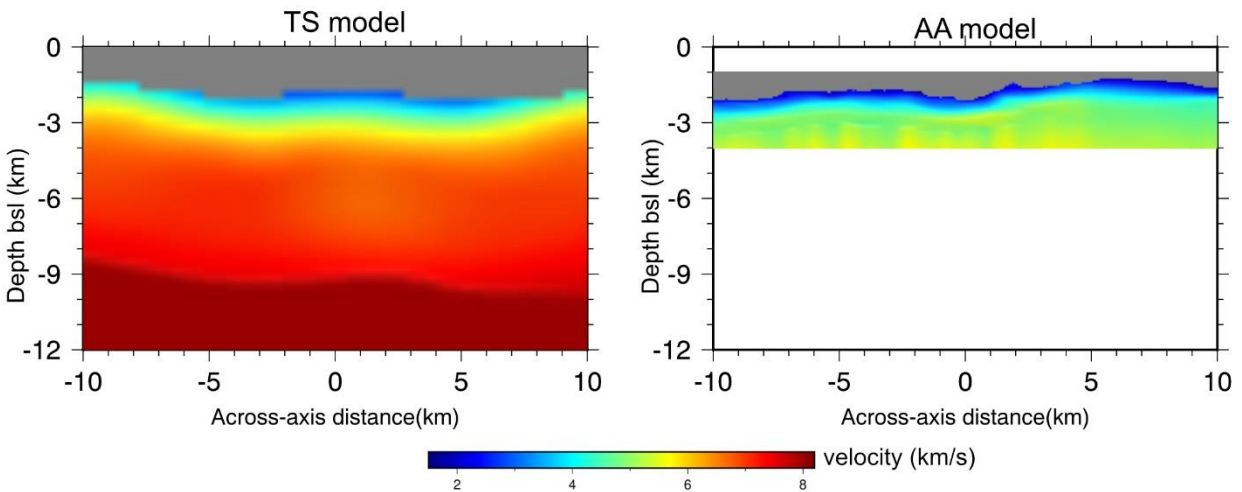


Figure A9. Original (a) TS model and (b) AA model.

APPENDIX A. DATA PROCESSING

The model is initially converted to a NLLoc velocity grid using NLLGrid (<https://github.com/clauidodsf/nllgrid>) instead of using the regular Vel2Grid program in NLLoc. The parameters used in NLLGrid are as follows.

```
# grid description
dgrd = 0.025
xorig = -16
yorig = -16
zorig = 0
grd = NLLGrid()
grd.array = slow_len
grd.dx = dgrd #km
grd.dy = dgrd #km
grd.dz = dgrd #km
grd.x_orig = x_orig #km
grd.y_orig = y_orig #km
grd.z_orig = z_orig #depth +ve in nlloc
grd.type = 'SLOW_LEN'
grd.orig_lat = 37.29084
grd.orig_lon = -32.28
grd.map_rot = -19
grd.first_std_parallel = 37.24
grd.second_std_parallel = 37.34
grd.proj_name = 'LAMBERT'
grd.proj_ellipsoid = 'WGS-84'
```

NLLGrid takes a 3D numpy array as input. So the `grd.array` above is a 3D numpy SLOWLENGTH (slowness * dgrid) array. The grid type has to be 'SLOW LEN' in order to further calculate the travel times in NLLoc using Grid2Time.

IMPORTANT: The initial velocity models (both 'AA' and 'TS' model) were rotated by $+19^{\circ}$ clockwise from North. In NLLoc, rotation is counterclockwise from the positive \hat{Y} -axis (see Notes on the TRANS statement on the NLLoc software guide). So, the model grid is rotated by -19° as -19° counterclockwise rotation w.r.t to Y axis is similar to $+19^{\circ}$ clockwise rotation of grid w.r.t to North (Figure A10).

Then the traveltimes and locations are then calculated in NLLoc using Grid2Time and NLLoc, same as 1D model.

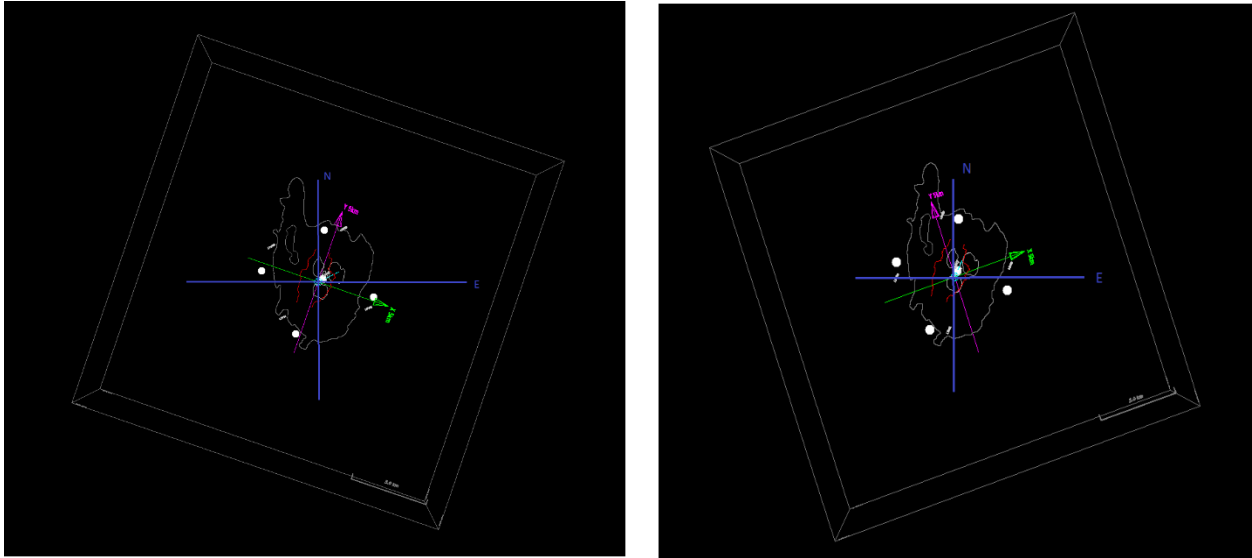


Figure A10. Comparison between -19° (Left) and $+19^\circ$ (Right) rotation of the grid (view from the top). Blue lines are Geographic North and East, Pink and Green arrow represents $+Y$ and $+X$ axis of the rotated grid respectively; white circles represent stations.

A.6 Earthquake relocation in HypoDD

I used the HypoDD software that uses a double difference earthquake relocation procedure (Waldhauser & Ellsworth, 2000). This technique has been developed in order to precisely re-locate clusters of events. It works on the assumption that if two events have a similar location then the ray-path from earthquakes to receiver is equivalent.

HypoDD makes clusters of events based on phase picks and correlation measurements. Initially it calculates travel times in a layered velocity model for the hypocenters previously located. It determines residuals for pairs of events at each station of the network and minimized those in an iterative manner using least-squares inversion. It also does cross-correlation between events waveforms and produces a correlation factor that indicates how similar the traces are to each other. For a group of events, the technique allows to calculate the cross-correlation for each pair of events. After clustering, it calculates the double-difference hypocenter locations by minimizing the residuals between the observed and calculated traveltimes. HypoDD parameters used in this study are mentioned in Chapter-2.

Appendix B
Tests on geophone orientation

B.1 Introduction

Seismometers generally output three channels: one oriented vertically (named “Z”), one oriented N-S (named “N”) and the other oriented E-W (named “E”). A positive signal on each of these channels corresponds to a movement up/north/east respectively which is formalized in the “Dip” and “Azimuth” values provided in the station metadata and whose values are -90/0 (Z), 0/0 (N) and 0/90 (E) (SEED manual). If a station provides data with other orientations, the orientation codes should be different, and the dip/azimuth values should be changed accordingly.

We know of no published standards for the orientation of the geophones used in short period ocean-bottom seismometers (SPOBSs), which can lead to an inconsistent orientation of the horizontal channels. We know that vertical geophones have inverse polarity (a positive signal corresponds to a downward motion), but we were not sure about the polarity of the horizontal sensors. Without some kind of standard for orienting the horizontal geophones relative to one another, it is very complicated to correctly interpret their signals. Ocean-bottom seismometers are generally deployed to the seafloor in free-fall motion and therefore their horizontal sensors are not geographically oriented, but they can be reoriented if they obey the N/E geometry, and the station metadata are correctly specified.

In order to establish a “standard” geophone orientation, we conducted tests on the INSU IPGP SPOBSs both directly on the geophones and on a closed SPOBS. We define a “standard” orientation geometry, and we tested different procedures for determining if the geophones in a SPOBS have this geometry. We also evaluated the polarity of the hydrophone channel. Hydrophone data complement vertical channel and can also be used to determine if a wave is upgoing or downgoing, but there appears to be no standard for hydrophone polarity: it even appears that the same model of hydrophone can have different polarities (the manufacturer of our HiTech HTI-90U hydrophones was able to tell us their polarity, based on their serial numbers).

B.2 Instruments and Geometry

The INSU-IPGP SPOBSs have sensors with a three-component Mark Systems L-28 geophone (4.5 Hz) and a HiTech HTI-90U hydrophone (serial number 22xxx). The vertical geophone should have reverse polarity. The hydrophone returns a positive voltage for a decrease in pressure (email from HiTech based on first two numbers of the serial number), which also gives it a “reverse” polarity for upgoing waves. Our initial tests of the polarity of the horizontal geophones indicated

APPENDIX B. TESTS ON GEOPHONE ORIENTATION

that they, too, are reversed (a movement of the geophone towards the end with the electrical contacts (“pins”) gives a negative voltage). For these tests, we named the vertical channel “Z*”, the pin side of the top-most geophone “S*” and that of the middle one “W*” (Figure B1). We take this configuration and the wirings indicated in Table B1 to be standard. Note that the geophones are wired “single-sided” (all negatives to ground), but a differential wiring with the same wires going to positive would change the polarities. (But we would have to use more wires/colors for the negative pins.)

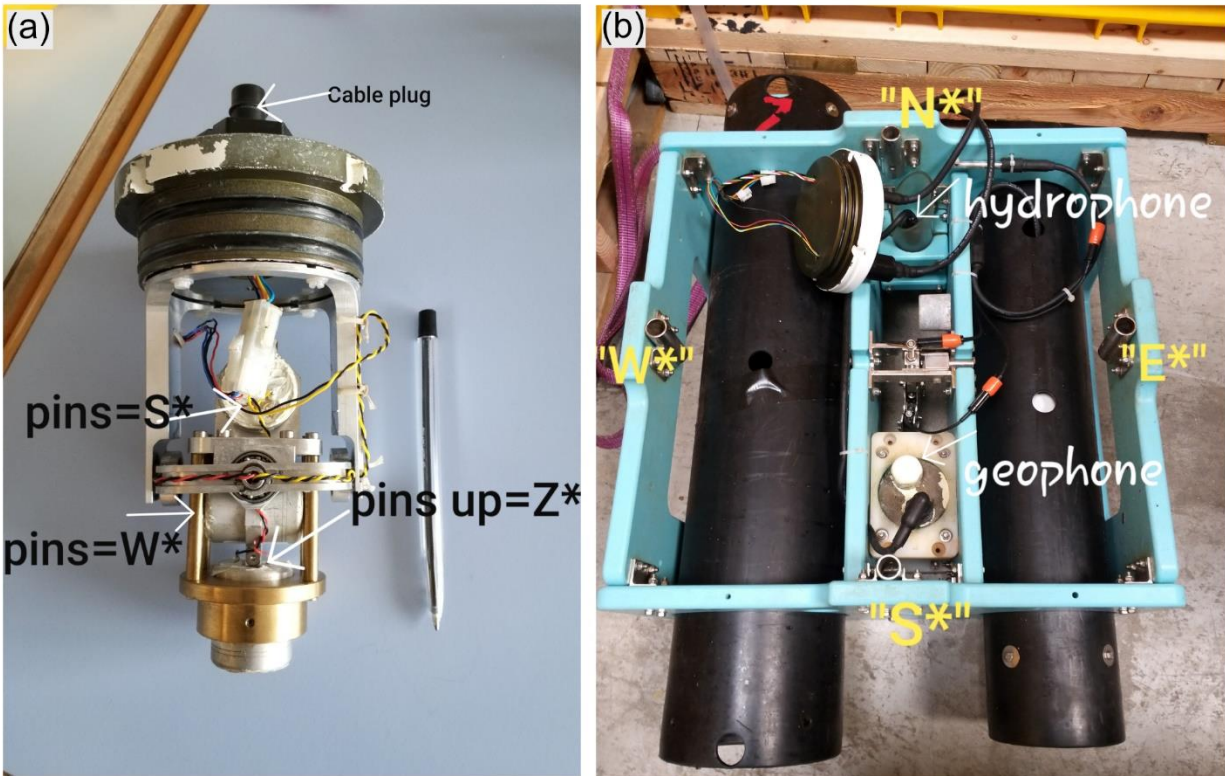


Figure B1. Configuration and wirings of (a) an open geophone and (b) a closed geophone with the sensors' reference directions.

Table B1. Configuration and wirings of the geophones.

Position in frame	Wire color	Wire pin number	Amplifier card no.	Amplifier card channel	DAS channel	Orientation code existing	Name used here
Top	Yellow	4	2	1	3	“1”	“S*”
Middle	Blue	3	1	2	2	“2”	“W*”
Bottom	Red	2	2	2	4	“3”	“Z*”

We also adopted the following configurations as a standard in the geophone case and SPOBS external frame:

1. The “S*” wired end is aligned with the cable plug on the geophone case.
2. The geophone case is oriented in the OBS frame so that the cable plug points OPPOSITE the hydrophone.

If this configuration is respected, the side of the frame hosting the geophone is the “S*” side. This was the case for the tests described here. All other tests should respect this geometry.

B.3 Data collection

We tested different procedures to determine the geometry and polarity of the geophones. First, we did tests on open geophones to directly establish the relation between the sensor orientations and responses, and then tried different tests on a closed geophone installed in a SPOBS frame to find out which tests are more useful. Most of the tests were repeated 3-6 times to determine if the test results were repeatable.

B.3.1 Tests on open geophone

The first set of tests was carried out on an open geophone to determine direct relationships between the geophone orientation and the output voltages. The data was recorded on an OBS logger, and the output voltages were observed in real time on an oscilloscope. We tried to create signals that would last more than a few samples, to simplify polarity picking.

B.3.1.1 Flipping the vertical geophone (Z^*) between pin-down and pin-up

The vertical geophone was turned from pin-down (upside down) to pin-up (right side up). In flipping, the mass goes down away from the pin, which is how it should move for an upward earth movement. The motion was then done from pin-up to pin-down, simulating a downward earth movement.

B.3.1.2 Rotating the horizontal geophones (S^* and W^*) through horizontal

The horizontal sensors were turned from 45^0 pin-up to 45^0 pin-down, simulating an earth movement away from the pin end (S^* , W^*). Then the sensors were turned from pin-down to pin-up, simulating an earth movement towards the pin end.

B.3.1.3 Tapping with a piece of cardboard

We gently tapped the pin side of each geophone with a piece of cardboard. The goal in using cardboard rather than a hammer is to dampen the shock so that the impact lasts more than a few samples. By tapping on the pin side, we simulated a movement down (Z^*), “northward” (S^*) and “eastward” (W^*). For the first 30 seconds we tapped softly, then for the next 30 seconds we tapped slightly harder.

B.3.1.4 Tapping with a rubber hammer

We “designed” a rubber hammer with a soft head, to give the softest and longest-lasting initial impact possible (a nerf hammer might have been even better), and then tapped on the pin side of each geophone.

B.3.1.5 Jumping at a distance

A person jumped at a fixed distance (3-4m) from the geophone. Again, the goal was to create a low-enough frequency signal that would cover several samples. We jumped from two directions (on the pin side of and aligned with the S^* geophone, and on the pin side of and aligned with the W^* geophone) and at two fixed distances (~1 m and ~4-5 m).

B.3.1.6 Hitting a hammer on the ground at a distance

We could not always see the jumps on the oscilloscope, so we also tried tapping the hammer on the ground at ~1 m and ~4-5 m from the S^* and W^* directions.

B.3.2 Tests on a closed geophone in the SPOBS frame

The following tests were performed with a closed geophone (NOT the one previously tested), which was installed in OBS frame 09 with the geometry indicated in Figure B1b.

B.3.2.1 Lift different ends of the OBS

Starting in the horizontal position (the SPOBS sitting flat on the ground), one end was lifted. The idea is that the horizontal mass aligned with this movement should move towards the new “down” end, simulating an earth motion towards the lifted end. So, lifting the S^* side of the OBS will simulate a ground motion towards the south, and so on.

B.3.2.2 Tapping with a rubber hammer

This was done following the same procedure as for the open geophone, but we had to tap on the part of the frame that was best coupled to the geophone. We tapped at about the depth of the middle of the geophone case to minimize rotational/shear motions. For the W* geophone, we tapped on the geophone holder on the W* side from inside the case, simulating a movement towards the east. For the S* geophone, we tapped on the outside of the OBS frame on the S* side, directly in front of the geophone, simulating a ground movement towards the north.

B.3.2.3 Jumping

Similar to the open geophone tests, but we only jumped at 1m distance (we probably should have done at several meters as well).

B.3.2.4 Hitting hammer on the ground

This was done following the same procedure as for the open geophone.

B.3.3 Second set of tests on a closed geophone in the SPOBS frame (3rd part)

The following tests were performed on the same OBS the following morning, to confirm the results suggested by the previous tests and to see if there were not some more conclusive tests possible with the OBS frame.

B.3.3.1 Lift different ends of the OBS, crossing the horizontal

Since lifting different ends of the OBS, starting at horizontal, didn't give conclusive results, we tried starting with one end up and switching to the other one up, hoping that in doing so we would get a clearer signal. So, we started with the S* (W*) end of the sensor already lifted and the first movement at 00 second was moving the S* (W*) end down and the N* (E*) end up simultaneously. At 10 sec we did the reverse movement, and so on.

B.3.3.2 Slow lifting of OBS

Here 2 people lifted the SPOBS slowly from the floor, arriving at a straight leg position in 1-2 seconds. The goal is to initiate upward motion with no precursor, which would simulate an upward motion of the sea floor.

B.3.3.3 Fast lifting of OBS

This was done as above but lifting as fast as possible (0.5-1s).

B.3.3.4 Rotate the E-W side to the vertical position

Starting with the OBS flat on the ground, the W* side was tilted up until the OBS sat on its E* side. After 10 seconds, the OBS was tilted back down to flat. After a sequence of these motions, the same motions were done with the E* side moving up. No N* and S* tests were run because these sides don't have a flat edge to sit on.

B.3.3.5 Squeeze the hydrophone

The hydrophone was squeezed, simulating a positive pressure signal, held for 10 sec, and then released.

B.4 Results

B.4.1 Open geophone

B.4.1.1 Flipping the vertical geophone (Z*) between pin-down and pin-up

Going from pin-up to pin-down (mass goes towards the pin, simulating a downward ground motion), the signal goes up (Figure B2a-1). This indicates that the sensor is indeed inverted and the "Z*" channel should have dip=90. In agreement the signal goes down when the pin is flipped from pin down to up (Figure B2b-1).

B.4.1.2 Rotating the horizontal geophones (S* and W*) through horizontal

When we rotated the horizontal geophones from pins down to up (mass moves away from the pin simulating a movement towards the pin end), the signal goes down (Figure B2b-2, b-3). This agrees with our assumption and both the horizontal channels are "INVERTED".

APPENDIX B. TESTS ON GEOPHONE ORIENTATION

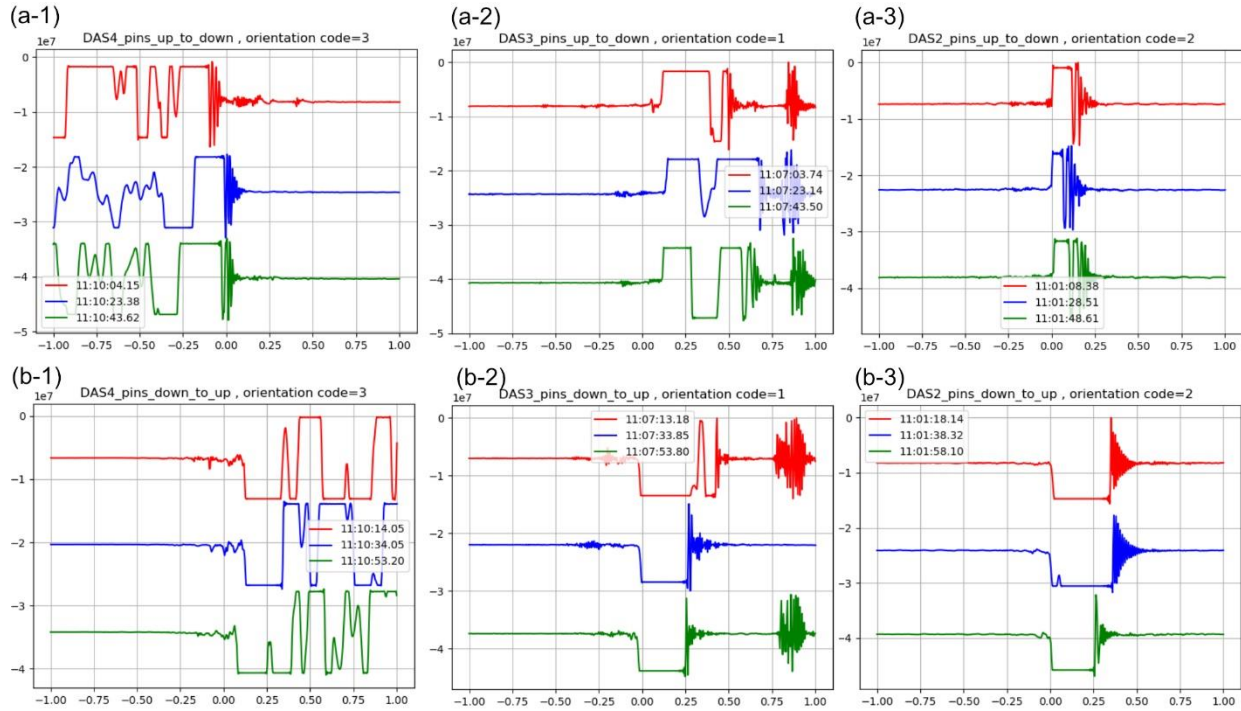


Figure B2. Signals of (a1-a3) DAS pin up to down and, (b1-b3) pin down to up for Z^* , S^* and W^* sensors, respectively.

B.4.1.3 Tapping with a piece of cardboard

The signal went up when tapped on the S^* , W^* and top (Z^*) sides (N^* , E^* and down motions) agreeing with our hypothesis that all sensors are inverted with respect to their pins (Figure B3). This can be corrected on the horizontals by simply naming their pin ends “S” and “W”, but it cannot be corrected on the vertical because we cannot put the pin end downward (the sensor would not function).

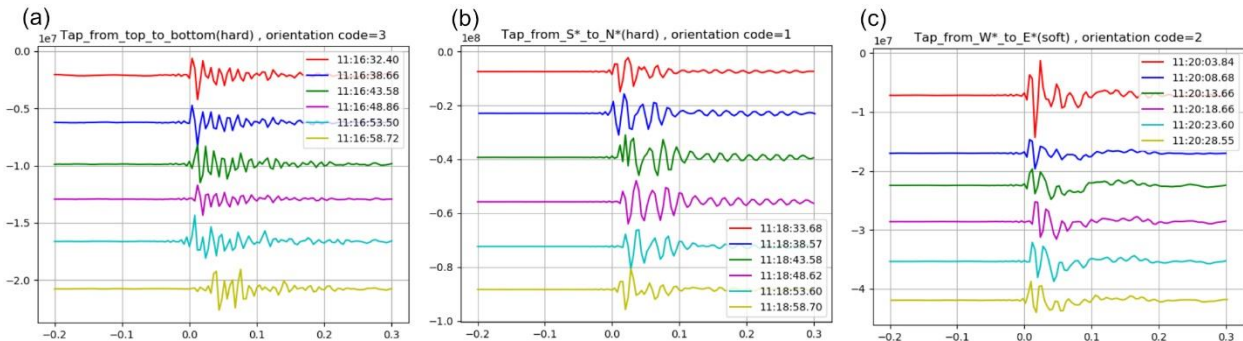


Figure B3. Signals of tapping with a cardboard on the (a) top (Z^*), (b) S^* and (c) W^* of an open geophone.

B.4.1.4 Tapping with a rubber hammer

Gave the same result as for cardboard (Figure B4) and the signal appears to be a little lower frequency (clearer). But one of the taps on the top looked like the signal went down first instead of up (Figure B4d).

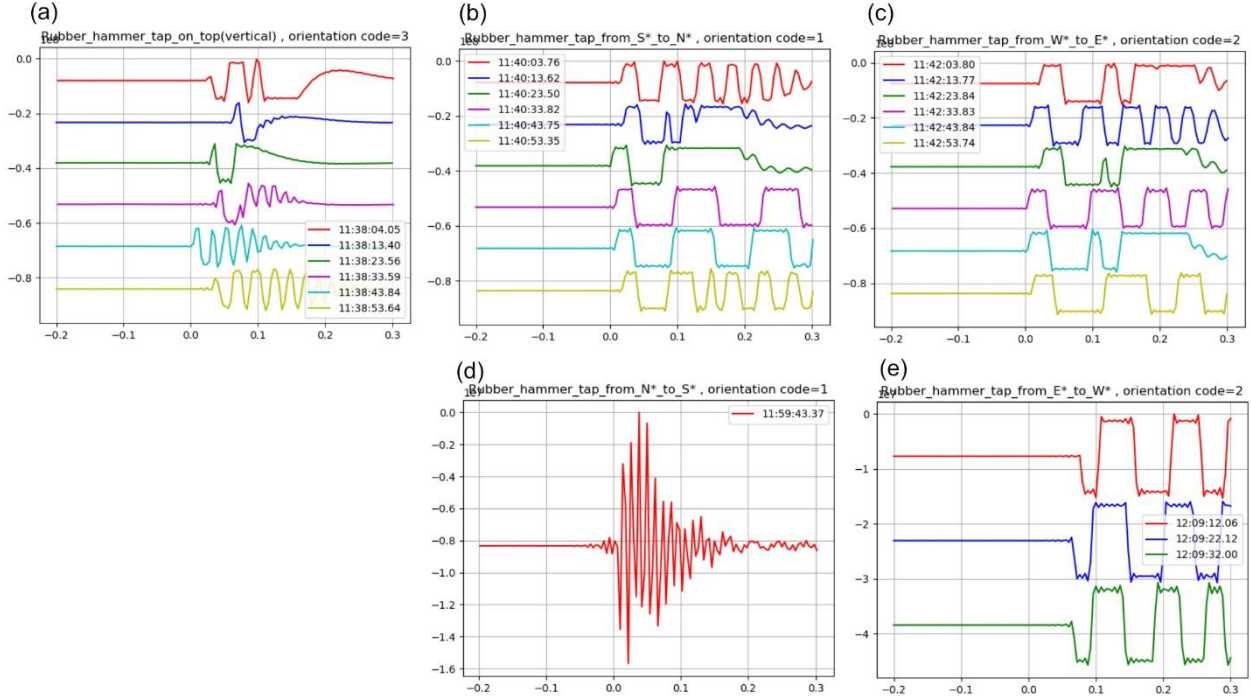


Figure B4. Signals of tapping with a rubber hammer on the (a) top(Z^*), (b) S^* , (c) W^* , (d) N^* , and (e) E^* of an open geophone.

B.4.1.5 Jumping at a distance

The jumping signal is mostly vertical (first motion downward) and so the signal went up on the Z^* channel (Figure B5a-1, b-1). Particle motion plots show that there is a strong alignment parallel to the direction to the jumper (Figure B5a-4, b-4), which should allow us to identify misaligned geophones within the frames. This does not, however, appear to allow us to determine the horizontal channel polarity (Figure B5b-2, b-3, c-2, c-3).

APPENDIX B. TESTS ON GEOPHONE ORIENTATION

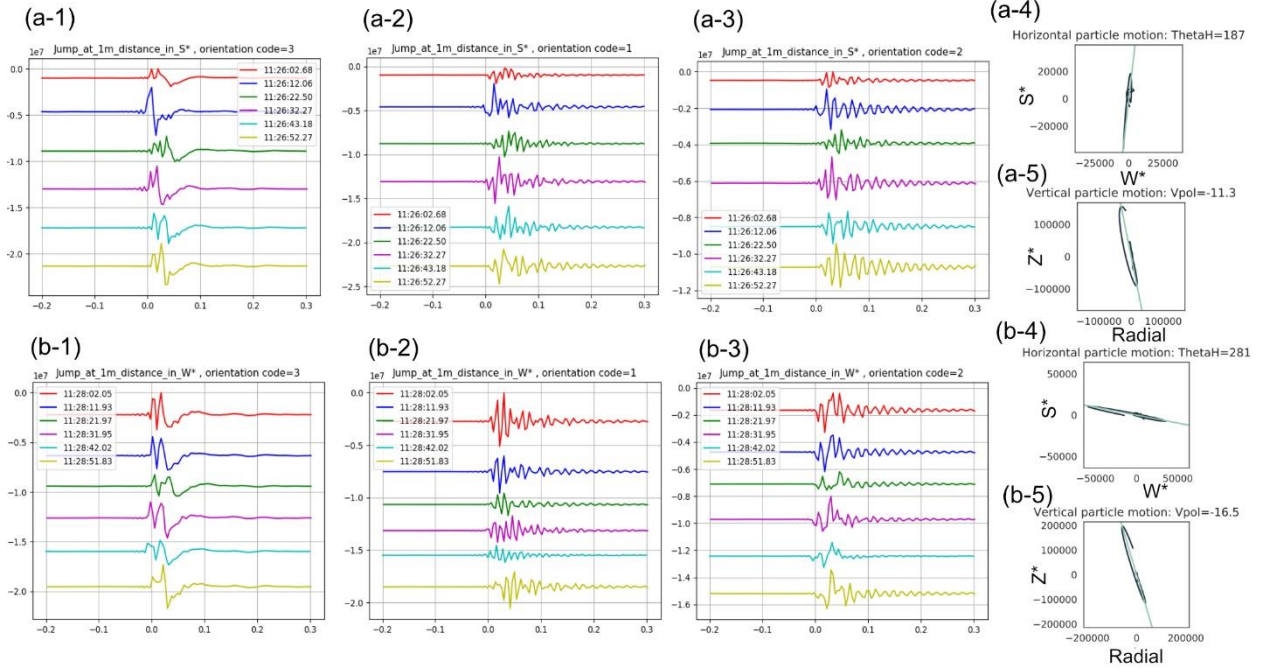


Figure B5. Signals of jumping at 1 m distance from S^* end in (a-1) Z^* , (a-2) S^* , and (3) W^* sensors. (a-4) & (a-5) are the horizontal and vertical particle motions, respectively. (b1-b5) Same as (a1-a5), but the jumping was performed at 1 m distance from W^* end.

B.4.1.6 Hitting a hammer on the ground at a distance

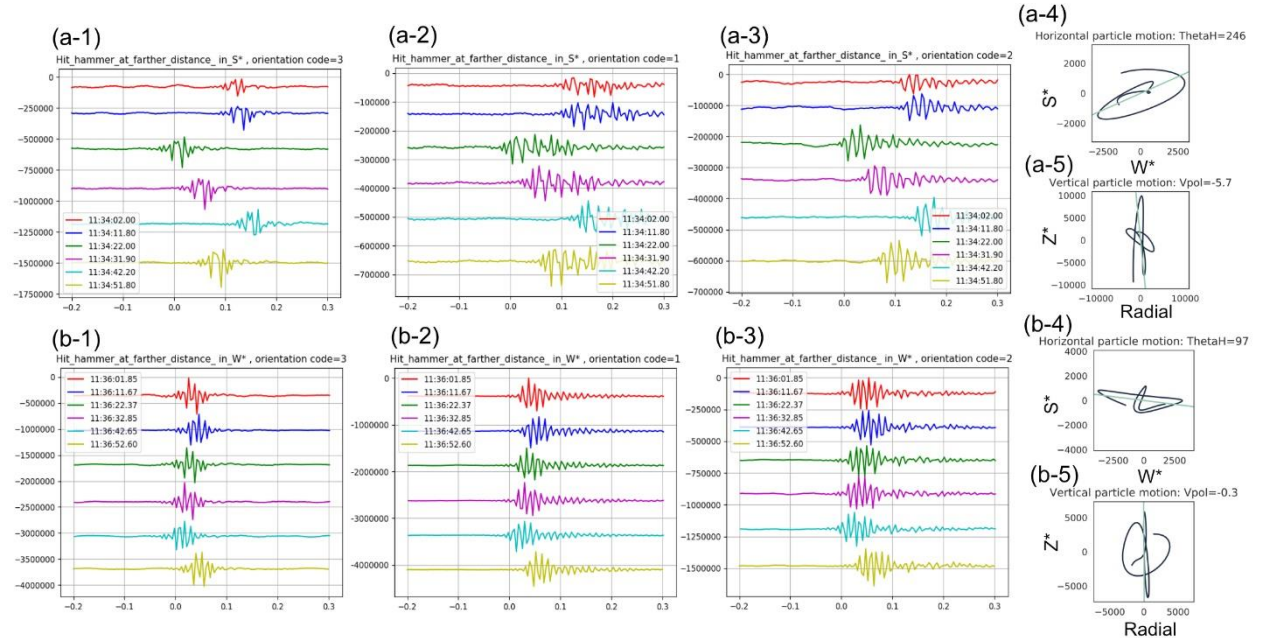


Figure B6. Signals of hitting hammer at a distance from S^* end in (a-1) Z^* , (a-2) S^* , and (3) W^* sensors. (a-4) & (a-5) are the horizontal and vertical particle motions, respectively. (b1-b5) Same as (a1-a5), but at a distance from W^* end.

APPENDIX B. TESTS ON GEOPHONE ORIENTATION

For hitting a hammer on the ground at a distance aligned to S^* and W^* directions, there was signal in all the three channels, but it is too noisy/high frequency to infer whether it was positive or negative. The particle motion analysis was done to distinguish the horizontal channels, but it is difficult to differentiate between the N and E (Figure B6).

B.4.2 Closed geophone

B.4.2.1 Lift different ends of the OBS

The goal of this test was to see if rotation tests made any sense with the geophone closed. The response was more complicated than when rotating the geophone directly, probably because the geophones are in gimbals, but there was generally a moment where the value went to one end for about 0.25s, which probably corresponds to the mass dropping to the other end. For Lifting Southern and Western end (simulating an earth movement towards S^* and W^* respectively), the signal went down (Figure B7a-1, a-2) and while lifting Northern and Eastern end (simulating an earth movement towards N^* and E^* respectively), the signal went up (Figure B7b-1, b-2). This agrees with the result of open geophone suggesting INVERTED horizontal channels. Lifting for a longer amount of time might give better results.

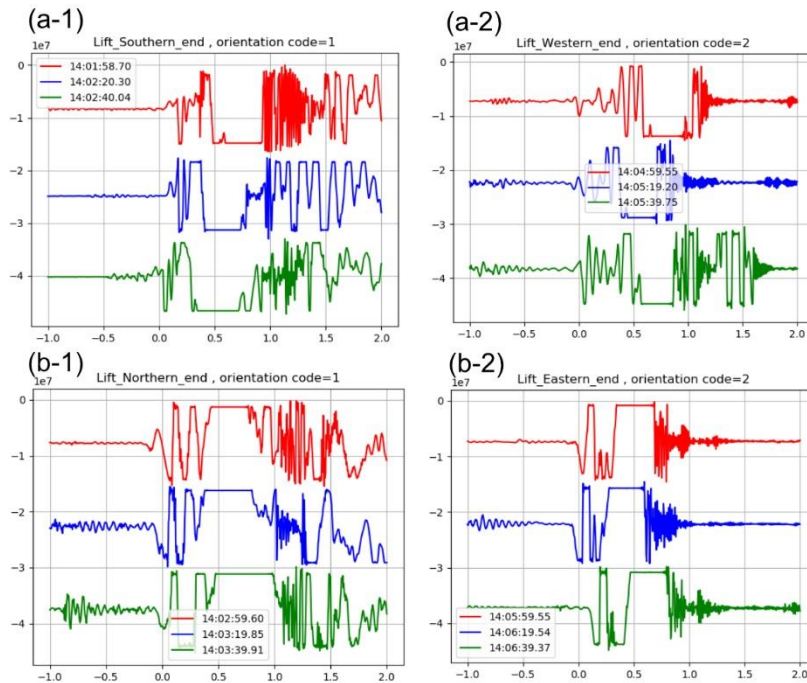


Figure B7. Signals of lifting (a-1) Southern (S^*), (a-2) Western (W^*), (b-1) Northern (N^*), and (b-2) Eastern (E^*) end of a closed geophone from a static position.

APPENDIX B. TESTS ON GEOPHONE ORIENTATION

B.4.2.2 Tapping with a rubber hammer

Like the results with an open geophone, when tapped from S^* , W^* and top, the signal went up fairly clearly (Figure B8).

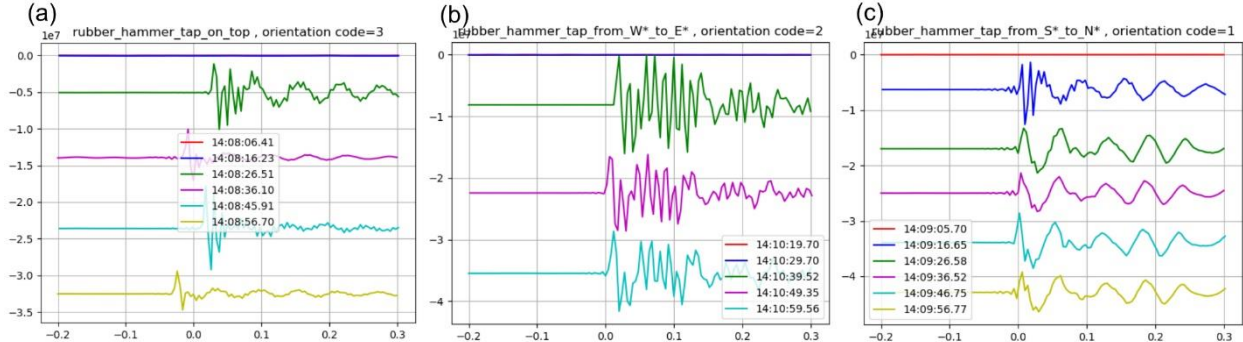


Figure B8. Signals of tapping with a cardboard on the (a) top(Z^*), (b) W^* and (c) S^* of a closed geophone.

B.4.2.3 Jumping

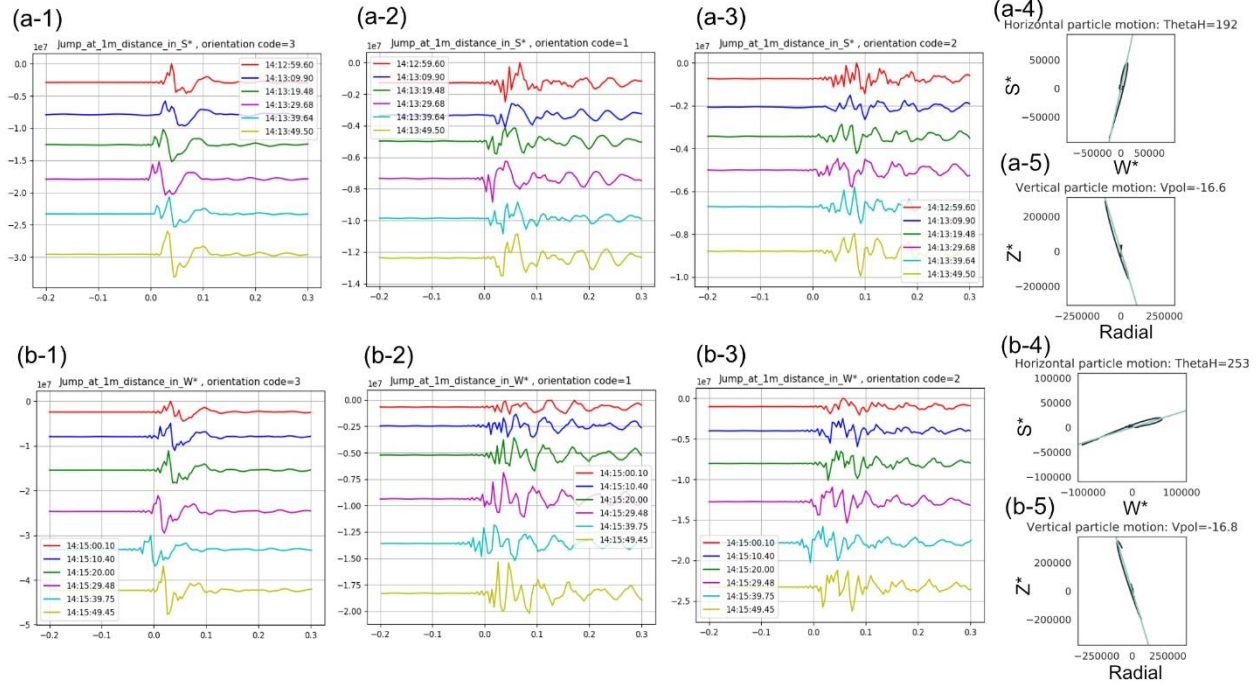


Figure B9. Signals of jumping at 1 m distance from S^* end in (a-1) Z^* , (a-2) S^* , and (3) W^* sensors. (a-4) & (a-5) are the horizontal and vertical particle motions respectively. (b1-b5) Same as (a1-a5), but the jumping was performed at 1 m distance from W^* end.

For jumping in the West direction, the signal went up in the vertical channel (Figure B9b-1), went down in channel-2, but in channel-1 it was difficult to detect any direction. Similarly, for jumping in the South direction, the signal went up in the vertical channel (Figure B9a-1), went down in channel-1, and went up in channel-2 (probably). This seems inconclusive to differentiate

APPENDIX B. TESTS ON GEOPHONE ORIENTATION

between N and E. However, the particle motion analysis of this test seems more conclusive and Jumping in South test gave a strong N-S motion (Figure B9a-4) while particle motion analysis of Jumping in West test gave almost E-W motion (Figure B9b-4). Maybe the alignment is not so good for E-W motion.

B.4.2.4 Hitting hammer on the ground

For this test, the signal went up in the vertical channel when hit in the South and West. But it is difficult to tell the direction in horizontal channels in both cases. Particle motion analysis does not give any good result either (Figure B10).

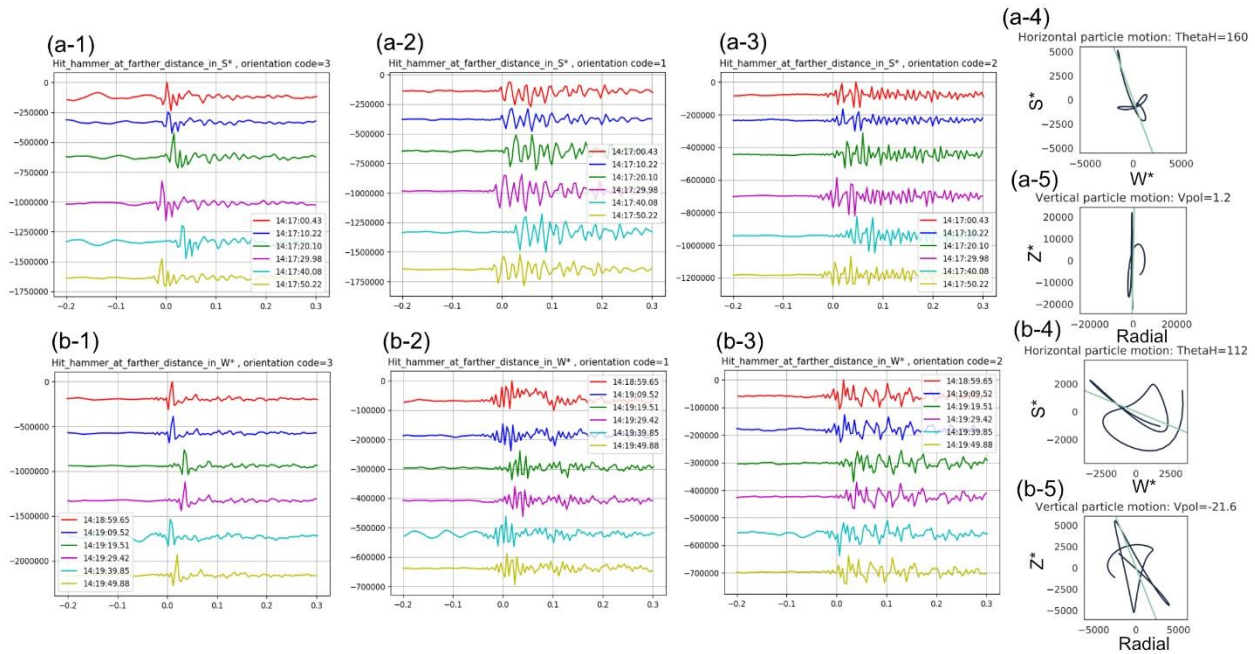


Figure B10. Signals of hitting hammer at a distance from S^* end in (a-1) Z^* , (a-2) S^* , and (3) W^* sensors. (a-4) & (a-5) are the horizontal and vertical particle motions, respectively. (b1-b5) Same as (a1-a5), but at a distance from W^* end.

B.4.3 Closed geophone (second set of tests)

B.4.3.1 Lift different ends of the OBS, crossing the horizontal

When lifting the Eastern and Western end while the other end was already lifted, it gave the same result as lifting from a static position. For the Western end, the signal goes down (Figure B11a) and for the Eastern end, the signal goes up (Figure B11b). For a similar test in N-S direction, the signal was lost due to the movement.

APPENDIX B. TESTS ON GEOPHONE ORIENTATION

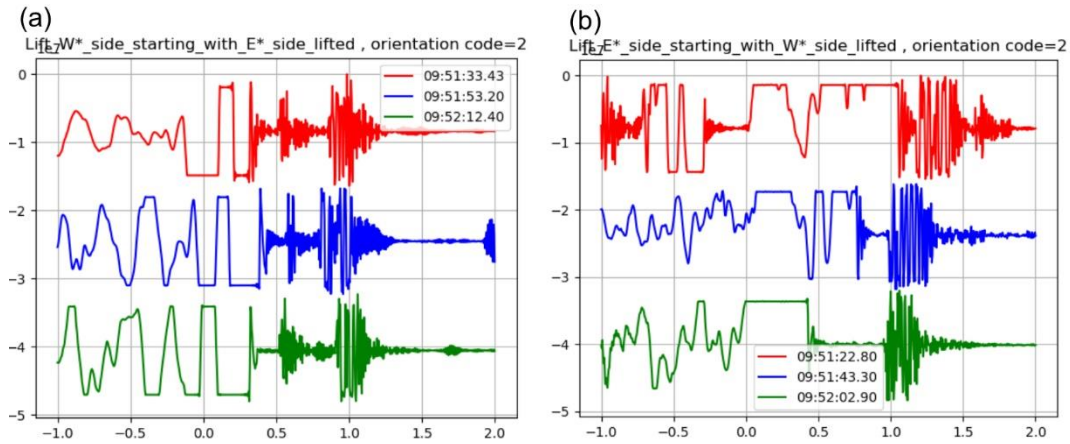


Figure B11. Signals of lifting (a) Southern (S^*) and (b) Western (W) end of a closed geophone while the opposite end lifted.

B.4.3.2 Slow lifting of OBS

When the OBS was lifted slowly, the movement was in vertically upward direction and so the signal went down in the vertical channel (Figure B12a).

B.4.3.3 Fast lifting of OBS

The signal went down similar to the above test, but it has a higher frequency than when lifted slowly. Slow lifting gives a cleaner signal and thus is more reliable (Figure B12b).

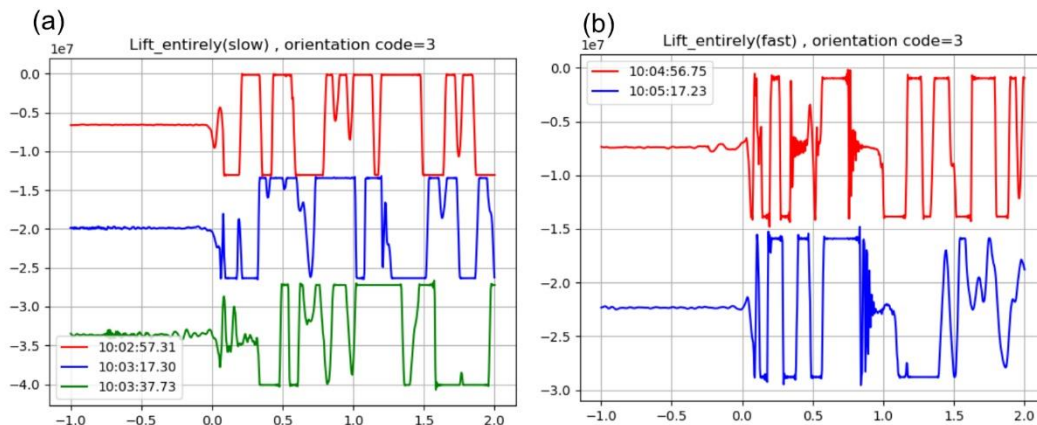


Figure B12. Signals of (a) slow, and (b) fast lifting the closed geophone entirely.

B.4.3.4 Rotate the E-W side to the vertical position

When the West side was rotated to the vertical, the signal went up first and then went down (probably when it came to the stable position, Figure B13a). And for the East side, the signal went down first and then went up (Figure B13b).

APPENDIX B. TESTS ON GEOPHONE ORIENTATION

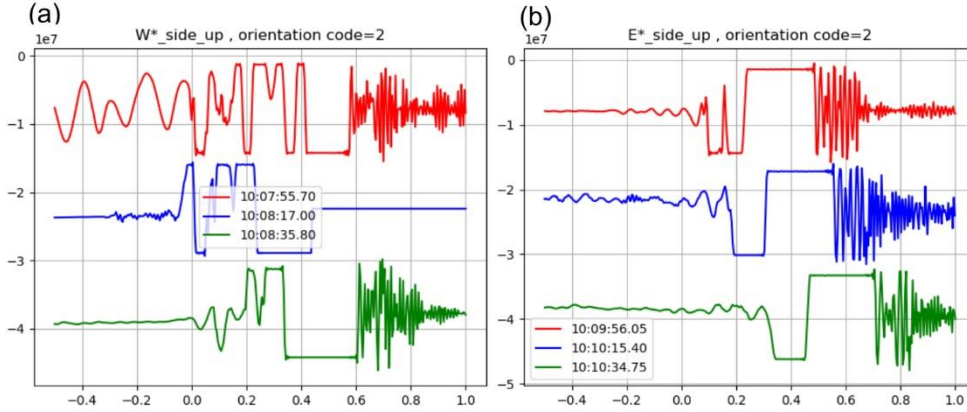


Figure B13. Signals of rotating (a) W^* , and (b) E^* side of the closed geophone to vertical position.

B.4.3.5 Squeeze the hydrophone

For squeezing the hydrophone, the signal looks complicated mostly because the hydrophone response quickly goes back to zero and it is difficult to maintain a constant pressure while squeezing. However, the first signal went down and back up exponentially and when it was released, the last signal went up and then back down exponentially. It agrees with our assumption of reverse polarity in the hydrophone (Figure B14).

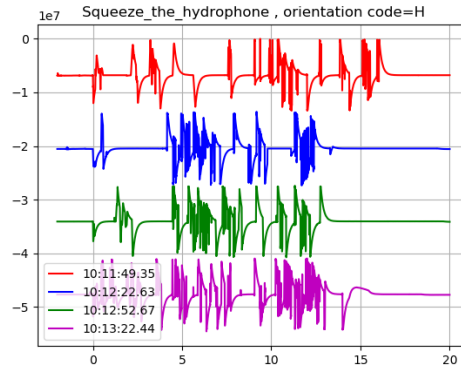


Figure B14. Signals of squeezing the hydrophone.

B.5 Recommendation

B.5.1 Naming the channels

Since both of our horizontal sensors are inverted, their relative orientation remains the same and we don't need to name the channels. So, the wired end of the N-S and E-W sensor is S^* and W^* respectively (Figure B15a). And the vertical channel should not be named "Z" and should be assigned a dip of "90".

B.5.2 Orientation of sensor in a closed OBS

The geophone case's cable plug should be away from the hydrophone. Call this end S* (Figure B15b).

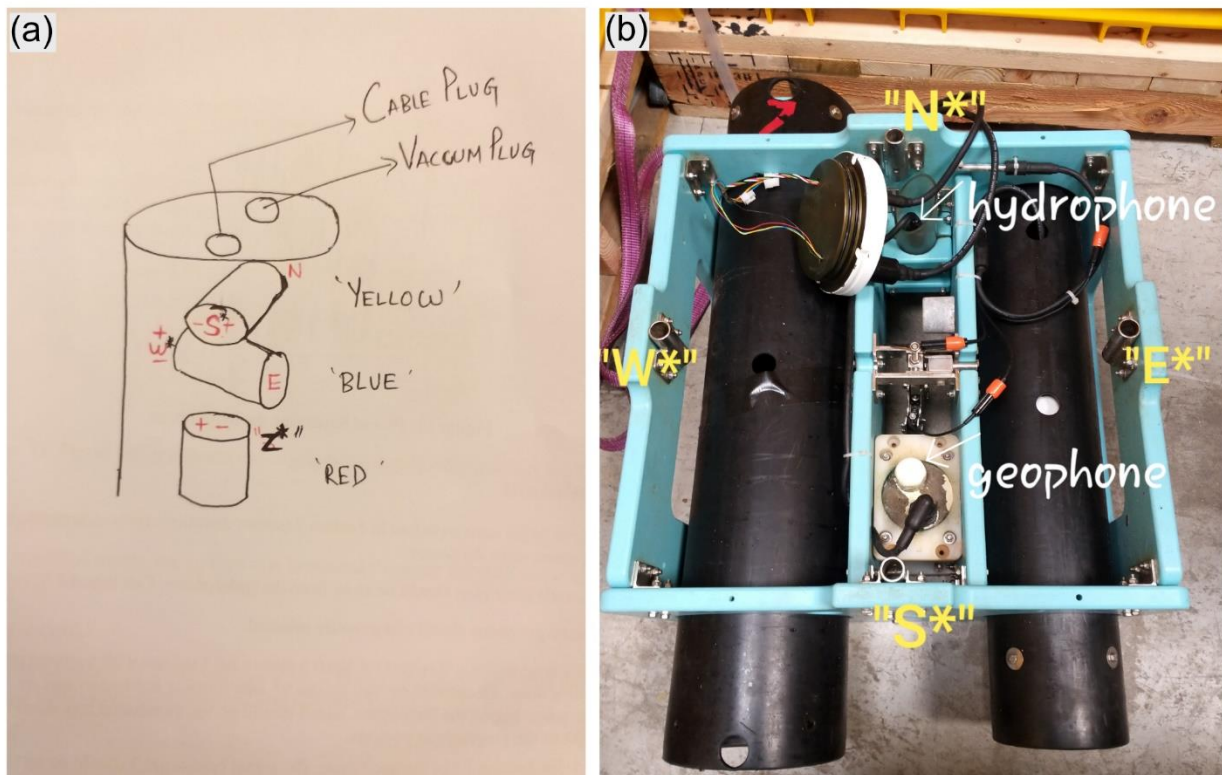


Figure B15. Recommended sensor orientations in (a) an open geophone and (b) a closed geophone.

B.5.3 Results of tests on a closed geophone

Hitting softly with cardboard or a soft hammer is probably the best way to determine polarity, while jumping at a precise angle to the sensor is probably the best way to determine if the horizontal channels are misaligned and by how much. Lifting the OBS slowly is a good second test for polarity of the vertical sensor and squeezing and releasing the hydrophone is useful for determining its polarity, but the moment of the first squeeze and the release must be carefully noted: a few seconds of calm after releasing will help you to identify which was the final release.

Tilting the OBS on its side could give some useful backup information, but it would have to be repeated several times in both directions to make sure that the results are stable. There seems to be no advantage to tilting the OBS through horizontal, which is a lot more work (needs two people) or to tilting the OBS up completely on its side, which only works in the E-W direction.

B.5.4 Recommended tests to perform on an SPOBS

1. Verify that the geophone case is oriented within the SPOBS case as shown in Figure B1b.
2. Prepare a sheet to note all actions and their times and have a watch/clock that is synchronized with the OBS clock.
3. Hit the top of the geophone with a soft rubber (or Nerf) hammer, at 5 second intervals, for 1 minute. Rest 1 minute, then hit the S* side (outside the frame with the hammer, at 5 second intervals, for 1 minute. Rest 1 minute, then hit on the W* side (over the datalogger tube) with the same pattern. Horizontal hits should be as close to the mid-height on the geophone as possible (Figure B8).
4. Jump at 2 m distance S* of the geophone, every 10 s for 1 minute. The signal on channel “3” should go up and the particle motion should be strongly N-S (Figure B9a)
5. Jump at 2 m distance W* of the geophone, every 10 s for 1 minute. The signal on channel “3” should go up the particle motion should be strongly E-W (Figure B9b).
6. Lift each end of the OBS for 15 s, put down for 15 seconds, then lift again: 4 cycles for each end. When lifting the S* (W*) ends, the channel “1” (“2”) signal should go down. When lifting the N* (E*) end, the channel “1” (“2”) signal should go up (Figure B7).
7. Lift the OBS slowly (in 1-2 s), then put it down. Repeat every 15 seconds (writing down the lift time) for one minute: The signal on channel “3” should go down (Figure B12).
8. Squeeze the hydrophone for 10 sec then release for 10 sec. Repeat the cycle 3-4 times (Figure B14).

B.5.5 Orientation in an open geophone case

If possible, open geophone and confirm that sensors are oriented/wired as specified in Table B1.

1. To check the polarity: Rubber hammer tap from S*, W* and top direction. It should give a positive signal if it has reverse polarity (Figure B4).
2. To distinguish between N* and E*: Jump at 1m distance from the geophone in S* and W* direction and do particle motion analysis. Jump in S* and W* should give N-S and E-W horizontal particle motion respectively (Figure B5).
3. Put serial numbers on all the geophone cases.

References

- Aki, K. (1965). Maximum likelihood estimate of b in the formula $\log N = a - bM$ and its confidence limits. *Bull. Earthq. Res. Inst. Tokyo Univ.*, *43*, 237–239.
- Ark, E. M. V., Detrick, R. S., Canales, J. P., Carbotte, S. M., Harding, A. J., Kent, G. M., et al. (2007). Seismic structure of the Endeavour Segment, Juan de Fuca Ridge: Correlations with seismicity and hydrothermal activity. *Journal of Geophysical Research: Solid Earth (1978–2012)*, *112*(B2). <https://doi.org/10.1029/2005jb004210>
- Arnulf, A. F., Harding, A. J., Kent, G. M., Singh, S. C., & Crawford, W. C. (2014). Constraints on the shallow velocity structure of the Lucky Strike Volcano, Mid-Atlantic Ridge, from downward continued multichannel streamer data. *Journal of Geophysical Research: Solid Earth*, *119*(2), 1119–1144. <https://doi.org/10.1002/2013jb010500>
- Arnulf, A. F., Harding, A. J., Singh, S. C., Kent, G. M., & Crawford, W. C. (2014). Nature of upper crust beneath the Lucky Strike volcano using elastic full waveform inversion of streamer data. *Geophysical Journal International*, *196*(3), 1471–1491. <https://doi.org/10.1093/gji/ggt461>
- Arnulf, A. F., Harding, A. J., Kent, G. M., & Wilcock, W. S. D. (2018). Structure, Seismicity, and Accretionary Processes at the Hot Spot-Influenced Axial Seamount on the Juan de Fuca Ridge. *Journal of Geophysical Research: Solid Earth*, *123*(6), 4618–4646. <https://doi.org/10.1029/2017jb015131>
- Baillard, C., Crawford, W. C., Ballu, V., Hibert, C., & Mangeney, A. (2014). An Automatic Kurtosis-Based P- and S-Phase Picker Designed for Local Seismic Networks. *Bulletin of the Seismological Society of America*, *104*(1), 394–409. <https://doi.org/10.1785/0120120347>
- Baillard, C., Crawford, W. C., Ballu, V., Régnier, M., Pelletier, B., & Garaebiti, E. (2015). Seismicity and shallow slab geometry in the central Vanuatu subduction zone. *Journal of Geophysical Research: Solid Earth*, *120*(8), 5606–5623. <https://doi.org/10.1002/2014jb011853>
- Ballu, V., Barreyre, T., Cannat, M., Testut, L., Crawford, W., Escartin, J., & Coulombier, T. (2019). What happened in 2015 at the Lucky Strike volcano? *Geophysical Research Abstracts*, *21*.

REFERENCES

- Barreyre, T., & Sohn, R. A. (2016). Poroelastic response of mid-ocean ridge hydrothermal systems to ocean tidal loading: Implications for shallow permeability structure. *Geophysical Research Letters*, 43(4), 1660–1668. <https://doi.org/10.1002/2015gl066479>
- Barreyre, T., Escartín, J., Garcia, R., Cannat, M., Mittelstaedt, E., & Prados, R. (2012). Structure, temporal evolution, and heat flux estimates from the Lucky Strike deep-sea hydrothermal field derived from seafloor image mosaics. *Geochemistry, Geophysics, Geosystems*, 13(4), n/a-n/a. <https://doi.org/10.1029/2011gc003990>
- Barreyre, T., Escartin, J., Sohn, R., & Cannat, M. (2014). Permeability of the Lucky Strike deep-sea hydrothermal system: Constraints from the poroelastic response to ocean tidal loading. *Earth and Planetary Science Letters*, 408, 146–154. <https://doi.org/10.1016/j.epsl.2014.09.049>
- Barreyre, T., Escartín, J., Sohn, R. A., Cannat, M., Ballu, V., & Crawford, W. C. (2014). Temporal variability and tidal modulation of hydrothermal exit-fluid temperatures at the Lucky Strike deep-sea vent field, Mid-Atlantic Ridge. *Journal of Geophysical Research: Solid Earth*, 119(4), 2543–2566. <https://doi.org/10.1002/2013jb010478>
- Barreyre, T., Olive, J., Crone, T. J., & Sohn, R. A. (2018). Depth-Dependent Permeability and Heat Output at Basalt-Hosted Hydrothermal Systems Across Mid-Ocean Ridge Spreading Rates. *Geochemistry, Geophysics, Geosystems*, 19(4), 1259–1281. <https://doi.org/10.1002/2017gc007152>
- Beaulieu, Stace. E., & Szafranski, K. M. (2020). InterRidge Global Database of Active Submarine Hydrothermal Vent Fields Version 3.4. *PANGAEA*. <https://doi.org/10.1594/pangaea.917894>
- Behn, M. D., & Ito, G. (2008). Magmatic and tectonic extension at mid-ocean ridges: 1. Controls on fault characteristics. *Geochemistry, Geophysics, Geosystems*, 9(8), n/a-n/a. <https://doi.org/10.1029/2008gc001965>
- Bischoff, J. L., & Rosenbauer, R. J. (1985). An empirical equation of state for hydrothermal seawater (3.2 percent NaCl). *American Journal of Science*, 285, 725–763.
- Bohnenstiehl, D. R., Waldhauser, F., & Tolstoy, M. (2008). Frequency-magnitude distribution of microearthquakes beneath the 9°50'N region of the East Pacific Rise, October 2003 through April 2004. *Geochemistry, Geophysics, Geosystems*, 9(10), n/a-n/a. <https://doi.org/10.1029/2008gc002128>
- Bohnenstiehl, DelWayne R., & Carbotte, S. M. (2001). Faulting patterns near 19°30'S on the East Pacific Rise: Fault formation and growth at a superfast spreading center. *Geochemistry, Geophysics, Geosystems*, 2(9), n/a-n/a. <https://doi.org/10.1029/2001gc000156>
- Bohnenstiehl, DelWayne R., Dziak, R. P., Tolstoy, M., Fox, C. G., & Fowler, M. (2004). Temporal and spatial history of the 1999–2000 Endeavour Segment seismic series, Juan de

REFERENCES

- Fuca Ridge. *Geochemistry, Geophysics, Geosystems*, 5(9), n/a-n/a.
<https://doi.org/10.1029/2004gc000735>
- Buck, W. R., Lavier, L. L., & Poliakov, A. N. B. (2005). Modes of faulting at mid-ocean ridges. *Nature*, 434(7034), 719–723. <https://doi.org/10.1038/nature03358>
- Butterfield, D. A., Roe, K. K., Lilley, M. D., Huber, J. A., Baross, J. A., Embley, R. W., & Massoth, G. J. (2004). Mixing, Reaction and Microbial Activity in the Sub-seafloor Revealed by Temporal and Spatial Variation in Diffuse Flow Vents at Axial Volcano. *The Subseafloor Biosphere at Mid-Ocean Ridges Geophysical Monograph Series*, 144.
- Canales, J. P., Dunn, R. A., Arai, R., & Sohn, R. A. (2017). Seismic imaging of magma sills beneath an ultramafic-hosted hydrothermal system. *Geology*, 45(5), 451–454.
<https://doi.org/10.1130/g38795.1>
- Cann, J. R., & Strens, M. R. (1989). Modeling periodic megaplume emission by black smoker systems. *Journal of Geophysical Research: Solid Earth*, 94(B9), 12227–12237.
<https://doi.org/10.1029/jb094ib09p12227>
- Cann, J. R., Blackman, D. K., Smith, D. K., McAllister, E., Janssen, B., Mello, S., et al. (1997). Corrugated slip surfaces formed at ridge–transform intersections on the Mid-Atlantic Ridge. *Nature*, 385(6614), 329–332. <https://doi.org/10.1038/385329a0>
- Cannat, M. (1993). Emplacement of mantle rocks in the seafloor at mid-ocean ridges. *Journal of Geophysical Research: Solid Earth*, 98(B3), 4163–4172. <https://doi.org/10.1029/92jb02221>
- Cannat, M., Mevel, C., Maia, M., Deplus, C., Durand, C., Gente, P., et al. (1995). Thin crust, ultramafic exposures, and rugged faulting patterns at the Mid-Atlantic Ridge (22°–24°N). *Geology*, 23(1), 49–52. [https://doi.org/10.1130/0091-7613\(1995\)023<0049:tcuear>2.3.co;2](https://doi.org/10.1130/0091-7613(1995)023<0049:tcuear>2.3.co;2)
- Carbotte, S., & Macdonald, K. (1992). East Pacific Rise 8°–10°30'N: Evolution of ridge segments and discontinuities from SeaMARC II and three-dimensional magnetic studies. *Journal of Geophysical Research: Solid Earth*, 97(B5), 6959–6982.
<https://doi.org/10.1029/91jb03065>
- Carbotte, S., Canales, J. P., Nedimović, M., Carton, H., & Mutter, J. (2012). Recent Seismic Studies at the East Pacific Rise 8°20'–10°10'N and Endeavour Segment: Insights into Mid-Ocean Ridge Hydrothermal and Magmatic Processes. *Oceanography*, 25(1), 100–112.
<https://doi.org/10.5670/oceanog.2012.08>
- Carbotte, S. M., Marjanović, M., Carton, H., Mutter, J. C., Canales, J. P., Nedimović, M. R., et al. (2013). Fine-scale segmentation of the crustal magma reservoir beneath the East Pacific Rise. *Nature Geoscience*, 6(10), 866–870. <https://doi.org/10.1038/ngeo1933>

REFERENCES

- Carbotte, S. M., Arnulf, A., Spiegelman, M., Lee, M., Harding, A., Kent, G., et al. (2020). Stacked sills forming a deep melt-mush feeder conduit beneath Axial Seamount. *Geology*, 48(7), 693–697. <https://doi.org/10.1130/g47223.1>
- Carbotte, S. M., Marjanović, M., Arnulf, A. F., Nedimović, M. R., Canales, J. P., & Arnoux, G. M. (2021). Stacked Magma Lenses Beneath Mid-Ocean Ridges: Insights From New Seismic Observations and Synthesis With Prior Geophysical and Geologic Findings. *Journal of Geophysical Research: Solid Earth*, 126(4). <https://doi.org/10.1029/2020jb021434>
- Carlson, R. L. (1998). Seismic velocities in the uppermost oceanic crust: Age dependence and the fate of layer 2A. *Journal of Geophysical Research: Solid Earth*, 103(B4), 7069–7077. <https://doi.org/10.1029/97jb03577>
- Carlson, R. L. (2014). The influence of porosity and crack morphology on seismic velocity and permeability in the upper oceanic crust. *Geochemistry, Geophysics, Geosystems*, 15(1), 10–27. <https://doi.org/10.1002/2013gc004965>
- Carlson, R. L., & Raskin, G. S. (1984). Density of the ocean crust. *Nature*, 311(5986), 555–558. <https://doi.org/10.1038/311555a0>
- Chadwick, J., Perfit, M., Ridley, I., Jonasson, I., Kamenov, G., Chadwick, W., et al. (2005). Magmatic effects of the Cobb hot spot on the Juan de Fuca Ridge. *Journal of Geophysical Research: Solid Earth*, 110(B3). <https://doi.org/10.1029/2003jb002767>
- Chatelain, J. L. (1978). *Etude fine de la sismicité en zone de collision continentale au moyen d'un réseau de stations portables : la région Hindu-Kush Pamir*.
- Chen, J., Cannat, M., Tao, C., Sauter, D., & Munschy, M. (2021). 780 Thousand Years of Upper-Crustal Construction at a Melt-Rich Segment of the Ultraslow Spreading Southwest Indian Ridge 50°28'E. *Journal of Geophysical Research: Solid Earth*, 126(10). <https://doi.org/10.1029/2021jb022152>
- Christeson, G. L., Purdy, G. M., & Fryer, G. J. (1992). Structure of young upper crust at the East Pacific Rise near 9°30'N. *Geophysical Research Letters*, 19(10), 1045–1048. <https://doi.org/10.1029/91gl00971>
- Christeson, G. L., Purdy, G. M., & Fryer, G. J. (1994). Seismic constraints on shallow crustal emplacement processes at the fast spreading East Pacific Rise. *Journal of Geophysical Research: Solid Earth*, 99(B9), 17957–17973. <https://doi.org/10.1029/94jb01252>
- Christeson, G. L., Goff, J. A., & Reece, R. S. (2019). Synthesis of Oceanic Crustal Structure From Two-Dimensional Seismic Profiles. *Reviews of Geophysics*, 57(2), 504–529. <https://doi.org/10.1029/2019rg000641>

REFERENCES

- Christeson, Gail L., McIntosh, K. D., & Karson, J. A. (2007). Inconsistent correlation of seismic layer 2a and lava layer thickness in oceanic crust. *Nature*, 445(7126), 418–421.
<https://doi.org/10.1038/nature05517>
- Combiér, V., Seher, T., Singh, S. C., Crawford, W. C., Cannat, M., Escartín, J., & Dusanur, D. (2015). Three-dimensional geometry of axial magma chamber roof and faults at Lucky Strike volcano on the Mid-Atlantic Ridge. *Journal of Geophysical Research: Solid Earth*, 120(8), 5379–5400. <https://doi.org/10.1002/2015jb012365>
- Cooper, M. J., Elderfield, H., & Schultz, A. (2000). Diffuse hydrothermal fluids from Lucky Strike hydrothermal vent field: Evidence for a shallow conductively heated system. *Journal of Geophysical Research: Solid Earth*, 105(B8), 19369–19375.
<https://doi.org/10.1029/2000jb900138>
- Corliss, J. B., Dymond, J., Gordon, L. I., Edmond, J. M., Herzen, R. P. von, Ballard, R. D., et al. (1979). Submarine Thermal Springs on the Galápagos Rift. *Science*, 203(4385), 1073–1083.
<https://doi.org/10.1126/science.203.4385.1073>
- Coumou, D., Driesner, T., & Heinrich, C. A. (2008). The Structure and Dynamics of Mid-Ocean Ridge Hydrothermal Systems. *Science*, 321(5897), 1825–1828.
<https://doi.org/10.1126/science.1159582>
- Coumou, D., Driesner, T., Geiger, S., Paluszny, A., & Heinrich, C. A. (2009). High-resolution three-dimensional simulations of mid-ocean ridge hydrothermal systems. *Journal of Geophysical Research: Solid Earth (1978–2012)*, 114(B7).
<https://doi.org/10.1029/2008jb006121>
- Coumou, Dim, Driesner, T., Geiger, S., Heinrich, C. A., & Matthäi, S. (2006). The dynamics of mid-ocean ridge hydrothermal systems: Splitting plumes and fluctuating vent temperatures. *Earth and Planetary Science Letters*, 245(1–2), 218–231.
<https://doi.org/10.1016/j.epsl.2006.02.044>
- Crawford, W. C., Singh, S. C., Seher, T., Combiér, V., Dusanur, D., & Cannat, M. (2010). Crustal Structure, Magma Chamber, and Faulting Beneath the Lucky Strike Hydrothermal Vent Field.
- Crawford, W. C., Rai, A., Singh, S. C., Cannat, M., Escartín, J., Wang, H., et al. (2013). Hydrothermal seismicity beneath the summit of Lucky Strike volcano, Mid-Atlantic Ridge. *Earth and Planetary Science Letters*, 373, 118–128.
<https://doi.org/10.1016/j.epsl.2013.04.028>
- Crawford, Wayne C., Web, Spahr C., & Hildebrand, J. (1999). Constraints on melt in the lower crust and Moho at the East Pacific Rise, 9°48'N, using seafloor compliance measurement.
- Cuvelier, D., Sarrazin, J., Colaço, A., Copley, J., Desbruyères, D., Glover, A. G., et al. (2009). Distribution and spatial variation of hydrothermal faunal assemblages at Lucky Strike (Mid-

REFERENCES

- Atlantic Ridge) revealed by high-resolution video image analysis. *Deep Sea Research Part I: Oceanographic Research Papers*, 56(11), 2026–2040.
<https://doi.org/10.1016/j.dsr.2009.06.006>
- Dawson, P. B., Benítez, M. C., Lowenstern, J. B., & Chouet, B. A. (2012). Identifying bubble collapse in a hydrothermal system using hidden Markov models. *Geophysical Research Letters*, 39(1), n/a-n/a. <https://doi.org/10.1029/2011gl049901>
- Demartin, B., Hirth, G., & Evans, B. (2004). Experimental Constraints on Thermal Cracking of Peridotite at Oceanic Spreading Centers. *Geophysical Monograph Series*, 167–185.
<https://doi.org/10.1029/148gm07>
- deMartin, B. J., Sohn, R. A., Canales, J. P., & Humphris, S. E. (2007). Kinematics and geometry of active detachment faulting beneath the Trans-Atlantic Geotraverse (TAG) hydrothermal field on the Mid-Atlantic Ridge. *Geology*, 35(8), 711–714. <https://doi.org/10.1130/g23718a.1>
- DeMets, C., 2, R. G. G., 3, D. F. A., & Stein, and Seth. (1994). Effect of recent revisions to the geomagnetic reversal time scale on estimates of current plate motions.
- Detrick, R. S., Needham, H. D., & Renard, V. (1995). Gravity anomalies and crustal thickness variations along the Mid-Atlantic Ridge between 33°N and 40°N.
- Doran, A. K., & Laske, G. (2017). Ocean-Bottom Seismometer Instrument Orientations via Automated Rayleigh-Wave Arrival-Angle Measurements Ocean-Bottom Seismometer Instrument Orientations via Automated Rayleigh-Wave Arrival-Angle Measurements. *Bulletin of the Seismological Society of America*, 107(2), 691–708.
<https://doi.org/10.1785/0120160165>
- Duennebier, F. K., Anderson, P. N., & Fryer, G. J. (1987). Azimuth determination of and from horizontal ocean bottom seismic sensors. *Journal of Geophysical Research: Solid Earth*, 92(B5), 3567–3572. <https://doi.org/10.1029/jb092ib05p03567>
- Dunn, R. A., Toomey, D. R., & Solomon, S. C. (2000). Three-dimensional seismic structure and physical properties of the crust and shallow mantle beneath the East Pacific Rise at 9°30'N. *Journal of Geophysical Research: Solid Earth*, 105(B10), 23537–23555.
<https://doi.org/10.1029/2000jb900210>
- Dziak, R., Hammond, S., & Fox, C. (2011). A 20-Year Hydroacoustic Time Series of Seismic and Volcanic Events in the Northeast Pacific Ocean. *Oceanography*, 24(3), 280–293.
<https://doi.org/10.5670/oceanog.2011.79>
- Dziak, R. P., Haxel, J. H., Bohnenstiehl, D. R., Chadwick, W. W., Nooner, S. L., Fowler, M. J., et al. (2012). Seismic precursors and magma ascent before the April 2011 eruption at Axial Seamount. *Nature Geoscience*, 5(7), 478–482. <https://doi.org/10.1038/ngeo1490>

REFERENCES

- Dziak, Robert P., & Fox, C. G. (1999). The January 1998 Earthquake swarm at Axial Volcano, Juan de Fuca Ridge: Hydroacoustic evidence of seafloor volcanic activity. *Geophysical Research Letters*, 26(23), 3429–3432. <https://doi.org/10.1029/1999gl002332>
- Dziak, Robert P., Smith, D. K., Bohnenstiehl, D. R., Fox, C. G., Desbruyeres, D., Matsumoto, H., et al. (2004). Evidence of a recent magma dike intrusion at the slow spreading Lucky Strike segment, Mid-Atlantic Ridge. *Journal of Geophysical Research: Solid Earth (1978–2012)*, 109(B12). <https://doi.org/10.1029/2004jb003141>
- Edmond, J. M., Measures, C., Mangum, B., Grant, B., Sclater, F. R., Collier, R., et al. (1979). On the formation of metal-rich deposits at ridge crests. *Earth and Planetary Science Letters*, 46(1), 19–30. [https://doi.org/10.1016/0012-821x\(79\)90062-1](https://doi.org/10.1016/0012-821x(79)90062-1)
- Edmond, J. M., Measures, C., McDuff, R. E., Chan, L. H., Collier, R., Grant, B., et al. (1979). Ridge crest hydrothermal activity and the balances of the major and minor elements in the ocean: The Galapagos data. *Earth and Planetary Science Letters*, 46(1), 1–18. [https://doi.org/10.1016/0012-821x\(79\)90061-x](https://doi.org/10.1016/0012-821x(79)90061-x)
- Elderfield, H., & Schultz, A. (1996). MID-OCEAN RIDGE HYDROTHERMAL FLUXES AND THE CHEMICAL COMPOSITION OF THE OCEAN. *Earth and Planetary Science Letters*, 191–224. <https://doi.org/10.1146/annurev.earth.24.1.191>
- Escartín, J., & Canales, J. P. (2011). Detachments in Oceanic Lithosphere: Deformation, Magmatism, Fluid Flow, and Ecosystems. *Eos, Transactions American Geophysical Union*, 92(4), 31–31. <https://doi.org/10.1029/2011eo040003>
- Escartín, J., Smith, D. K., Cann, J., Schouten, H., Langmuir, C. H., & Escrig, S. (2008). Central role of detachment faults in accretion of slow-spreading oceanic lithosphere. *Nature*, 455(7214), 790–794. <https://doi.org/10.1038/nature07333>
- Escartín, J., Soule, S. A., Cannat, M., Fornari, D. J., Düşünür, D., & Garcia, R. (2014). Lucky Strike seamount: Implications for the emplacement and rifting of segment-centered volcanoes at slow spreading mid-ocean ridges. *Geochemistry, Geophysics, Geosystems*, 15(11), 4157–4179. <https://doi.org/10.1002/2014gc005477>
- Escartín, J., Barreyre, T., Cannat, M., Garcia, R., Gracias, N., Deschamps, A., et al. (2015). Hydrothermal activity along the slow-spreading Lucky Strike ridge segment (Mid-Atlantic Ridge): Distribution, heatflux, and geological controls. *Earth and Planetary Science Letters*, 431, 173–185. <https://doi.org/10.1016/j.epsl.2015.09.025>
- Escartín, J., Mével, C., Petersen, S., Bonnemains, D., Cannat, M., Andreani, M., et al. (2017). Tectonic structure, evolution, and the nature of oceanic core complexes and their detachment fault zones (13°20'N and 13°30'N, Mid Atlantic Ridge). *Geochemistry, Geophysics, Geosystems*, 18(4), 1451–1482. <https://doi.org/10.1002/2016gc006775>

REFERENCES

- Evans, Rob. L. (1994). Constraints On the Large-Scale Porosity and Permeability Structure of Young Oceanic Crust From Velocity and Resistivity Data. *Geophysical Journal International*, 119(3), 869–879. <https://doi.org/10.1111/j.1365-246x.1994.tb04023.x>
- Fisher, A. T., Davis, E. E., & Becker, K. (2008). Borehole-to-borehole hydrologic response across 2.4 km in the upper oceanic crust: Implications for crustal-scale properties. *Journal of Geophysical Research: Solid Earth (1978–2012)*, 113(B7). <https://doi.org/10.1029/2007jb005447>
- Fontaine, F. J., & Wilcock, W. S. D. (2007). Two-dimensional numerical models of open-top hydrothermal convection at high Rayleigh and Nusselt numbers: Implications for mid-ocean ridge hydrothermal circulation. *Geochemistry, Geophysics, Geosystems*, 8(7), n/a-n/a. <https://doi.org/10.1029/2007gc001601>
- Fontaine, F. J., Olive, J., Cannat, M., Escartin, J., & Perol, T. (2011). Hydrothermally-induced melt lens cooling and segmentation along the axis of fast- and intermediate-spreading centers. *Geophysical Research Letters*, 38(14), n/a-n/a. <https://doi.org/10.1029/2011gl047798>
- Fontaine, F. J., Cannat, M., Escartin, J., & Crawford, W. C. (2014). Along-axis hydrothermal flow at the axis of slow spreading Mid-Ocean Ridges: Insights from numerical models of the Lucky Strike vent field (MAR). *Geochemistry, Geophysics, Geosystems*, 15(7), 2918–2931. <https://doi.org/10.1002/2014gc005372>
- Fontaine, F. R., Barruol, G., Kennett, B. L. N., Bokelmann, G. H. R., & Reymond, D. (2009). Upper mantle anisotropy beneath Australia and Tahiti from P wave polarization: Implications for real-time earthquake location. *Journal of Geophysical Research: Solid Earth*, 114(B3). <https://doi.org/10.1029/2008jb005709>
- Fornari, D. J., Haymon, R. M., Perfit, M. R., Gregg, T. K. P., & Edwards, M. H. (1998). Axial summit trough of the East Pacific Rise 9°–10°N: Geological characteristics and evolution of the axial zone on fast spreading mid-ocean ridge. *Journal of Geophysical Research: Solid Earth*, 103(B5), 9827–9855. <https://doi.org/10.1029/98jb00028>
- Fouquet, Y., Ondréas, H., Charlou, J.-L., Donval, J.-P., Radford-Knoery, J., Costa, I., et al. (1995). Atlantic lava lakes and hot vents. *Nature*, 377(6546), 201–201. <https://doi.org/10.1038/377201a0>
- Frohlich, C. (2001). Display and quantitative assessment of distributions of earthquake focal mechanisms. *Geophysical Journal International*, 144(2), 300–308. <https://doi.org/10.1046/j.1365-246x.2001.00341.x>
- Grigoli, F., Cesca, S., Dahm, T., & Krieger, L. (2012). A complex linear least-squares method to derive relative and absolute orientations of seismic sensors. *Geophysical Journal International*, 188(3), 1243–1254. <https://doi.org/10.1111/j.1365-246x.2011.05316.x>

REFERENCES

- Guo, Z., Rüpke, L. H., Fuchs, S., Iyer, K., Hannington, M. D., Chen, C., et al. (2020). Anhydrite-Assisted Hydrothermal Metal Transport to the Ocean Floor—Insights From Thermo-Hydro-Chemical Modeling. *Journal of Geophysical Research: Solid Earth*, 125(7). <https://doi.org/10.1029/2019jb019035>
- Harding, A. J., Kent, G. M., & Orcutt, John. A. (1993). A multichannel seismic investigation of upper crustal structure at 9°N on the East Pacific Rise: Implications for crustal accretion. *Journal of Geophysical Research: Solid Earth*, 98(B8), 13925–13944. <https://doi.org/10.1029/93jb00886>
- Hess, H. H. (1962). Petrologic Studies, 599–620. <https://doi.org/10.1130/petrologic.1962.599>
- Hooft, E. E. E., Patel, H., Wilcock, W., Becker, K., Butterfield, D., Davis, E., et al. (2010). A seismic swarm and regional hydrothermal and hydrologic perturbations: The northern Endeavour segment, February 2005. *Geochemistry, Geophysics, Geosystems*, 11(12), n/a-n/a. <https://doi.org/10.1029/2010gc003264>
- Horning, G., Sohn, R. A., Canales, J. P., & Dunn, R. A. (2018). Local Seismicity of the Rainbow Massif on the Mid-Atlantic Ridge. *Journal of Geophysical Research: Solid Earth*, 123(2), 1615–1630. <https://doi.org/10.1002/2017jb015288>
- Humphris, S. E., & McCollom, T. (1998). The cauldron beneath the seafloor. *Oceanus*, 41, 18.
- Humphris, S. E., & Tivey, M. K. (2000). A synthesis of geological and geochemical investigations of the TAG hydrothermal field: Insights into fluid-flow and mixing processes in a hydrothermal system. *Special Papers-Geological Society of America*, 213–236.
- Humphris, S.E., Herzig, P. M., & Miller, D. J. (1996). Ocean Drilling Program Initial Reports Volume 158, 158.
- Humphris, Susan E., & Cann, J. R. (2000). Constraints on the energy and chemical balances of the modern TAG and ancient Cyprus seafloor sulfide deposits. *Journal of Geophysical Research: Solid Earth*, 105(B12), 28477–28488. <https://doi.org/10.1029/2000jb900289>
- Humphris, Susan E., & Kleinrock, M. C. (1996). Detailed morphology of the TAG Active Hydrothermal Mound: Insights into its formation and growth. *Geophysical Research Letters*, 23(23), 3443–3446. <https://doi.org/10.1029/96gl03079>
- Humphris, Susan E., Fornari, D. J., Scheirer, D. S., German, C. R., & Parson, L. M. (2002). Geotectonic setting of hydrothermal activity on the summit of Lucky Strike Seamount (37°17'N, Mid-Atlantic Ridge). *Geochemistry, Geophysics, Geosystems*, 3(8), 1–25. <https://doi.org/10.1029/2001gc000284>
- Humphris, Susan E., Tivey, M. K., & Tivey, M. A. (2015). The Trans-Atlantic Geotraverse hydrothermal field: A hydrothermal system on an active detachment fault. *Deep Sea Research*

REFERENCES

- Part II: Topical Studies in Oceanography*, 121, 8–16.
<https://doi.org/10.1016/j.dsr2.2015.02.015>
- Janiszewski, H. A., & Abers, G. A. (2015). Imaging the Plate Interface in the Cascadia Seismogenic Zone: New Constraints from Offshore Receiver Functions. *Seismological Research Letters*, 86(5), 1261–1269. <https://doi.org/10.1785/0220150104>
- Jian, H., Singh, S. C., Chen, Y. J., & Li, J. (2017). Evidence of an axial magma chamber beneath the ultraslow-spreading Southwest Indian Ridge. *Geology*, 45(2), 143–146. <https://doi.org/10.1130/g38356.1>
- Jian, H., Chen, Y. J., Singh, S. C., Li, J., Zhao, M., Ruan, A., & Qiu, X. (2017). Seismic structure and magmatic construction of crust at the ultraslow-spreading Southwest Indian Ridge at 50°28'E. *Journal of Geophysical Research: Solid Earth*, 122(1), 18–42. <https://doi.org/10.1002/2016jb013377>
- Juniper, S. K., Martineu, P., Sarrazin, J., & G elinas, Y. (1995). Microbial-mineral floc associated with nascent hydrothermal activity on CoAxial Segment, Juan de Fuca Ridge. *Geophysical Research Letters*, 22(2), 179–182. <https://doi.org/10.1029/94gl02436>
- Jupp, T. E., & Schultz, A. (2004). Physical balances in subseafloor hydrothermal convection cells. *Journal of Geophysical Research: Solid Earth*, 109(B5). <https://doi.org/10.1029/2003jb002697>
- Kedar, S., Sturtevant, B., & Kanamori, H. (1996). The origin of harmonic tremor at Old Faithful geyser. *Nature*, 379(6567), 708–711. <https://doi.org/10.1038/379708a0>
- Kedar, S., Kanamori, H., & Sturtevant, B. (1998). Bubble collapse as the source of tremor at Old Faithful Geyser. *Journal of Geophysical Research: Solid Earth*, 103(B10), 24283–24299. <https://doi.org/10.1029/98jb01824>
- Kelley, D. S., Delaney, J. R., & Juniper, S. K. (2014). Establishing a new era of submarine volcanic observatories: Cabling Axial Seamount and the Endeavour Segment of the Juan de Fuca Ridge. *Marine Geology*, 352, 426–450. <https://doi.org/10.1016/j.margeo.2014.03.010>
- Klischies, M., Petersen, S., & Devey, C. W. (2019). Geological mapping of the Menez Gwen segment at 37°50'N on the Mid-Atlantic Ridge: Implications for accretion mechanisms and associated hydrothermal activity at slow-spreading mid-ocean ridges. *Marine Geology*, 412, 107–122. <https://doi.org/10.1016/j.margeo.2019.03.012>
- Krischer, L. (2015). hypoDDpy: hypoDDpy 1.0. <https://doi.org/10.5281/zenodo.18907>
- Lalou, CLAUDE, REYSS, J.-L., BRICHET, E., ARNOLD, M., THOMPSON, G., FOUQUET, Y., & RONA, P. A. (1993). New Age Data for Mid-Atlantic Ridge Hydrothermal Sites' TAG and Snakepit Chronology Revisited. *Journal of Geophysical Research*.

REFERENCES

- Lalou, Claude, Reyss, J., Brichet, E., Rona, P. A., & Thompson, G. (1995). Hydrothermal activity on a 105-year scale at a slow-spreading ridge, TAG hydrothermal field, Mid-Atlantic Ridge 26°N. *Journal of Geophysical Research: Solid Earth*, 100(B9), 17855–17862. <https://doi.org/10.1029/95jb01858>
- Langmuir, C., Humphris, S., Fornari, D., Dover, C. V., Damm, K. V., Tivey, M. K., et al. (1997). Hydrothermal vents near a mantle hot spot: the Lucky Strike vent field at 37°N on the Mid-Atlantic Ridge. *Earth and Planetary Science Letters*, 148(1–2), 69–91. [https://doi.org/10.1016/s0012-821x\(97\)00027-7](https://doi.org/10.1016/s0012-821x(97)00027-7)
- Leet, R. C. (1988). Saturated and subcooled hydrothermal boiling in groundwater flow channels as a source of harmonic tremor. *Journal of Geophysical Research: Solid Earth*, 93(B5), 4835–4849. <https://doi.org/10.1029/jb093ib05p04835>
- Levy, S., Bohnenstiehl, D. R., Sprinkle, P., Boettcher, M. S., Wilcock, W. S. D., Tolstoy, M., & Waldhauser, F. (2018). Mechanics of fault reactivation before, during, and after the 2015 eruption of Axial Seamount. *Geology*, 46(5), 447–450. <https://doi.org/10.1130/g39978.1>
- Lienert, Barry R., & Havskov, J. (1995). A Computer Program for Locating Earthquakes Both Locally and Globally. *Seismological Research Letters*, 66(5), 26–36. <https://doi.org/10.1785/gssrl.66.5.26>
- Lienert, BARRY R., BERG, E., & FRAZER, L. N. (1986). HYPOCENTER: AN EARTHQUAKE LOCATION METHOD USING CENTERED, SCALED, AND ADAPTIVELY DAMPED LEAST SQUARES. *Bulletin of the Seismological Society of America*.
- Lim, H., Kim, Y., Song, T.-R. A., & Shen, X. (2017). Measurement of seismometer orientation using the tangential P-wave receiver function based on harmonic decomposition. *Geophysical Journal International*, 212(3), 1747–1765. <https://doi.org/10.1093/gji/ggx515>
- Lin, J., Purdy, G. M., Schouten, H., Sempere, J.-C., & Zervas, C. (1990). Evidence from gravity data for focused magmatic accretion along the Mid-Atlantic Ridge. *Nature*, 344(6267), 627–632. <https://doi.org/10.1038/344627a0>
- Lister, C. R. B. (1972). On the Thermal Balance of a Mid-Ocean Ridge. *Geophysical Journal of the Royal Astronomical Society*, 26(5), 515–535. <https://doi.org/10.1111/j.1365-246x.1972.tb05766.x>
- Liu, Y., Liu, S., Wang, C., & Wang, L. (2014). A New North-seeking Method Based on MEMS Gyroscope. *Sensors & Transducers*, 178(9), 14–19.
- Lomax, A., Virieux, J., Volant, P., & Berge-Thierry, C. (2000). Advances in Seismic Event Location. *Modern Approaches in Geophysics*, 101–134. https://doi.org/10.1007/978-94-015-9536-0_5

REFERENCES

- Lonsdale, P. (1977). Clustering of suspension-feeding macrobenthos near abyssal hydrothermal vents at oceanic spreading centers. *Deep Sea Research*, 24(9), 857–863. [https://doi.org/10.1016/0146-6291\(77\)90478-7](https://doi.org/10.1016/0146-6291(77)90478-7)
- Lowell. (1995). Seafloor hydrothermal systems.
- Lowell. (2010). Hydrothermal Circulation at Slow Spreading Ridges: Analysis of Heat Sources and Heat Transfer Processes.
- Lowell, R. P., & Germanovich, L. N. (1997). Evolution of a brine-saturated layer at the base of a ridge-crest hydrothermal system. *Journal of Geophysical Research: Solid Earth*, 102(B5), 10245–10255. <https://doi.org/10.1029/97jb00264>
- Lowell, Robert P., & Burnell, D. K. (1991). Mathematical modeling of conductive heat transfer from a freezing, convecting magma chamber to a single-pass hydrothermal system: implications for seafloor black smokers. *Earth and Planetary Science Letters*, 104(1), 59–69. [https://doi.org/10.1016/0012-821x\(91\)90237-c](https://doi.org/10.1016/0012-821x(91)90237-c)
- Lowell, Robert P., & Yao, Y. (2002). Anhydrite precipitation and the extent of hydrothermal recharge zones at ocean ridge crests. *Journal of Geophysical Research: Solid Earth*, 107(B9), EPM 2-1-EPM 2-9. <https://doi.org/10.1029/2001jb001289>
- Lowell, Robert P., Yao, Y., & Germanovich, L. N. (2003). Anhydrite precipitation and the relationship between focused and diffuse flow in seafloor hydrothermal systems. *Journal of Geophysical Research: Solid Earth*, 108(B9). <https://doi.org/10.1029/2002jb002371>
- Lucazeau, F. (2019). Analysis and Mapping of an Updated Terrestrial Heat Flow Data Set. *Geochemistry, Geophysics, Geosystems*, 20(8), 4001–4024. <https://doi.org/10.1029/2019gc008389>
- Lucazeau, Francis, Bonneville, A., Escartin, J., Herzen, R. P. V., Gouze, P., Carton, H., et al. (2006). Heat flow variations on a slowly accreting ridge: Constraints on the hydrothermal and conductive cooling for the Lucky Strike segment (Mid-Atlantic Ridge, 37°N). *Geochemistry, Geophysics, Geosystems*, 7(7), n/a-n/a. <https://doi.org/10.1029/2005gc001178>
- Macdonald, K., Sempere, J., & Fox, P. J. (1984). East Pacific Rise from Siqueiros to Orozco Fracture Zones: Along-strike continuity of axial neovolcanic zone and structure and evolution of overlapping spreading centers. *Journal of Geophysical Research: Solid Earth*, 89(B7), 6049–6069. <https://doi.org/10.1029/jb089ib07p06049>
- Macdonald, K. C. (2001). Encyclopedia of Ocean Sciences. *Article Titles: M*, (Nature3221986), 1798–1813. <https://doi.org/10.1006/rwos.2001.0094>
- MACDONALD, K. C., SCHEIRER, D. S., & CARBOTTE, S. M. (1991). Mid-Ocean Ridges: Discontinuities, Segments and Giant Cracks. *Science*, 253(5023), 986–994. <https://doi.org/10.1126/science.253.5023.986>

REFERENCES

- Madsen, J. A., Forsyth, D. W., & Detrick, R. S. (1984). A new isostatic model for the East Pacific Rise crest. *Journal of Geophysical Research: Solid Earth*, 89(B12), 9997–10015. <https://doi.org/10.1029/jb089ib12p09997>
- Marjanović, M., Carbotte, S. M., Carton, H., Nedimović, M. R., Mutter, J. C., & Canales, J. P. (2014). A multi-sill magma plumbing system beneath the axis of the East Pacific Rise. *Nature Geoscience*, 7(11), 825–829. <https://doi.org/10.1038/ngeo2272>
- Marjanović, M., Carbotte, S. M., Carton, H. D., Nedimović, M. R., Canales, J. P., & Mutter, J. C. (2018). Crustal Magmatic System Beneath the East Pacific Rise (8°20' to 10°10'N): Implications for Tectonomagmatic Segmentation and Crustal Melt Transport at Fast-Spreading Ridges. *Geochemistry, Geophysics, Geosystems*, 19(11), 4584–4611. <https://doi.org/10.1029/2018gc007590>
- Marjanović, M., Barreyre, T., Fontaine, F. J., & Escartín, J. (2019). Investigating Fine-Scale Permeability Structure and Its Control on Hydrothermal Activity Along a Fast-Spreading Ridge (the East Pacific Rise, 9°43'–53'N) Using Seismic Velocity, Poroelastic Response, and Numerical Modeling. *Geophysical Research Letters*, 46(21), 11799–11810. <https://doi.org/10.1029/2019gl084040>
- Mendel, V., Sauter, D., Rommevaux-Jestin, C., Patriat, P., Lefebvre, F., & Parson, L. M. (2003). Magmato-tectonic cyclicity at the ultra-slow spreading Southwest Indian Ridge: Evidence from variations of axial volcanic ridge morphology and abyssal hills pattern. *Geochemistry, Geophysics, Geosystems*, 4(5), n/a-n/a. <https://doi.org/10.1029/2002gc000417>
- Mével, C. (2003). Serpentinization of abyssal peridotites at mid-ocean ridges. *Comptes Rendus Geoscience*, 335(10–11), 825–852. <https://doi.org/10.1016/j.crte.2003.08.006>
- Miller, A. D., Foulger, G. R., & Julian, B. R. (1998). Non-double-couple earthquakes 2. Observations. *Reviews of Geophysics*, 36(4), 551–568. <https://doi.org/10.1029/98rg00717>
- Mittelstaedt, E., Escartín, J., Gracias, N., Olive, J., Barreyre, T., Davaille, A., et al. (2012). Quantifying diffuse and discrete venting at the Tour Eiffel vent site, Lucky Strike hydrothermal field. *Geochemistry, Geophysics, Geosystems*, 13(4), n/a-n/a. <https://doi.org/10.1029/2011gc003991>
- Olive, J., & Crone, T. J. (2018). Smoke Without Fire: How Long Can Thermal Cracking Sustain Hydrothermal Circulation in the Absence of Magmatic Heat? *Journal of Geophysical Research: Solid Earth*, 123(6), 4561–4581. <https://doi.org/10.1029/2017jb014900>
- Ondréas, H., Cannat, M., Fouquet, Y., Normand, A., Sarradin, P. M., & Sarrazin, J. (2009). Recent volcanic events and the distribution of hydrothermal venting at the Lucky Strike hydrothermal field, Mid-Atlantic Ridge. *Geochemistry, Geophysics, Geosystems*, 10(2), n/a-n/a. <https://doi.org/10.1029/2008gc002171>

REFERENCES

- Parnell-Turner, R., Sohn, R. A., Peirce, C., Reston, T. J., MacLeod, C. J., Searle, R. C., & Simão, N. M. (2017). Oceanic detachment faults generate compression in extension. *Geology*, *45*(10), 923–926. <https://doi.org/10.1130/g39232.1>
- Parnell-Turner, R., Sohn, R. A., Peirce, C., Reston, T. J., MacLeod, C. J., Searle, R. C., & Simão, N. M. (2020). Seismicity trends and detachment fault structure at 13°N, Mid-Atlantic Ridge. *Geology*, *49*(3), 320–324. <https://doi.org/10.1130/g48420.1>
- Parson, L. M., Murton, B. J., Searle, R. C., Booth, D., Evans, J., Field, P., et al. (1993). En echelon axial volcanic ridges at the Reykjanes Ridge: a life cycle of volcanism and tectonics. *Earth and Planetary Science Letters*, *117*(1–2), 73–87. [https://doi.org/10.1016/0012-821x\(93\)90118-s](https://doi.org/10.1016/0012-821x(93)90118-s)
- Penrose. (1972). Penrose field conference on ophiolites. *Geomatics*, *17*, 24–25.
- Perrot, J. (2012). HYDROBS-MOMAR 2012 cruise, RV Thalassa. <https://doi.org/10.17600/12040070>
- Pontbriand, C. W., & Sohn, R. A. (2014). Microearthquake evidence for reaction-driven cracking within the Trans-Atlantic Geotraverse active hydrothermal deposit. *Journal of Geophysical Research: Solid Earth*, *119*(2), 822–839. <https://doi.org/10.1002/2013jb010110>
- Raitt, M. (1963). The crustal rocks. *The Sea*, *3*, 85–102.
- Ross, A., Foulger, G. R., & Julian, B. R. (1996). Non-double-couple earthquake mechanisms at the Geysers Geothermal Area, California. *Geophysical Research Letters*, *23*(8), 877–880. <https://doi.org/10.1029/96gl00590>
- Sánchez-Mora, D., Jamieson, J., Cannat, M., Escartín, J., & Barreyre, T. (2022). Age and Rate of Accumulation of Metal-Rich Hydrothermal Deposits on the Seafloor: The Lucky Strike Vent Field, Mid-Atlantic Ridge. *Journal of Geophysical Research: Solid Earth*, *127*(6). <https://doi.org/10.1029/2022jb024031>
- Sauter, D., Cannat, M., Rouméjon, S., Andreani, M., Birot, D., Bronner, A., et al. (2013). Continuous exhumation of mantle-derived rocks at the Southwest Indian Ridge for 11 million years. *Nature Geoscience*, *6*(4), 314–320. <https://doi.org/10.1038/ngeo1771>
- Scherbaum, F., & Bouin, M. (1997). FIR filter effects and nucleation phases. *Geophysical Journal International*, *130*(3), 661–668. <https://doi.org/10.1111/j.1365-246x.1997.tb01860.x>
- Scholz, J.-R., Barruol, G., Fontaine, F. R., Sigloch, K., Crawford, W. C., & Deen, M. (2016). Orienting ocean-bottom seismometers from P -wave and Rayleigh wave polarizations. *Geophysical Journal International*, *208*(3), 1277–1289. <https://doi.org/10.1093/gji/ggw426>

REFERENCES

- Schulte-Pelkum, V., Masters, G., & Shearer, P. M. (2001). Upper mantle anisotropy from long-period P polarization. *Journal of Geophysical Research: Solid Earth*, 106(B10), 21917–21934. <https://doi.org/10.1029/2001jb000346>
- Searle, M. (2013). Crustal melting, ductile flow, and deformation in mountain belts: Cause and effect relationships. *Lithosphere*, 5(6), 547–554. <https://doi.org/10.1130/rlf.1006.1>
- Searle, R. C., Murton, B. J., Achenbach, K., LeBas, T., Tivey, M., Yeo, I., et al. (2010). Structure and development of an axial volcanic ridge: Mid-Atlantic Ridge, 45°N. *Earth and Planetary Science Letters*, 299(1–2), 228–241. <https://doi.org/10.1016/j.epsl.2010.09.003>
- Seher, T., Crawford, W. C., Singh, S. C., Cannat, M., Combier, V., & Dusanur, D. (2010). Crustal velocity structure of the Lucky Strike segment of the Mid-Atlantic Ridge at 37°N from seismic refraction measurements. *Journal of Geophysical Research: Solid Earth (1978–2012)*, 115(B3). <https://doi.org/10.1029/2009jb006650>
- Shi, Y., & Bolt, B. A. (1982). The standard error of the magnitude-frequency b value. *Bulletin of the Seismological Society of America*, 72(5), 1677–1687. <https://doi.org/10.1785/bssa0720051677>
- Sigmundsson, F., Hooper, A., Hreinsdóttir, S., Vogfjörð, K. S., Ófeigsson, B. G., Heimisson, E. R., et al. (2015). Segmented lateral dyke growth in a rifting event at Bárðarbunga volcanic system, Iceland. *Nature*, 517(7533), 191–195. <https://doi.org/10.1038/nature14111>
- Singh, S. C., Crawford, W. C., Carton, H., Seher, T., Combier, V., Cannat, M., et al. (2006). Discovery of a magma chamber and faults beneath a Mid-Atlantic Ridge hydrothermal field. *Nature*, 442(7106), 1029–1032. <https://doi.org/10.1038/nature05105>
- Sinha, M. C., Navin, D. A., MacGregor, L. M., Constable, S., Peirce, C., White, A., et al. (1997). Evidence for accumulated melt beneath the slowspreading MidAtlantic Ridge. *Philosophical Transactions of the Royal Society of London. Series A: Mathematical, Physical and Engineering Sciences*, 355(1723), 233–253. <https://doi.org/10.1098/rsta.1997.0008>
- Sinton, J. M., & Detrick, R. S. (1992). Mid-ocean ridge magma chambers. *Journal of Geophysical Research: Solid Earth*, 97(B1), 197–216. <https://doi.org/10.1029/91jb02508>
- Small, C. (1998). Faulting and Magmatism at Mid-Ocean Ridges. *Geophysical Monograph Series*, 1–25. <https://doi.org/10.1029/gm106p0001>
- Snoke, J. A., Lee, W. H. K., Kanamori, H., Jennings, P. C., & Kisslinger, C. (2003). FOCMEC: Focal mechanism determinations. *International Handbook of Earthquake and Engineering Seismology*.
- Sohn, R., Crawford, W., & Webb, S. (1999). Local seismicity following the 1998 eruption.

REFERENCES

- Sohn, R. A., Hildebrand, J. A., & Webb, S. C. (1999). A microearthquake survey of the high-temperature vent fields on the volcanically active East Pacific Rise (9°50'N). *Journal of Geophysical Research: Solid Earth*, 104(B11), 25367–25377. <https://doi.org/10.1029/1999jb900263>
- Sohn, R. A., Barclay, A. H., & Webb, S. C. (2004). Microearthquake patterns following the 1998 eruption of Axial Volcano, Juan de Fuca Ridge: Mechanical relaxation and thermal strain. *Journal of Geophysical Research: Solid Earth (1978–2012)*, 109(B1). <https://doi.org/10.1029/2003jb002499>
- Soule, S. A., Escartín, J., & Fornari, D. J. (2009). A record of eruption and intrusion at a fast spreading ridge axis: Axial summit trough of the East Pacific Rise at 9–10°N. *Geochemistry, Geophysics, Geosystems*, 10(10), n/a-n/a. <https://doi.org/10.1029/2008gc002354>
- Spieß, F. N., Macdonald, K. C., Atwater, T., Ballard, R., Carranza, A., Cordoba, D., et al. (1980). East Pacific Rise: Hot Springs and Geophysical Experiments. *Science*, 207(4438), 1421–1433. <https://doi.org/10.1126/science.207.4438.1421>
- Spudich, P., & Orcutt, J. (1980). A new look at the seismic velocity structure of the oceanic crust. *Reviews of Geophysics*, 18(3), 627–645. <https://doi.org/10.1029/rg018i003p00627>
- Stachnik, J. C., Sheehan, A. F., Zietlow, D. W., Yang, Z., Collins, J., & Ferris, A. (2012). Determination of New Zealand Ocean Bottom Seismometer Orientation via Rayleigh-Wave Polarization. *Seismological Research Letters*, 83(4), 704–713. <https://doi.org/10.1785/0220110128>
- Stein, S. and. (1994). Constraints on hydrothermal heat flux through the oceanic lithosphere from global heat flow.
- Tan, Y. J., Tolstoy, M., Waldhauser, F., & Wilcock, W. S. D. (2016). Dynamics of a seafloor-spreading episode at the East Pacific Rise. *Nature*, 540(7632), 261–265. <https://doi.org/10.1038/nature20116>
- Tapponnier, P., & Francheteau, J. (1978). Necking of the lithosphere and the mechanics of slowly accreting plate boundaries. *Journal of Geophysical Research: Solid Earth*, 83(B8), 3955–3970. <https://doi.org/10.1029/jb083ib08p03955>
- Tarantola, A., & Valette, B. (1982). Generalized nonlinear inverse problems solved using the least squares criterion. *Reviews of Geophysics*, 20(2), 219–232. <https://doi.org/10.1029/rg020i002p00219>
- Tivey, M. (2007). Generation of Seafloor Hydrothermal Vent Fluids and Associated Mineral Deposits. *Oceanography*, 20(1), 50–65. <https://doi.org/10.5670/oceanog.2007.80>
- Tolstoy, M., Cowen, J. P., Baker, E. T., Fornari, D. J., Rubin, K. H., Shank, T. M., et al. (2006). A Sea-Floor Spreading Event Captured by Seismometers. *Science*.

REFERENCES

- Tolstoy, M., Waldhauser, F., Bohnenstiehl, D. R., Weekly, R. T., & Kim, W.-Y. (2008). Seismic identification of along-axis hydrothermal flow on the East Pacific Rise. *Nature*, *451*(7175), 181–184. <https://doi.org/10.1038/nature06424>
- Tolstoy, Maya, Harding, A. J., & Orcutt, J. A. (1993). Crustal Thickness on the Mid-Atlantic Ridge: Bull's-Eye Gravity Anomalies and Focused Accretion. *Science*, *262*(5134), 726–729. <https://doi.org/10.1126/science.262.5134.726>
- Toomey, D. R., Solomon, S. C., & Purdy, G. M. (1994). Tomographic imaging of the shallow crustal structure of the East Pacific Rise at 9°30'N. *Journal of Geophysical Research: Solid Earth*, *99*(B12), 24135–24157. <https://doi.org/10.1029/94jb01942>
- Trabattoni, A., Barruol, G., Dreo, R., Boudraa, A. O., & Fontaine, F. R. (2019). Orienting and locating ocean-bottom seismometers from ship noise analysis. *Geophysical Journal International*. <https://doi.org/10.1093/gji/ggz519>
- Tucholke, B. E., Behn, M. D., Buck, W. R., & Lin, J. (2008). Role of melt supply in oceanic detachment faulting and formation of megamullions. *Geology*, *36*(6), 455–458. <https://doi.org/10.1130/g24639a.1>
- Vera, E. E., Mutter, J. C., Buhl, P., Orcutt, J. A., Harding, A. J., Kappus, M. E., et al. (1990). The structure of 0- to 0.2-m.y.-old oceanic crust at 9°N on the East Pacific Rise from expanded spread profiles. *Journal of Geophysical Research: Solid Earth*, *95*(B10), 15529–15556. <https://doi.org/10.1029/jb095ib10p15529>
- Von-Damm, K. L., & Lilley, M. D. (2004). Diffuse flow hydrothermal fluids from 9 50'N East Pacific Rise: Origin, evolution and biogeochemical controls. *{Washington DC American Geophysical Union Geophysical Monograph Series, 144, 245–268.*
- Waldhauser, F., & Ellsworth, W. L. (2000). A Double-Difference Earthquake Location Algorithm: Method and Application to the Northern Hayward Fault, California. *Bulletin of the Seismological Society of America*, *90*(6), 1353–1368. <https://doi.org/10.1785/0120000006>
- Waldhauser, F., & Tolstoy, M. (2011). Seismogenic structure and processes associated with magma inflation and hydrothermal circulation beneath the East Pacific Rise at 9°50'N. *Geochemistry, Geophysics, Geosystems*, *12*(8), n/a-n/a. <https://doi.org/10.1029/2011gc003568>
- Wang, X., & Cochran, J. R. (1993). Gravity anomalies, isostasy, and mantle flow at the East Pacific Rise crest. *Journal of Geophysical Research: Solid Earth*, *98*(B11), 19505–19531. <https://doi.org/10.1029/93jb01551>
- Weekly, R. T., Wilcock, W. S. D., Hooft, E. E. E., Toomey, D. R., McGill, P. R., & Stakes, D. S. (2013). Termination of a 6 year ridge-spreading event observed using a seafloor seismic network on the Endeavour Segment, Juan de Fuca Ridge. *Geochemistry, Geophysics, Geosystems*, *14*(5), 1375–1398. <https://doi.org/10.1002/ggge.20105>

REFERENCES

- Wheeler, B. (2021). *From the magma chamber to microhabitats: dynamics of diffuse hydrothermal circulations at mid-ocean ridges*. Thesis prepared at the Institut de Physique du Globe de Paris Université de Paris.
- White, R. S., McKenzie, D., & O'Nions, R. K. (1992). Oceanic crustal thickness from seismic measurements and rare earth element inversions. *Journal of Geophysical Research: Solid Earth*, 97(B13), 19683–19715. <https://doi.org/10.1029/92jb01749>
- Wichers, S., Singh, H., & Reves-Sohn, R. (2005). *Verification of numerical models for hydrothermal plume water through field measurements at TAG*. -Joint Program in Applied Ocean Science and Engineering, Massachusetts Institute of Technology, Dept. of Ocean Engineering; and the Woods Hole Oceanographic Institution, Cambridge, Mass.
- Wiemer, S., & Wyss, M. (2002). Mapping spatial variability of the frequency-magnitude distribution of earthquakes. *In Advances in Geophysics (Vol. 45, Pp. 259-V)*. Elsevier.
- Wilcock, W. S. D. (1998). Cellular convection models of mid-ocean ridge hydrothermal circulation and the temperatures of black smoker fluids.
- Wilcock, William S. D., Archer, S. D., & Purdy, G. M. (2002). Microearthquakes on the Endeavour segment of the Juan de Fuca Ridge. *Journal of Geophysical Research: Solid Earth (1978–2012)*, 107(B12), EPM 4-1-EPM 4-21. <https://doi.org/10.1029/2001jb000505>
- Wilcock, William S. D., Hooft, E. E. E., Toomey, D. R., McGill, P. R., Barclay, A. H., Stakes, D. S., & Ramirez, T. M. (2009). The role of magma injection in localizing black-smoker activity. *Nature Geoscience*, 2(7), 509–513. <https://doi.org/10.1038/ngeo550>
- Wilcock, William S. D., Tolstoy, M., Waldhauser, F., Garcia, C., Tan, Y. J., Bohnenstiehl, D. R., et al. (2016). Seismic constraints on caldera dynamics from the 2015 Axial Seamount eruption. *Science*, 354(6318), 1395–1399. <https://doi.org/10.1126/science.aah5563>
- Wilcock, William S.D., & Delaney, J. R. (1996). Mid-ocean ridge sulfide deposits: Evidence for heat extraction from magma chambers or cracking fronts? *Earth and Planetary Science Letters*, 145(1–4), 49–64. [https://doi.org/10.1016/s0012-821x\(96\)00195-1](https://doi.org/10.1016/s0012-821x(96)00195-1)
- Woessner, J., & Wiemer, S. (2005). Assessing the Quality of Earthquake Catalogues: Estimating the Magnitude of Completeness and Its Uncertainty. *Bulletin of the Seismological Society of America*, 95(2), 684–698. <https://doi.org/10.1785/0120040007>
- Wolfe, C. J., Purdy, G. M., Toomey, D. R., & Solomon, S. C. (1995). Microearthquake characteristics and crustal velocity structure at 29°N on the Mid-Atlantic Ridge: The architecture of a slow spreading segment. *Journal of Geophysical Research: Solid Earth*, 100(B12), 24449–24472. <https://doi.org/10.1029/95jb02399>
- Xu, W., Yuan, S., Wang, W., Luo, X., & Li, L. (2020). Comparing Orientation Analysis Methods for a Shallow-Water Ocean-Bottom Seismometer Array in the Bohai Sea, China.

REFERENCES

Bulletin of the Seismological Society of America, 110(6), 3174–3184.
<https://doi.org/10.1785/0120200174>

Zha, Y., Webb, S. C., & Menke, W. (2013). Determining the orientations of ocean bottom seismometers using ambient noise correlation. *Geophysical Research Letters*, 40(14), 3585–3590. <https://doi.org/10.1002/grl.50698>

Zhu, G., Yang, H., Lin, J., & You, Q. (2020). Determining the Orientation of Ocean-Bottom Seismometers on the Seafloor and Correcting for Polarity Flipping via Polarization Analysis and Waveform Modeling. *Seismological Research Letters*, 91(2A), 814–825.
<https://doi.org/10.1785/0220190239>